

**PHOTON PRODUCTION IN NUCLEUS
NUCLEUS COLLISIONS
AT FORWARD RAPIDITIES AT RHIC
ENERGIES**

A THESIS SUBMITTED TO THE
JADAVPUR UNIVERSITY
FOR THE DEGREE OF
DOCTOR OF PHILOSOPHY IN SCIENCE
(PHYSICS)
FEBRUARY, 2007

By
PAWAN KUMAR NETRAKANTI

VARIABLE ENERGY CYCLOTRON CENTRE, KOLKATA 700 064,
INDIA

CERTIFICATE FROM THE SUPERVISOR

This is to certify that the thesis entitled “**Photon production in nucleus nucleus collisions at forward rapidities at RHIC energies**” submitted by **Mr. Pawan Kumar Netrakanti**, who got his name registered on 28.06.2005 for the award of Ph.D. (Science) degree of Jadavpur University, is absolutely based upon his own work under the supervision of Dr. Y. P. Viyogi and that neither this thesis nor any part of it has been submitted for any degree / diploma or any other academic award anywhere before

Dr. Y.P. Viyogi

(Signature of the supervisor and date with official seal)

Variable Energy Cyclotron Centre

Kolkata

Acknowledgments

First of all I would like to thank Dr. Y. P. Viyogi, my thesis advisor at the Variable Energy Cyclotron Centre, for his invaluable guidance, encouragement and his constant support throughout my research period at VECC.

I would also like to express my sincere thanks to Dr. Bedangadas Mohanty of VECC, who is the foremost important person responsible for motivating me to pursue research as a career. His in-depth knowledge and practical experiences about the field helped me not only in pursuing physics challenges which I came across during my research period but also helped me to initiate ideas and accomplish them successfully in my life. I cannot forget the long sessions of discussion and the pains taken by him to help me in learning c++ programming and basics of heavy ion physics.

I would like to express my sincere thanks to Prof. B. Sinha Director of VECC and SINP for his help and encouragement in all respect. I would like to express my sincere thanks to Dr. D. K. Srivastava, Dr. S. Pal, Dr. S. K. Basu, Dr. A. Chaudhuri, Dr. A. Dhara, Dr. P. Barat and Dr. S. Bhattacharya for their advice, support, constant encouragement and good wishes for me. I thank Dr. J. Alam and Dr. S. Sarkar for many interesting and stimulating discussions which I had with them.

It was a nice experience working with Dr. S. Chattopadhyay, Dr. T. K. Nayak, Dr. Z. Ahammed, Dr. P. Ghosh, Mr. G. S. N. Murthy, Mr. M. R. Duttamazumdar, Mr. R. N. Singaraju, Mr. S. Pal, Mr. V. Singhal and Mr. J. Saini of PMD group at VECC. I feel I was very fortunate to work with a number of research scholar friends in the collaboration, Mr. D. Das, Mr. S. Das and Mr. P. Ghosh of VECC, Ms. M. Sharma of Panjab university, Mr. S. Bhardwaj of Rajasthan University, Mr. R. Sahoo and Mr. D. Mishra from IOP Bhubaneswar and Mr. S. M. Dogra of Jammu University, I thank them for their help and co-operation.

I would like to thank the RHIC Operations Group, the RHIC Computing Facility at BNL and NERSC center at LBL for their support.

I would like to thank our spokes-person, Dr. T. Hallman for his interest in my work and his support which helped me in working closely with the BNL heavy ion group. He has always supported me and my work. I also express my sincere thanks to Dr. Z. Xu from BNL for inviting me for a period of three months at BNL to work on challenging project of particle identification at high transverse momentum using the relativistic rise in ionization energy loss in STAR TPC. During this stay I learned lot of interesting things about the detectors from him. The work was completed and the results were published in Physics Letters. I would also like to thank Dr. P. Seyboth, Mrs. J. Seyboth, Dr. E. Hjort and Dr. F. Simon for spending time with me and helping me in understanding the various aspects of FTPC data during my stay at BNL . I would like to thank Dr. N. Xu, LBL for his advice regarding my future career path. I would thank Dr. J. Lauret from BNL for many interesting discussions on computing and other topics and for his invaluable help towards my BNL visits and research. I would also like to sincerely thank Dr. W. Christie, Dr. R. Brown, Dr. B. Stringfellow, Dr. A. Lebedev and Dr. T. Ljubicic for the invaluable help during PMD installation and commissioning and helping me during the PMD servicing and maintenance period. I thank every member of the STAR collaboration for their hard work to make the experiment run smoothly and successfully.

It was equally interesting to work closely with other members of the PMD group. It includes Dr. M. M. Aggarwal, Dr. A .K. Bhati and their group in Panjab University, Chandigarh, Dr. S. Raniwala and their group from University of Rajasthan, Jaipur, Dr. L. K. Mangotra and their group at Jammu University, Jammu, Dr. D. P. Mohapatra, Dr. S .C. Phatak and their group at Institute of Physics, Bhubaneswar, Dr. R. Varma and Dr. B. K. Nandi at Indian Institute of Technology, Bombay. There suggestions and comments during the collaboration meetings helped me a lot to improve my physics analysis and results.

I would also like to thank my friend Mr. Apu Sarkar who also joined with me in research at the same time in VECC. I enjoyed the chat which we used to have almost daily in the night during taking tea at the Canteen. I will always remember the enjoyable discussions and moments spent with Dr. L. Damodaran, Dr. M. Madhegowda and Mr. P. Jakl during my stay at BNL. I am also thankful to all the staff of VECC library, the people who have maintained our computer center and all the administrative and non-academic staff of VECC, for their support, co-operation and help at every stage.

My humble regards, respect and thanks goes to my parents for their patience and encouragement during my research period. It is because of their love, affection and blessings that I could complete this thesis.

Date:

Pawan Kumar Netrakanti

Synopsis

According to the theory of strong interactions, Quantum Chromodynamics(QCD), quarks are almost noninteracting at short distances and the interactions become stronger as the distance increases between them. This leads to the confinement of quarks within hadrons. Later it was shown by lattice calculations that at high temperature, high density QCD behaves qualitatively different from that at low temperature and density. At high temperatures ($T \sim 200$ MeV) or high baryon density (~ 5 to 10 times normal nuclear matter density), QCD allows the possibility of a state of matter, called Quark Gluon Plasma (QGP), where the quarks and gluons from the nuclei are weakly interacting and no longer confined inside hadrons. Such matter can be produced by colliding two nuclei in the laboratory at relativistic energies.

One of the primary goals of the heavy-ion program at the Relativistic Heavy-Ion Collider (RHIC) at Brookhaven National Laboratory is to search for the possible formation of Quark-Gluon Plasma. In such collisions we correlate information obtained from various global observables (e.g multiplicity of photons , charged particles and transverse energy) in order to understand the dynamics of particle production and evolution of the system. Photons are produced at all stages of the system created in heavy ion collisions. They have large mean free paths and are therefore good carriers of information about the history of the collision. The multiplicity measurement of photons on an event by event basis can be used to extract information on the various aspects of the reaction mechanism in the heavy ion collisions. Even though several measurements have been done for photons at mid-rapidity, almost no effort is made to detect photon at forward rapidities. Forward rapidity, in heavy ion collisions, constitutes an environment which precludes the use of a calorimeter because of enormous overlap of fully developed showers.

Keeping this in mind, a highly granular photon multiplicity detector (PMD) was fabricated and installed in STAR experiment at RHIC, by our group at Variable Energy Cyclotron Centre, Kolkata in the year 2002. PMD has taken data for

Au on Au collisions at 200 and 62.4 GeV center of mass energy. PMD measures the multiplicity and pseudorapidity distribution of photons in the forward rapidity (2.3 to 3.7). The PMD is located 5.4 meters away from the nominal interaction point along the beam axis. It consists of two planes (preshower and charged particle veto) of an array consists of 41472 cellular gas proportional counters in each plane. A 3 radiation length thick lead plate located between the two planes was used as a photon converter. A gas mixture of *Ar* and *CO₂* in the ratio 70:30 by weight was used as the sensitive medium. The cells in each plane are placed inside 12 high voltage insulated and gas-tight chambers called super modules (SM). A photon passing through the converter produces an electromagnetic shower and the electrons and positrons from the shower are detected by the preshower plane behind the converter. By using a suitable threshold on the energy deposition and the number of cells in a cluster, one can discriminate photons and hadrons in the detected sample of clusters.

In the thesis, I plan to study the photon multiplicity and spatial distribution of photons on an event-by-event basis for various collision systems and energies (as available at RHIC) as a function of collision centrality. By studying the scaling of the photon production at forward rapidities with the number of participating nucleons, I would like to understand the dynamics of particle production in heavy ion collisions. It will be interesting to study the pseudorapidity distribution of photons per participating nucleon pair as a function of pseudorapidity shifted by beam rapidity. This will help us to understand the limiting fragmentation phenomena. I would like to explore the energy and the centrality dependence of limiting fragmentation for measured photons. I would also like to make a comparison between the measured photon distributions with the charged particles distribution in order to understand the charge and neutral production mechanisms in heavy ion collisions. The results from the experimental data taken by PMD will be compared with the various model calculations. More specifically, I will be comparing the results from photon measurements to a model based on perturbative QCD processes which lead to multiple jet production and jet interactions in the matter. I will also compare the data to a multiphase transport model which includes initial partonic and final hadronic interactions.

List of Publications

1. **Identified hadron spectra at large transverse momentum in $p+p$ and $d+Au$ collisions at $\sqrt{s_{NN}} = 200$ GeV,**
STAR Collaboration, J. Adams *et. al.*,
Phys. Lett. B 637 (2006) 161.

- *2. **Multiplicity and pseudorapidity distributions of charged particles and photons at forward pseudorapidity in Au+Au collisions at $\sqrt{s_{NN}} = 62.4$ GeV,**
STAR Collaboration, J. Adams *et. al.*,
Phys. Rev. C 73 (2006) 034906.

3. **Directed flow in Au+Au collisions $\sqrt{s_{NN}} = 62.4$ GeV,**
STAR Collaboration, J. Adams *et. al.*,
Phys. Rev. C 73 (2006) 034903.

4. **Incident energy dependence of p_T correlations at RHIC,**
STAR Collaboration, J. Adams *et. al.*,
J. Adams *et. al.*, STAR Collaboration,
Physical Review C 72 (2005) 044902.

- *5. **The width of the rapidity distribution in heavy ion collision,**
Pawan Kumar Netrakanti and Bedangadas Mohanty,
Physical Review C 71 (2005) 047901.

6. **Multi-strange baryon elliptic flow in Au+Au collisions at $\sqrt{s_{NN}} = 200$ GeV,**

STAR Collaboration, J. Adams *et. al.*,
Physical Review Letters 95 (2005) 122301.

7. Distributions of charged hadrons associated with high transverse momentum particles in pp and Au+Au collisions at $\sqrt{s_{NN}} = 200$ GeV,

STAR Collaboration, J. Adams *et. al.*,
Physical Review Letters 95 (2005) 152301.

***8. Multiplicity and pseudorapidity distributions of photons in Au+Au collisions at $\sqrt{s_{NN}} = 62.4$ GeV,**

STAR Collaboration, J. Adams *et. al.*,
Physical Review Letters 95 (2005) 062301.

9. $K^*(892)$ resonance production in Au+Au and p+p collisions at $\sqrt{s_{NN}} = 200$ GeV at STAR,

STAR Collaboration, J. Adams *et. al.*,
Physical Review C 71 (2005) 064902.

10. Pion interferometry in Au+Au collisions at $\sqrt{s_{NN}} = 200$ GeV,

STAR Collaboration, J. Adams *et. al.*,
Physical Review C 71 (2005) 044906.

11. Experimental and theoretical challenges in the search for the quark gluon plasma : The STAR Collaboration's critical assessment of the evidence from RHIC collisions,

STAR Collaboration, J. Adams *et. al.*,
Nuclear Physics A 757 (2005) 102.

12. Open charm yields in d+Au collisions at $\sqrt{s_{NN}} = 200$ GeV,

STAR Collaboration, J. Adams *et. al.*,
Physical Review Letters 94 (2005) 062301.

13. Transverse-momentum dependent modification of dynamic texture in central Au+Au collisions at $\sqrt{s_{NN}} = 200$ GeV,

STAR Collaboration, J. Adams *et. al.*,
Physical Review C 71 (2005) 031901.

15. **Pion,kaon, proton and anti-proton transverse momentum distributions from p+p and d+Au collisions at $\sqrt{s_{NN}} = 200$ GeV,**
STAR Collaboration, J. Adams *et. al.*,
Physics Letters B 616 (2005) 8.
13. **ϕ meson production in Au+Au collisions at $\sqrt{s_{NN}} = 200$ GeV,**
STAR Collaboration, J. Adams *et. al.*,
Physics Letters B 612 (2005) 181.
14. **Azimuthal anisotropy and correlations at large transverse momenta in p+p and Au+Au collisions at $\sqrt{s_{NN}} = 200$ GeV,**
STAR Collaboration, J. Adams *et. al.*,
Physical Review Letters 93 (2004) 252301.
15. **Pseudorapidity asymmetry and centrality dependence of charged hadron spectra in d+Au collisions at $\sqrt{s_{NN}} = 200$ GeV,**
STAR Collaboration, J. Adams *et. al.*,
Physical Review C 70 (2004) 064907.
16. **Measurements of transverse energy distributions in Au+Au collisions at $\sqrt{s_{NN}} = 200$ GeV,**
STAR Collaboration, J. Adams *et. al.*,
Physical Review C 70 (2004) 054907.
17. **Centrality and pseudorapidity dependence of charged hadron production at intermediate p_T in Au+Au collisions at $\sqrt{s_{NN}} = 130$ GeV,**
STAR Collaboration, J. Adams *et. al.*,
Physical Review C 70 (2004) 044901.
18. **Production of e^+e^- pairs accompanied by nuclear dissociation in ultra-peripheral heavy ion collision,**
STAR Collaboration, J. Adams *et. al.*,
Physical Review C 70 (2004) 031902.
19. **Azimuthally sensitive HBT in Au+Au collisions at $\sqrt{s_{NN}} = 200$ GeV,**
STAR Collaboration, J. Adams *et. al.*,
Physical Review Letters 93 (2004) 012301.

- *20. **Quark participants and global observables**,
Pawan Kumar Netrakanti and Bedangadas Mohanty,
Physical Review C 70 (2004) 027901.
- 21. **Azimuthal anisotropy and correlations at large transverse momenta in p+p and Au+Au collisions at $\sqrt{s_{NN}} = 200$ GeV**,
STAR Collaboration, J. Adams *et. al.*,
Physical Review Letters 93 (2004) 252301.

** Results from these publications are included in this thesis.*

Publications in Conferences, Symposia and Internal notes

1. **Identified particle transverse momentum spectra in p+p and d+Au collisions at $\sqrt{s} = 200$ GeV**,
P.K. Netrakanti (for STAR Collaboration),
e-Print Archive: nucl-ex/0601022,
Proceedings of Particles and Nuclei International Conference, Santa Fe, NM-
October 24-28 (2005).
2. **First results from Photon Multiplicity Detector at RHIC Au-Au collisions at $\sqrt{s} = 62.4$ GeV**,
P.K. Netrakanti (for STAR Collaboration),
Proceedings of XVI DAE High Energy Physics Symposium (2004) 65.
3. **First results from Photon Multiplicity Detector at RHIC Au-Au collisions at $\sqrt{s} = 62.4$ GeV**,
B.Mohanty, ..., P.K. Netrakanti, *et. al.*,
Proceedings of DAE symposium on Nuclear physics Vol.47B (2004) 388.
4. **Quark participants and global observables**,
P.K. Netrakanti and Bedangadas Mohanty,
Proceedings of DAE symposium on Nuclear physics Vol.47B (2004) 390.

Table of Contents

CERTIFICATE FROM THE SUPERVISOR	ii
Acknowledgments	iii
1 INTRODUCTION	1
1.1 Quark Hadron Phase Transition	1
1.2 Possible signatures of Quark-Gluon Plasma formation	6
1.2.1 Strange Particle production	6
1.2.2 Quarkonium Suppression	8
1.2.3 Mean transverse momentum and temperature	11
1.2.4 Fluctuation of transverse energy and multiplicity	13
1.2.5 Electromagnetic probes	15
1.3 Photon multiplicity measurements in heavy ion collisions	18
1.3.1 Photon Multiplicity Detector (PMD) at SPS	19
1.3.2 Photon pseudorapidity distribution at SPS energies	20
1.3.3 Scaling of photon multiplicity with N_{part} at SPS energies	22
1.4 Charged particle multiplicity measurements	23
1.4.1 Charged particle multiplicity measurements at SPS	23
1.4.2 Charged particle multiplicity measurements at RHIC	24
1.4.3 Charged particle multiplicity at mid-rapidity	25
1.4.4 Scaling of charged particle multiplicity with N_{part} at RHIC	26
1.4.5 Longitudinal scaling of charged particle pseudorapidity density	28
2 STAR EXPERIMENT	39
2.1 Introduction	39
2.2 STAR Detector	41
2.3 Trigger Detectors	43
2.3.1 Central Trigger Barrel	44

2.3.2	Zero degree Calorimeter	44
2.3.3	Multi-Wire Counter	47
2.3.4	Beam-Beam Counter	47
2.4	DAQ and Triggering	49
2.5	STAR Magnet	50
2.6	Time Projection Chamber	52
2.6.1	TPC design	52
2.6.2	Tracking Efficiency	54
2.6.3	Vertex resolution	55
2.6.4	Particle identification using dE/dx	56
2.6.5	Centrality selection	58
2.7	Electromagnetic Calorimeters	59
2.7.1	Barrel electromagnetic calorimeter	59
2.7.2	Endcap electromagnetic calorimeter	60
2.8	Time-of-flight detector	61
2.9	Forward time projection chamber	62
2.9.1	FTPC design	63
2.9.2	Readout Chamber	65
2.9.3	Readout Electronics	66
2.10	Photon multiplicity detector	68
2.10.1	The PMD Detector	71
2.10.2	Front end electronics and Readout	76
2.10.3	Trigger and Data acquisition	77
3	PHOTON RECONSTRUCTION	84
3.1	Data selection	85
3.2	Data cleanup	91
3.3	Cell-to-Cell Gain Calibration	97
3.4	Occupancy	109
3.5	Clustering	110
3.5.1	Algorithm	110
3.5.2	Photon conversion efficiency	114
3.5.3	Clustering efficiency	117
3.5.4	Track, clusters and optimization of clustering algorithm	118
3.5.5	Discrimination of photons and charged hadrons	129
3.6	Photon counting efficiency and purity of photon sample	133
3.7	Consistency checks	137

3.7.1	Consistency check using simulated data	138
3.7.2	Consistency check using real data	139
3.7.3	Consistency check for the cell-to-cell gain variation	140
4	CHARGED PARTICLE RECONSTRUCTION	142
4.1	Reconstruction and simulation of the experimental data	142
4.1.1	Reconstruction of track points (Cluster finding)	143
4.1.2	Cluster deconvolution and fitting of track points	145
4.1.3	Calibration of electronics	145
4.1.4	Gain Tables	146
4.2	Track reconstruction and particle momenta	147
4.3	Procedure to obtain performance parameters of FTPC	147
4.3.1	The embedding procedure	149
4.3.2	Checks with the embedded data	151
4.4	Tracking efficiency and momentum resolution	153
4.4.1	Matching of reconstruction and simulation	153
4.4.2	Tracking efficiency and purity	155
4.4.3	Momentum resolution and charge determination error	158
4.4.4	Limitations	160
5	PHOTON AND CHARGED PARTICLE PRODUCTION	166
5.1	Photon and charged particle pseudorapidity and multiplicity distributions	168
5.1.1	Multiplicity distributions for photons and charged particles	168
5.1.2	Fluctuation of N_γ and N_{ch}	169
5.1.3	Pseudorapidity distributions for photons and charged particles	170
5.1.4	Model comparison of pseudorapidity distributions for photons and charged particles	171
5.1.5	Energy dependence of pseudorapidity distributions for photons and charged particles	174
5.1.6	Parametrization of pseudorapidity distribution for charged particles at RHIC	176
5.1.7	Comparison of N_{ch} and N_γ	177
5.2	Width of rapidity and pseudorapidity distributions	178
5.2.1	\sqrt{s} and centrality dependence of width of rapidity and pseudorapidity distributions	179

5.2.2	Effect of longitudinal flow on width of rapidity and pseudo-rapidity distributions	181
5.2.3	Effect of velocity of sound on width of rapidity and pseudo-rapidity distributions	183
5.2.4	Effect of initial and final state re-scattering on width of rapidity and pseudorapidity distributions	185
5.2.5	Scaling of the width of pseudorapidity distributions at ISR and RHIC	186
5.3	Scaling of particle production	187
5.3.1	Scaling of particle production with N_{part}	189
5.3.2	Scaling of particle production with N_{coll}	189
5.3.3	Scaling of particle production with N_{qpart}	192
5.4	Longitudinal Scaling	195
5.4.1	Longitudinal scaling for $e^+ + e^-$, $p+p(\bar{p})$ and $p(d)+\text{Au}$ collision	197
5.4.2	Energy dependence of longitudinal scaling in nucleus-nucleus collisions	199
5.4.3	Centrality dependence of longitudinal scaling in nucleus-nucleus collisions	200
5.4.4	Species dependence of longitudinal scaling	203
5.4.5	Longitudinal scaling in particle production models	206
5.4.6	Longitudinal scaling in particle production models	206

6 CONCLUSION

Chapter 1

INTRODUCTION

1.1 Quark Hadron Phase Transition

At high density (several times ordinary nuclear matter density) or high temperature (beyond a few hundred MeV) all known hadrons are expected to dissolve into a plasma of their elementary constituents, the quarks and the gluons, forming a new state of matter: the quark gluon plasma (QGP) [1]. The transition from the QGP to hadronic matter is one of several transitions occurring in the early universe. It is supposed to take place during the first few microseconds after the big bang, when the temperature is of the order of 200 MeV. The study of this phase transition and of the corresponding plasma is an interesting and active field of research. Indeed, much of the present interest in the QGP is coming from the hope to observe it in laboratory experiments, by colliding heavy nuclei at high energies. An important experimental program is underway, both in the USA (RHIC at Brookhaven) [2] and in Europe at CERN Geneva [3], to understand the properties of matter formed in such collisions.

We know that quarks and gluons are confined inside the hadrons. Within the standard model of the strong interactions, which so far works very well, the interaction between two hadrons occurs via the interaction between the quarks of one and the quarks of the other, i.e. the exchange of gluons between quarks. Since quarks are confined, this means that gluons must cross the confinement barrier otherwise there would be no interaction. Strongly interacting matter is described at the fundamental level through the interaction of quarks by the exchange of gluons. Quantum chromodynamics (QCD), theory of strong interactions, exhibits a number of remarkable features:

1. At short distances or large momenta q , the effective coupling constant $\alpha_s(q^2)$ decreases logarithmically, i.e. quarks and gluons appear to be weakly coupled.
2. At large distances or small momenta, the effective coupling becomes strong, resulting in the phenomena of quark confinement and chiral symmetry breaking.
3. At low energies, the QCD vacuum is characterized by non-vanishing expectation values of certain operators, usually called vacuum condensates, which characterize the nonperturbative physical properties of the QCD vacuum.

Most important for our discussion are [4]:

- (a) the quark condensate and,
- (b) the gluon condensate.

The quark condensate describes the density of quark-antiquark pairs found in the QCD vacuum and is the expression of chiral symmetry breaking. The gluon condensate measures the density of gluon pairs in the QCD vacuum and is a manifestation of the breaking of scale invariance of QCD by quantum effects. It is not uncommon in nature that spontaneously broken symmetries are restored at high temperature through phase transitions. Well known examples are ferromagnetism, superconductivity, and the transition from solid to liquid. More closely connected to our subject, nuclear matter at low temperatures has a dense liquid phase, which goes over into a dilute gaseous phase at $T > 5$ MeV. Evidence for this phase transition has recently been seen in nuclear collisions at intermediate energies [5].

As the temperature increases in QCD, the interactions among quanta occur at even shorter distances, governed by weak coupling, while the long-range interactions become dynamically screened. This picture is supported by finite temperature perturbation theory, showing that the effective coupling constant $\alpha_s(T)$ falls logarithmically with increasing temperature [6] and also by more general arguments [7]. As a consequence, nuclear matter at very high temperature exhibits neither confinement nor chiral symmetry breaking and leads to formation of quark-gluon plasma.

The lattice QCD calculations predict a phase transition from hadronic gas to a quark-gluon plasma [8, 9]. The critical values of energy density ($\epsilon^{critical}$) predicted by these calculations are at ≈ 2 GeV/ fm^3 , at a critical temperature ($T^{critical}$) \approx

175–200 MeV. The relation of this phase transition to the various phases of nuclear matter can be seen in schematic diagram shown in Fig. 1.1. In most scenarios of

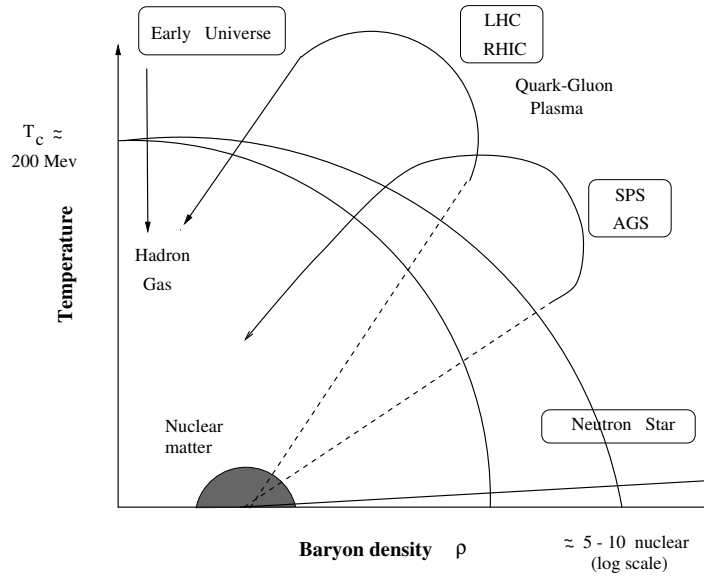


Figure 1.1: Schematic phase diagram for high energy nucleus nucleus collision. X-axis is the baryon density and Y-axis is the temperature.

cosmology, a quark-gluon plasma should have existed less than a second after the Big Bang. According to astrophysics, the plasma may exist in the cores of the neutron stars and in other dense stellar objects. Very high energy nucleus-nucleus collisions may provide the conditions necessary for formation of a quark-gluon plasma and a means of studying it in laboratory.

The formation of a quark-gluon plasma in very high energy collisions of heavy nuclei has been studied in various theoretical models. In collision process, the energy and baryon densities are expected to increase and reach critical values where the quark constituents of the incident nucleons, bound in nuclei, form an extended volume of freely interacting quarks, antiquarks and gluons. The system must sustain these conditions for a time longer than the transition time of the two interacting nuclei in order for quark-gluon plasma phase to form without dilution by subsequent interactions. These high baryon and energy densities necessary for the formation of a quark-gluon plasma may best be reached in collisions of heavy nuclei at very high energies given adequate thermalization.

While possible formation of a quark-gluon plasma is the underlying motivation for this field of physics, a study of the dynamics of the collision processes is of fundamental importance for understanding the microscopic structure of hadronic interactions at high densities, at the level of quarks and gluons, and the conditions for formation of the plasma. The primary goal of the Relativistic Heavy Ion Collider (RHIC) program at Brookhaven National Laboratory is to create such a system of quark gluon plasma and study its properties in detail. This is believed to be achieved by colliding two heavy ions (mostly Au+Au), using a dedicated accelerator for heavy ion collisions, at various center of mass energies ($\sqrt{s_{NN}}$) between 20 to 200 GeV. The space-time evolution of the system formed in the heavy ion

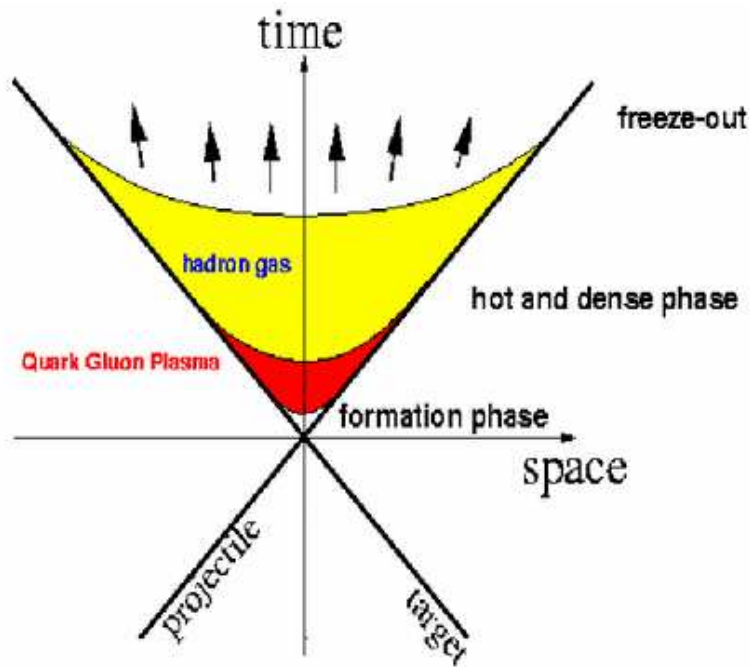


Figure 1.2: The space-time picture and the different evolution stages of a relativistic heavy ion collision.

collisions is shown diagrammatically in Fig. 1.2. In high energy heavy ion collision experiments, two nuclei are accelerated to required collision energy. They approach each other with velocities very close to the velocity of light. As a result the nuclei, which are normally spherical in shape (mostly Au or Pb are collided), are Lorentz contracted along the direction of their motion (beam direction or Z-axis

by convention). This results in their shape to be like a pancake. At the moment of collision or impact we consider $Z=0$ and time $t=0$. After a certain initial time of the order of $\sim 0.2 - 1 \text{ fm}$ depending on beam energy, the nucleons inside the overlap regions of the two nuclei start interacting to produce a dense matter with densities much higher than normal nuclear matter density. The energy density and the temperatures reached can be so high that it may melt down the constituents of the colliding nucleons into a soup of quarks and gluons. After a certain time the system will reach equilibrium and the deconfined quarks and gluons again will start to hadronize. If this phase transition from quarks and gluons to hadrons is of first order then it will go through a mixed phase at a certain critical temperature. In the mixed phase the temperature of the system is expected to be constant with increase in entropy and there will be co-existence of hadrons, quarks and gluons. In the mixed phase the latent heat is used up to convert the quarks and gluons to hadrons. When all the quark and gluon degrees of freedom are converted to hadronic degrees of freedom the mixed phase ends. The interactions however persists and the system expands and cools. When the inelastic interactions stops, resulting in no more new particles being produced, we say the system has reached a chemical equilibrium. The particle ratios are fixed at this point. The system keeps on expanding, and as a result it keeps on further cooling. A time and temperature is reached when the distance between any two particles in the medium is larger than the average mean free path. At this point of time the elastic collisions also stop.

We call this time (temperature) as kinetic freeze out time (temperature). The particles at this point come out of the system and gets detected in the detectors. Finally only 5 kinds of stable charged particles are mostly detected in the detector systems, they are - electrons, muons, pions, kaons and protons along with their anti-particles. Among the neutral particles , we detect neutrons and photons.

To find evidence for the formation of the quark gluon plasma in such collisions, several signatures have been proposed [10]. These predicted signatures are briefly discussed in the next section. Also mentioned are the present understanding of results on these signatures from experiments at SPS [11, 12, 13] and RHIC [14, 15, 16, 17].

1.2 Possible signatures of Quark-Gluon Plasma formation

Experimental investigations of the quark-gluon plasma require the identification of appropriate experimental observables and techniques for observing its formation and understanding its properties. One serious problem is that the size and lifetime of the plasma are expected to be small, at most a few fm in diameter and perhaps 5 to 10 fm/c in duration. Furthermore, signals of the quark-gluon plasma compete with backgrounds emitted from the hot hadronic gas phase that follows the hadronization of the plasma, and are modified by final state interactions in the hadronic phase. In spite of this, a wealth of ideas has been proposed in the past decade as to how the identification and investigation of the short-lived quark-gluon plasma phase could be accomplished. More details can be found elsewhere [18, 19, 20, 21].

1.2.1 Strange Particle production

One of the earliest predictions for a signature of the deconfinement transition is an enhancement of s and \bar{s} quarks in a quark-gluon plasma in thermal and chemical equilibrium [22]. In a QGP, gluons are abundantly produced and many quark-antiquark pairs are created via gluon-gluon fusion. In this process, strange quark-antiquark would be produced more frequently than in the nucleon-nucleon collisions because of coupling of gluons to strange quarks and to light quarks is the same and the higher mass of strange quarks would not be important due to high available energy. The strangeness enhancement in a baryon rich matter can also be a result of the Pauli principle: suppression of $u\bar{u}$ and $d\bar{d}$ pair production in favor of $s\bar{s}$ pairs in initial u and d -rich environment remaining from the incident nuclei. Furthermore, the \bar{u} and \bar{d} anti-quarks annihilate with u and d quarks, while $s\bar{s}$ annihilation occurs less frequently until saturation of the s and \bar{s} abundances. Most calculations predict an enhancement in the observed \bar{s} yield as a signature of plasma formation while s quark yields, although enhanced, differ only slightly in a plasma compared to a hadron gas. The strangeness enhancement factor is defined as the yield per participating nucleon of a given type of strange particle in the heavy ion collisions (either Pb+Pb at SPS or Au+Au at RHIC) relative to strange particle yield in p +Be at SPS and p + p at RHIC. Fig. 1.3 shows the strangeness enhancement factor in Pb+Pb collisions relative to p +Be collisions at $\sqrt{s_{NN}} =$

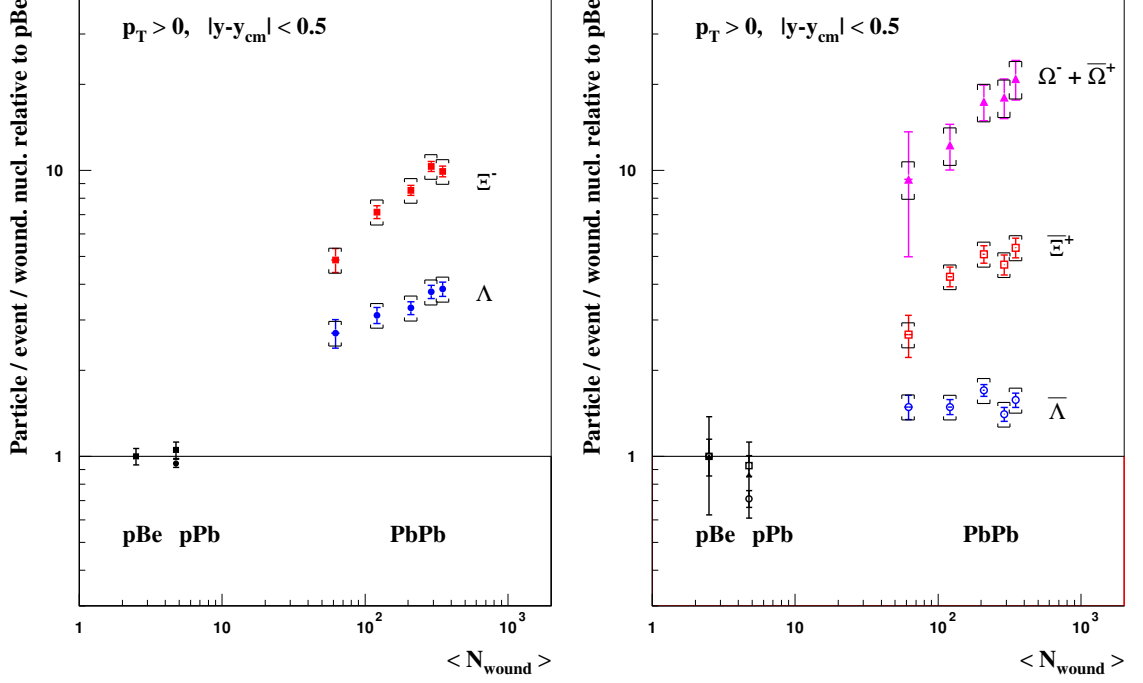


Figure 1.3: Measurements on strange particle enhancements for $\sqrt{s_{NN}} = 17.3$ GeV Pb+Pb collisions in NA57 experiment at SPS as function of number of wounded nucleons (collision centrality).

17.3 GeV in NA57 experiment at SPS [23]. The Pb+Pb data exhibit a significant centrality dependence of the enhancements for all strange particle yields studied except $\bar{\Lambda}$.

Fig. 1.4 shows the strangeness enhancement factor in Au+Au collisions at $\sqrt{s_{NN}} = 200$ GeV in STAR experiment for Λ and Ξ along with their antiparticles [24]. We observe that the strange particles show significant enhancement in the yields, while \bar{p} (non strange particle) shows almost no enhancement as a function of collision centrality. Furthermore we observe that as the strangeness content (i.e. number of s quarks in a particle) increases the strangeness enhancement factor also increases at both SPS and RHIC energies.

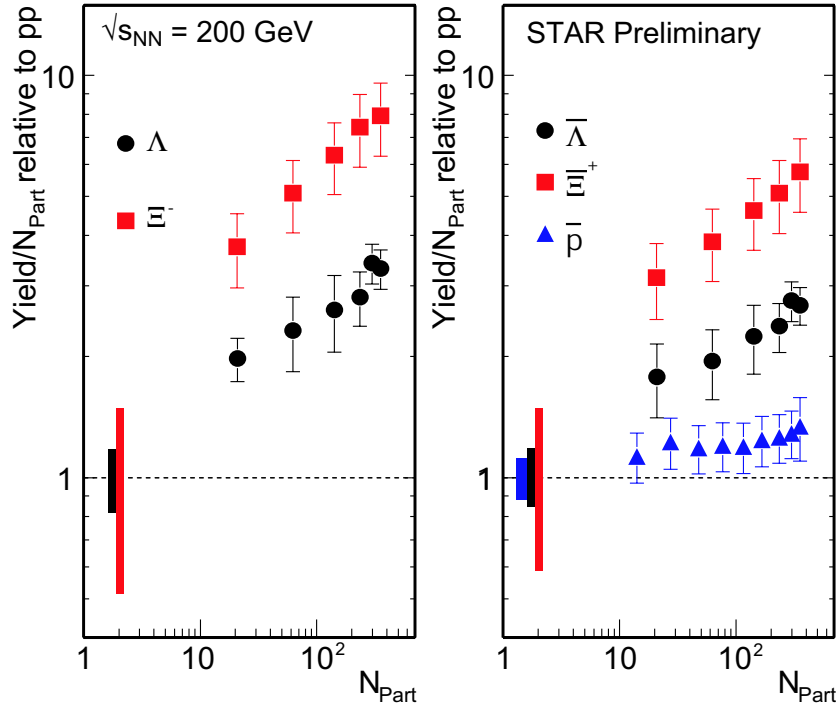


Figure 1.4: The enhancement in the strange particle yields per participating nucleon in Au+Au collisions relative to strange particle yields in $p+p$ collisions at $\sqrt{s_{\text{NN}}} = 200$ GeV as a function of collision centrality from STAR experiment. The uncertainties shown are a combination of statistical and systematic errors added in quadrature.

1.2.2 Quarkonium Suppression

The suppression of J/Ψ production in a quark-gluon plasma occurs because a $c\bar{c}$ pair formed by fusion of two gluons from the colliding nuclei cannot bind inside the quark-gluon plasma [25]. Lattice simulations of SU(3) gauge theory [26, 27] show that this condition should be satisfied already slightly above the deconfinement temperature ($T_c \sim 160\text{-}190$ MeV). The screening length appears to be even shorter when dynamical fermions are included in the lattice simulations [28, 29]. Excited states of the $(c\bar{c})$ system, such as Ψ' and χ_c , are more easily dissociated and should disappear as soon as the temperature exceeds T_c . For the heavier $\Upsilon(b\bar{b})$ system similar considerations apply, although shorter screening lengths are required than for the charmonium states [30]. The dissociation temperature of the Υ ground

state is predicted to be around $2.5 T_c$, that of the larger Υ' state only slightly above T_c .

Owing to its finite size, the formation of a $(c\bar{c})$ bound state requires a time of the order of $1 fm/c$ [31, 32, 33]. The J/Ψ may still survive, if it escapes from the region of high density and temperature before the $c\bar{c}$ pair has been spatially separated by more than the size of the bound state [25]. This will happen either if the quark-gluon plasma cools very fast, or if the J/Ψ has sufficiently high transverse momentum [34, 35, 36, 37]. On the other hand, the charmonium may also be destroyed by sufficiently energetic collisions with comoving hadrons, leading to dissociation into a pair of D -mesons [38, 39]. Dissociation via quark exchange with mesons composed of light quarks, such as the ρ -meson, has been estimated in a non-relativistic quark model [40] to have cross section reaching several mb . Similar values are obtained, if J/Ψ production is fed by a large fraction of easily absorbed color-octet $(c\bar{c})$ states [41]. Additional effects that can contribute to J/Ψ suppression even in hadron nucleus interactions are nuclear shadowing of soft gluons, initial state scattering of partons resulting in a widened transverse momentum distribution, and final state absorption on nucleons [42, 43, 44]. Suppression mechanisms based on interactions with comoving particles generally predict that the Ψ' state should be more strongly suppressed than the J/Ψ [30, 45]. This holds equally for a quark-gluon plasma as for a comoving thermalized gas of hadrons.

At SPS the suppression of J/Ψ [46] and Ψ' [47] production relative to that of the Drell-Yan continuum in most central nucleus-nucleus collisions has been measured at $\sqrt{s_{NN}} = 17.3$ GeV. The suppression of the Ψ' is observed to be larger than that of the J/Ψ in central nucleus-nucleus collisions. Such suppression is predicted to result from color screening of the $c\bar{c}$ pair in a deconfined medium [25]. It has also been predicted to occur as a result of final-state interactions in a dense hadronic medium [48]. A similar suppression has also been seen in J/Ψ production in hadron-nucleus interactions [49] and μ -nucleus interactions [50], lending credence to a hadronic mechanism to describe the observed suppression. However, Ψ'/Ψ ratios have been measured in proton-proton and proton-nucleus interactions and found to be constant, independent of the nuclear mass of the target [51].

So if we observe a suppression in J/Ψ production in nucleus-nucleus collisions relative to nucleon-nucleon and nucleon-nucleus collisions, then it can be considered as a good signature of QGP. Further one can study the centrality dependence of J/Ψ production, a suppression in central collisions relative to peripheral events can also be considered as a good signature for QGP.

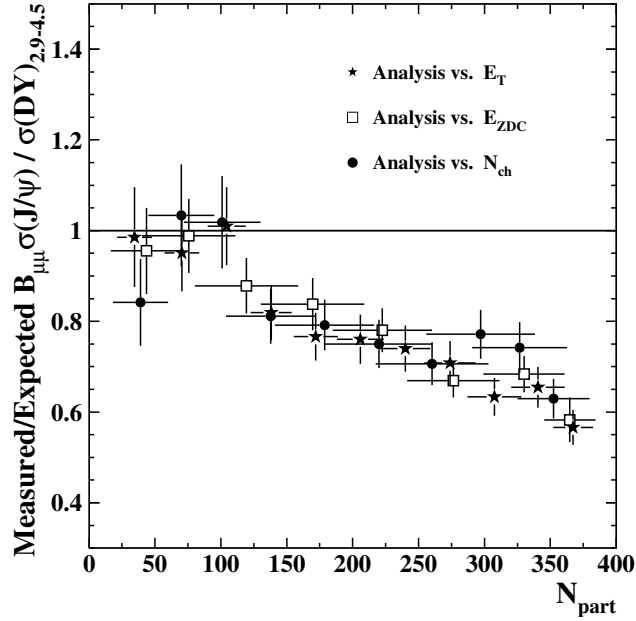


Figure 1.5: The $(J/\Psi)/$ Drell-Yan cross-sections ratio as a function of N_{part} for three analyses of the Pb+Pb data sample taken in the year 2000 at $\sqrt{s_{\text{NN}}} = 17.3$ GeV, divided by the normal nuclear absorption values. The data are from NA50 experiment at SPS.

Fig. 1.5 shows the $(J/\Psi)/$ Drell-Yan cross-sections ratio as a function of N_{part} for three analyses (using transverse energy, forward energy and charged particle multiplicity for centrality selection) of the Pb+Pb data sample taken in the year 2000 at $\sqrt{s_{\text{NN}}} = 17.3$ GeV, divided by the normal nuclear absorption values. The data are from NA50 experiment at SPS [52]. The value of this ratio is less than unity for central collisions and around unity for peripheral collisions. This indicates a clear suppression of J/Ψ production in central Pb+Pb collisions at $\sqrt{s_{\text{NN}}} = 17.3$ GeV in SPS.

Fig. 1.6 shows the nuclear modification factor R_{AA} (yields normalized to those from p+p collisions after appropriate binary collision scaling in nucleus-nucleus collisions) for J/Ψ production in Au+Au and Cu+Cu collisions as a function of the number of participants for two different rapidity ranges from PHENIX experiment at RHIC for $\sqrt{s_{\text{NN}}} = 200$ GeV [53]. All data points seem to follow the same general

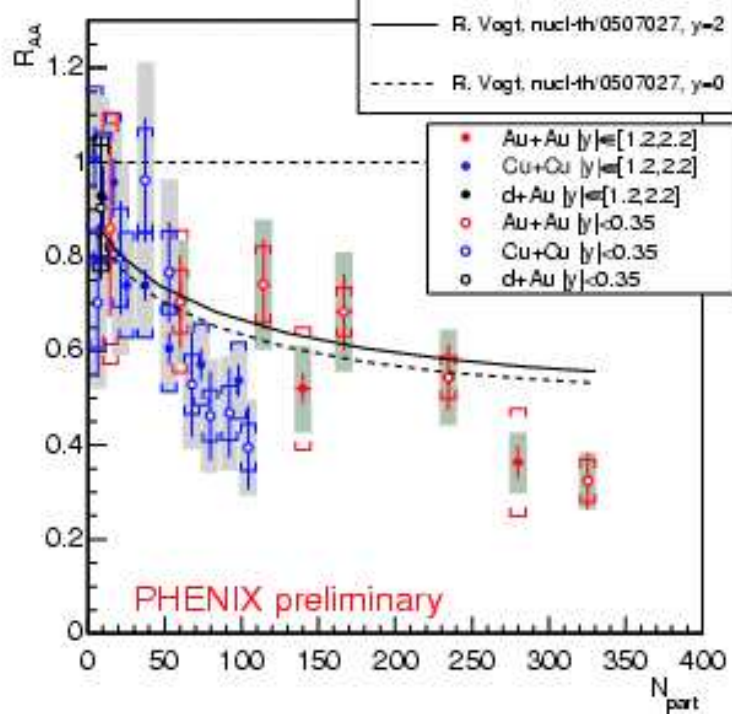


Figure 1.6: J/Ψ nuclear modification factor (R_{AA}) as a function of the number of participants at two different rapidity regions for Au+Au, Cu+Cu and d +Au at $\sqrt{s_{NN}} = 200$ GeV from PHENIX experiment at RHIC. Vertical bars show statistical errors, brackets show point-to-point and boxes show global systematic errors. The data is compared to baseline calculation of the normal-nuclear-absorption model. The results are preliminary.

trend. In the most central collisions a suppression of about a factor 3 relative to binary-scaled p+p collisions is observed. To interpret the results the data is compared to the baseline calculation of the normal-nuclear-absorption model [54]. The model cannot describe the suppression observed in the data for the most central collisions.

1.2.3 Mean transverse momentum and temperature

In analogy to the phase change of melting ice, that of the deconfinement transition from hadrons to quark-gluon plasma (if it is a first order phase transition) can be represented by Fig. 1.7. The phase diagram can be understood as follows.

The temperature of the system increases as the entropy is increased until transition temperature. At this point the phase transition occurs and the temperature remains constant with two phases coexisting until all the matter has undergone the transition. Above this point the temperature will increase again as the entropy increases. The mean transverse momentum $\langle p_T \rangle$ of hadrons reflects the temperature [55]. The rapidity density of produced hadrons reflects the entropy of the system formed in heavy ion collisions. An observation of temperature of the system as function of incident energy or particle density exhibiting a trend similar to Fig. 1.7 can be considered as a signature of first order phase transition. Such a signature was proposed in Ref. [56]. In this paper it is proposed to study the correlations between $\langle p_T \rangle$ and the multiplicity per unit rapidity dN/dy to study phase transition in the heavy ion collision. A detailed study on this can be performed using the heavy ion data at different center-of-mass energies with different colliding nuclei and for different centralities provided if one can handle normalizations properly.

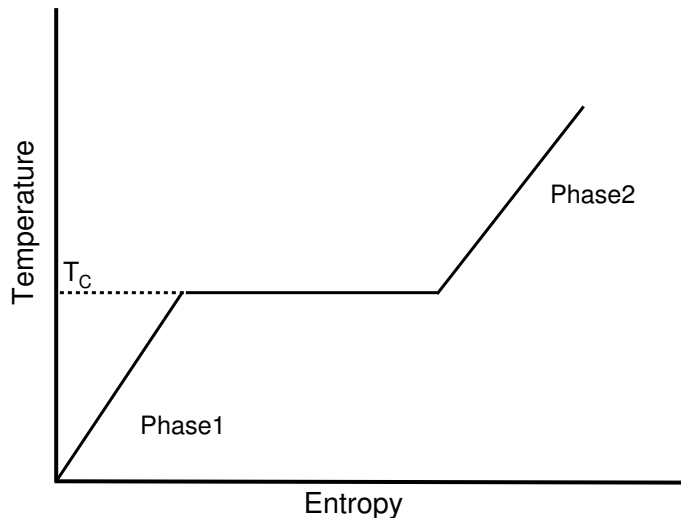


Figure 1.7: Typical diagram of temperature vs. entropy for a system undergoing first order phase transition. The mixed phase is reflected as the plateau of the diagram at critical temperature (T_C).

However, a complication of this scheme is that the temperature is usually measured from the p_T spectra of hadrons at the freezeout stage. It has been proposed

that direct photons or dilepton pairs be measured since their interaction probabilities with nuclear matter are small. These probes should then provide information on the hot plasma phase of the collision process. In Fig. 1.8 the variation of $\langle m_T \rangle$ with charge multiplicity is depicted for pions, kaons and protons at AGS ($\sqrt{s_{NN}} \sim 2$ to 4.6 GeV), SPS ($\sqrt{s_{NN}} \sim 8$ to 17.3 GeV) and RHIC ($\sqrt{s_{NN}} \sim 19.6$ to 200 GeV) energies around mid-rapidity. The experimental data on transverse mass spectra at all energies has been parametrized as,

$$\frac{dN}{m_T dm_T} \sim C \exp\left(-\frac{m_T}{T_{eff}}\right), \quad (1.1)$$

where the inverse slope parameter T_{eff} is the effective temperature (effective because it includes the contribution due to both the thermal and collective motion in the transverse direction). The data shown here correspond to central events (top 5% to 10% of the cross section) for different colliding systems, produced particle types and center of mass energies [57]. The SPS results are from Pb+Pb collisions while the AGS and RHIC results are from Au+Au collisions. The effect on the results obtained from these two colliding species (Pb+Pb at SPS and Au+Au at AGS,RHIC) is not expected to be much because of their similar size. The spectra are fitted in the range $0.1 < (m_T - m_0) < 1.0$ GeV. The average transverse mass of the particle corresponding to the transverse mass distribution of Eq. 1.1 is calculated as :

$$\langle m_T \rangle = T_{eff} + m_0 + \frac{(T_{eff})^2}{m_0 + T_{eff}}. \quad (1.2)$$

where m_0 rest mass of the particle. From the results shown in Fig. 1.8, one observes an increase in $\langle m_T \rangle$ with dN_{ch}/dy for AGS energies followed by a plateau for charge multiplicities corresponding to SPS energies for all the particle types, pions, kaons and protons. This may hint at the possible co-existence of the quark and hadron phases. For charged particle multiplicities corresponding to RHIC energies, the $\langle m_T \rangle$ is higher than the constant value observed at SPS energies, indicating the possibility of a pure QGP formation at RHIC.

1.2.4 Fluctuation of transverse energy and multiplicity

Event-by-event fluctuation of the transverse energy per unit rapidity has been proposed [58] as a signature of a first order phase transition. With such a transition large amounts of energy will be liberated in the system, perhaps localized in space, leading to deflagration or detonation and explosion. These localized explosions

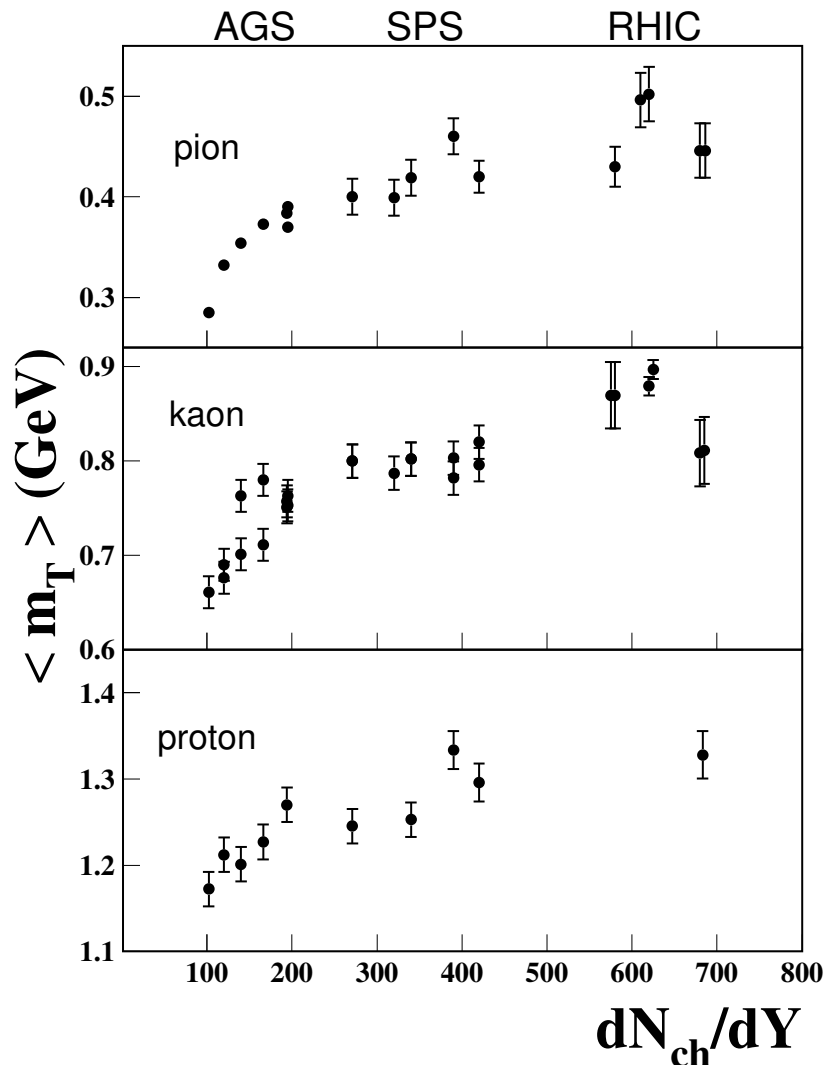


Figure 1.8: Variation of $\langle m_T \rangle$ ($m_T = \sqrt{p_T^2 + m_0^2}$) with produced charged particles per unit rapidity at mid-rapidity for central collisions corresponding to different $\sqrt{s_{NN}}$ spanning from AGS to RHIC. The error bars reflect both the systematic and statistical errors in obtaining $\langle m_T \rangle$.

result in large fluctuations in the production of matter and energy as a function of the rapidity of the products formed in the collisions. Therefore, distributions of dE_t/dy or dN/dy as a function of rapidity y may exhibit large fluctuations at the rapidities of the deflagration or detonations providing possible signatures of plasma formation.

1.2.5 Electromagnetic probes

Photons and lepton pairs provide probes of the interior of the quark-gluon plasma during the earliest and hottest phase of the evolution of the fireball since they are not affected by final state interactions. Unfortunately, these probes have rather small yields and must compete with relatively large backgrounds from hadronic processes, especially electromagnetic hadron decays.

Many of the early calculations on lepton pairs as probes of the quark-gluon plasma [59, 60, 61, 62, 63, 64] concentrated on invariant masses in the range below the ρ -meson mass. With an improved understanding of the collision dynamics and the hadronic backgrounds, it has since become clear that lepton pairs from the quark-gluon plasma can probably only be identified for invariant masses above 1 – 1.5 GeV. At the high-mass end, the yield of Drell-Yan pairs from first nucleon-nucleon collisions exceeds the thermal dilepton yield.

Recent progress in understanding the mechanisms of thermalization has revealed that the yield of high-mass dileptons critically depends on, and provides a measure of, the thermalization time [65]. Lepton pairs from the equilibrating quark-gluon plasma may dominate over the Drell-Yan background up to masses in the range 5 – 10 GeV, as predicted by the parton cascade and other models of the early equilibration phase of the nuclear collision. If this turns out to be true, the early thermal evolution of the quark-gluon phase can be traced in a rather model independent way [66]. Dileptons from charm decay are predicted to yield a substantial contribution to the total dilepton spectrum and could, because of their different kinematics, provide a measure of the total charm yield, which may be enhanced due to rescattering of gluonic partons, if the direct background is sufficiently well understood.

If a photon is produced in a QGP it leaves the hot plasma with a small probability of interacting with the matter formed in the collision. It would keep the memory of the temperature in which it was created and would therefore be a good signature of the QGP. In order to see whether there are directly produced photons in the QGP we must study inclusive photon production and find out whether

there are some kinematical differences between the sample of the selected inclusive photons and the photons which are known to originate from the normal hadron decays. Direct photons as a signature of QGP has been discussed in Ref. [67] and the references therein.

However, a clear signal of photons from the quark-gluon plasma could be visible for transverse momenta p_T in the range 2 – 5 GeV/ c if a very hot plasma is formed initially [66]. The photon spectrum in the p_T range 1 – 2 GeV/ c is mostly emitted from the mixed phase. Transverse flow effects make the separation of the contributions from the different phases more difficult [68], and destroy the correlation between the slope of the photon spectrum in the intermediate p_T range and the temperature of the mixed phase [69].

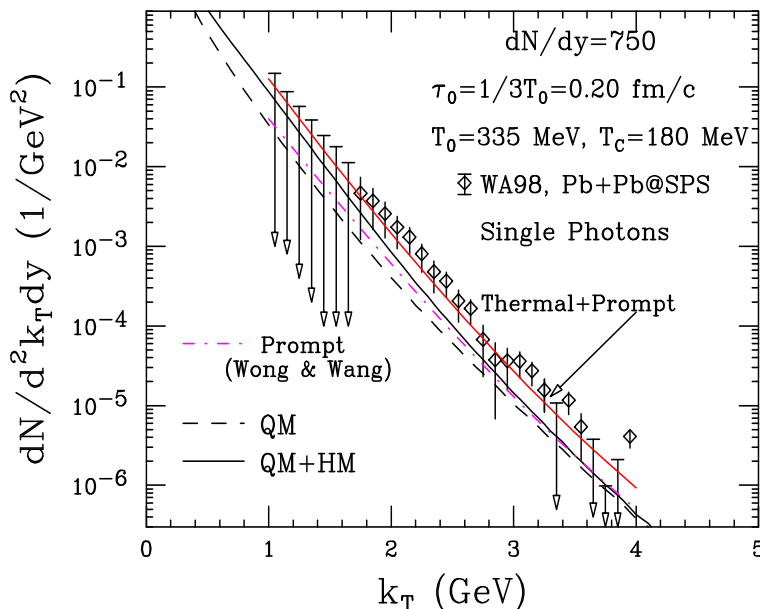


Figure 1.9: The invariant direct photon multiplicity for central Pb+Pb collisions at $\sqrt{s_{NN}} = 17.3$ GeV. The error bars indicate the combined statistical and systematical errors. Data points with downward arrows indicate unbounded 90% CL upper limits. The model calculation shown in form of lines and are described in the text.

At top SPS energy of $\sqrt{s_{NN}} = 17.3$ GeV, observation of direct photons was made in the WA98 experiment [70]. In Fig. 1.9 we show the invariant direct photon multiplicity for central Pb+Pb collisions at $\sqrt{s_{NN}} = 17.3$ GeV [70]. The model calculations shown in form of lines in Fig. 1.9 are from Ref. [71]. The calculation assumes that a chemically and thermally equilibrated quark-gluon plasma is formed

at $\tau_0 = 1/3T_0$ which expands, cools, enters into a mixed phase and undergoes freeze-out from a hadronic phase. QM stands for radiations from the quark matter in the QGP phase and the mixed phase. HM, likewise denotes the radiation from the hadronic matter in the mixed phase and the hadronic phase. T_0 is the initial temperature of the system and τ_0 initial time.

At RHIC, the PHENIX experiment has obtained significant yield of direct photons in Au + Au collisions at $\sqrt{s_{NN}} = 200$ GeV, this is shown in Fig. 1.10. A theoretical analysis of the direct photon data in Ref. [72] shows the following interesting conclusions can be drawn. Dashed line indicates hard photons from NLO pQCD calculations and the solid (dot-dashed) line depicts the total (pQCD + thermal) photon yield obtained from QGP initial state with $T_i = 400$ MeV and $\tau_i = 0.2 fm/c$ ($T_i = 592$ MeV $\tau_i = 0.15 fm/c$). In medium effects on hadrons are included (ignored) in the results shown by solid (dot-dashed) line. The data can be reproduced by assuming a deconfined state of quarks and gluons with initial temperature ~ 400 MeV and thermalization time scale $\sim 0.2 fm/c$. The extracted

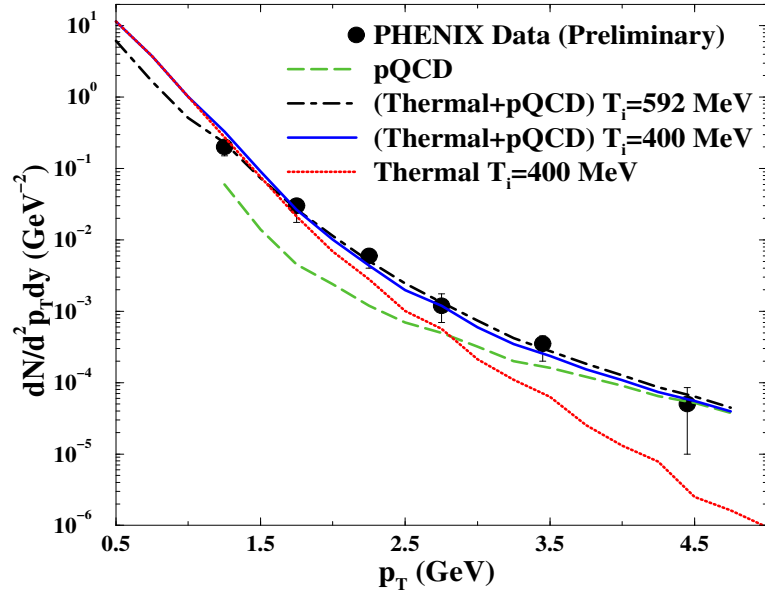


Figure 1.10: Direct photon spectra at RHIC energies measured by PHENIX Collaboration. The lines are from a theory calculation, details of which are described in the text.

average temperature (T_{av}) from photon spectra is found to be ~ 265 MeV for the p_T range 1.25 to 2.25 GeV where thermal contributions dominate. This indicates

that the temperature of the system formed after the collisions is higher than the transition temperature for deconfinement.

In the subsequent sections we review the recent results on photon multiplicity measurements at lower energies in CERN Super Proton Synchrotron (SPS) and charged particle multiplicity measurements at RHIC. This forms an introduction to the *first* photon multiplicity measurements at forward rapidity at RHIC and charged particle measurements for Au+Au collisions at $\sqrt{s_{NN}} = 62.4$ GeV at RHIC, presented in this thesis.

1.3 Photon multiplicity measurements in heavy ion collisions

There has been a few measurements of photon multiplicity distributions reported earlier in high energy heavy ion collisions [74, 75]. Most of the studies have been carried out with charged particle measurements (a review of charged particle measurements can be found in [76]), due to the difficulty of precise measurement of photon distributions.

Measurement of photon multiplicity in relativistic heavy-ion collisions will definitely give a better understanding to the well established methods of charged hadron measurements. It also shows a great promise in studying the various aspects of the reaction mechanism of phase transition from hadronic matter to Quark-Gluon Plasma and the dynamics of particle production. In heavy-ion collisions it is important to correlate information obtained from various global observables (such as charged particle multiplicity, mean transverse momentum ($\langle p_T \rangle$) and transverse energy (E_T)) for proper understanding of the physics processes occurring in the reaction. Photon multiplicity is an additional global observable. More specifically photon multiplicity provides a unique opportunity to study the changes in the relative population of the electromagnetic and hadronic components of the multi-particle final state to look for the formation of Disoriented Chiral Condensates [77]. Photon measurements can also be used to study flow [78] and intermittency behavior of events accompanying a possible phase transition.

In this section we present a brief review of the photon multiplicity and pseudorapidity distributions in previous experiments carried out at CERN SPS. The physics results reviewed will lead the motivation for photon multiplicity measurements at RHIC and provide the basic introduction for studying the photon multiplicity which is the major part of this thesis.

Table 1.1: PMD in WA93 and WA98 experiments

Basic features	WA93	WA98
Data taking	1991 and 1992	1994 to 1996
Beam and target	S+Au & S+S	Pb+Pb, Pb+Ni & Pb+Nb
Center of mass Energy	19.4 GeV	17.3 GeV
No. of scintillator pads	7500	53000
Readout	CCD camera	CCD camera
Distance from target	10.09 m	21.5 m
η coverage	2.8 to 5.2	2.5 to 4.2
η coverage with full ϕ	3.3 to 4.8	3.2 to 4.0
Photon counting Efficiency (central to peripheral)	65 - 75%	68 - 73 %
Purity of photon sample(central to peripheral)	70%	65 - 54 %

1.3.1 Photon Multiplicity Detector (PMD) at SPS

A fine granularity preshower Photon Multiplicity Detector (PMD) was fabricated and installed in the WA93 experiment at CERN SPS [79], allowing the measurement of multiplicity, rapidity and azimuthal distribution of photons in ultra-relativistic heavy-ion collisions. The basic features of the detector are given in Table 1.1. The minimum bias distribution of the photon multiplicity as measured

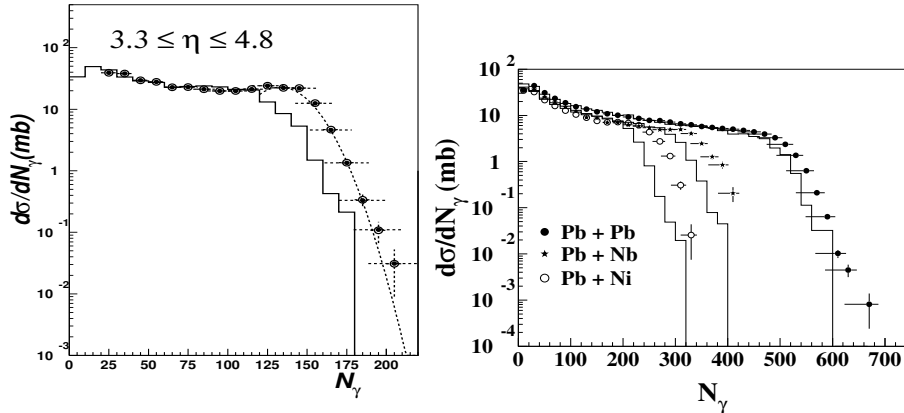


Figure 1.11: Minimum bias inclusive photon cross section for S+Au reaction at $\sqrt{s_{NN}} = 19.4$ GeV (left) and for Pb+Ni, Pb+Nb, and Pb+Pb reactions at $\sqrt{s_{NN}} = 17.3$ GeV (right). Solid histograms are the corresponding distributions obtained from the VENUS event generator.

by the PMD for S+Au at $\sqrt{s_{NN}} = 19.4$ GeV in WA93 experiment is shown in Fig. 1.11. The distribution has been obtained for the full azimuthal coverage(2π of

the PMD and has been compared to results obtained from the VENUS event generator [80]. It is observed that VENUS underpredicts photon multiplicity for central events. Subsequently the PMD was also installed in the WA98 experiment [81]. The basic features of the PMD in WA98 experiment are also given in Table 1.1. The minimum bias distribution of photon multiplicity as measured by the PMD in WA98 experiment is shown in Fig. 1.11. The experimental results for different target ions have been compared to those obtained from the VENUS event generator. VENUS is found to underpredict photon multiplicity for central collisions at 17.3 GeV in center of mass frame, and it underpredicts more for asymmetric ion collisions (Pb+Nb and Pb+Ni).

1.3.2 Photon pseudorapidity distribution at SPS energies

One of the challenges in relativistic heavy-ion collisions is to measure the large number of particles produced. Measurement of particle density in rapidity is a convenient way to describe heavy-ion collisions. It has also been suggested that fluctuations in pseudorapidity distributions is a signature of phase transition from hadronic matter to Quark-Gluon Plasma. Further, pseudorapidity density can be related to a thermodynamic quantity, entropy density, in heavy-ion collisions. All these physics issues motivate people to study the pseudorapidity distributions of photons ($dN_\gamma/d\eta$) in addition to the same for charged particles also. These distributions for S+Au and Pb+Pb reactions for different centralities, measured in the WA93 and WA98 experiments respectively are shown in Fig. 1.12 [74, 75].

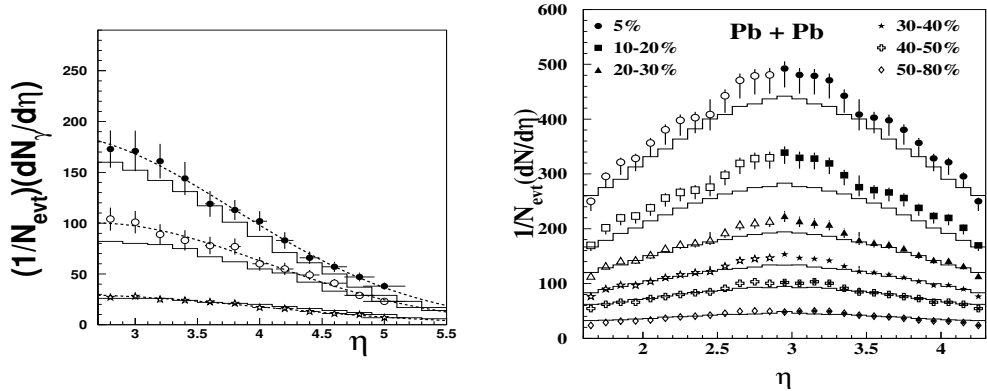


Figure 1.12: Pseudo-rapidity distributions of photons for S+Au reaction at $\sqrt{s_{NN}} = 19.4$ GeV (left) and Pb+Pb reaction at $\sqrt{s_{NN}} = 17.3$ GeV (right). The solid histograms are the corresponding distributions obtained from the VENUS event generator.

These distributions followed a Gaussian behavior. The results from VENUS are also shown in the figures. One observes that VENUS underpredicts the data for central collisions.

The best way to study the pseudorapidity distribution is to look at the shape parameters of the distribution. The shape parameters are the following:

- (a) The pseudorapidity density at mid-rapidity (ρ_{max}),
- (b) width of the pseudorapidity distribution (σ), and
- (c) pseudorapidity peak (η_{peak}).

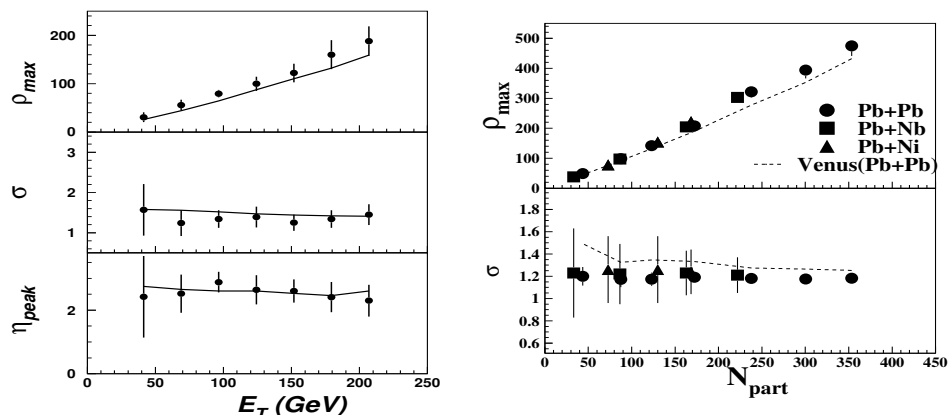


Figure 1.13: Pseudorapidity density (ρ_{max}), and width of the pseudorapidity distribution (σ) are shown as a function of centrality of the reaction (defined through the E_T values for WA93 data (left) and number of participating nucleons for WA98 data (right)).

These parameters are shown in Fig. 1.13 as a function of transverse energy and number of participating nucleons for the photon data from WA93 and WA98 experiments respectively. The results have been compared to those obtained from VENUS event generator. The pseudorapidity density at mid-rapidity is found to increase with increase in centrality, which can be understood from simple geometrical picture of the collision. Results from VENUS are also found to follow the similar trend. For higher centrality of the reaction VENUS underpredicts the data. The widths of the pseudorapidity distributions for various centralities are found to be similar within the quoted errors and the trend is consistent with the results from VENUS. The pseudorapidity peak for the WA98 experiment was found to be 2.92. This value corresponds to the pseudorapidity in center of mass frame of Pb+Pb collision.

1.3.3 Scaling of photon multiplicity with N_{part} at SPS energies

Another important aspect which was studied in the SPS experiments is the scaling of particle multiplicity as they test the various models for particle production. Also various experimental signatures require comparison of observables of different system sizes, hence a proper understanding of scaling is essential. While scaling with number of collisions arises naturally in a picture of superposition of nucleon-nucleon collisions, with possible modifications by initial state effects, the participant scaling is more naturally related to a system with strong final state re-scattering, where the incoming particles lose their memory and every participant contributes a similar amount of energy. The scaling behavior can therefore carry important information on the reaction dynamics. It is therefore of interest

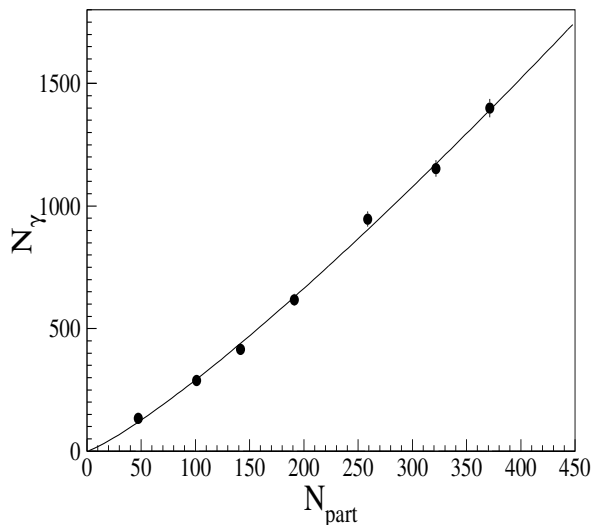


Figure 1.14: Scaling behavior of photons. Integrated number of photons are plotted as a function of number of participating nucleons. The solid lines show power-law fit to the data, which yields the value of exponent, $\alpha = 1.12 \pm 0.03$.

to study the scaling properties with respect to number of participants or number of collisions. We have studied the scaling of total number of photons with number of participating nucleons [75]. The results for photons from Pb+Pb collisions at $\sqrt{s_{NN}} = 17.3$ GeV are shown in Fig. 1.14. Fitting the data points to the function $C \times N_{part}^\alpha$, yields the value of α to be 1.12 ± 0.03 . This indicates that photon production deviates from the naive Wounded Nucleon Model [82] ($\alpha = 1$). In this

thesis we will address these issues by using data of Au+Au collisions at a higher center of mass energy $\sqrt{s_{\text{NN}}} = 62.4$ GeV. In addition we will use the lower energy SPS data to arrive at a very interesting longitudinal scaling behavior of photon production for different center of mass energies.

1.4 Charged particle multiplicity measurements

This thesis also deals with measurement and study of charged particle multiplicity distributions at forward rapidity in STAR experiment. So it will be beneficial to have a brief review of some results at SPS energies and some interesting results from charged particle multiplicity measurements at RHIC. We discuss the results from WA98 experiment at SPS and from two experiments at RHIC, namely BRAHMS and PHOBOS, which had wide pseudorapidity coverage to study the inclusive charged particle production. The measurements at forward rapidity in STAR experiment which is also part of this thesis work, will be discussed in Chapter 4.

1.4.1 Charged particle multiplicity measurements at SPS

The gross features of charged particle production in nucleon-nucleus collisions and reactions of light nuclei are well described in the framework of the Wounded Nucleon Model [82], in which the number of participating nucleons plays an important role. In this model the transverse energy and charged particle production in $p+A$ and $A+A$ reactions are calculated by assuming a constant contribution from each participating nucleon. This kind of scaling has also been observed by the WA80 collaboration in reactions of ^{16}O and ^{32}S projectiles with various targets where $dE_T/d\eta|_{max}$ was found to depend approximately linearly on the average total number of participants [83].

The charged particle multiplicity in the WA98 experiment at SPS was measured with a circular Silicon Pad Multiplicity Detector (SPMD) located 32.8 cm downstream of the target [85]. This detector provided full azimuthal coverage in the pseudorapidity region $2.35 < \eta < 3.75$ with 180 ϕ -bins and 22 η -bins. The charged particle multiplicity in an η -ring was determined from the sum of the measured energy losses of the charged particles traversing the η -ring divided by the average energy loss per charged particle.

Fig. 1.15 shows the pseudorapidity density of N_{ch} at mid-rapidity as a function of the number of participants for $p+p$ [84] and $\text{Pb}+\text{Pb}$ collisions at $\sqrt{s_{\text{NN}}} =$

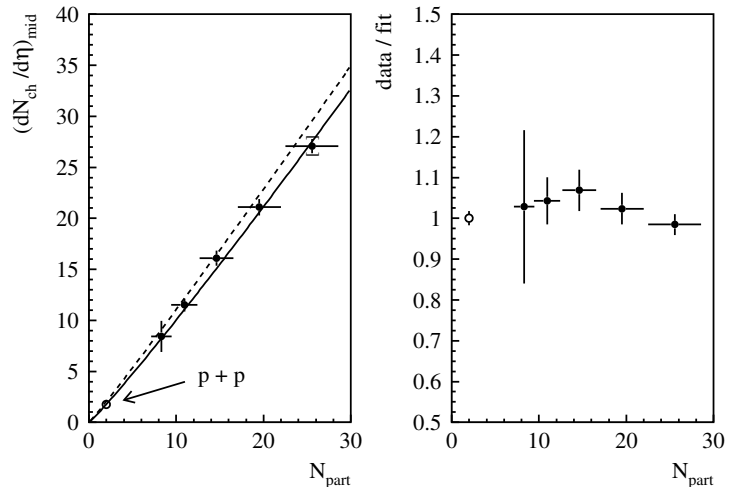


Figure 1.15: Charged particle pseudorapidity density at mid-rapidity as a function of the number of participants for $p+p$ and Pb+Pb collisions. The fit function are described in the text. On the right hand side the ratio of the data to the fit function is shown.

17.3 GeV. The fit function plotted as a solid line is of the form $\frac{dN_{ch}}{d\eta} \sim N_{part}^{\alpha}$. The dashed function is the fit result using the participant values from the FRITIOF calculation. The value of $\alpha = 1.07 \pm 0.05$ [86]. Within the quoted systematic errors the value of α are similar for both photons (discussed earlier) and charged particles, indicating a deviation obtained from the picture of a naive Wounded Nucleon Model ($\alpha = 1$).

1.4.2 Charged particle multiplicity measurements at RHIC

The properties of charged particle production at RHIC energies are found to follow a number of simple scaling behaviors, some of which are also observed at lower energies or in simpler systems. As a function of centrality, the total number of charged particles scales with the number of participating nucleons. The measured values of charged particle pseudorapidity density were found to be independent of energy over a broad range of pseudorapidities when effectively viewed in the rest frame of one of the colliding nuclei, a property referred to as “Limiting fragmentation or longitudinal scaling”. Such scalings for charged particles and photons are discussed in this thesis in detail in Chapter 4 from RHIC and SPS data. This study is extensively carried out as a function of centrality and for identified particles, which led to some interesting results discussed in Chapter 4. Before that we would like to briefly summarize the results for charge particles at mid-rapidity

from AGS, SPS and RHIC.

1.4.3 Charged particle multiplicity at mid-rapidity

The first results on charged particle multiplicity at mid-rapidity from RHIC were reported by PHOBOS collaboration [87]. The data were taken for Au+Au collisions at $\sqrt{s_{NN}} = 200$ GeV. It is interesting to note that the measured charged particle density at mid-rapidity at RHIC was lower than the predictions of most models (see the left panel of Fig. 1.16. From top to bottom, the references for the models

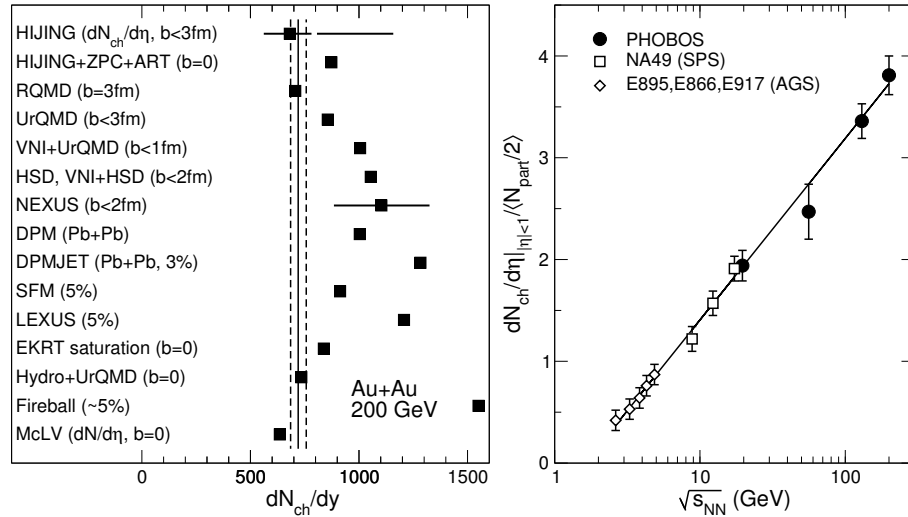


Figure 1.16: Left : Results of PHOBOS measurements of the charged particle density near mid-rapidity in central Au+Au at $\sqrt{s_{NN}} = 200$ GeV (shown by the vertical line with the dashed lines denoting the systematic uncertainty) compared to theoretical predictions. Right : Normalized pseudorapidity density of charged particles emitted within $|\eta| \leq 1$ in central collisions (Au+Au at AGS, RHIC and Pb+Pb at SPS) as a function of $\sqrt{s_{NN}}$.

are [91, 92, 93, 94, 95, 96, 97, 98, 99, 100, 101, 102, 103, 104, 105]). Among the models which predicted a value close to that seen in the data were two which invoked the concept of saturation in either the initial state [105] or the produced partons [102]. Related concepts were used in more recent formulations which describe the formation of a Color Glass Condensate (CGC). The search for other evidence for possible parton saturation effects is a topic of interest at RHIC.

The right panel of Fig. 1.16 is a compilation of the evolution of the charged particle density at mid-rapidity, $dN_{ch}/d\eta|_{|\eta|\leq 1}$, per participating nucleon pair, $N_{part}/2$, as a function of collision energy from PHOBOS [88, 111, 112, 89, 87, 90] and lower energy heavy ion reactions at the SPS [113, 114] and AGS [106, 107, 108, 109, 110]. The data follow a simple logarithmic extrapolation from lower energies as shown by the line drawn to guide the eye. The charged particle density at mid-rapidity at the top RHIC energy is about a factor of two higher than the maximum value seen at the SPS.

1.4.4 Scaling of charged particle multiplicity with N_{part} at RHIC

One of the interesting features of total particle production in Au+Au collisions at RHIC is the proportionality of the total charged-particle multiplicity to the number of participant pairs [115], as shown in Fig. 1.17 and compared to $\bar{p}+p$ [116] and $d+Au$ collisions [117].

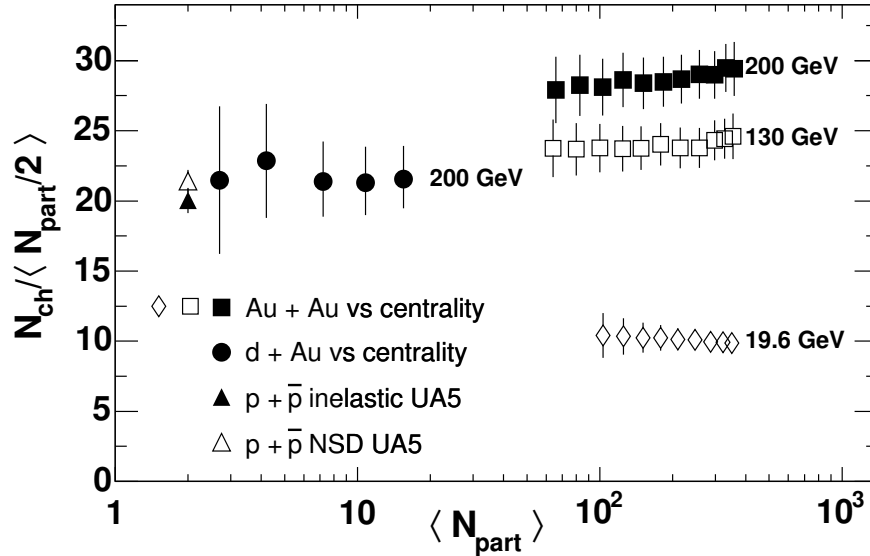


Figure 1.17: Total integrated charged particle multiplicity per participant pair as a function of number of participants for Au+Au collisions at $\sqrt{s_{NN}} = 19.6, 130$ and 200 GeV, as well as $d+Au$ and $\bar{p} + p$ at 200 GeV. The vertical bars include both statistical and systematic (90% C.L.) uncertainties.

The figure also shows that the total charged particle multiplicity is proportional to the number of participating nucleons in Au+Au collisions at all three energies from $\sqrt{s_{NN}} = 19.6$ to 200 GeV. The data suggest that number of charge particles produced per participating nucleon pair in very central d +Au collisions are not close to the values obtained for Au+Au collisions. This makes it more interesting to study the evolution of a similar quantity with rapidity, to see if different η regions at RHIC exhibit different scaling behaviors.

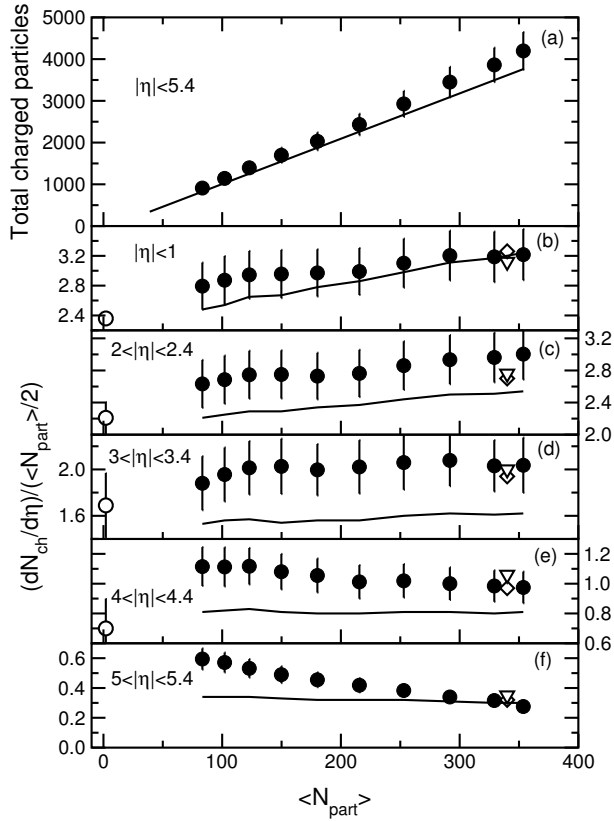


Figure 1.18: (a): Total number of charged particles detected within the range $|\eta| < 5.4$ for Au+Au collisions at $\sqrt{s_{NN}} = 200$ GeV. (b)-(f): Centrality dependence of $dN_{ch}/d\eta$ for different ranges of $|\eta|$ for Au+Au collisions at $\sqrt{s_{NN}} = 200$ GeV. See text for description.

A more detailed study of the centrality dependence of the charged particle density from PHOBOS is given in Fig. 1.18(a-f). In panel (a) of Fig. 1.18 shows the total charge particles detected within the range $|\eta| < 5.4$ for Au+Au collisions at $\sqrt{s_{NN}} = 200$ GeV. The filled symbols are the measured data, and the line represents

the prediction of the event generator HIJING. The error bars reflect systematic uncertainties. The panels (b-f) in Fig. 1.18, shows the N_{part} dependence of $dN_{ch}/d\eta$ per participating nucleon pair ($\langle N_{part}/2 \rangle$), plotted for five pseudorapidity bins ranging from $|\eta| < 1$ to $5 < |\eta| < 5.4$. The open diamonds and triangles refer to the predictions of the AMPT, and LUCIFER models respectively for the 6% most central Au+Au collisions at $\sqrt{s_{NN}} = 200$ GeV. Also plotted are data from pp [118] and $p\bar{p}$ [119] collisions, scaled as described below, as open circles, and predictions from the HIJING model as solid lines. The increase of $dN_{ch}/d\eta/\langle N_{part}/2 \rangle$ at mid-rapidity at RHIC was first reported by PHENIX experiment [120] which was subsequently verified by BRAHMS [121], PHOBOS [122] and STAR [123] experiments. The observed trend at forward rapidity in Figs. 1.18(d-f) is also verified in the study presented in this thesis. It is interesting to note the evolution of $dN_{ch}/d\eta/\langle N_{part}/2 \rangle$ from mid-rapidity to forward rapidity is such that the total charged particle multiplicity per participating nucleon pair is a constant quantity.

1.4.5 Longitudinal scaling of charged particle pseudorapidity density

At RHIC longitudinal scaling of charged particle production was observed for heavy ion collisions. This feature was earlier observed in elementary collisions also. A very general picture of elementary hadron-hadron collisions emerged in the late 1960's, consisting of two sources of particle production. This concept led to the prediction of two types of scaling laws for the distributions of final state particles in the regions of the longitudinal momentum space which are either near to or far from the colliding partners.

Particles near beam and target rapidity were thought to be governed by the “limiting fragmentation hypothesis” [124]. In this model, the momentum distribution of particles of species in the rest frame of one of the original colliding hadrons (commonly denoted with a prime to distinguish it from the center-of-mass frame), $E d^3N/dp'^3$, or equivalently $d^3N/p_T dy' dp_T d\phi$, becomes energy-independent at high enough collision energy. The central concept is that the “projectile” hadron, when seen in the frame of the “target”, is Lorentz-contracted into a very narrow strongly-interacting pancake which passes through the target. This interaction leaves behind a complicated excited state whose properties do not depend in detail on the energy or even identity of the projectile, and which then “fragments” into a final

state distribution of particles, Ed^3N/dp^3 . It was generally assumed that this process produced particles primarily in a restricted window of rapidity around $y'=0$, possibly even leading to a complete lack of particles at mid-rapidity in a very high energy hadron-hadron collision [125].

In contrast, particles near mid-rapidity in the center-of-mass frame were expected to form a rapidity plateau with a constant dN/dy , independent of energy and the nature of the hadrons in the initial collision [126, 127]. Similarly, in heavy ion collisions, a boost-invariant central plateau where the initial conditions are invariant with respect to [longitudinal] Lorentz transformations (i.e. observables are independent of y) was predicted [130]. Furthermore, the extent of this boost-invariant region was expected to grow with energy. Fig. 1.19 shows $dN/d\eta$

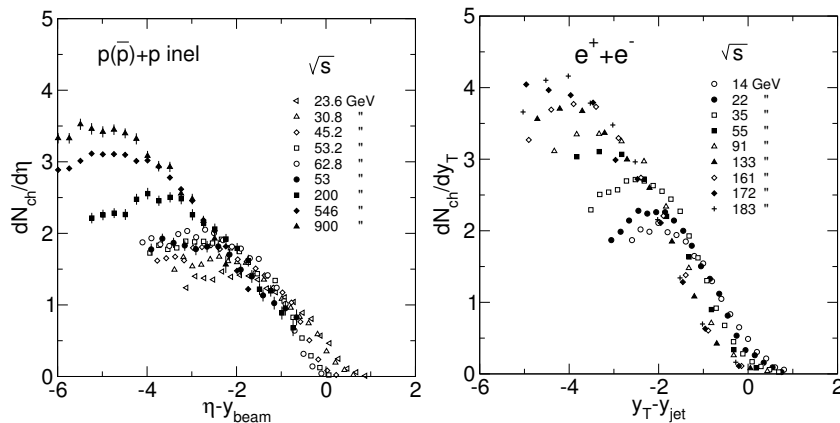


Figure 1.19: Left : Distributions of pseudorapidity density of charged particles emitted in $p(\bar{p})+p$ collisions at a range of energies versus the variable $\eta - y_{beam}$. Right : Similar data for particles emitted along the jet axis in an e^+e^- collision versus the variable $y_T - y_{jet}$.

for $p(\bar{p})+p$ collisions [118, 128] and $dN/d(y_T)$ for e^+e^- collisions [129]. In both cases, when effectively viewed in the “target” rest frame, these collisions exhibit longitudinal scaling (energy independence). Lorentz boosts of pseudorapidity, η , are not as trivial as those of rapidity, but $\eta' \equiv \eta - y_{beam}$ (or $\eta + y_{beam}$) approximates y' . Furthermore, as noted above, the limiting fragmentation concept implies scaling in the full distribution, Ed^3N/dp^3 . Since η' is just a function of (y', p_T, m) , scaling in $dN/d\eta'$ is also implied directly. Limiting fragmentation behavior

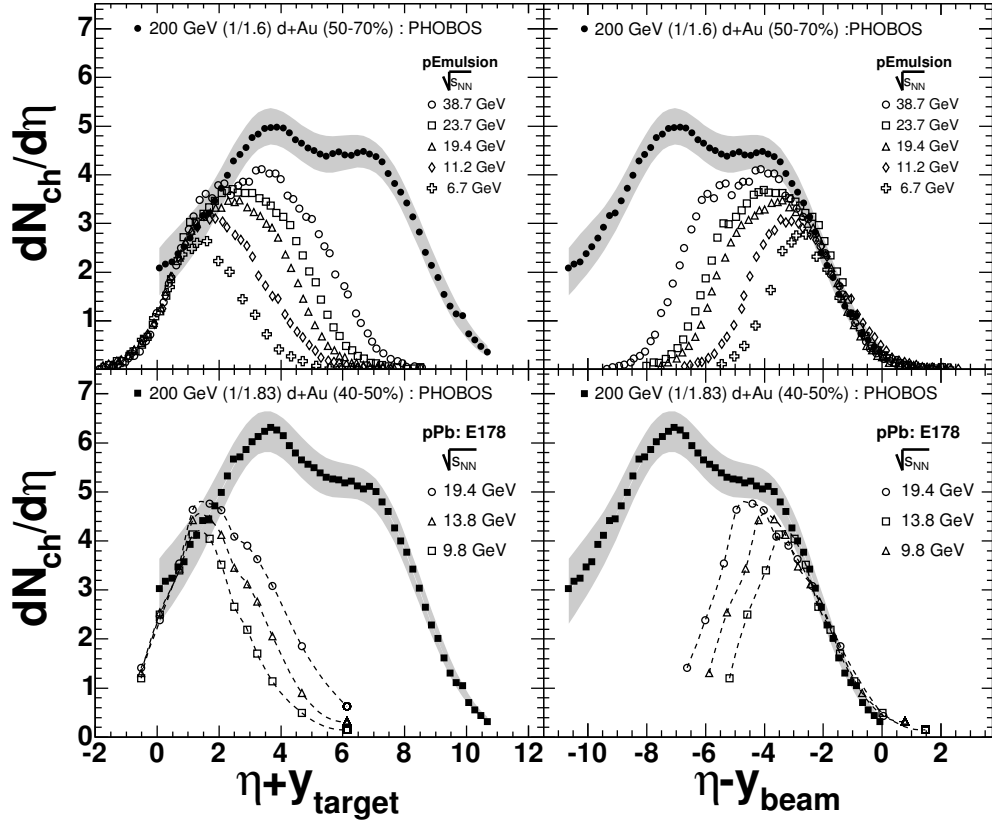


Figure 1.20: The $dN_{ch}/d\eta$ for various energies and collision systems plotted as a function of $\eta + y_{target}$ and $\eta - y_{beam}$. Grey tracks are included in the distributions shown for emulsion data.

is observed in elementary collisions. They are also observed in asymmetric collision systems (hadron-nucleus). The concept of extended longitudinal scaling in such cases can be explored separately in the rest frame of the target and projectile and are shown in Fig. 1.20. A compilation of distributions of pseudorapidity densities of charged particles emitted in $p+A$ and $d+A$ collisions at a variety of energies [117, 131, 132, 133]. Grey tracks are included in the distributions shown for emulsion data. The data are plotted versus the variables $\eta + y_{target}$ and $\eta - y_{beam}$ calculated using the rapidity of the larger (left panels) or smaller (right panels) of the colliding species. Note that the data at all energies and at both ends of the pseudorapidity range follow common curves. In Fig. 1.21, the data are effectively shifted to the rest frame of one of the gold nuclei [88]. In the far right panel, data for positive and negative η have been averaged to generate data versus $|\eta| - y_{beam}$. The data at both centralities show an extended scaling with the longitudinal velocity in the rest frame of one of the projectiles, identical behavior to that seen in simpler systems (see, for example, [116, 134, 135, 136]). Similar behavior in nucleus-nucleus collisions over a narrower range in η' was first observed by BRAHMS [137, 138]. However there was two contradictory results (one of few rare instances at RHIC)

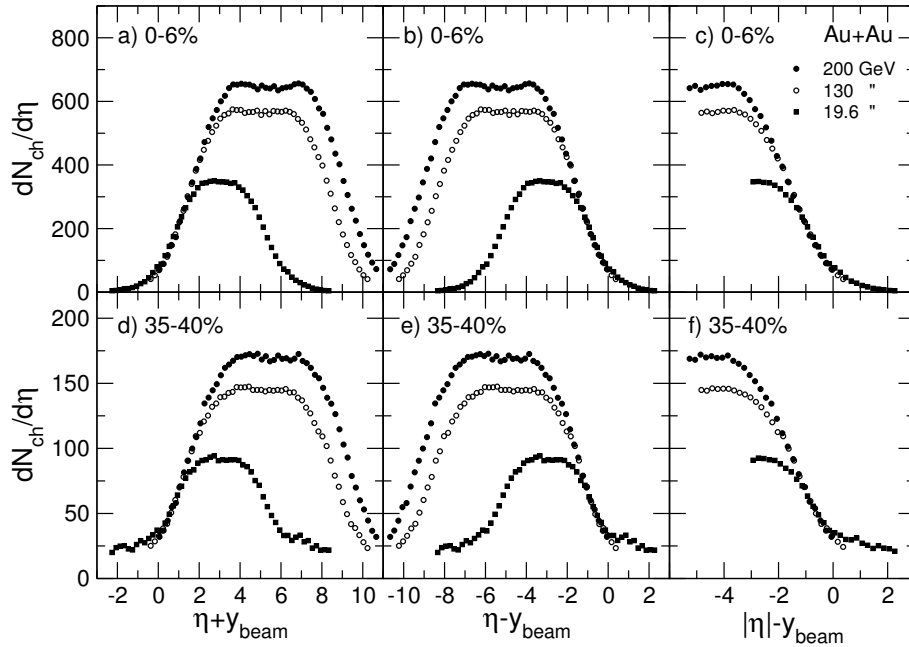


Figure 1.21: Distributions of pseudorapidity densities of charged particles emitted in Au+Au collisions at three energies and two centrality ranges are plotted versus $\eta' \equiv \eta - y_{beam}$ (or $\eta + y_{beam}$). Systematic errors are not shown and statistical errors are smaller than the symbols.

published by PHOBOS and BRAHMS on centrality dependence of longitudinal scaling. While BRAHMS claimed observation of longitudinal scaling as discussed above to be independent of collision centrality [138, 139], PHOBOS found the scaling to be broken when studied as a function of collision centrality [122]. One of the main focus of this thesis is to study through the simultaneous measurement of photon and charged particles in a common region of forward η coverage which of the results are correct and what are the possible explanations of the observations.

Bibliography

- [1] J. P. Blaizot & E. Iancu, Phys. Rept. **359** (2002) 355.
- [2] <http://www.bnl.gov/rhic/>.
- [3] <http://public.web.cern.ch/Public/Content/Chapters/AboutCERN/>.
- [4] M. A. Shifman, Ann. Rev. Nucl. Part. Sci. **33** (1983) 199.
- [5] J. Pochodzalla *et al.*, Phys. Rev. Lett. **75** (1995) 1040.
- [6] J. C. Collins & M. Perry, Phys. Lett. **34** (1975) 1353.
- [7] A. M. Polyakov, Phys. Lett. **72B** (1997) 224.
- [8] T. Biró , P. Levai, B. Müller, Phys. Rev. **D42** (1990) 3078.
- [9] A. Peshier, B. Kämpfer, O. P. Pavlenko, G. Soff, Phys. Lett. **B337** (1994) 235.
- [10] J. W. Harris & B. Müller, Ann. Rev. Nucl. Part. Sci. **46** (1996) 71.
- [11] *Proceedings of Quark Matter '1999*, Nucl. Phys. **A661** (1999).
- [12] *Proceedings of Quark Matter '2001*, Nucl. Phys. **A698** (2002) .
- [13] *Proceedings of Quark Matter '2002*, Nucl. Phys. **A715** (2002).
- [14] BRAHMS Collaboration, I. Arsene *et al.*, Nucl. Phys. **A 757** (2005) 1.
- [15] PHOBOS Collaboration, B. B. Back *et al.*, Nucl. Phys. **A 757** (2005) 28.
- [16] STAR Collaboration, J. Adams *et al.*, Nucl. Phys. **A 757** (2005) 102.
- [17] PHENIX Collaboration, K. Adcox *et al.*, Nucl. Phys. **A 757** (2005) 184.

- [18] K. Kajantie, L. McLerran, *Ann. Rev. Nucl. Part. Sci.* **37** (1987) 293 and references therein.
- [19] V. Bernard, *Quark-Gluon Plasma Signatures*, (Editions Frontières, Paris, 1990) and references therein.
- [20] C. P. Singh, *Phys. Rep.* **236** (1993) 147 and references therein.
- [21] B. Müller, *Rep. Prog. Phys.* **58** (1995) 611 and references therein.
- [22] P. Koch, B. Müller & J. Rafelski, *Phys. Rep.* **142** (1986) 167.
- [23] NA57 Collaboration, F. Antinori *et al.*, *J. Phys. G* **32** (2006) 427.
- [24] Helen Caines (for the STAR collaboration), nucl-ex/0601014.
- [25] T. Matsui & H. Satz, *Phys. Lett.* **178B** (1986) 416; F. Karsch, M. T. Mehr & H. Satz, *Z. Phys.* **C37** (1988) 617.
- [26] T. A. DeGrand & C. E. DeTar, *Phys. Rev. D* **34** (1986) 2469.
- [27] K. Kanaya & H. Satz, *Phys. Rev. D* **34** (1986) 3193.
- [28] F. Karsch & H. W. Wyld, *Phys. Lett.* **213B** (1988) 505.
- [29] D. Blaschke, *Nucl. Phys.* **A525** (1991) 269c.
- [30] F. Karsch & H. Satz, *Z. Phys.* **C51** (1991) 209.
- [31] V. Černý, *et al.*, *Z. Phys.* **C46** (1990) 481.
- [32] J. Hüfner, P. Povh & S. Gardner, *Phys. Lett.* **B238** (1990) 103.
- [33] J. Cleymans, R. L. Thews, *Z. Phys.* **C45** (1990) 391.
- [34] J. P. Blaizot & J. Y. Ollitrault, *Phys. Lett.* **199B** (1987) 499.
- [35] F. Karsch & R. Petronzio, *Phys. Lett.* **212B** (1998) 255.
- [36] M. Gaździcki & S. Mrówczyński, *Z. Phys.* **C49** (1991) 546.
- [37] R. Lietava, *Z. Phys.* **C50** (1991) 107.
- [38] S. Gavin, M. Gyulassy & A. Jackson *Phys. Lett.* **207B** (1998) 257.

- [39] R. Vogt *et al.*, Phys. Lett. **208B** (1998) 263.
- [40] K. Martins, D. Blaschke & E. Quack, Phys. Rev. **C51** (1995) 2723.
- [41] D. Kharzeev & H. Satz, preprint CERN-TH-95-214 (hep-ph/9508276)
- [42] S. Gupta & H. Satz, Phys. Lett. **B283L** (1992) 439.
- [43] R. Vogt, S. J. Brodsky & P. Hoyer, Nucl. Phys. **B383** (1992) 643.
- [44] M. A. Doncheski, M. B. Gay Ducati & F. Halzen, Phys. Rev. **D49** (1994) 1231.
- [45] S. Gavin *et. al.*, Z. Phys. **C61** (1994) 351; S. Gavin, Nucl. Phys. **A566** (1994) 383c.
- [46] C. Baglin *et al.*, Phys. Lett. **B220** (1989) 471; Phys. Lett. **B251** (1990) 465; Phys. Lett. **B262** (1991) 362; Phys. Lett. **B268** (1991) 453; Phys. Lett. **B270** (1991) 105.
- [47] M. C. Abreu *et al.*, Nucl. Phys. **A566** (1994) 77c; Nucl. Phys. **A566** (1994) 371c; Nucl. Phys. **A590** (1995) 117c.
- [48] S. Gavin *et al.*, Z. Phys. **C61** (1994) 351; S. Gavin, Nucl. Phys. **A566** (1994) 383c.
- [49] D. M. Alde *et al.*, Phys. Rev. Lett. **66** (1991) 133.
- [50] P. Amandruz *et al.*, CERN-PPE-91-198 Preprint (1991) unpublished.
- [51] S. Ramos *et al.*, Nucl. Phys. **A590** (1995) 117c.
- [52] NA50 Collaboration, M. C. Abreu *et al.*, Phys. Lett. **B 410** 1997 327; NA50 Collaboration, M. C. Abreu *et al.*, Phys. Lett. **B 410** 1997 337.
- [53] H. Büsching (for the PHENIX Collaboration), nucl-ex/0511044.
- [54] R. Vogt, nucl-th/0507027.
- [55] K. Redlich & H. Satz, Phys. Rev. **D33** (1986) 3747; E. V. Shuryak & O. V. Zhirov, Phys. Lett. **B89** (1980) 253.
- [56] L. Van. Hove, Phys. Lett. **118B** (1982) 138.

- [57] B. Mohanty *et al.*, Phys. Rev. **C68** (2003) 021901.
- [58] L. Van. Hove, Z. Phys. **C27** (1985) 135.
- [59] E. L. Feinberg, Nuovo Cim. **34A** (1976) 391.
- [60] E. V. Shuryak, Phys. Lett. **78B** (1978) 150.
- [61] R. Hwa & K. Kajantie, Phys. Rev. **D32** (1985) 1109.
- [62] K. Kajantie *et al.*, Phys. Rev. **D34** (1986) 811.
- [63] J Kapusta *et al.*, Phys. Rev. **D34** (1986) 2746.
- [64] S. Raha & B. Sinha, Phys. Rev. Lett. **58** (1987) 101.
- [65] J. Kapusta, L. McLerran & D. K. Srivastava, Phys. Lett. **B283** (1992) 145.
- [66] M. T. Strickland, Phys. Lett. **B331** (1994) 245.
- [67] J. Alam, B. Sinha & S. Raha, Phys. Rept. **273** (1996) 243.
- [68] J. Alam *et al.* Phys. Rev. **D48** (1993) 1117.
- [69] J. J. Neumann, D. Seibert, & G. Fai, Phys. Rev. **C51** (1995) 1460.
- [70] WA98 Collaboration, M.M. Aggarwal *et al.*, Phys. Rev. Lett. **85** (2000) 3595.
- [71] D.K. Srivastava & B. Sinha, Phys. Rev. **C 64** (2001) 034902.
- [72] J. Alam *et al.*, nucl-th/0508043.
- [73] PHENIX Collaboration, S. Bathe, nucl-ex/0511042.
- [74] WA93 Collaboration, M. M. Aggarwal *et al.*, Phys. Rev. **C58** (1998) 1146.
- [75] WA98 Collaboration, M. M. Aggarwal *et al.*, Phys. Lett. **B458** (1999) 422.
- [76] J. Stachel & G. R. Young, Ann. Rev. Nucl. Part. Sc. **44** (1994) 537.
- [77] B. Mohanty & J. Serreau, Phys. Rept. **414** (2005) 263; WA98 Collaboration, M. M. Aggarwal *et al.*, Phys. Rev. **C64** (2001) 011901(R).
- [78] WA93 Collaboration, M. M. Aggarwal *et al.*, Phys. Lett. **B403** (1997) 390; WA98 Collaboration, M. M. Aggarwal *et al.*, Eur. Phys. J. **C41** (2005) 287.

- [79] WA93 Collaboration, M. M. Aggarwal *et al.*, Nucl. Instr. and Meth. in Phys. Res. **A372** (1996) 143.
- [80] K. Werner, Phys. Rep. **C232** (1993) 87.
- [81] WA98 Collaboration, M. M. Aggarwal *et al.*, Nucl. Instr. and Methods in Phys. Res. **A424** (1999) 395.
- [82] A. Bialas, A. Bleszynski & W. Czyz, Nucl. Phys. **B 111** (1976) 461.
- [83] WA80 collaboration, R. Albrecht *et al.*, Phys. Rev. **C 44** (1998) 2736.
- [84] C. DeMarzo *et al.*, Phys. Rev. **D 26** (1982) 1019.
- [85] W.T Lin *et al.*, Nucl. Instr. and. Meth. **A 389** (1997) 415.
- [86] WA98 Collaboration, M. M. Aggarwal *et al.*, Eur. Phys. J. **C18** (2001) 651.
- [87] PHOBOS Collaboration, B. B. Back *et al.*, Phys. Rev. **C 65** (2002) 061901R.
- [88] PHOBOS Collaboration, B. B. Back *et al.*, Phys. Rev. Lett. **91** (2003) 052303.
- [89] PHOBOS Collaboration, B. B. Back *et al.*, Phys. Rev. Lett. **88** (2002) 022302.
- [90] PHOBOS Collaboration, B. B. Back *et al.*, Phys. Rev. **C 70** (2004) 021902R.
- [91] X. -N. Wang, in [95], (1999) 210c.
- [92] B. Zhang, in [95], (1999) 220c.
- [93] H. Sorge, in [95], (1999) 217c; arXiv:nucl-th/9905008 (1999).
- [94] M. Bleicher, in [95], (1999) 218c.
- [95] S. A. Bass *et al.*, Nucl. Phys. **A 661** (1999) 205c.
- [96] W. Cassing, in [95], (1999) 222c.
- [97] H. J. Drescher, in [95], (1999) 216c.
- [98] A. Capella, A. Kaidalov, J. Tran Thanh Van, Heavy Ion Phys. **9** (1999) 169; arXiv:hep-ph/9903244 (1999).
- [99] J. Ranft, arXiv:hep-ph/9911213 (1999).

- [100] N. Armesto, C. Pajares, Int. J. Mod. Phys. **A 15** (2000) 2019; arXiv:hep-ph/0002163 (2000).
- [101] S. Jeon, J. Kapusta, Contest on the RHIC predictions, June 2000.
- [102] K. J. Eskola *et al.*, Nucl. Phys. **B 570** (2000) 379.
- [103] S. A. Bass *et al.*, Phys. Rev. **C 60** (1999) 021902.
- [104] J. Stachel, in [95], (1999) 226c.
- [105] A. Krasnitz, R. Venugopalan, Phys. Rev. Lett **86** (2001) 1717.
- [106] E866 Collaboration, L. Ahle *et al.*, Phys. Rev. **C 57** (1998) 466R.
- [107] E917 Collaboration, B. B. Back *et al.*, Phys. Rev. **C 66** (2002) 054901.
- [108] E866 Collaboration, L. Ahle *et al.*, Phys. Lett. **B 490** (2000) 53.
- [109] E895 Collaboration, J. L. Klay *et al.*, Phys. Rev. **C 68** (2003) 054905.
- [110] J. Dunlop, Mass. Inst. of Tech. PhD. Thesis (1999).
- [111] PHOBOS Collaboration, B. B. Back *et al.*, Phys. Rev. Lett. **85** (2000) 3100.
- [112] PHOBOS Collaboration, B. B. Back *et al.*, Phys. Rev. **C 65** (2002) 031901R.
- [113] NA49 Collaboration, S. V. Afanasiev *et al.*, Phys. Rev. **C 66** (2002) 054902.
- [114] NA49 Collaboration, T. Anticic *et al.*, Phys. Rev. **C 69** (2004) 024902.
- [115] PHOBOS Collaboration, B. B. Back *et al.*, arXiv:nucl-ex/0301017 (2003).
- [116] UA5 Collaboration, G. J. Alner *et al.*, Phys. Rep. **154** (1987) 247.
- [117] PHOBOS Collaboration, B. B. Back *et al.*, arXiv:nucl-ex/0409021.
- [118] UA5 Collaboration, G. J. Alner *et al.*, Z. Phys. **C 33** (1986) 1.
- [119] UA5 Collaboration, F. Abe *et al.*, Phys. Rev. **D41** 2330 (1990).
- [120] PHENIX Collaboration, K. Adcox *et al.*, Phys. Rev. Lett. **86** (2001) 3500.
- [121] BRAHMS Collaboration, I. G. Bearden *et al.*, Phys. Rev. Lett. **88** (2002) 202301;

- [122] PHOBOS Collaboration, B. B. Back *et al.*, Phys. Rev. Lett. **87** (2001) 102303;
PHOBOS Collaboration, B. B. Back *et al.*, Phys. Rev. Lett. **91** (2003) 052303.
- [123] STAR Collaboration, J. Adams *et al.*, e-Print Archive: nucl-ex/0311017.
- [124] J. Benecke *et al.*, Phys. Rev. **188** (1969) 2159.
- [125] T. T. Chou, C. -N. Yang, Phys. Rev. Lett. **25** (1970) 1072.
- [126] R. P. Feynman, Phys. Rev. Lett. **23** (1969) 1415.
- [127] R. P. Feynman, Photon-Hadron Interactions (W.A. Benjamin Inc., 1972) p. 237-249.
- [128] W. Thomé, *et al.*, Nucl. Phys. **B 129** (1977) 365.
- [129] DELPHI Collaboration, P. Abreu *et al.*, Phys. Lett. **B 459** (1999) 397.
- [130] J. D. Bjorken, Phys. Rev. **D 27** (1983) 140.
- [131] E178 Collaboration, J. E. Elias *et al.*, Phys. Rev. **D 22** (1980) 13.
- [132] I. Otterlund *et al.*, Nucl. Phys. **B 142** (1978) 445, and references therein.
- [133] S. Fredriksson *et al.*, Phys. Rep. **144** (1987) 187, and references therein.
- [134] J. Whitmore, Phys. Rep. **10** (1974) 273.
- [135] J. Whitmore, Phys. Rep. **27** (1976) 187.
- [136] E178 Collaboration, C. Halliwell *et al.*, Phys. Rev. Lett. **39** (1977) 1499.
- [137] BRAHMS Collaboration, I. G. Bearden *et al.*, Phys. Lett. **B 523** (2001) 227.
- [138] BRAHMS Collaboration, I. G. Bearden, *et al.*, Phys. Rev. Lett. **88** (2002) 202301.
- [139] BRAHMS Collaboration, I. G. Bearden, *et al.*, Phys. Lett. **B522** (2001) 227.

Chapter 2

STAR EXPERIMENT

2.1 Introduction

The Relativistic Heavy Ion Collider (RHIC) built in Brookhaven National Laboratory [1] gives a unique opportunity to accelerate the heavy ions and polarized protons. The RHIC machine can be operated at wide range of energies. For heavy ions it can accelerate from $\sqrt{s_{\text{NN}}} = 20$ GeV to 200 GeV, and for polarized protons upto $\sqrt{s_{\text{NN}}} = 500$ GeV. By doing this, it addresses many important physics challenges which are of primary interest in the quest of understanding the formation of the matter at Early universe and the origin of the proton spin. Other important aspect of RHIC was to provide beams of very high luminosities, making possible the measurements of rare processes having small cross-sections.

For a process with the cross-section σ_i the event rate (R_i) is given by $R_i = \sigma_i \cdot \mathcal{L}$. The luminosity \mathcal{L} is given by $\mathcal{L} = fn \frac{N_1 N_2}{A}$ where N_1 and N_2 are the number of particles contained in each bunch, A is the cross-sectional area of the overlap between the two colliding beams of particles, f is the revolution frequency, and n is the number of bunches per beam. High luminosities can therefore be achieved by maximizing f , n and decreasing the beam profile.

Fig. 2.1 shows the BNL accelerator complex including the accelerators used to bring the beam upto the RHIC injection energy. To accelerate the beams to such high energies, a multi step process is involved starting from the Tandem Van de Graaff facility, a proton linear accelerator, the Booster synchrotron, the Alternating Gradient Synchrotron (AGS), and ultimately the RHIC synchrotron ring. For Au+Au operations, Au ions with charge $Q = 1$ are created using the Pulsed Sputter Ion Source. They are then accelerated through the Tandem Van de

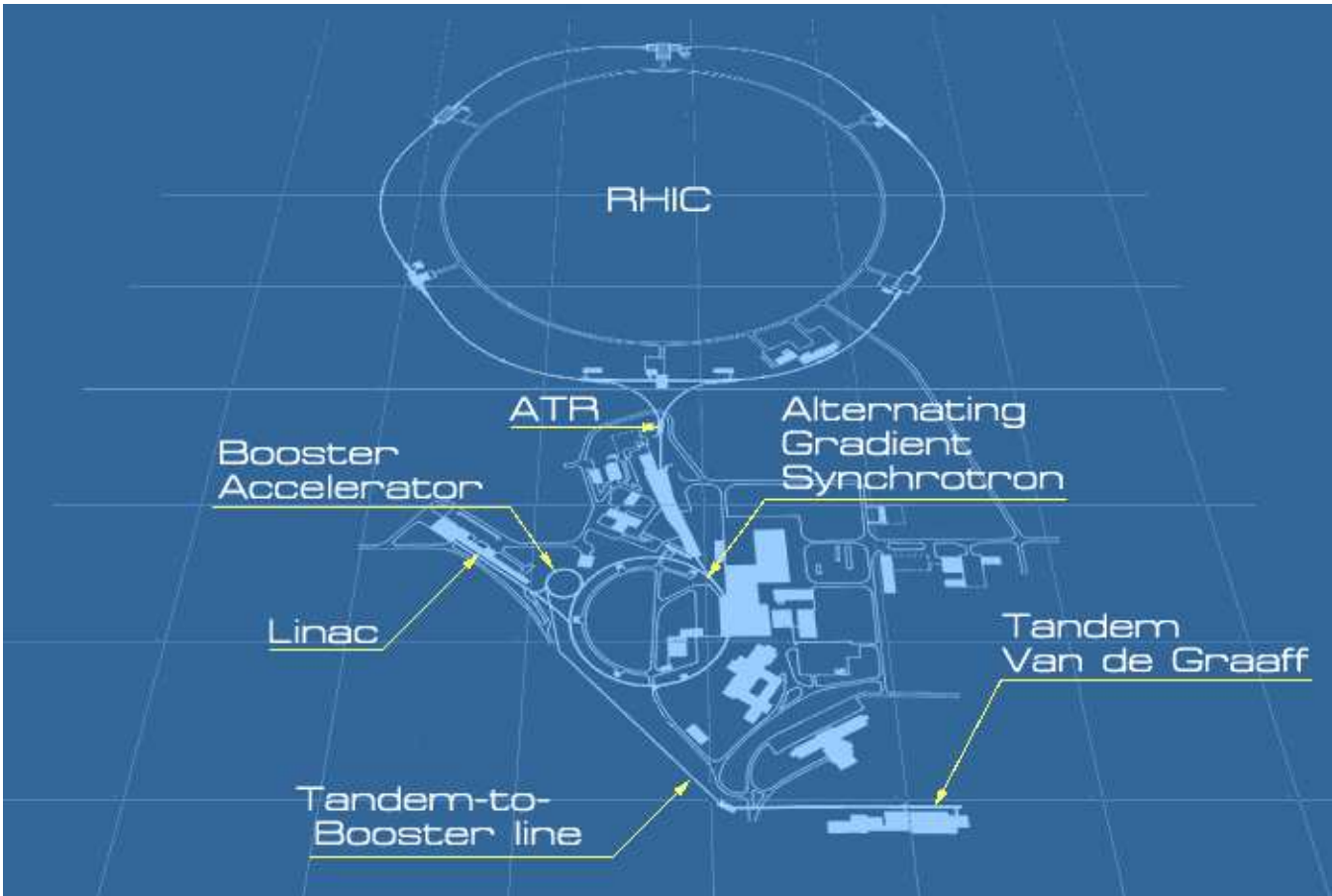


Figure 2.1: A diagram of the Brookhaven National Laboratory collider complex including the accelerators that bring the heavy ions upto RHIC injection energy (10.8 GeV/nucleon for Au).

Graaff accelerator and a series of stripping foils, ultimately yielding Au ions of kinetic energy 1 MeV/nucleon and a net charge $Q = +32$. The ions are then directed into the booster synchrotron via 550 m transfer line. The booster accelerates the Au ions to an energy of 95 MeV/nucleon. The Au ions then leave the booster, are further stripped to $Q = +77$ and are transferred into the AGS, where they are accelerated to 10.8 GeV/nucleon and sorted into four final bunches. Finally, the ions are transferred from AGS to RHIC and stripped to bare charge state of $Q = +79$ during the transfer. RHIC consists of two 3.8 km concentric quasi-circular superconducting storage accelerator rings that are called the blue and yellow ring, respectively. The rings share a common horizontal plane inside the tunnel, with each ring having an independent set of bending and focusing magnets as well as radio frequency acceleration cavities. The ring consists of six arc sections and six interaction points, allowing for simultaneous collisions at six locations. The bending magnets are cryogenically cooled to $< 4.7^\circ$ K and yield a nominal magnetic field value of ~ 3.8 T at the top of the ramp. The rings are focused for the collision at the interaction regions by a common set of dipole magnets, the DX and D0 magnets, located at 10 m and 23 m, respectively. These common dipoles slightly reduces the independence of the blue and yellow rings. To date, RHIC has been run in Cu+Cu, Au+Au, $p+p$ and $d+Au$ configurations.

The RHIC complex houses four experiments at four different interaction points. Out of these four experiments Solenoidal Tracker At RHIC (STAR) [2] and Pioneering High Energy Nuclear Interaction eXperiment (PHENIX) [3] are the big experiments and Broad RAnge Hadron Magnetic Spectrometers (BRAHMS) [4] and PHOBOS [5] (named after moon of Mars) are small experiments, in terms of the assembly and number of detectors involved.

2.2 STAR Detector

The STAR detector [2] has been designed to investigate the behavior of strongly interacting matter at high energy density and to search for signatures of quark-gluon plasma (QGP) formation. The pictorial view of STAR detectors in the initial stages of data taking is shown in Fig. 2.2. STAR measures many observables simultaneously to study signatures of a possible phase transition from hadronic matter to QGP and to understand the space-time evolution of the collision process in ultra-relativistic heavy ion collisions. The goal is to obtain a fundamental understanding of the microscopic structure of these hadronic interactions at high energy

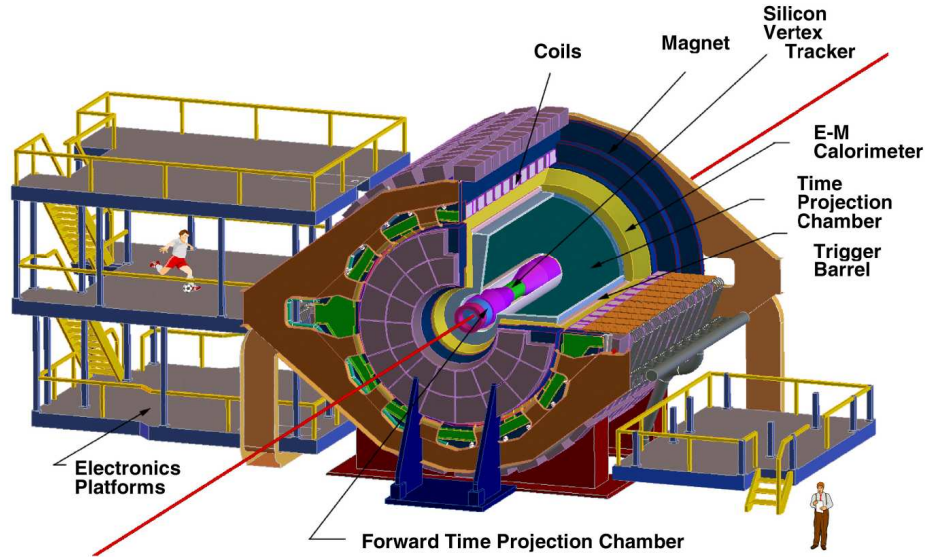


Figure 2.2: Perspective view of the STAR detector, with a cutaway for viewing inner detector systems [2].

densities.

In heavy ion collisions, the high track multiplicities allow for the extraction of the global observables such as centrality, temperature, reaction plane, and mean transverse energy. In order to accomplish this, STAR [2] was designed primarily for measurements of hadron production over a large solid angle, featuring detector systems for high precision tracking, momentum analysis, and particle identification and electromagnetic calorimetry at center of mass rapidity. The large acceptance of STAR makes it particularly well suited for event-by-event characterizations of heavy ion collisions and for the detection of hadron jets. Additionally, STAR is instrumented with a high level trigger system that allows real-time selection of the rare processes such as high transverse momentum jets, direct photons, and heavy quarkonia production.

A room temperature solenoidal magnet with a maximum magnetic field of 0.5 T provides a uniform magnetic field for charged particle momentum analysis. Charged particle tracking close to the interaction region is accomplished by a Silicon Vertex Tracker (SVT) [6] consisting of 216 silicon drift detectors (equivalent to a total of 13 million pixels) arranged in three cylindrical layers at distances of approximately 7, 11 and 15 *cm* from the beam axis. The Silicon Strip Detectors (SSD) [7] are present as a part of the inner tracker. The silicon detectors cover

a pseudo-rapidity range $|\eta| \leq 1$ with complete azimuthal symmetry ($\Delta\phi = 2\pi$). Silicon tracking close to the interaction allows precision localization of the primary interaction vertex and identification of secondary vertices from weak decays of, for example, Λ , Ξ , and Ω s. A large volume Time Projection Chamber (TPC) [8] for charged particle tracking and particle identification is located at a radial distance from 50 to 200 *cm* from the beam axis. The TPC is 4.2 *m* long and it covers a pseudo-rapidity range $|\eta| \leq 1.8$ for tracking with complete azimuthal symmetry ($\Delta\phi = 2\pi$) providing the equivalent of 70 million pixels via 136,608 channels of front end electronics (FEE). Both the SVT and TPC contribute to particle identification using ionization energy loss, with an anticipated combined energy loss resolution (dE/dx) of 7 % (σ). The momentum resolution of the SVT and TPC reach a value of $\delta p/p = 0.02$ for a majority of the tracks in the TPC. The $\delta p/p$ resolution improves as the number of hit points along the track increases and as the particle's momentum decreases, as expected.

For detection of electromagnetic particles STAR has a set of calorimeters. The full-barrel electromagnetic calorimeter (BEMC) [9] covers $|\eta| < 1$ and endcap electromagnetic calorimeter (EEMC) [10] covers $1 < \eta \leq 2$. Both these calorimeters are azimuthally symmetric. The calorimeters (EEMC and BEMC) includes shower-maximum detectors to distinguish high momentum single photons from photon pairs resulting from π and η meson decays. The EMC will also provide prompt charged particle signals essential to discriminate against pileup tracks in the TPC, arising from other beam crossings falling within the 40 μs drift time of the TPC, which are anticipated to be prevalent at RHIC pp collisions luminosities ($\approx 10^{32} cm^{-2} s^{-1}$). To extend the forward tracking, a forward radial-drift TPC (FTPC) [11] is installed covering $2.5 < |\eta| < 4$, also with complete azimuthal coverage and symmetry. For detection of photons in the forward region STAR has a Photon Multiplicity Detector (PMD) [12] covering $-3.9 < \eta < -2.3$ with full azimuthal symmetry. A time-of-flight (TOF) [13] patch covers $-1 < \eta < 0$ and $\Delta\phi = 0.04\pi$ which will help in extending particle identification to even higher transverse momentum regions. A brief description of the main detectors in STAR is given in the subsequent sections.

2.3 Trigger Detectors

The slow detectors like Time Projection Chamber (TPC), Silicon Vertex Tracker (SVT), Forward TPC (FTPC), Shower Max Detector (SMD), Photon Multiplicity

Detector (PMD) and Time-of-Flight-patch (TOF) provide the particle identification and/or momentum on which our physics conclusions are based, but they can only operate at rates of ~ 100 Hz. Interaction rates approach the RHIC crossing rates typically ~ 10 MHz for the highest luminosity beams, so the fast detectors must provide means to reduce the rate by almost 5 orders of magnitude. Interactions are selected based on the distributions of particles and energy obtained from the fast trigger detectors. Interactions that pass selection criteria in four successive trigger levels are sent to storage at a rate of ~ 5 Hz (~ 50 MB/s). The final trigger decision is made in Level 3 based on tracking in the slow detectors.

There are five primary trigger detectors for STAR: CTB, ZDC, MWC, BBC, and BEMC briefly described below.

2.3.1 Central Trigger Barrel

The CTB [14] consists of 240 scintillator slats arranged in 4 cylindrical bands each covering $1/2$ unit of pseudo rapidity. The CTB slats cover the outer shell of the 4m diameter TPC as shown in Fig. 2.3.

Each slat consists of a scintillator, light guide, and mesh dynode photomultiplier tube (PMT - Hamamatsu R5946). The slats are housed in aluminum trays to ease handling and mounting on STAR, with two slats end-to-end in each tray. The slats were tested with cosmic rays uniformly distributed over the slat. The width of the ADC response to cosmic rays is 25%, in reasonable agreement with simulation. The largest single contribution to this measured width is the calculated 16% variation in scintillator response. The wrapping scheme achieves a signal uniformity over the slat with an RMS of 6% as determined by testing with a source.

2.3.2 Zero degree Calorimeter

Each of the RHIC experiments constructed a pair of Zero Degree Calorimeter detectors [15] to provide the accelerator operators a common tool for monitoring interactions at each region. These are placed at nearly identical positions along the beamlines on either side of the intersection regions. In the zero degree region produced particles and other secondaries deposit negligible energy when compared with that of the beam fragmentation neutrons. The purpose of STAR zero degree calorimeters is to detect neutrons emitted within the cone $|\theta| < 2$ milliradians along both beam directions and measure their total energy. The energy measured by the ZDCs is proportional to the neutron multiplicity, which is known to be

Central Trigger Barrel

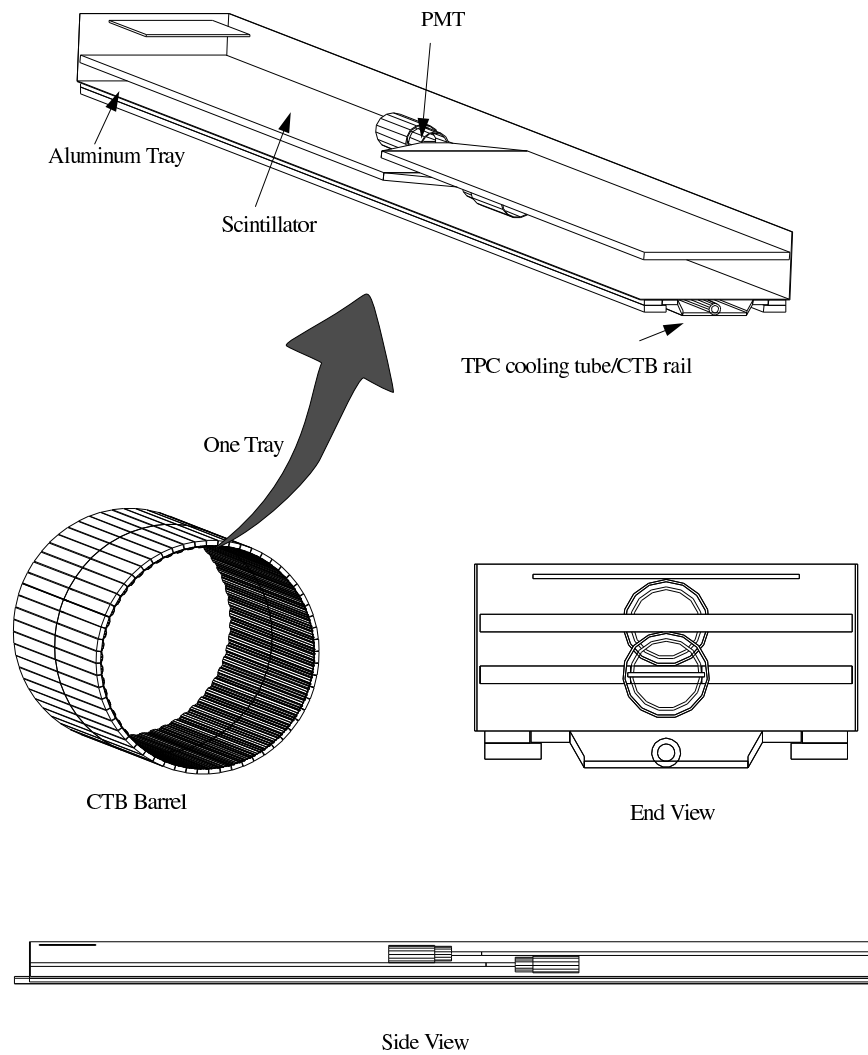


Figure 2.3: CTB cylinder and detail of tray and slat.

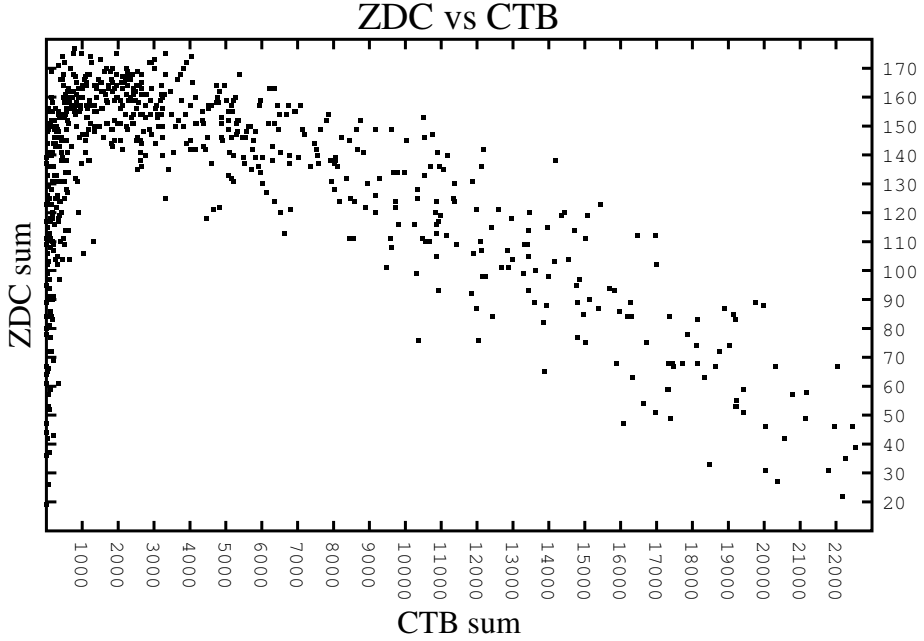


Figure 2.4: Correlation of ZDC and CTB signals

correlated with the event geometry and can be used to measure collision centrality.

Each ZDC consists of three modules. Each module consists of a series of tungsten plates alternating with layers of wavelength shifting fibers which are connected to a PMT. The ZDCs are used for beam monitoring, triggering, and locating interaction vertices.

The ZDCs operate as fast detectors for the STAR trigger. The hadronic minimum bias trigger requires a coincidence between the two STAR ZDCs of summed signals greater than $\sim 40\%$ of a single neutron signal. Comparison of the times from ZDC East and ZDC West gives a measure of the interaction location. Many of our triggers cut on the location of the interaction vertex being within ~ 25 cm of the center of the TPC. The correlation between the signals from ZDC and CTB is shown in Fig. 2.4. The correlation is as per expectation. This is because in more central collisions we expect large number of charged particles to hit the CTB while less number of spectator neutrons to fall on ZDC. In peripheral collisions, we expect comparatively less number of charged particles falling on CTB and larger number of spectator neutrons giving signal in ZDC.

2.3.3 Multi-Wire Counter

The Multi-Wire Counter (MWC) is not a separate detector, but simply uses the TPC anode wires as a fast detector. The primary function of the TPC anode wires is to provide (avalanche) gas gain for the clouds of electrons that drift through the gas volume and are admitted through the gating grid. The images of these avalanches form the pad signals used for tracking in the TPC. Ionization from charged particle tracks that pass directly through the anode wire region also avalanches onto the wires. These signals can be used to measure the multiplicity of such tracks, which is useful for Level 0 trigger formation. The electronics used to process these “prompt” signals must

- (1) provide a low AC impedance for the wires to prevent the wires from “bouncing” and injecting signals into all the pads under them,
- (2) produce a logic level signal for each minimum ionizing track with good efficiency (threshold $<0.5 \text{ MIP}^1$),
and
- (3) perform numerical calculations to derive multiplicities within the Level 0 trigger logic timing constraints ($1.5\mu s$).

2.3.4 Beam-Beam Counter

The STAR Beam-Beam Counters (BBC) consists of large and small hexagonal scintillator tiles as show in Fig. 2.5. They are mounted around beam pipe on the East and West sides outside the pole-tip of the STAR magnet at $\pm 3.7 \text{ m}$ from the interaction point. The 2×18 array of small hexagonal tiles cover a full ring of 9.6 cm inner and 48 cm outer diameter, corresponding to the pseudorapidity region of $3.4 < |\eta| < 5.0$. The small hexagon in the center of the BBC (marked “B” in Fig. 2.5) is reserved for the beam pipe. The 2×18 arrays of large hexagonal tiles span a ring of 38 cm to 193 cm in diameter, corresponding to the pseudorapidity region of $2.1 < |\eta| < 3.6$. Each scintillator tile has four wavelength shifting (WLS) optical fibers inserted into circular groves inscribed within the hexagonal scintillator to collect scintillation light.

¹Minimum Ionizing Particle (MIP): The mean rate of energy loss for charged particles in a medium is given by Bethe-Bloch equation. Most relativistic particles have energy loss rates close to a minimum value, and are said to be minimum ionizing particles or mips [16].

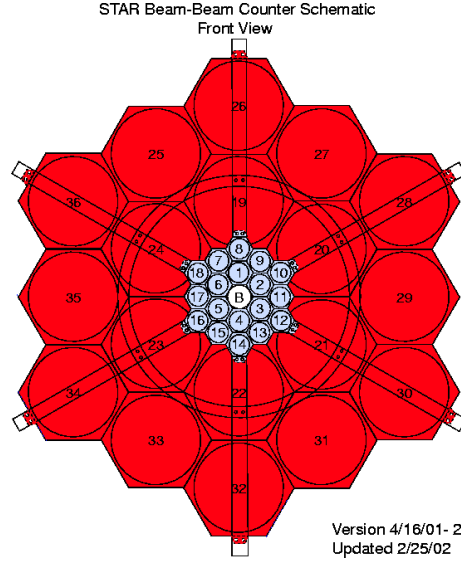


Figure 2.5: Schematic view of the Beam-Beam Counter (BBC) components. The active components are the small 18 small tiles (blue) arranged in a hexagonal shape. The location of the beam pipe is designated by “B”

The BBCs mainly provide a minimum bias trigger for $p+p$ collisions. In terms of the trigger, the main difference between $p+p$ and Au+Au collisions is the multiplicity. A typical central Au+Au event produces about 4000 charged particles, and a minimum bias trigger can be implemented based on the many mid-rapidity tracks and spectator neutrons. Both of these signatures are absent in $p+p$ collisions.

Charged particles traversing through the BBCs produces light in their scintillator tiles. Both BBCs were required to fire to trigger minimum bias $p+p$ collisions. Due to the dual-arm configuration of the BBCs, the trigger is sensitive to the non-singly diffractive (NSD) cross-section which in turn is the sum of the non-diffractive and doubly diffractive cross section. The inelastic cross-section is the sum of the NSD and singly diffractive cross section.

Apart from providing a minimum bias trigger for $p+p$ collisions, BBC coincidences were used to reject beam gas events, to measure the absolute beam luminosity \mathcal{L} with 15% precision, and to measure the relative luminosities R for different proton spin orientations with high precision.

2.4 DAQ and Triggering

Another important aspect of STAR is to collect and store the data taken by all the detectors in these collisions. This is achieved by the STAR Data Acquisition System (DAQ) [17] which is very fast and flexible. It receives data from multiple detectors and these detectors have a wide range of readout rates. The event size is of order 200 MB and the events are processed at input rates up to 100 Hz.

The STAR trigger system [14] is a 10 MHz pipelined system which is based on input from fast detectors to control the event selection for the much slower tracking detectors. The trigger system is functionally divided into different layers with level 0 being the fastest while level 1 and level 2 are slower but they apply more sophisticated constraints on the event selection.

Approximately 800 bytes of data from the trigger detectors (CTB, ZDC MWC and BEMC) come into the Level 0 system every bunch crossing (i.e., every 107 ns). Additional data coming into Level 0 includes the LIVE/BUSY status bits from the other detectors, any requests for calibration triggers, and information from RHIC (including number and fill status of each bunch). In Level 0, the raw data from each detector are analyzed to determine whether a requested type of interaction occurred in this crossing. Level 0 issues a trigger within $1.5\mu s$ of the occurrence of the interaction if it detects a requested signal and the detectors are LIVE. If it does not detect an interesting signal, it can issue calibration triggers for any LIVE detectors requesting them, or it can simply wait for the next crossing. The description of an interaction often requires the detected particle multiplicity and the distribution of these particles in η , ϕ space. This description involves summing the number of hits on the CTB slats and the number of hit MWC wires. The digitization and summing process takes longer than the 107 ns between bunch crossings. To minimize deadtime in the trigger we designed a pipelined synchronous system based on custom VME modules. There are four types of custom boards in this system, as well as the CDB and MWC receiver boards discussed above. These are the Data Storage and Manipulation (DSM), the Trigger Control Unit (TCU), the Trigger Clock Distribution (TCD), and the RHIC Clock and Control (RCC) boards. All of these are 9U VME boards that are controlled by the RHIC clock, whose period is the time between bunch crossings. Level 0 analysis uses a tree of DSM boards. Each board receives new data every RHIC clock tick, performs a simple calculation (eg., a part of the sum), and passes the result to the next DSM board in the tree in time for the next RHIC clock tick. The tree narrows to one DSM board, which passes the final results to the TCU.

If the event is selected, then a trigger is issued. The Action Word, Trigger Word, token, and a copy of the RHIC strobe are passed to the TCD crate for distribution to the detector subsystems. The data is also stored in three output FIFOs on the TCU with the input from the last DSM board and the LIVE bits. The FIFOs are read by the Level 1 Control CPU (L1CTL), which starts the next stage of trigger processing to run in parallel with the digitization cycle of the slow detectors. Once a trigger is issued, there is a period of several milliseconds during which the selected detectors are busy digitizing their data. This period allows time for more detailed analyses of the trigger data to determine whether the event meets more finely grained criteria. If it does not, then the digitization process is aborted, freeing the detectors for a new trigger. The analysis is split into two pieces that roughly match the digitization phase and the data transmission phase of the TPC: Level 1 with a time budget of $\sim 100\mu s$ and Level 2 with a budget of ~ 5 ms. Level 1 works on a subset of the trigger data that is stored in the input buffers of the DSM boards in the TCU crate, the coarse pixel array in η, ϕ space.

The Level 1 system also contains a control section, responsible for the overall flow control of events that pass through the trigger system. If an event is not aborted by the Level 1 analysis, it is passed to Level 2. Level 2 uses the full trigger data set, including the raw data that forms the fine pixel array. Again, the event can be accepted or aborted. If the event is accepted, both the detector subsystems and DAQ are notified. Levels 1 and 2 are implemented in several Motorola 2306 VME CPUs. The CPUs are linked together by an SCI ring and are connected to DAQ by a SCRAMNET link.

STAR has a third level trigger which performs complete online reconstruction of the events in a dedicated CPU farm. The Level 3 trigger can process central Au+Au collisions at a rate of 50 Hz including simple analysis of physics observables such as particle momentum and rate of energy loss. The Level 3 trigger system includes an online display so that individual events can be visually inspected in real time.

2.5 STAR Magnet

A Time Projection Chamber (TPC) (described in next section) is the central detector in the STAR. The accuracy of space point reconstruction from which the particle momenta and trajectories are determined depends on detailed knowledge of the electric and magnetic fields.

The STAR magnet [18] is roughly cylindrical in geometry and consists of 30 flux return bars (backlegs), four end rings and two poletips. The 6.85 *m* long flux return bars are trapezoidal in cross section and weigh 18 tons each. They form the outer wall of the cylinder which encloses the main and space trim coils and are attached to an inner and outer end ring pair at each end of the magnet. The inner end rings have an inner diameter of 5.27 *m* with 30 chord surfaces on the 6.28 *m* outer diameter to fix the azimuth location of each flux return bar. Each inner ring has an axial thickness of 285 mm and weighs 25 tons. To maintain magnetic field quality, deflections in the magnet structure are minimized to less than 1 mm. The magnetic components were precision fabricated and mating connections used high-strength bolts and pinned connections.

There are three types of magnet coils: Main, Space Trim and Poletip Trim. The Main and Space Trim coils are built from two layer pancakes wound two-in-hand (bifilar) fashion in 13 turns. Each pancake contains two parallel water circuits approximately 120 *m* in length. The magnet contains ten Main coils with four pancakes each and two Space Trim coils containing two pancakes each. These coils are connected in series electrically, while the (88) cooling water circuits are connected in parallel. At the maximum field of 0.5 T, the current through these coils is 4500 A, with an additional 12-13% current through the Space Trim coils. Total power consumption is 3.5 MW.

Field optimization (tuning of the trim/poletip currents) and calibration of the absolute magnetic field were initially performed using an NMR probe which was moved along the central axis. The excitation function of the main coil and each trim and pole tip coil was separately determined at values near their nominal settings in order to minimize the nonlinear effects of saturation in the steel. The optimal settings were then computed by minimization of the axial field variations with respect to these currents. Partial maps were taken with the mapper arms set at $\phi = 0^\circ$ and 90° to confirm the optimum setting by direct variation around the computed minima.

The stabilization of the field due to all effects (temperature, power supply settling, etc.) takes approximately 10-20 seconds. The reproducibility of the absolute field was better than ± 0.5 Gauss. The central positive and negative fields are the same magnitude to better than 0.25 Gauss for both full and half field settings. Complete field maps were taken at full field positive and negative, as well as at half field positive. A nearly complete map was taken at half field negative. Due to independent trim coil optimization, the half field maps are slightly different

in shape than the full field maps, especially away from the magnet center. The maximum excursion of the radial component for full(half) field is approximately ± 50 Gauss (± 25 Gauss). The ϕ component of the field is less than ± 3 Gauss (± 1.5 Gauss) .

2.6 Time Projection Chamber

The STAR detector [19, 20] uses the TPC as its primary tracking device [8, 21, 22]. The TPC records the tracks of particles, measures their momenta, and identifies the particles by measuring their ionization energy loss (dE/dx). Its acceptance covers ± 1.8 units of pseudo-rapidity through the full azimuthal angle. Particles are identified over a momentum range from 100 MeV/ c to greater than 1 GeV/ c and momenta are measured over a range of 100 MeV/ c to 30 GeV/ c . By using the relativistic rise in the ionization energy loss, we have achieved particle identification for momenta greater than 2.5 GeV/ c upto 12 GeV/ c as described in Ref. [23].

2.6.1 TPC design

The STAR TPC is shown schematically in Fig. 2.6. It sits in a large solenoidal magnet that operates at 0.5 T [18]. The TPC is 4.2 m long and 4 m in diameter. It is an empty volume of gas in a well defined uniform electric field of ≈ 135 V/ cm . The paths of primary ionizing particles passing through the gas volume are reconstructed with high precision from the released secondary electrons which drift to the readout end caps at the ends of the chamber. The uniform electric field which is required to drift the electrons is defined by a thin conductive Central Membrane (CM) at the center of the TPC, concentric field cage cylinders and the read out end caps. Electric field uniformity is critical since track reconstruction precision is within few mm and electron drift paths are up to 2 m .

The readout system is based on the same principle as used in Multi Wire Proportional Chambers (MWPC) with readout pads. The drifting electrons avalanche in the high fields at the 20 μm anode wires providing an amplification of 1000 to 3000. The positive ions created in the avalanche induce a temporary image charge on the pads which disappears as the ions move away from the anode wire. The image charge is measured by a preamplifier/shaper/waveform digitizer system. The induced charge from an avalanche is shared over several adjacent pads, so the original track position can be reconstructed to a small fraction of a pad width. There

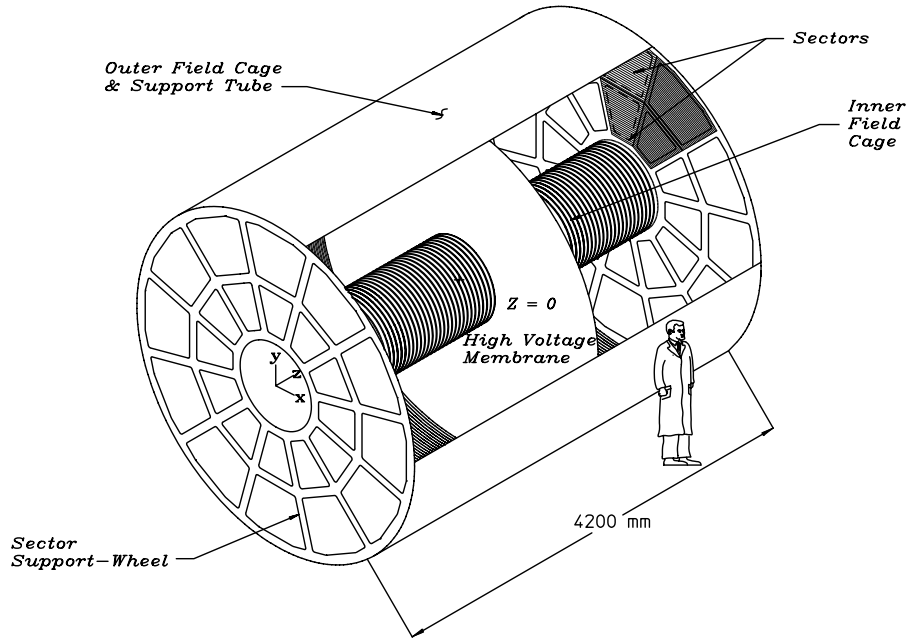


Figure 2.6: The STAR TPC surrounds a beam-beam interaction region at RHIC. The collisions take place near the center of the TPC.

are a total of 136,608 pads in the readout system.

The TPC is filled with P10 gas (10% methane, 90% argon) regulated at 2 *mbar* above atmospheric pressure [24]. Its primary attribute is a fast drift velocity which peaks at a low electric field. Operating on the peak of the velocity curve makes the drift velocity stable and insensitive to small variations in temperature and pressure. Low voltage greatly simplifies the field cage design.

The design and specification strategy for the TPC have been guided by the limits of the gas and the financial limits on size. Diffusion of the drifting electrons and their limited number defines the position resolution. Ionization fluctuations and finite track length limit the dE/dx particle identification. The design specifications were adjusted accordingly to limit cost and complexity without seriously compromising the potential for tracking precision and particle identification.

2.6.2 Tracking Efficiency

The tracking efficiency depends on the acceptance of the detector, the electronics detection efficiency, as well as the two-hit separation capability of the system. The acceptance of the TPC is 96% for high momentum tracks traveling perpendicular the beamline. The 4% inefficiency is caused by the spaces between the sectors which are required to mount the wires on the sectors. The software also ignores any space points that fall on the last 2 pads of a pad row. This fiducial cut is applied to avoid position errors that result from tracks not having symmetric pad coverage on both sides of the track. It also avoids possible local distortions in the drift field. This fiducial cut reduces the total acceptance to 94%.

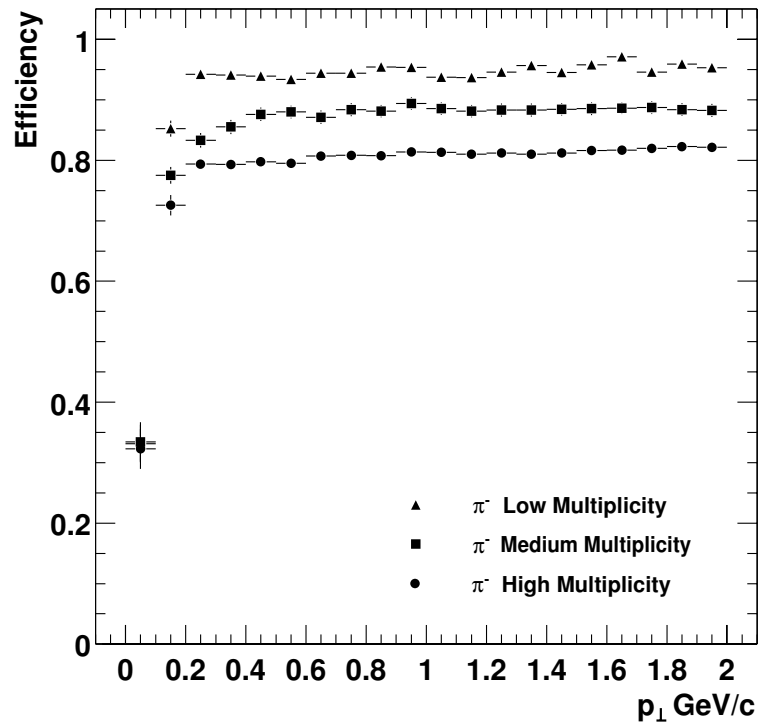


Figure 2.7: The pion tracking efficiency in STAR for central Au+Au events at RHIC for different multiplicities. Tracks with $|y| < 0.5$ were used to generate the figure and the magnetic field was set to 0.25 T.

The detection efficiency of the electronics is essentially 100% except for dead

channels and the dead channel count is usually below 1% of the total. However, the system cannot always separate one hit from two hits on adjacent pads and this merging of hits reduces the tracking efficiency. The software also applies cuts to the data. For example, a track is required to have hits on at least 10 pad rows because shorter tracks are too likely to be broken track fragments. But this cut can also remove tracks traveling at a small angle with respect to the beamline and low momentum particles that curl up in the magnetic field. Since the merging and minimum pad rows effects are non-linear, we can not do a simple calculation to estimate their effects on the data. We can simulate them, however.

In order to estimate the tracking efficiency, we embed simulated tracks inside real events and then count the number of simulated tracks that are in the data after the track reconstruction software has done its job. The technique allows us to account for detector effects and especially the losses related to a high density of tracks. The simulated tracks are very similar to the real tracks and the simulator tries to take into account all the processes that lead to the detection of particles including: ionization, electron drift, gas gain, signal collection, electronic amplification, electronic noise, and dead channels. The results of the embedding studies indicate that the systematic error on the tracking efficiency is about 6%.

Fig. 2.7 shows the pion reconstruction efficiency in Au+Au collisions with different multiplicities as a function of the transverse momentum of the primary particle. In high multiplicity events it reaches a plateau of 80% for high p_T particles. Below 300 MeV/ c the efficiency drops rapidly because the primary particles spiral up inside the TPC and don't reach the outer field cage. In addition, these low momentum particles interact with the beam pipe and the inner field cage before entering the tracking volume of the TPC. As a function of multiplicity, the efficiency goes up to the geometrical limit, minus software cuts, for low multiplicity events.

2.6.3 Vertex resolution

The primary vertex can be used to improve the momentum resolution of the tracks and the secondary vertices can be separated from the primary vertices if the vertex resolution is good enough. Many of the strange particles produced in heavy ion collisions can be identified this way. The primary vertex is found by considering all of the tracks reconstructed in the TPC and then extrapolating them back to the origin. The global average is the vertex position. The primary vertex resolution is shown in Fig. 2.8. It is calculated by comparing the position of the vertices that are

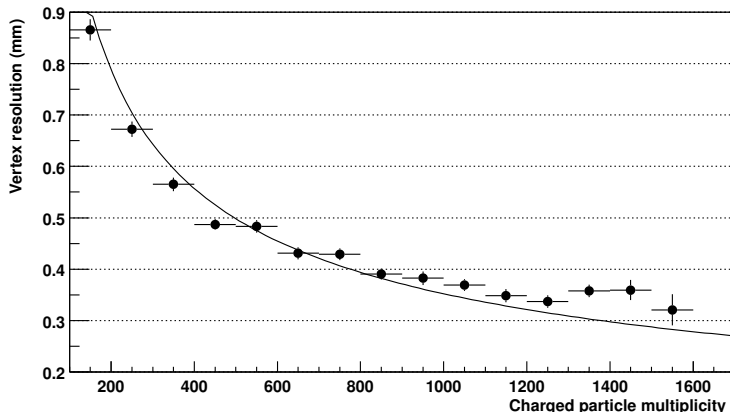


Figure 2.8: Primary vertex resolution in the transverse plane as a function of centrality.

reconstructed using each side of the TPC, separately. As expected, the resolution decreases as the square root of the number of tracks used in the calculation. A resolution of $350 \mu\text{m}$ is achieved when there are more than 1,000 tracks.

2.6.4 Particle identification using dE/dx

Energy lost in the TPC gas is a valuable tool for identifying particle species. It works especially well for low momentum particles but as the particle energy rises, the energy loss becomes less mass-dependent and it is hard to separate particles with velocities $v > 0.7c$. STAR was designed to be able to separate pions and protons up to $1.2 \text{ GeV}/c$. This requires a relative dE/dx resolution of 7%. The challenge, then, is to calibrate the TPC and understand the signal and gain variations well enough to be able to achieve this goal.

The dE/dx is extracted from the energy loss measured on up to 45 padrows. The length over which the particle energy loss is measured (pad length modulo the crossing and dip angles) is too short to average out ionizations fluctuations. Indeed, particles lose energy going through the gas in frequent collisions with atoms where a few tenths of eV are released, as well as, rare collisions where hundredths of eV are released [25]. Thus, it is not possible to measure accurately the average dE/dx . The most probable energy loss is measured instead, which requires to discard the large ionization clusters. The truncated mean, where a given fraction

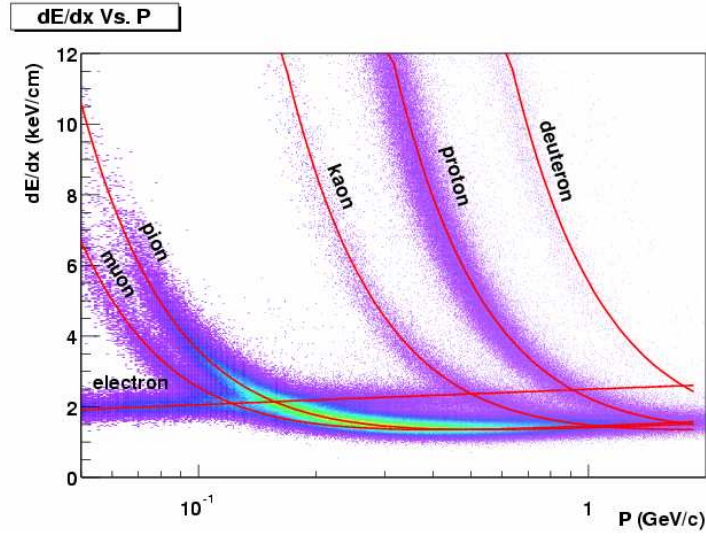


Figure 2.9: The energy loss distribution for primary and secondary particles in the STAR TPC as a function of the p_T of the primary particle. The magnetic field was 0.25 T.

(typically 30%) of the clusters having the largest signal are removed, is an efficient way to measure the most probable dE/dx . However, fitting the dE/dx distribution including all clusters associated to a given track was found to be more effective. It also allows to account for the variation of the most probable energy loss with the length of the ionization samples (dx) [26].

Fig. 2.9 shows the energy loss for particles in the TPC as a function of the particle momentum. The data have been corrected for signal and gain variations and the data are plotted using a 70% truncated mean. The magnetic field setting is 0.25 T. The resolution is 8% for a track that crosses 40 pad-rows. At 0.5 T, the dE/dx resolution improves because the transverse diffusion is smaller and this improves the signal to noise ratio for each cluster. Fig. 2.9 includes both primary and secondary particles. The prominent proton, deuteron, and muon bands come from secondary interactions in the beam pipe and IFC, and from pion and kaon decays. Pions and protons can be separated from each other up to 1 GeV/ c .

2.6.5 Centrality selection

In heavy ion experiments one of the challenges is to measure the impact parameter of the two colliding ions. In actual experiment it is not feasible to measure the impact parameter of the colliding nuclei. So we use the term centrality to define the impact parameter of the collision in heavy ion experiments. By knowing the centrality of the collision we can study the behavior of the different global observables as a function of centrality. In general centrality is defined as the overlap region of the two colliding ions or classifying the events according to the number of participants. The central collision means that the two nuclei have suffered head on collision and the overlap volume is maximum. On the other hand if the number of participants in the overlap region of two colliding nuclei is very less it is termed as peripheral collision.

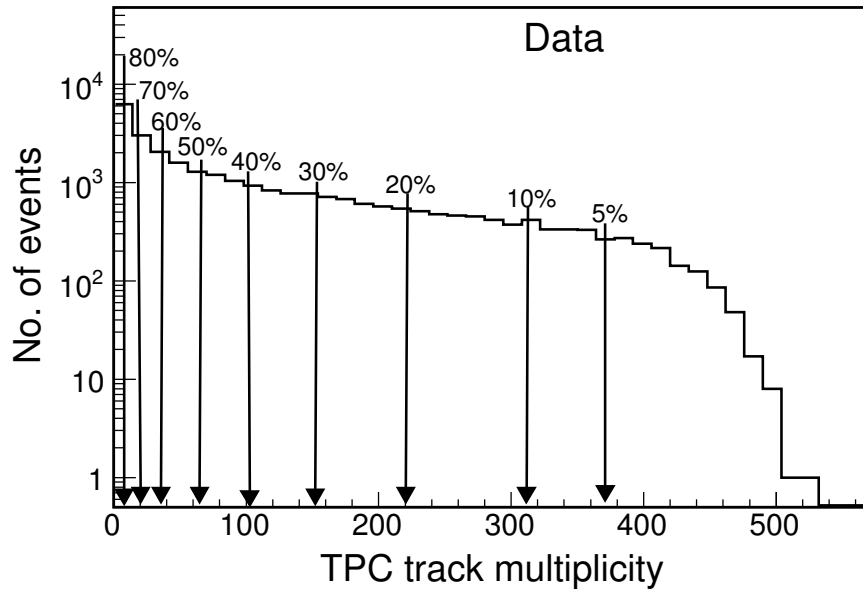


Figure 2.10: The minimum-bias distribution of the charge particles from the TPC within $|\eta| < 0.5$ for Au+Au collisions at $\sqrt{s_{NN}} = 62.4$ GeV. The arrows represent the various centrality classes.

In STAR experiment the centrality of the collision is determined by counting the total charge particles event by event in the TPC within the $|\eta| < 0.5$ coverage. Fig. 2.10 shows the minimum bias distribution of the charge particles over a large number of events from the TPC in Au+Au collisions. The arrows show the number

of charged particles used for defining each centrality class. The total % of events used with the minimum bias trigger condition for the analysis of the data and centrality determination for Au+Au at $\sqrt{s_{\text{NN}}} = 62.4$ GeV was $\sim 80\%$. This number was not 100% because of the triggering inefficiency and vertex determination inefficiency in the low multiplicity events.

2.7 Electromagnetic Calorimeters

STAR, which is nominally a slow detector, utilizes the EMC to trigger on and study rare, high p_T processes (jets, leading hadrons, direct photons, heavy quarks) and provide large acceptance for photons, electrons, π^0 and η mesons in systems spanning polarized $p+p$ through Au+Au collisions. Other applications include general event characterization in heavy ion collisions including ultra peripheral collisions. In order to achieve these physics goals STAR has two electromagnetic calorimeters which are briefly discussed below.

2.7.1 Barrel electromagnetic calorimeter

The STAR Barrel electromagnetic calorimeter [9] covers the pseudo-rapidity region $|\eta| < 1$ with full azimuth. The total area covered is about 100 m^2 . It being a sampling calorimeter, consists of alternate layers of lead and scintillator planes. It has 20 layers of lead plates and 21 layers of scintillator. The lead plates and 19 scintillator plates are of 0.5 cm thick, the remaining two layers of scintillator are 0.6 cm in thickness. The total radiation length of the calorimeter including the steel support structures is $\sim 20X_0$. The 21 active scintillating layers of the calorimeter is made of a material named Kuraray SCSN81 (5 mm and 6 mm thick). The calorimeter is modular in design. It consists of 120 modules, each subtends 6° in $\Delta\phi$ (~ 0.1 radian) and 1.0 unit in η . The dimensions in terms of centimeters are the following : Each module is roughly 26 cm wide by 293 cm long with an active depth of 23.5 cm plus about 6.6 cm in structural plates (of which $\approx 1.9 \text{ cm}$ lies in front of the detector). Each module is further segmented in η and ϕ . Each module is divided into 40 towers, 2 in ϕ and 20 in η . Each tower then has the granularity of 0.05 in both $\Delta\phi$ and $\Delta\eta$. The full calorimeter has 4800 towers. There exists a shower maximum detector located about 5 radiation lengths from the front of the lead-scintillator stack in each module.

2.7.2 Endcap electromagnetic calorimeter

A single endcap electromagnetic calorimeter (EEMC) [10] was installed in 2002-3 on the west poletip of the STAR detector. The EEMC provides coverage for pseudorapidity values $1 < \eta \leq 2$, over the full azimuthal range, supplementing the barrel EMC (BEMC) described in the preceding section. Within this acceptance, it adds the capabilities to detect photons and electromagnetically decaying mesons (π^0 , η), to identify electrons and positrons, and to trigger on high-energy particles of these types. The EEMC also includes a shower-maximum detector optimized to discriminate between photons and π^0 or η mesons over the 10-40 GeV energy region, as well as preshower and postshower layers intended for electron *vs.* hadron discrimination. Furthermore, this significantly enhanced the acceptance and triggering capabilities of STAR for jets. The greatest demand for such forward calorimetry arises from the program of experiments to be carried out with colliding polarized proton beams at RHIC.

The above physics opportunities set the requirements for the EEMC. In particular, we note the need to cover a very wide dynamic range (nearly 1000:1 in energy), with excellent π^0/γ and hadron/electron suppression, and accurate absolute calibration of the calorimeter energy scale. The focus on p-p rather than A-A collisions relaxes somewhat the demand on tower segmentation, in comparison with the STAR BEMC. These requirements then dictate a tradeoff, in which the granularity of readout channels for the calorimeter towers is reduced, but a more expensive scintillator solution is used for the shower-maximum detector (SMD). For the higher-energy showers that characterize the p_T range of interest in the endcap η region, the scintillator SMD promises significantly better performance, in both transverse shower profile delineation and energy deposition resolution, than the gaseous BEMC SMD counters. A traditional Pb/plastic scintillator sampling calorimeter for the EEMC design was chosen, primarily due to advantages in cost, simplicity and sharing of technology with STAR's BEMC. A scintillator strip shower maximum detector (SMD) with high position resolution is located after the 5th radiator plate. Light from the towers and SMD is carried on optical fibers outside the STAR magnet, to photomultiplier tubes mounted on the rear of the poletip.

2.8 Time-of-flight detector

Resistive Plate Chambers(RPCs) were developed in 1980s, and were originally operated in streamer mode. This was suitable for getting high detection efficiency ($> 95\%$) and time resolution (1 ns), for low fluxes of incident particles. At higher fluxes ($> 200 \text{ Hz}/\text{cm}^2$), RPCs begin to lose their efficiency. A way to overcome this problem was to operate the RPCs in avalanche mode. The Multi-gap Resistive Plate Chambers(MRPC) was developed less than 10 years ago. It consists of a stack of resistive plates, separated one from other with equal sized spaces creating a series of gas gaps. Electrodes are connected to the outer surfaces of the stack of the resistive plates while all the internal plates are left electrically floating. Initially voltage on these internal plates is given by electrostatics, but they are kept at the correct voltage due to the flow of the electrons and ions created in the avalanches. MRPC, as a new kind of detector for time-of-flight system, operated in avalanche mode with a non flammable gas mixture of 90% F134A, 5% SF_6 , can fulfill all these requirements: high efficiency ($> 95\%$), excellent intrinsic time resolution ($< 100 \text{ ps}$), high rate handling capability ($500 \text{ Hz}/\text{cm}^2$), high modularity and simplicity in construction, good uniformity of response, high granularity/low occupancy and large acceptance.

The main goal of the STAR Time-Of-Flight (TOF) [13] system was to provide information that extends the hadronic particle identification capabilities of the experiment. It consists of a highly-segmented cylindrical detector immediately surrounding TPC and it is to be arranged in 120 trays. Each individual tray is 2.4 m long, 21.3 cm wide and 8.5 cm deep ($z \times \phi \times r$). In 2003, the TOF based on the multi-gap resistive plate chamber(MRPC) technology was installed in STAR experiment. It extends the particle identification up to $p_T \sim 3 \text{ GeV}/c$ for protons and anti-protons. This tray was installed in the $-1.0 < \eta < 0$ covering 60° in azimuth at a radius of $\sim 220 \text{ cm}$. It contains 28 MRPC modules which were partially instrumented during the 2003 run. Since acceptance of TOF is small, a special trigger selected events with a valid pseudo vertex position detectors (pVPD) coincidence and at least one TOF hit was used in 2003 run. For full TOF coverage at STAR, there will be 120 trays, with 60 on east side and 60 on west side. For each tray, there will be 33 MRPC's. For each MRPC, there are 6 readout channels. The MRPCs are tiled differently so that each MRPC is most projective to the average primary vertex location $z = 0$.

2.9 Forward time projection chamber

There are two cylindrical forward TPC detectors [11] in STAR, which were constructed to extend the phase space coverage of the STAR experiment to the region $2.5 < |\eta| < 4.0$. For optimal use of the available space and in order to cope with the high track density of central Au+Au collisions at RHIC, a novel design was developed using radial drift in a low diffusion gas. A 2-track resolution of 1 - 2 *mm* was achieved. These FTPCs situated on both sides of STAR along the beam pipe, measure momenta and production rates of positively and negatively charged particles as well as neutral strange particles. Also, due to the high multiplicity, approximately 1000 charged particles in a central Au+Au collision, event-by-event observables like $\langle p_T \rangle$, fluctuations of charged particle multiplicity and collective flow anisotropies can be studied. The design and construction was carried out by the group from MPI Munich with contributions from LBNL Berkeley, BNL Brookhaven, UC Davis, UCLA Los Angeles, and MEPHI Moscow [11, 27, 28].

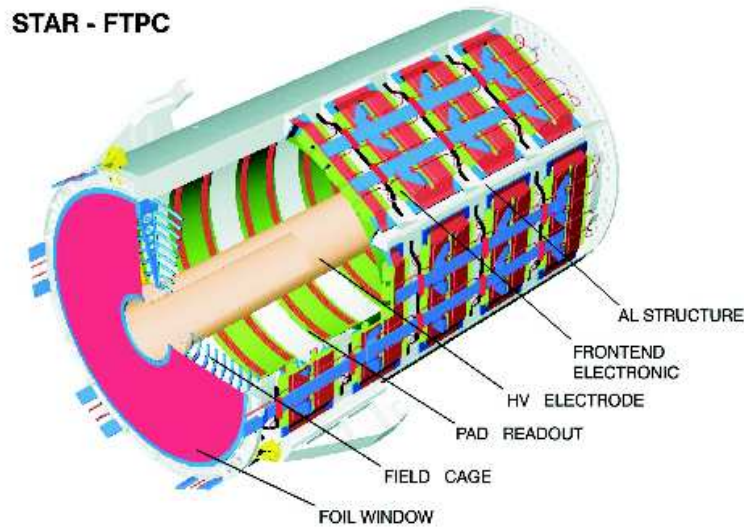


Figure 2.11: Schematic diagram of an FTPC for the STAR experiment

2.9.1 FTPC design

The FTPC concept was determined mainly by two considerations: Firstly by the high particle density with tracks under small angles with respect to the beam direction and secondly by the restricted available space inside the TPC [29], where the FTPCs are located. In Fig. 2.11 the final design is shown and the design parameters are listed in Table. 2.1. It is a cylindrical structure, 75 *cm* in diameter and 120 *cm* long, with a radial drift field and readout chambers located in 5 rings on the outer cylinder surface. Each ring has two padrows and is subdivided azimuthally into 6 readout chambers. The radial drift configuration was chosen to improve the two-track separation in the region close to the beam pipe where the particle density is highest. The field cage is formed by the inner HV-electrode, a thin metalized plastic tube, and the outer cylinder wall at ground potential. The field region at both ends is closed by a planar structure of concentric rings, made of thin aluminum pipes. The front end electronics (FEE), which amplifies, shapes, and digitizes the signals, is mounted on the back of the readout chambers. Each particle trajectory is sampled up to 10 times. The ionization electrons are drifted to the anode sense wires and induced signals on the adjacent cathode surface are read out by 9600 pads (each $1.6 \times 20 \text{ mm}^2$).

The above design has some unusual and new features for a TPC:

- (i) The electrons drift in a radial electrical field perpendicular to the solenoidal magnetic field.
- (ii) Curved readout chambers are used to keep the radial field as ideal as possible.
- (iii) A two-track separation of 1-2 mm is expected, which is an order of magnitude better than in all previously built TPCs with pad readout.

Due to the short drift length of only 23 *cm* a gas mixture with CO₂ or DME can be used. It has a low diffusion coefficient for electrons and a small Lorentz angle [30]. After extensive measurements on Ar/CO₂ (50%/50%) mixture was selected which is nonflammable, shows no or little aging effect in comparison to hydrocarbons and is chemically less aggressive than a mixture with DME.

Table 2.1: FTPC parameters

PARAMETER	VALUE
Configuration	
# of TPC	2
rows per TPC	10
sectors per pad row	6
pads per sector	2×160
Sensitive Volume	
inner radius	8.0 <i>cm</i>
outer radius	30.5 <i>cm</i>
chamber length	120.0 <i>cm</i> ($150 < z < 270$ <i>cm</i>)
acceptance	$2.5 < \eta < 4.0$ ($2.0^\circ < \theta < 9.3^\circ$)
Field Cage	
drift cathode voltage	10-15 kV
drift electrical field	240-1400 V/ <i>cm</i> (radial)
solenoid magnetic field	0.5 T
Gas	
gas mixture	Ar(50%)-CO ₂ (50%)
drift velocity	0.3 - 2.0 <i>cm</i> / μ s
trans. diffusion D_T	100-130 μ m/ $\sqrt{\text{cm}}$
long. diffusion D_L	100-130 μ m/ $\sqrt{\text{cm}}$
Lorentz angle	4 deg. (at 0.5 T)
gas gain	$\sim 1\text{-}2 \times 10^3$
Readout	
# of pads	19200
time bins per pad	256
pad pitch	1.9 mm
pad length	20 mm
anodewire-pad gap	1.5 mm
shaping time (FWHM)	350 ns
SCA time bin size	218 ns
ADC dynamic range	10 bits

2.9.2 Readout Chamber

In a conventional TPC the anode (amplification) wires are orthogonal to the axial direction of the pads. This is impossible in the case of a curved readout chamber. The wires can not be parallel to the pads and therefore to the cylinder axis either, because focusing effects then lead to periodic shifts in the position measurement. This is demonstrated in fig. 2.12. However, if two or more wires cross the pad

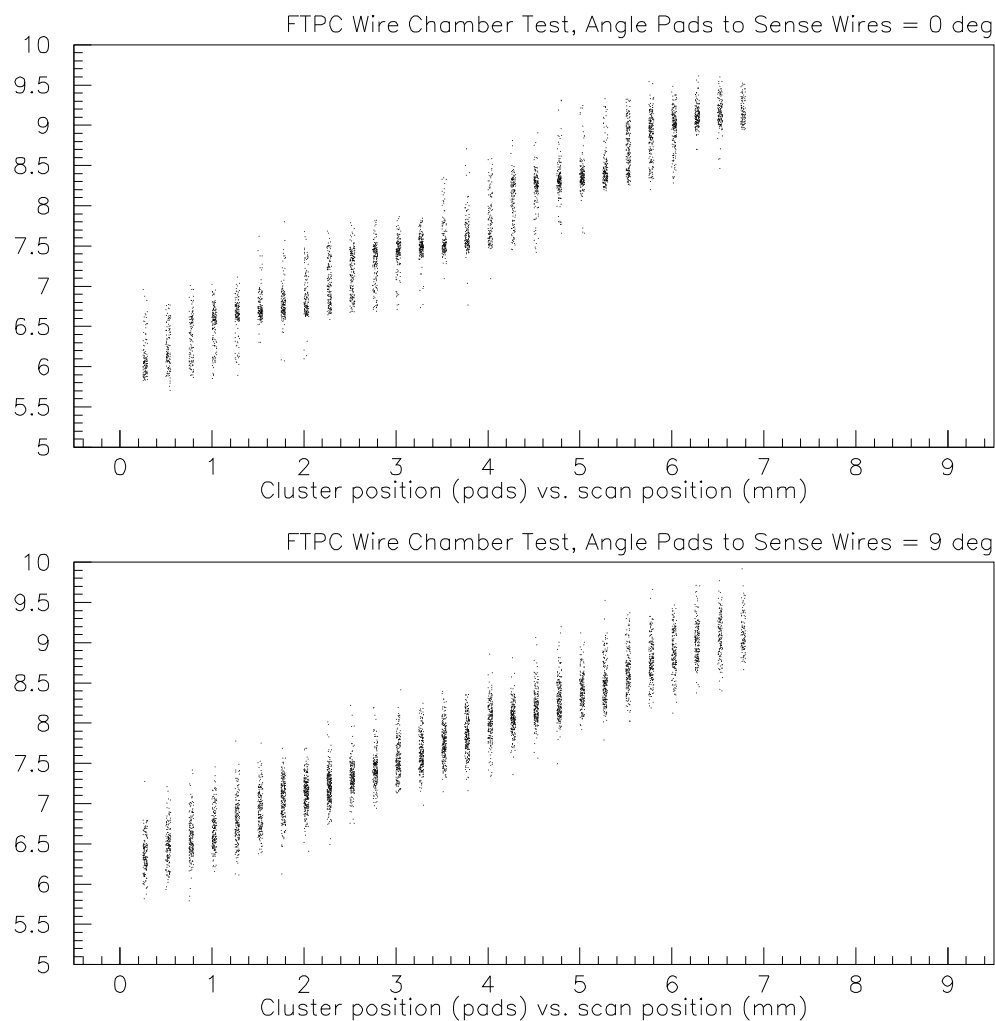


Figure 2.12: Measured position of a laser beam for two crossing angles between the anode wires and the pad axis. For 0° (top) systematic shifts due to the wire structure are observed, which disappear for 9° angle (bottom).

under a small angle this effect already vanishes. For the FTPC design an angle of 17.4° was chosen resulting in three wires crossing each pad for the selected pad-wire geometry. The anode wires are first glued on the flat pad plate with conductive epoxy. Afterwards the plate is bent between 3 rollers to the final curvature without breaking the wires. A complete readout chamber with 2 padrows is shown in fig. 2.13.

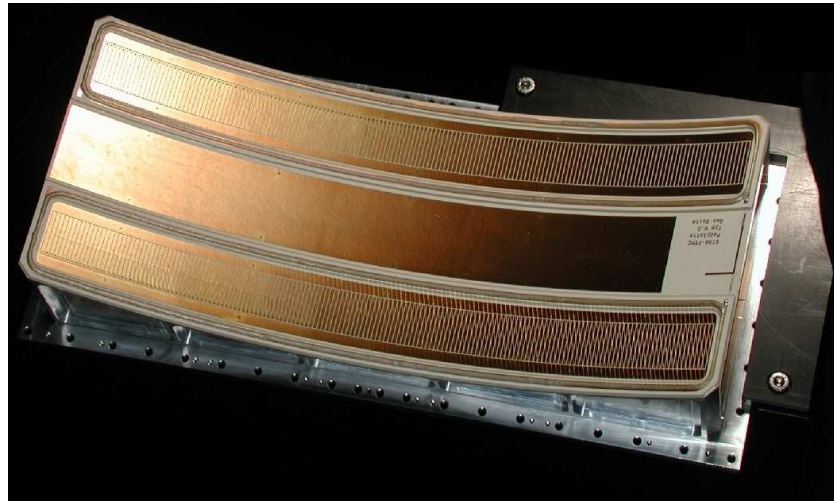


Figure 2.13: Photograph of a FTPC readout chamber. The bending radius is 305 mm and each of the two padrows has 160 pads.

With only 1.5 mm distance between the anode wires and the pad plane the spread of the signal (the so-called Pad Response Function) is of similar narrow width. This together with the low electron diffusion and the radial drift principle results in the required 2-track separation of about 1 mm as can be seen in fig. 2.14.

2.9.3 Readout Electronics

The two FTPCs have 19,200 channels of electronics, capable of measuring the charge drifting to the readout chambers in short time samples. The drift time of about 50 μs for the 23 cm maximum drift length is subdivided into 256 time bins. Because of the slow drift gas and the resulting long duration of the collection of the electron cloud from a track crossing a shaping time of 350 ns is used. The sampling rate is 5 MHz. The design of the front end electronics closely follows that of the central TPC [31]. Each pad is read out by a low-noise STAR preamplifier/shaper

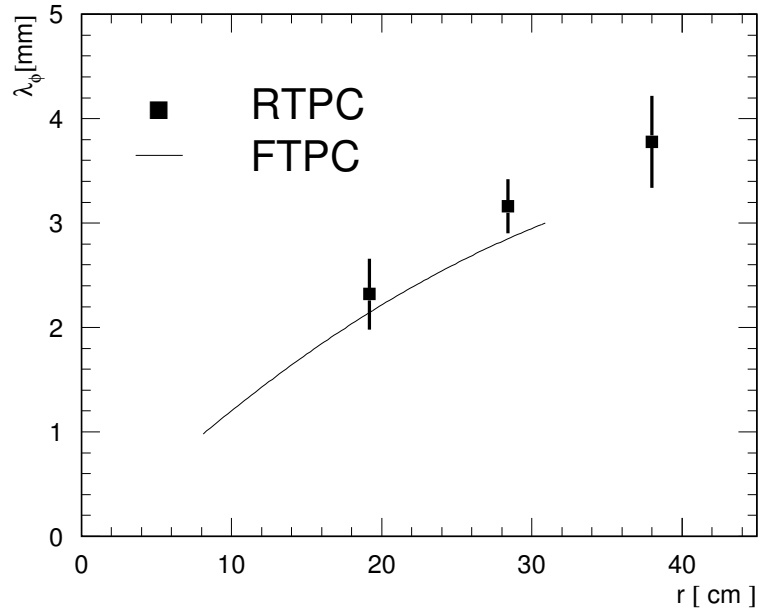


Figure 2.14: Measured 2-track resolution in the prototype RTPC (data points) and expected resolution in the FTPC (line) as a function of the radial distance r from the beam axis.

(SAS), which sends signals to a switched capacitor array/ADC chip (SCA/ADC). Four of these chip sets, handling 64 channels, are mounted on a small FEE card, which is positioned directly on the detector, parallel to the readout chambers. Fifteen FEE cards are read out by a readout board, which sends the signals via a 1.2 Gbit/s fiber-optic link to the data acquisition system. The readout board also controls the FEE cards, utilizing signals from the clock and trigger distribution system, and the slow control links. For maintaining the proper operating temperature the FEE and readout boards are water cooled using a leak less, low pressure circulation system [32]. The FTPCs are remotely operated through a VME based supervision system. Data logging and visualization are performed by a software package developed within the EPICS mainframe [33].

2.10 Photon multiplicity detector

A preshower Photon Multiplicity Detector (PMD) is installed on the east wall of the wide angle hall in STAR. Fig. 2.15 shows the STAR PMD after complete installation in the STAR experiment at Brookhaven national Laboratory in year 2004. This detector is designed to measure photon multiplicity in the forward region where high particle density precludes the use of a calorimeter [12]. Fig. 2.16 shows the PMD relative to other detectors within the STAR setup as implemented through GEANT simulation [34]. The inclusion of the PMD enhances the phase space coverage of STAR with photons considerably, in pseudorapidity upto $\eta = 3.5$ with full azimuthal acceptance and in p_T down to about 25 MeV/c [35, 36].

Using the measurement of multiplicity and spatial distribution of photons on an event by event basis and combining the information from other detectors, the PMD will be able to address the following broad topics in physics :

- (a) Determination of reaction plane and the probes of thermalization via studies of azimuthal anisotropy and flow,
- (b) Critical phenomena near the phase boundary leading to fluctuations in global observables like multiplicity and pseudorapidity distributions,
- (c) Signals of chiral symmetry restoration (e.g., disoriented chiral condensates) using information on charged particles from FTPC.

The basic principle of the measurement of photon multiplicity using the PMD is similar to those of preshower detectors used in WA93 and WA98 experiments at CERN SPS [37, 38]. It consists of highly segmented detector placed behind a lead converter of suitable thickness. A photon produces an electromagnetic shower on passing through the converter. These shower particles produce signals in several cells of the sensitive volume of the detector. Charged hadrons usually affect only one cell and produce a signal resembling those of Minimum Ionizing Particles (MIPs). The thickness of the converter is optimized such that the conversion probability of photons is high and transverse shower spread is small to minimize shower overlap in a high multiplicity environment. In order to have better hadron rejection capability, another plane of the detector of identical dimension and granularity as those of the preshower part is placed before the lead plate, which acts as a veto for charged particles.

The detector is based on a proportional counter design using a 70:30 ratio by weight of Ar + CO₂ gas mixture as the sensitive medium. This gas mixture

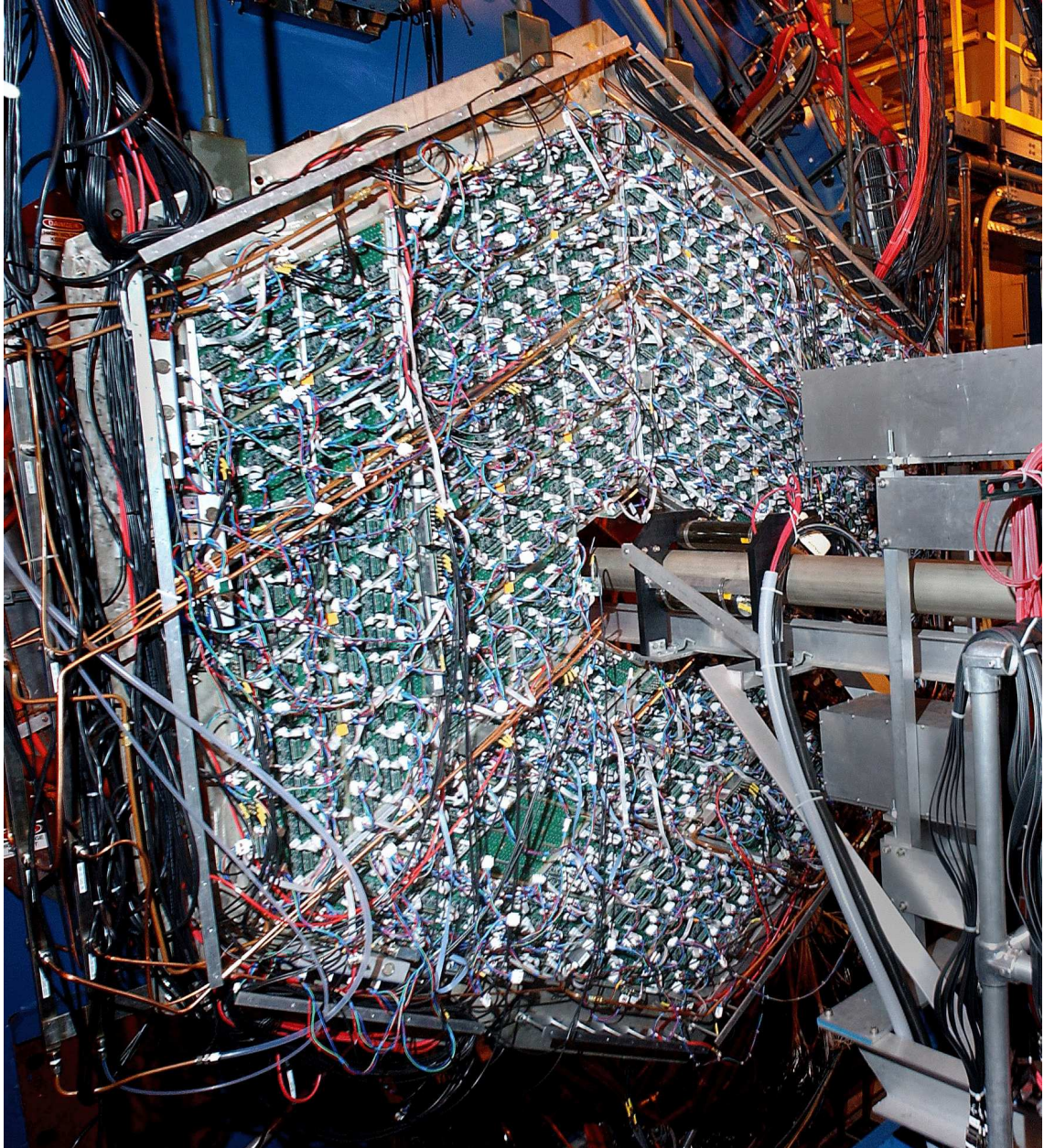


Figure 2.15: The STAR PMD after complete installation of electronic at the STAR experiment

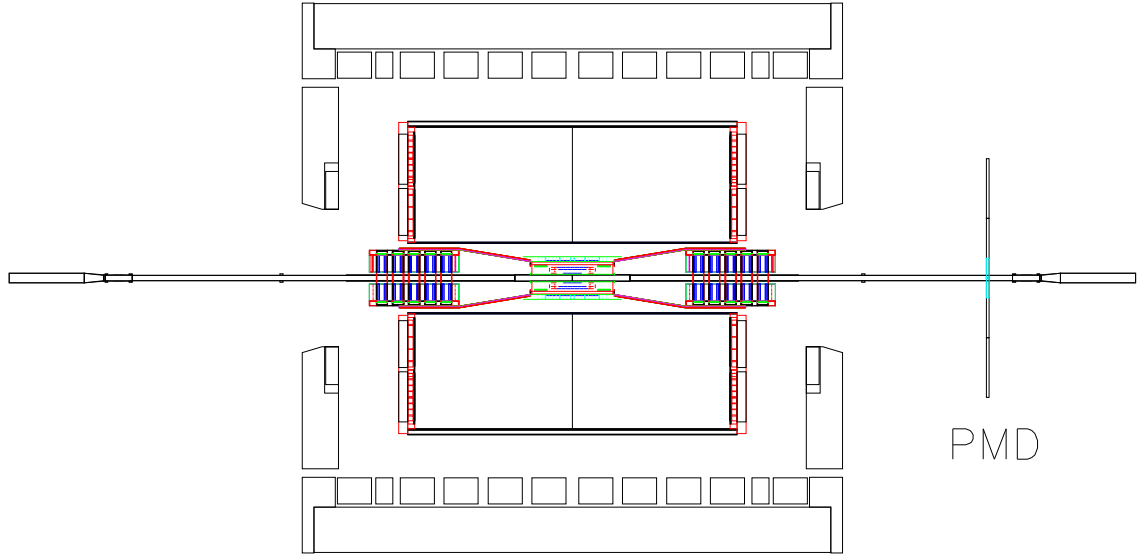


Figure 2.16: The PMD in the STAR set up relative to central detector TPC. The PMD is located at 540 cm from vertex and kept outside the STAR magnet.

is preferred because of its insensitivity to neutrons. To handle the high particle density in the forward region, the detector technology has been chosen with the considerations that

- (i) Multihit probability should be less,
- (ii) Charged hadron signal should be contained in one cell,
- (iii) Low energy δ -electrons should be prevented from traveling to nearby cells and causing cross-talk among adjacent cells.

Requirement of granularity and isolation of cells require the segmentation of the detector gas volume with material effective for reducing δ -electrons from crossing one cell to other. We have used honeycomb cellular geometry with wire readout. The copper honeycomb body forms the common cathode and is kept at a large negative potential. It also supports the printed circuit boards (PCBs) which are used for signal collection and for extension of the cathode required for proper field shaping. Details can be found in [36, 39].

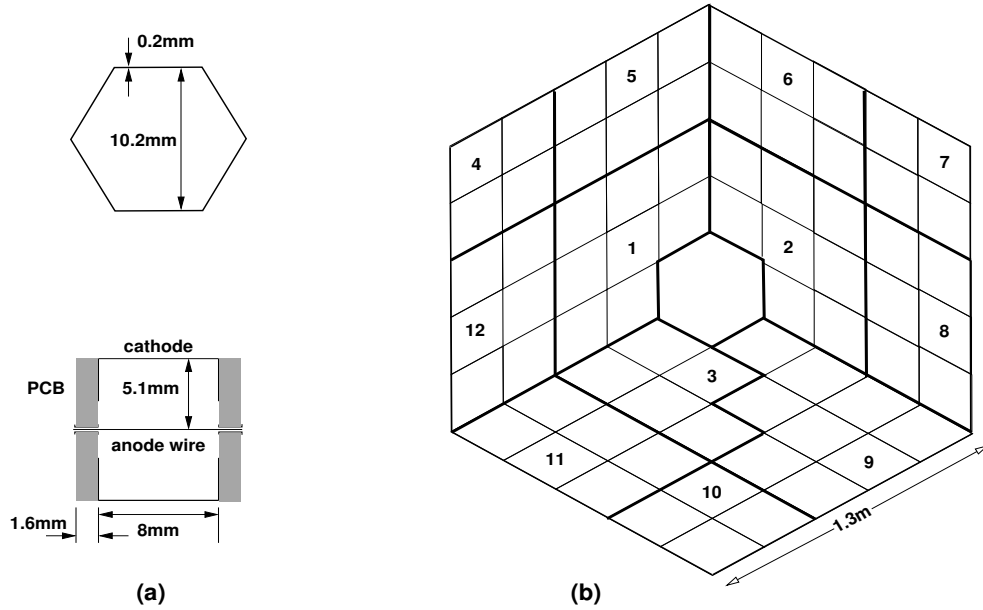


Figure 2.17: (a) Unit cell schematic with cross-section showing the dimensions and the cathode extension, (b) Layout of the STAR PMD. Thick lines indicate supermodule boundaries. There are 12 supermodules each in the preshower plane and the veto plane. Divisions within a supermodule denote unit modules.

2.10.1 The PMD Detector

The detector consists of an array of hexagonal cells. A unit cell is shown schematically in Fig. 2.17 (a) along with a longitudinal section illustrating the use of extended cathode for field shaping. This design was arrived at after several simulation studies and prototype tests and ensures uniform charged particle detection efficiency throughout the cell [40].

A honeycomb of 24×24 cells forms a unit module. This is a rhombus of side approx. 254 mm having identical boundaries on all the four sides. Cell walls at the boundary are kept half as thick as those inside so that adjacent unit modules join seamlessly.

A set of unit modules are enclosed in a gas-tight chamber called a supermodule. The number of unit modules varies from 4 to 9 within a supermodule. The STAR PMD consists of 24 supermodules arranged in the form of a hexagon as shown in Fig. 2.17 (b). This geometry ensures full azimuthal coverage with minimum number of supermodules.

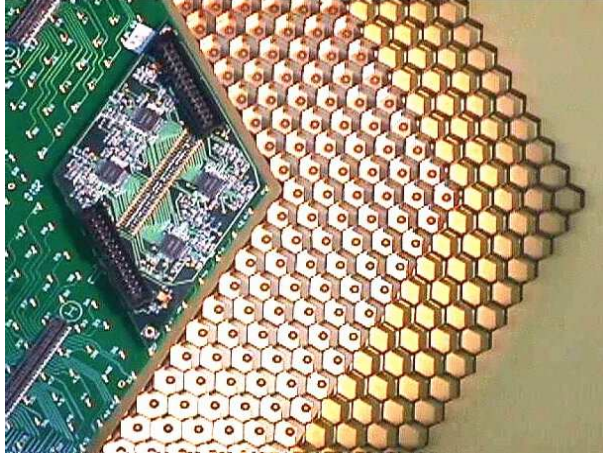


Figure 2.18: Components of a unit module : Copper honeycomb, placed between two PCBs. The top PCB is seen with connectors and a FEE board. The cathode extension on the inside of the bottom PCB and the island separating the anode wire with the cathode is visible through the honeycomb. The photograph was taken with unassembled components.

2.10.1.1 Unit Module

The components of a unit module are shown in Fig. 2.18. It consists of a custom-built copper honeycomb sandwiched between two PCBs which hold the anode wire and provide extension to cathode. The top PCB, containing the electronics boards, has solder-islands at the center of each cell with a 0.5 mm diameter gold-plated through-hole. Signal tracks from cluster of 64 cells are brought to a 70-pin connector. The PCBs on the bottom side have only soldering islands without signal tracks, serving as anchor points. The inner part of the PCBs are gold-plated, with circular islands near the anode wire and form part of the extended cathode.

A copper unit cell is the building block of the honeycomb. It is fabricated using 0.2 mm thick ETP grade copper sheets which are solder-coated on one side. The sheet is cut to precise dimensions along with notches and bent in hexagonal form with precision dies. These are arranged in a 24×24 matrix in a high precision jig of rhombus shape. Hexagonal Stainless Steel inserts, having dimensions matching the inner dimensions of the cell, are inserted in each cell. The assembly is heated so that soldered surfaces join to form a rigid honeycomb.

The honeycomb, after cleaning, is dip-coated with high conductivity graphite

paint having thickness of $\sim 10 \mu\text{m}$. The unit honeycomb module has stiff 1 mm diameter brass screws situated at 24 different locations, which act as guides for attaching the PCBs on both sides, ensuring proper alignment. They are also used to bring out the high voltage connections of the cathode onto the PCBs. The two PCBs are attached on both sides of the honeycomb, aligning with the screws. These screws protrude only 0.5 mm above the PCB surface and are fixed with thin nuts on the surrounding islands. The islands are covered with ABS plastic caps.

The gold-plated tungsten wires ($20 \mu\text{m}$ diameter) are inserted through the holes on the PCBs, using a needle and a tensioning jig. After applying tension of $\sim 30\%$ of the elastic limit, the wires are soldered onto the islands on the PCBs about 3 mm away from the hole (for details see Ref. [39]). The plated through-holes, where wires emerge, are then closed with a tiny amount of fast-setting epoxy to make them gas-tight. This scheme prevents creepage of solder flux into the cell and makes soldering easier.

A moulded FR4 edge frame is bonded to the top PCB. This frame has a beveled outer wall which forms a V-shaped groove between the boundaries of the adjoining unit modules.

Quality assessment for the fabrication of the unit module is done by several ways, viz, visual inspection of the solder joints and epoxy filling in the holes and measurement of resistance of each wire to monitor dry-soldering contacts. Resistance measurement shows that the RMS is within 5% for one unit module. In addition, high voltage tests are also performed after connecting the front-end electronics boards and the pedestals of chips monitored to test stable operation of the detector.

2.10.1.2 Supermodule

Supermodule is a gas-tight chamber made of 3 mm thick FR4 grade glass epoxy sheet as the base plate and a 7 mm thick and 25 mm high aluminum boundary wall. A schematic cross-section of a supermodule is shown in Fig. 2.19. The opposite sides of the boundary walls have gas-feed channels. Each channel has 24 openings into the chamber. This scheme, along with the notches in the cells, keep the gas flow impedance low. A set of assembled unit modules are placed to fill the inner area of the supermodule enclosure, leaving a gap of 1 mm on all sides to accommodate general assembly tolerance and to provide insulation between the honeycomb cathode and the boundary. Teflon spacers are inserted into this gap all along the boundary to arrest any movement of the unit modules and also to insulate

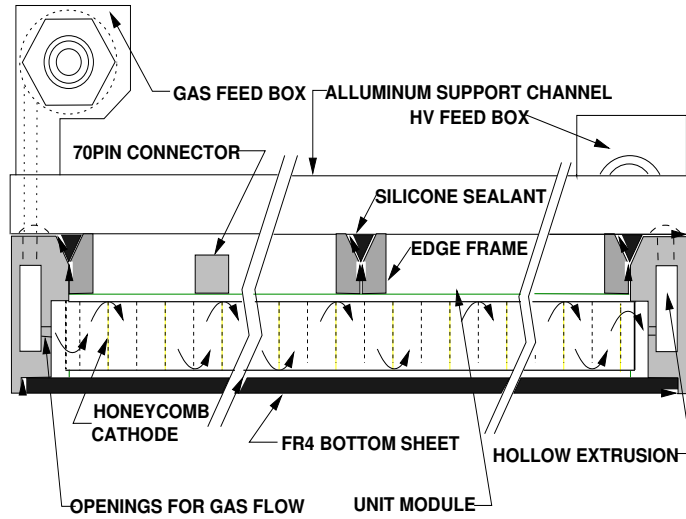


Figure 2.19: Schematic cross-section of a supermodule showing the boundary walls, gas flow channels, high voltage connection and gas-tight sealings.

the honeycomb cathode from the walls. The groove formed at the junctions of all the unit modules and between the boundary walls and the unit modules are filled with high viscosity silicone adhesive compound to make the chamber gas-tight.

Gas is fed through the connector at the end of the long gas feed channel. This channel has openings spaced at an interval of 25 mm throughout the channel. The gas enters through all the entry points in the channel simultaneously, at the depth of 4 mm from the bottom of the chamber. It then flows through the notches and exits at the other edge of the supermodule through the openings of the output channel. An aluminum enclosure containing one SHV connector, an HV limiting resistor and decoupling capacitor is now fixed at one corner of the supermodule very close to the HV tapping point.

2.10.1.3 Support Structure

The drawing of the support structure is shown in Fig. 2.20. It has two parts:

- (a) The support plates.
- (b) The suspension movement mechanisms.

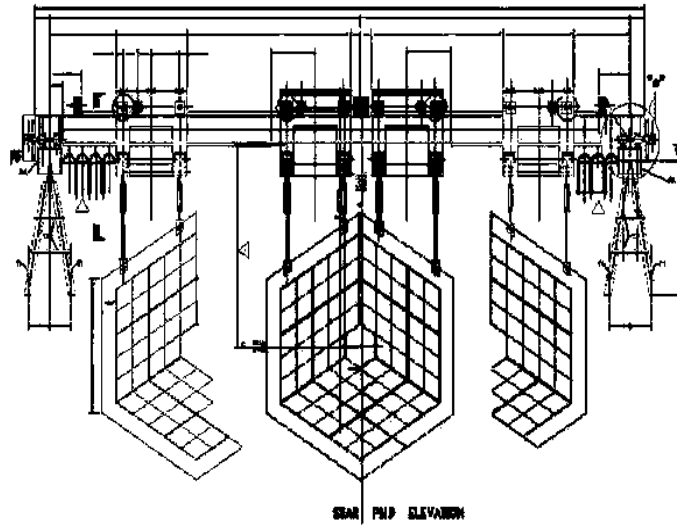


Figure 2.20: PMD support mechanism. The inner hexagonal part shows the two halves joined during data taking operation. The two halves, when separated for servicing, look as shown on the right and left.

A 5 mm thick flat stainless steel plate is used to support the lead converter plates and supermodules in each half of the PMD. It has tapped holes for screws corresponding to hole positions in the lead plates and in the supermodules. The lead converter plates are sandwiched between two layers of gas detectors.

The two halves of the detector are supported on the girders and hang freely in a vertical position. The support structure allows both x - and z - movements of the detector. Each half of the detector can be separated for access by a smooth independent movement controlled by limit switches. The hanging elements have free swinging pivots, fine adjustments for horizontal motion, and plane position adjustments for alignment of the detector. The services of the two halves are also independent. When fully open, the two halves provide sufficient clearance for the poletip support of the STAR magnet to move in.

The edges of the support plate are also used for mounting the gas feed manifolds, shoe boxes for low voltage supplies and general support for distribution of cables onto the detector.

2.10.2 Front end electronics and Readout

The front-end electronics for processing the PMD signals is based on the use of 16-channel GASSIPLEX chips developed at CERN [41] which provide analog multiplexed signals and readout using the custom built ADC board (C-RAMS) which were obtained from CAEN, Italy. Each readout chain is driven by the following components:

- (a) A translator board
- (b) 27 Front End Electronic Boards (FEE) each consisting of 4 GASSIPLEX chips and
- (c) A buffer amplifier board.

These three components are discussed in the following.

- (a) Translator Board: It converts NIM levels of all control signals into the level required for the operation of GASSIPLEX chips. Operating voltage for these chips is $\pm 2.75\text{V}$ and hence all the NIM signals are to be translated to 0 to 2.75V levels.
- (b) FEE board: The cells in the unit modules are arranged in clusters consisting of 8×8 cells connected to a 70-pin connector. This cluster of 64 cells is read out by a FEE having four GASSIPLEX chips. One such board is shown in Fig. 2.21. For geometrical considerations the FEE board is also made in rhombus shape. When all the boards are placed on the detector, they almost fully cover the detector area. This arrangement helps to reduce the material and also provides a ground shield for the detector.

To reduce voltage drops over a long chain of 1728 channels, a bus-bar like design has been adopted to provide power to the FEE boards. To protect the input channels against high voltage spikes, a provision has been made on the board layout to connect a diode protection circuit.

- (c) Buffer amplifier board: The buffer amplifier is used for the transmission of a train of analog multiplexed signals to the readout module via a low impedance cable.

Digitization using C-RAMS requires that all multiplexed pulses within a chain should have the same polarity. In order to read the full chain, the pedestals in

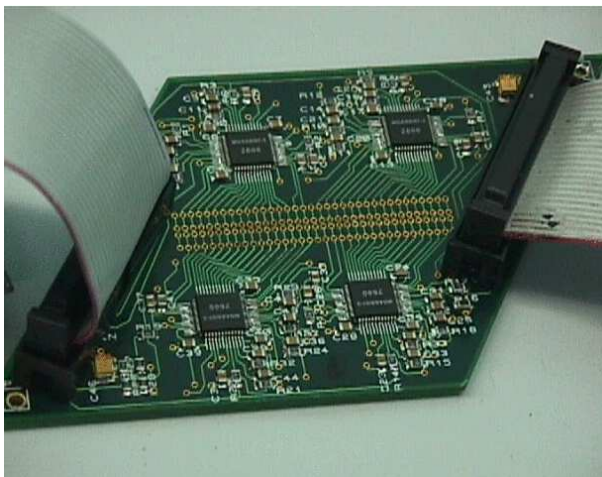


Figure 2.21: Photograph of a FEE board with four GASSIPLEX chips.

the chain need to be adjusted to the minimum of the pedestals in the chain. This shifting of the pedestal effectively reduces the dynamic range. To minimize the reduction in dynamic range due to pedestal adjustment, we need to select the chips for a chain having minimum pedestals in very close range. For proper quality control in the assembly of FEE boards, each GASSIPLEX chip has been tested for full functionality of each channel. In addition the pedestals of all the channels have been measured. The minimum pedestal as well as the spread in pedestal has been determined for each chip. Fig. 2.22 shows the distribution of pedestal minima and Fig. 2.23 scatter plot of pedestal minima vs. pedestal spread for 5000 chips. It is seen that we can select chips of four categories having close ranges of pedestal minima and pedestal spreads. The narrow width of the distribution shows that the usable number of chips is a large fraction of the total number of chips tested.

2.10.3 Trigger and Data acquisition

PMD gets a Pretrigger after 500 *ns* of the RHIC collision. PMD requires a pretrigger because of the GASSIPLEX chips used in the FEE boards. These chips needs a pick up time of 1.2 μs . The pretrigger to PMD is issued from ZDC. As soon as the ZDC gets any signal it sends a pretrigger to PMD and the charge accumulation in the GASSIPLEX chip of the PMD FEE starts.

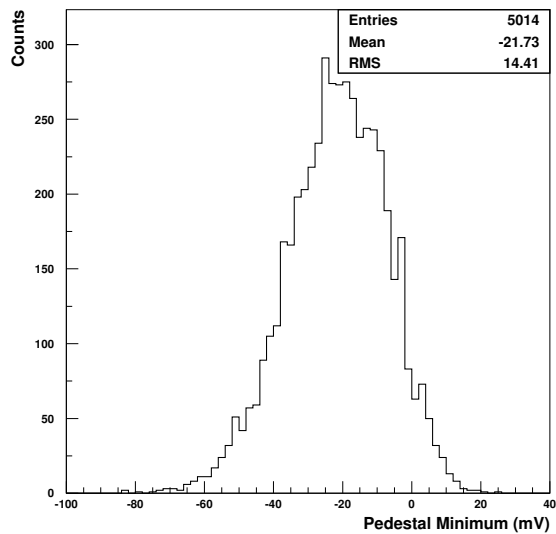


Figure 2.22: Pedestal minimum values (in mV) for 5000 chips

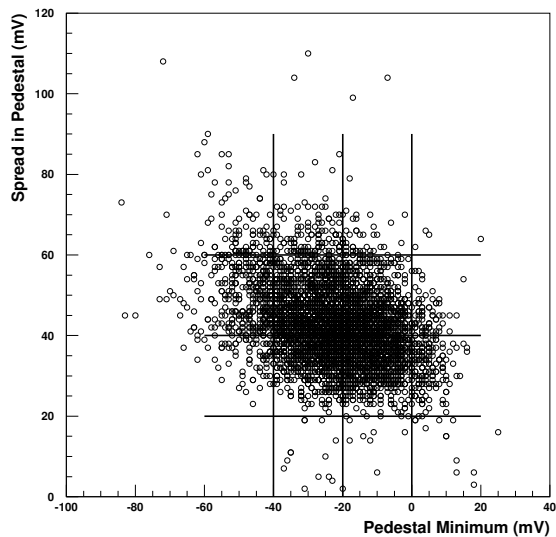


Figure 2.23: Pedestal minimum vs. pedestal spread for these chips. Lines are drawn to suggest the grouping of chips for a uniform chain.

When L0 arrives the signals are read out of the FEE boards as a signals from good event and send to the main data stream for data acquisition system.

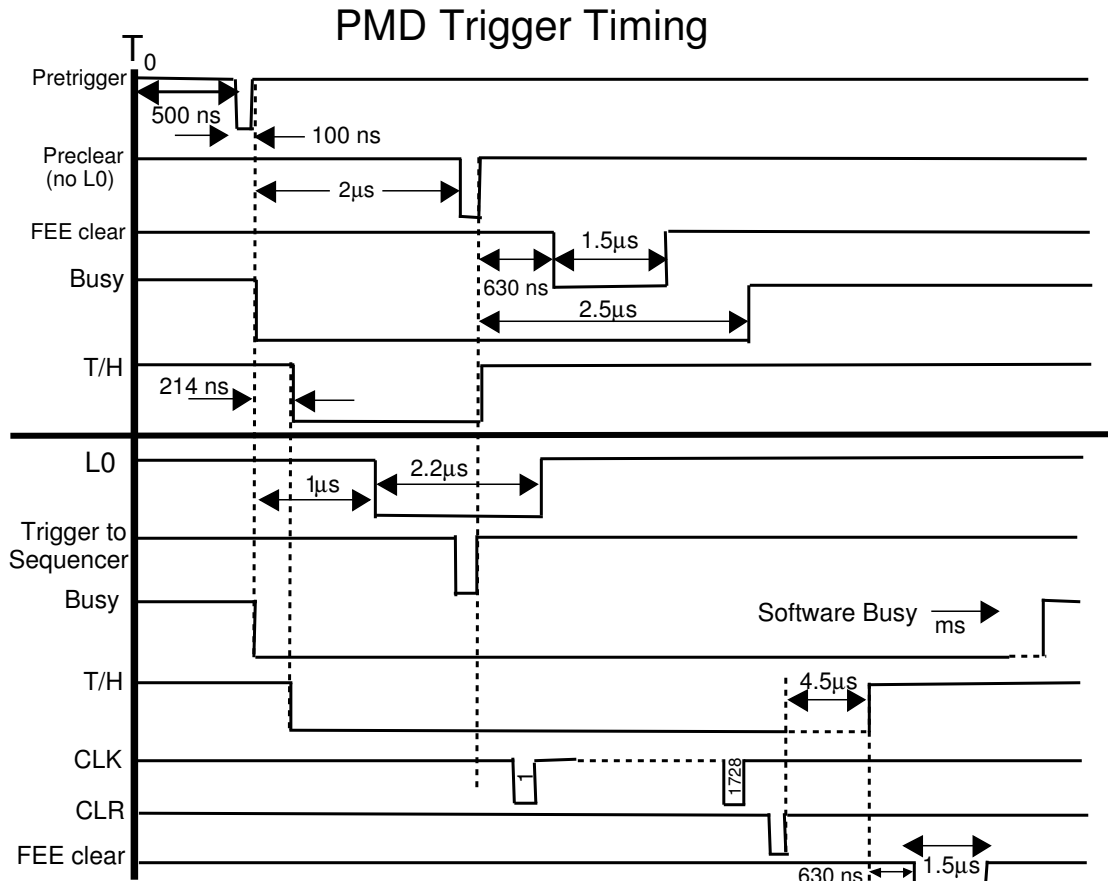


Figure 2.24: The PMD timing diagram is shown with different trigger signals arriving at the calculated times to record an event.

Now as per our electronics requirement we have implemented the following trigger scheme:

- (i) As soon as we get the Pretrigger we send the BUSY signal and after 814 ns (after the RHIC collision) we send the Track/Hold signals (T/H) to the FEE.
- (ii) Now there are two conditions :

- (a) L0 has not arrived within the Pre-defined time. In this case we clear the signals T/H and BUSY. BUSY is cleared after $4.5 \mu s$, from its start, as the baseline recovery time of FEE is $4.5 \mu s$.
- (b) L0 arrived within its Pre-defined time. We send signals T/H and BUSY and then check if for this L0 a corresponding Pre-trigger exists. If this is true then, we send Trigger signal to Sequencer and in turn Sequencer generates the signals Clocks, T/H, CLR, BUSY, and CONV. The clock signals are then sent to FAN IN and FAN OUT modules and distributed to various chains. Similar distribution is done for T/H and CLR signals. The CONV has to pass through the Delay module and feed to CRAMS. CRAMS will then digitize the analog signal and send the Ready signal to Sequencer and the readout of this digitized signal starts. After the readout, the FEE clear signal is sent and also the Software BUSY (VME_{BUSY}) is withdrawn.
- (c) If there no Pre-trigger corresponding to the L0, then we clear the BUSY.

In Fig. 2.24 the timing diagram of this logic as described above is shown schematically.

Bibliography

- [1] <http://www.bnl.gov/rhic/>.
- [2] K. H. Ackermann *et al.*, Nucl. Instr. Meth. A **499**, (2003) 624.
- [3] K. Adcox *et al.*, Nucl. Instr. Meth. A **499**, (2003) 469.
- [4] M. Adamczyk *et al.*, Nucl. Instr. Meth. A **499**, (2003) 437.
- [5] B. B. Back *et al.*, Nucl. Instr. Meth. A **499**, 603 (2003) 603.
- [6] R. Bellwied *et al.*, Nucl. Instrum. Meth. A **499**, (2003) 640;
- [7] L. Arnold *et al.*, Nucl. Instrum. Meth. A **499**, (2003) 652.
- [8] M. Anderson *et al.*, Nucl. Instrum. Meth. A **499**, (2003) 659.
- [9] M. Beddo *et al.*, Nucl. Instrum. Meth. A **499**, (2003) 725.
- [10] C. E. Allgower *et al.*, Nucl. Instrum. Meth. A **499**, (2003) 740.
- [11] K. H. Ackermann *et al.*, Nucl. Instr. Meth. A **499**, (2003) 713.
- [12] M. M. Aggarwal *et al.*, Nucl. Instr. Meth. A **499**, (2003) 751; M. M. Aggarwal *et al.*, Nucl. Instr. Meth. A **488**, (2002) 131.
- [13] B. Bonner *et al.*, Nucl. Instr. Meth. A **508**, (2003) 181.
- [14] F. S. Bieser *et al.*, Nucl. Instrum. Meth. A **499**, (2003) 766.
- [15] C. Adler *et al.*, Nucl. Instrum. Meth. A **470**, (2001) 488.
- [16] Particle Data Group, C. Caso *et al.*, Eur. J. Phys. C **3**, (1998) 1.
- [17] J. M. Landgraf *et al.*, Nucl. Instrum. Meth. A **499**, (2003) 762.

- [18] F. Bergsma *et al.*, Nucl. Instrum. Meth. A **499**, (2003) 633.
- [19] The STAR Collaboration, *The STAR Conceptual Design Report*, June 15, 1992 LBL-PUB-5347.
- [20] The STAR Collaboration, *STAR Project CDR Update*, Jan. 1993 LBL-PUB-5347 Rev.
- [21] H. Wieman *et al.*, IEEE Trans. Nuc. Sci. **44**, (1997) 671.
- [22] J. Thomas *et al.*, Nucl. Instum & Meth. **A478**, (2002) 166.
- [23] STAR Collaboration, J. Adams *et al.*, Phys. Lett. **B 637**, (2006) 161.
- [24] L. Kotchenda *et al.*, Nucl. Instrum. Meth. A **499**, (2003) 703.
- [25] H. Bichsel, “Energy loss in thin layers of argon”, STAR Note 418, <http://www.star.bnl.gov/star/starlib/doc/www/sno/ice/sn0418.html>
- [26] H. Bichsel, “Comparison of Bethe-Bloch and Bichsel Functions”, STAR Note 439, <http://www.star.bnl.gov/star/starlib/doc/www/sno/ice/sn0439.html>
- [27] F. Bieser *et al.*, The Forward Time Projection Chamber for the STAR Detector, *MPI PhE/98-3*, 1998
- [28] A. Schüttauf *et al.*, A Forward TPC for STAR, *Nucl. Phys.* **A 661** (1999) 677c
- [29] H. Wieman *et al.*, STAR TPC at RHIC, *IEEE Trans. Nucl. Sci.* **44** (1997) 671
- [30] X. Bittl *et al.*, Diffusion and Drift Studies of Ar-DME/CO₂/CH₄ Gas Mixtures for a radial TPC in the E×B Field, *Nucl. Instr. Meth.* **A 398** (1997) 249
- [31] S. Klein *et al.*, Front-End Electronics for the STAR TPC, *IEEE Trans. Nucl. Sci.* **43** (1996) 1768
- [32] M. Bosteels, Cern internal report, CERN/LHCC/99-33 (1999).
- [33] A. J. Kozubal et al., ICALEPS89 Proceedings, (Vancouver, 1989), 288.
- [34] V. Fine and P. Nevski, in *Proceedings of CHEP-2000*, Padova, Italy.

- [35] “A Preshower PMD for STAR Experiment”, STAR Note (1997) 310.
- [36] “Photon Multiplicity Detector for STAR : Technical Proposal”, VECC Internal Report VECC/EQG/00-04, May 2000, revised : Jan. 2001.
- [37] M.M. Aggarwal et al., Nucl. Instr. Meth. A372 (1996) 143.
- [38] M.M. Aggarwal et al., Nucl. Instr. Meth. A421 (1999) 558.
- [39] ALICE PMD Technical Design Report, CERN/LHCC 99-32 (1999).
- [40] M.M. Aggarwal et al., Nucl. Instr. Meth. sec. A, (in press), nucl-ex/0112016.
- [41] ALICE HMPID Technical Design Report, CERN/LHCC 98-19 (1998).
- [42] X-N. Wang and M. Gyulassy, Phys. Rev. D **44**, (1991) 3501.

Chapter 3

PHOTON RECONSTRUCTION

A photon passing through the lead converter in front of the preshower plane of the PMD gives electromagnetic showers. The electrons and positrons coming out of the shower then hit a group of cells on the preshower plane. So it is necessary to adapt a clustering algorithm to obtain the photon clusters in each event. Each cluster is characterized by its total ADC (E_{dep}) and (η, ϕ) position of its center. After clustering is done we have to use suitable discrimination algorithm to discriminate photon clusters from charged particle clusters. From the test beam and simulation studies it is seen that charged particles mostly hit one cell in our detector. The incident photon usually ($\sim 70\%$) gives signal in more than one cell. This we have discussed in detail later in this chapter using simulation studies. Another feature is that charged particles deposit less energy compared to photons in the preshower plane. A discrimination based on above mentioned features of the clusters can be used to get photon clusters from total detected clusters. The main steps for photon reconstruction is schematically shown in Fig. 3.1. In this chapter, using GEANT simulation and an event generator, the various features of photon clusters, photon counting efficiency and purity for the PMD have been studied in the actual environment of STAR experiment.

The main platform for the simulation study is a detailed Monte-Carlo simulation using HIJING [1] with default parameter settings and the detector simulation package GEANT [2], which incorporates the full STAR detector framework. Fig. 2.16 (in Chapter 2) shows the PMD relative to other detectors within the STAR setup as implemented through GEANT simulation [3].

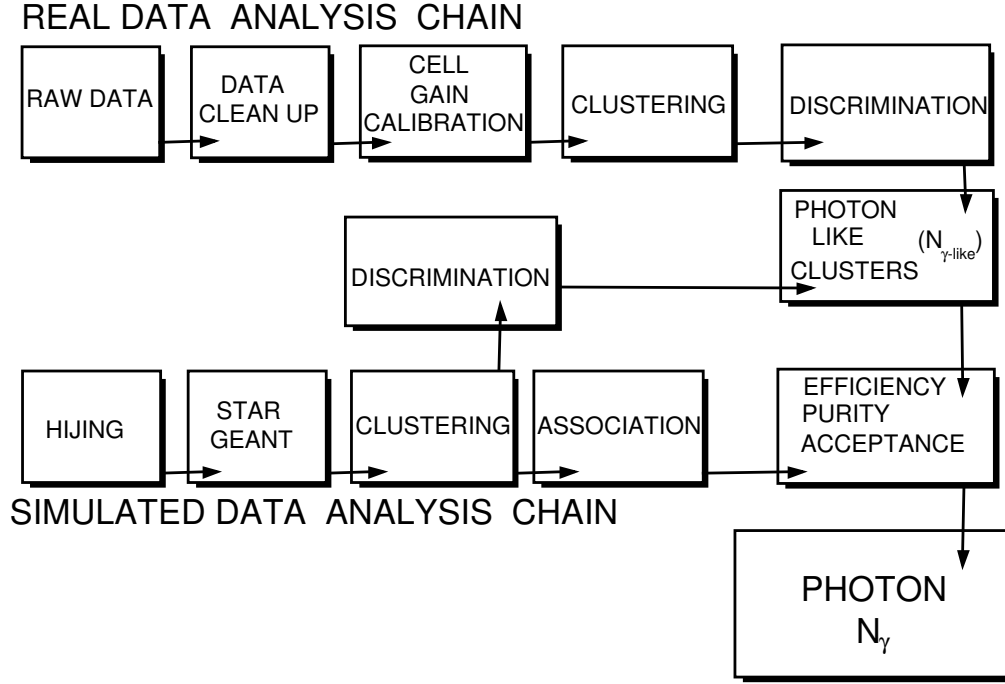


Figure 3.1: Flow chart for photon reconstruction from PMD in real data and simulation.

3.1 Data selection

The event and data selection for the present study involved following important steps :

- (a) Trigger selection : The minimum bias trigger was obtained using the charged particle hits from an array of scintillator slats arranged in a barrel, called the Central Trigger Barrel, surrounding the TPC, two zero degree hadronic calorimeters at $\pm 18 m$ from the detector center along the beam line, and two Beam-Beam Counters [4]. Details of trigger in STAR experiments are described in Chapter 2.
- (b) Vertex selection : Events have been selected with a collision vertex position less than $30 cm$ on both sides from the center of the TPC along the beam axis. Fig. 3.2 (a) shows the z -position of the vertex from data. This vertex selection led to a maximum and minimum η acceptance of PMD varying about 0.2 units in η beyond the nominal value. The variation of maximum and minimum η acceptance of PMD with z -position of the vertex is shown in Fig. 3.2 (c). Fig. 3.2 (b) shows the vertex z -position from simulation.

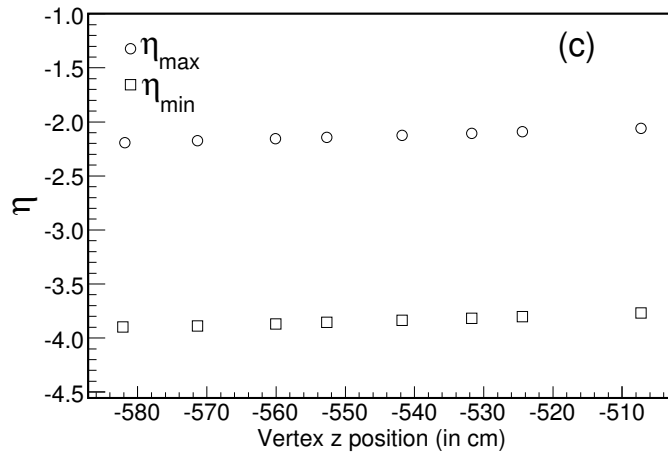
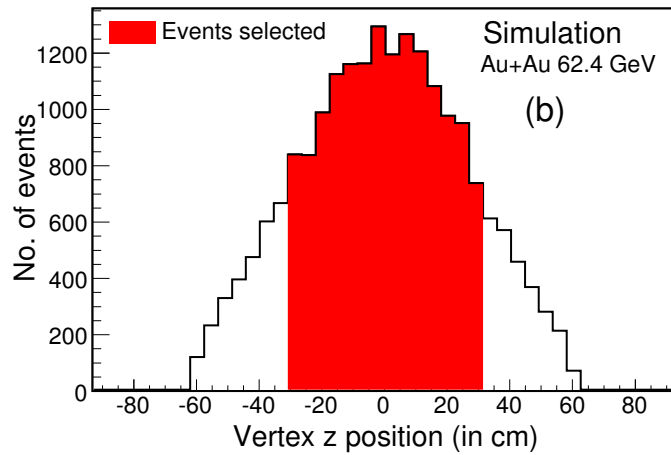
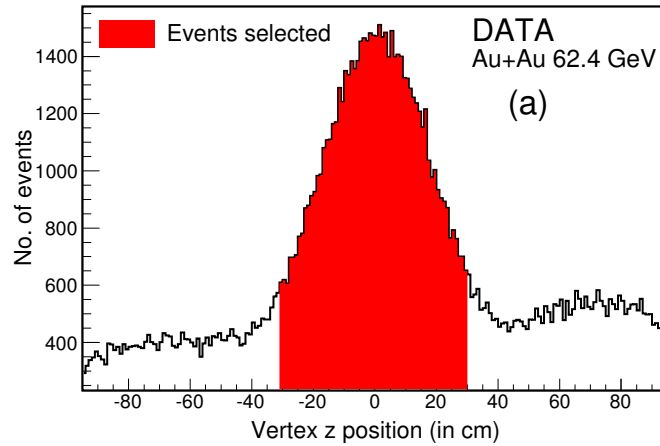


Figure 3.2: Distribution of z -position of the vertex in (a) data and (b) simulation for Au+Au collisions at $\sqrt{s_{NN}} = 62.4$ GeV. The shaded portion shows the z -position of the vertex accepted for data analysis. Also shown is the (c) variation of maximum and minimum η coverage of PMD with z -position.

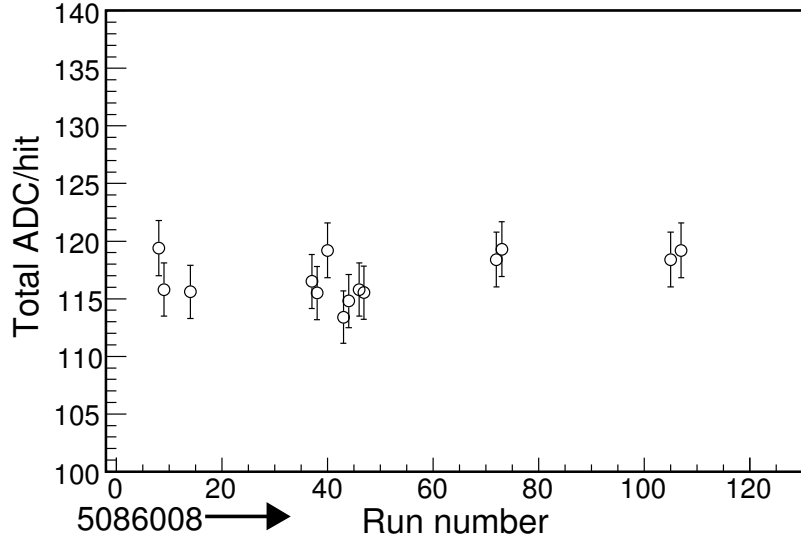


Figure 3.3: Variation of average total ADC per hit for various valid runs. Each valid run consists of a large number of events. The results are for Au+Au collisions at $\sqrt{s_{NN}} = 62.4$ GeV.

(c) Data set selection : We have studied in detail the total ADC per hit during different periods (RUN) of data taking. The events were taken from the minimum bias data set which had similar average total ADC per hit values. The constancy of the average total ADC per hit for different period of data taking is shown in Fig. 3.3. This shows the stable working of the detector during this period of data taking.

(d) Acceptance of PMD : Only those SMs of PMD were chosen for the analysis which had same applied high voltage (-1400 V) to the cathode of the cells and were working. Fig. 3.4 (top) shows the schematic diagram of the acceptance of the preshower plane of PMD which was used in the present analysis.

The acceptance correction factor used to correct the multiplicity results were estimated by implementing the dead cells in simulation and is also shown in Fig. 3.4 (bottom). Out of the total 41472 cells in the preshower plane, 21700 cells were working for the data presented in this thesis. The veto plane of PMD was not fully installed for the Au+Au 62.4 GeV data taking period. Hence data from this plane has not been used in the analysis presented in this thesis.

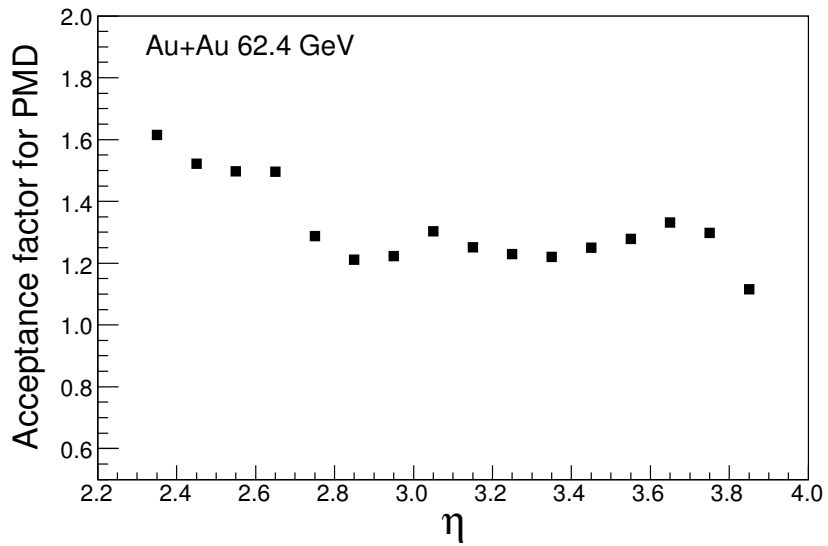
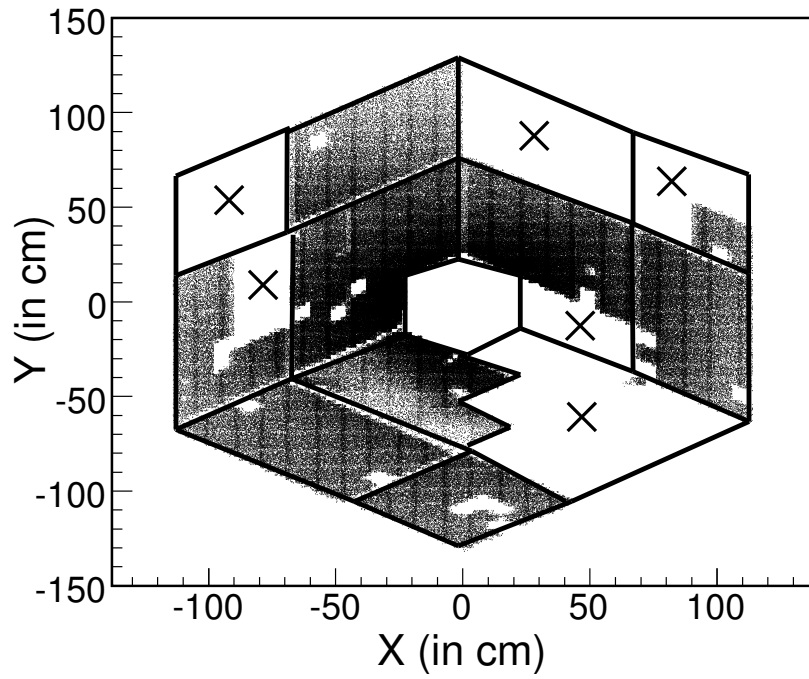


Figure 3.4: Top : XY display of hits on PMD. The regions marked by cross are the non working SMs/dead cells in the preshower plane of PMD in the data taking period of Au+Au collisions at $\sqrt{s_{NN}} = 62.4$ GeV. Bottom : Acceptance correction factor for PMD as a function of η in Au+Au collisions at $\sqrt{s_{NN}} = 62.4$ GeV.

- (e) Centrality selection : The centrality determination in this analysis uses the uncorrected charged particle multiplicity in the pseudorapidity region $|\eta| < 0.5$, as measured by the TPC [7]. Table 3.1 gives the percentage cross section, the corresponding uncorrected charged particle multiplicity ($N_{\text{ch}}^{\text{TPC}}$) in the pseudorapidity region $|\eta| < 0.5$, the number of participating nucleons (N_{part}) and the number of binary collisions (N_{coll}) used in this thesis.

Table 3.1: Centrality selection, number of participating nucleons (N_{part}) and number of binary collisions (N_{coll}). The upper and lower systematic errors are shown for N_{part} and N_{coll} values.

% cross section	$N_{\text{ch}}^{\text{TPC}}$	$\langle N_{\text{part}} \rangle$	$\langle N_{\text{coll}} \rangle$
0–5	> 373	$347.3^{+4.3}_{-3.7}$	$904.3^{+67.7}_{-62.4}$
5–10	373–313	$293.3^{+7.3}_{-5.6}$	$713.7^{+63.7}_{-54.8}$
10–20	313–222	$229.0^{+9.2}_{-7.7}$	$511.8^{+54.9}_{-48.2}$
20–30	222–154	$162.0^{+10.0}_{-9.5}$	$320.9^{+43.0}_{-39.2}$
30–40	154–102	$112.0^{+9.6}_{-9.1}$	$193.5^{+31.4}_{-30.4}$
40–50	102–65	$74.2^{+9.0}_{-8.5}$	$109.3^{+22.1}_{-21.8}$
50–60	65–38	$45.8^{+7.0}_{-7.1}$	$56.6^{+15.0}_{-14.3}$
60–70	38–20	$25.9^{+5.6}_{-5.6}$	$26.8^{+8.8}_{-9.0}$
70–80	20–9	$13.0^{+3.4}_{-4.6}$	$11.2^{+3.7}_{-4.8}$

The N_{part} and the N_{coll} numbers have been obtained from Monte-Carlo Glauber calculations [7] using Woods-Saxon distribution for the nucleons inside the Au nucleus. The systematic uncertainties on N_{part} and N_{coll} were determined by varying the Woods-Saxon parameters and by including a 5% uncertainty in the determination of the total measured Au+Au cross-section. The contributions from these sources were determined separately and were

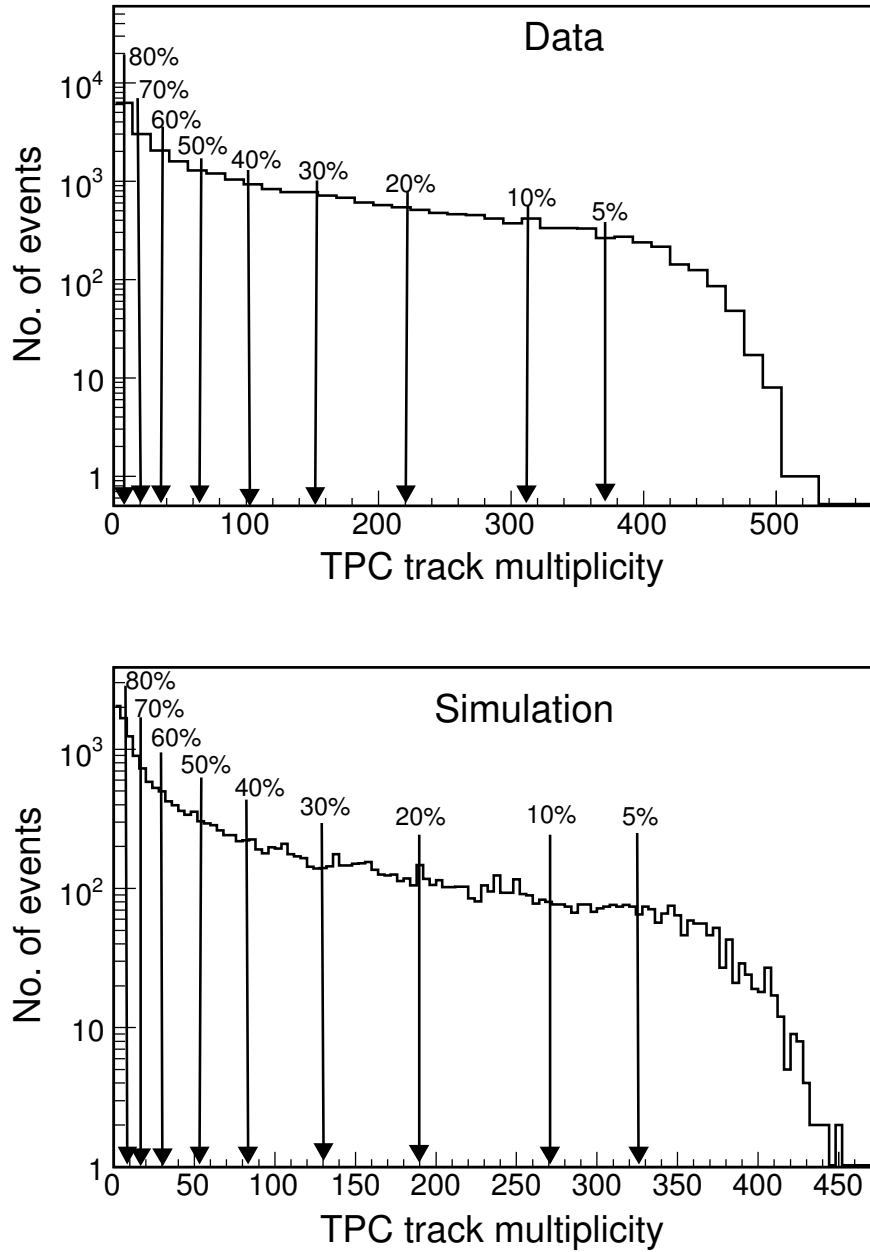


Figure 3.5: TPC track multiplicity within $|\eta| < 0.5$ from data (top) and simulation (bottom) for Au+Au collisions at $\sqrt{s_{\text{NN}}} = 62.4$ GeV. The arrows show the multiplicity value corresponding to various % cross section or collision centralities.

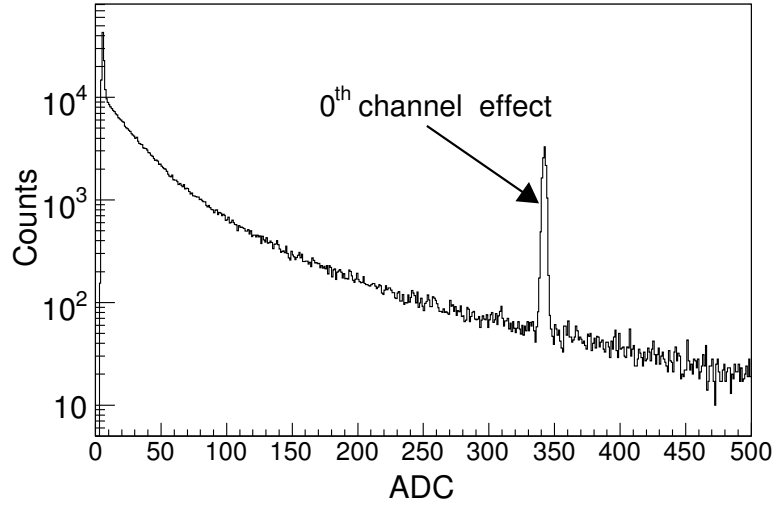


Figure 3.6: Typical cell ADC spectra for 1728 channels in a chain showing the channel zero effect. The channel number zero was kept as a reference channel during data acquisition, for which pedestal was not subtracted.

treated as fully correlated in the final systematic uncertainties associated in calculation of N_{part} and N_{coll} presented in the Table 3.1 as upper and lower errors. Fig. 3.5 shows the centrality selection from the $N_{\text{ch}}^{\text{TPC}}$ in data (top) and simulation (bottom).

3.2 Data cleanup

PMD data needs to be cleaned up due to the following reasons :

- (i) To remove the channel zero effect.
- (ii) To remove the hot channels.
- (iii) To remove events having the PMD data acquisition problems.
- (iv) To remove noise that is random in nature and having low ADC values.

Now we discuss each of these effects in detail.

The zeroth channel in each chain was kept as a reference channel and its signal was used in data acquisition. The pedestal value for this channel was not subtracted. As a result the signal from this channel was always much higher than the rest of the channels. The effect of this can be seen in the cell ADC distribution as shown in Fig. 3.6.

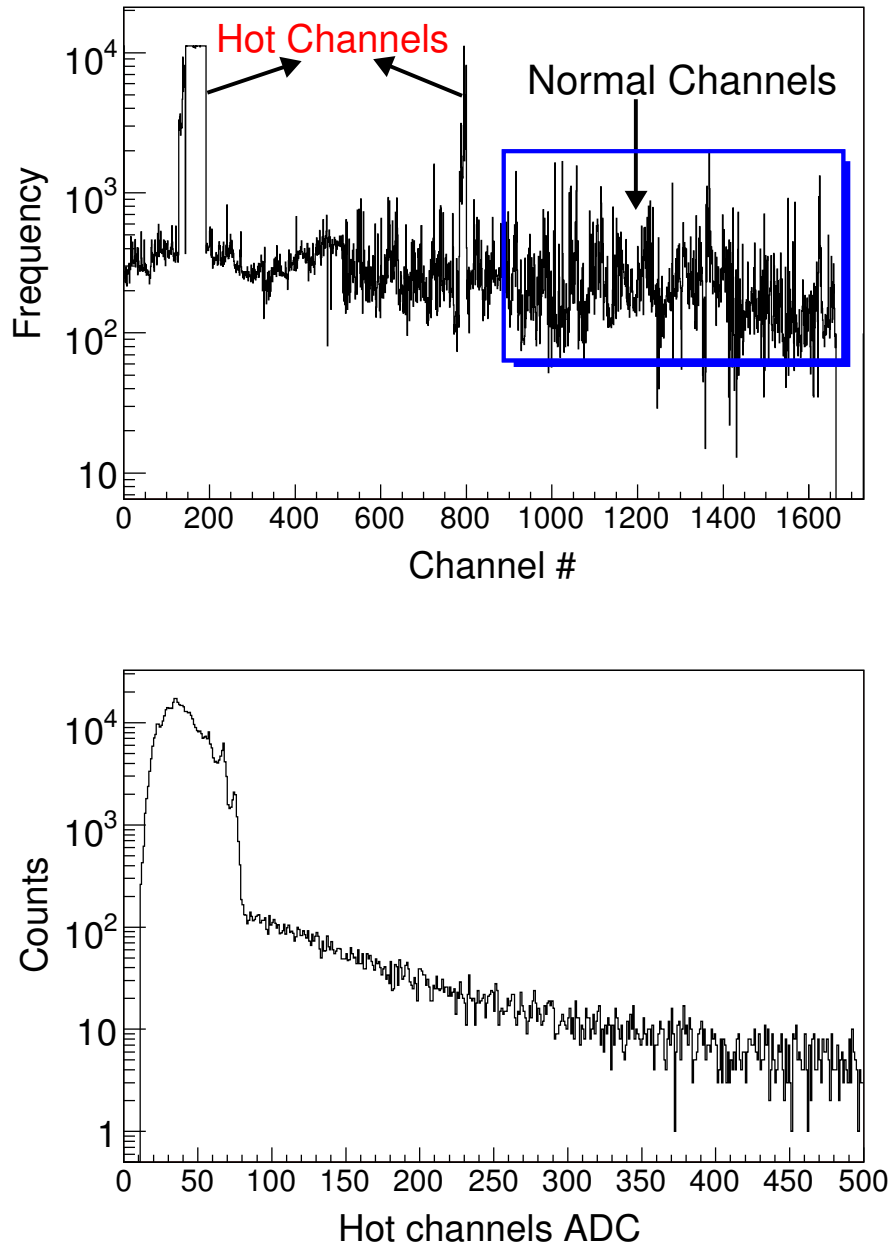


Figure 3.7: Top : Frequency of channels hit over a large number of events. The peak on the left reflects the hot channels. The frequency of these channels giving low ADC signals is very high compared to rest of the channels in the chain for the same set of events. Bottom : The cell ADC spectra for 1728 channels in a chain. The bump observed in the low ADC region is due to hot channels.

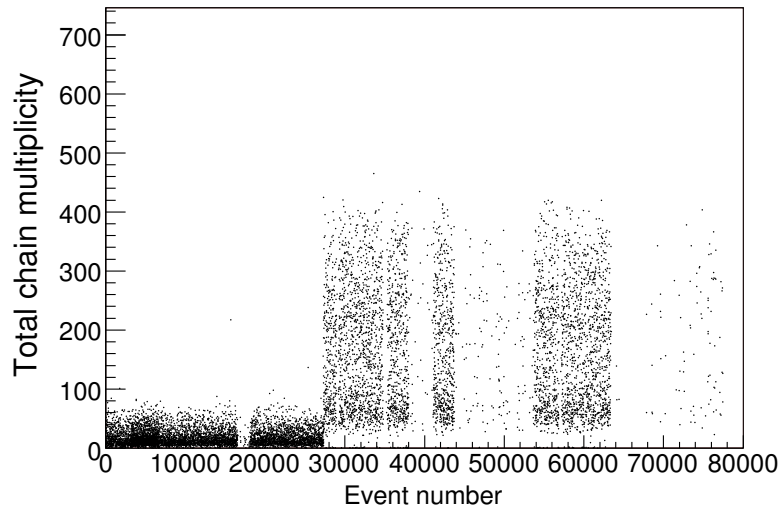


Figure 3.8: Total hits in a typical chain of PMD as a function of event number. The abrupt jump in chain multiplicity after a certain number of events collected by the DAQ is observed towards the right of the plot.

While data taking it was observed in some chains, few channels were giving signal abnormally large number of times (~ 10 to 100 times) more than the other channels in the chain for a similar multiplicity events. This effect can be easily visualized by looking at the frequency distribution of the channels shown in Fig. 3.7 (top) giving signals in a chain over a large number of events. Fig. 3.7 (bottom) show the ADC distributions of these channels were observed to be low ADC values (< 80 ADC).

A closer look at the events showed that for some particular set of events some chain occupancy shows an abrupt increase for the same trigger condition. It was also observed that the occupancy of some chains remain in such high values and return back to normal level only if the data acquisition system is reset. A typical example of this feature is shown in Fig. 3.8.

Apart from this a random low ADC values in some chains were also found over large number of events. The study of cell ADC distribution of chains showed that these noisy channels were always associated with the lower ADC values (< 7 ADC). These low ADC noisy channels were distributed randomly in the chains. Fig. 3.9 shows the ADC distribution (top) and row-column distribution (bottom) of such low ADC noisy channels in a chain. To remove such low ADC noisy channels we have applied a uniform cut of 10 ADC on the cell level.

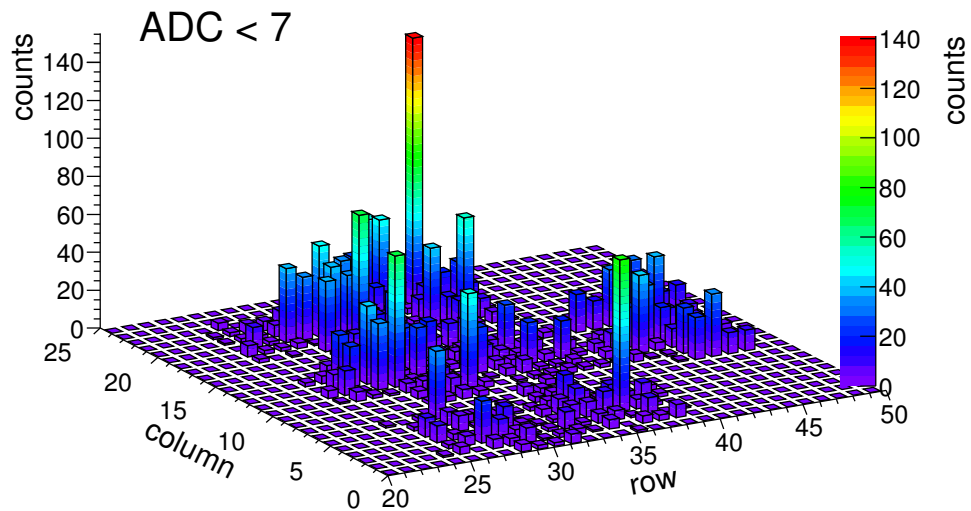
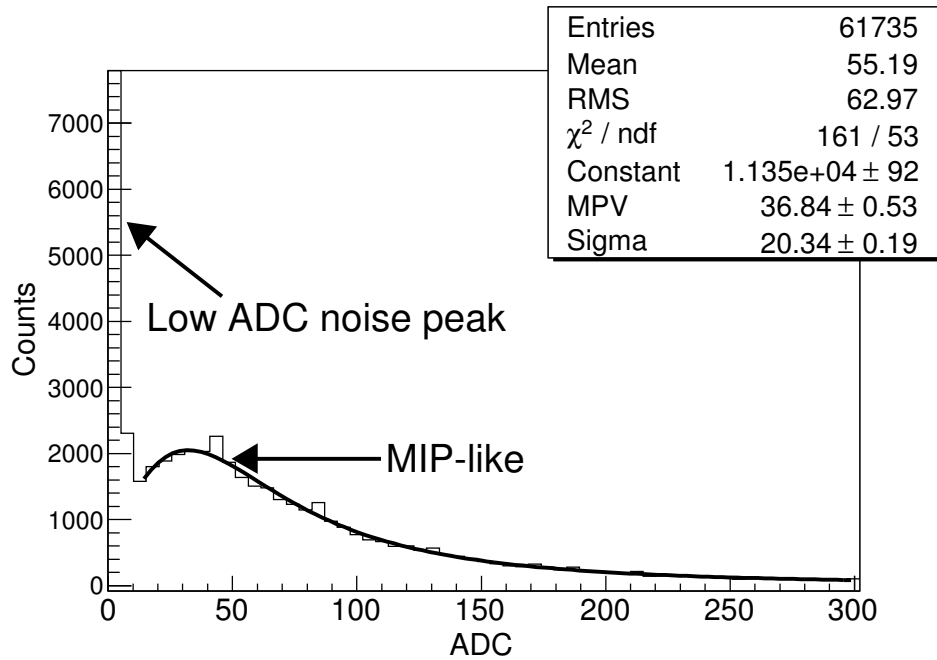


Figure 3.9: Top : The cell ADC spectra of isolated cells for a typical chain in PMD. The low ADC peak observed are due to noisy channels while the rest of the spectra follows a Landau distribution. Bottom : The distribution of the cells associated with the low ADC peak over the row and column number in PMD.

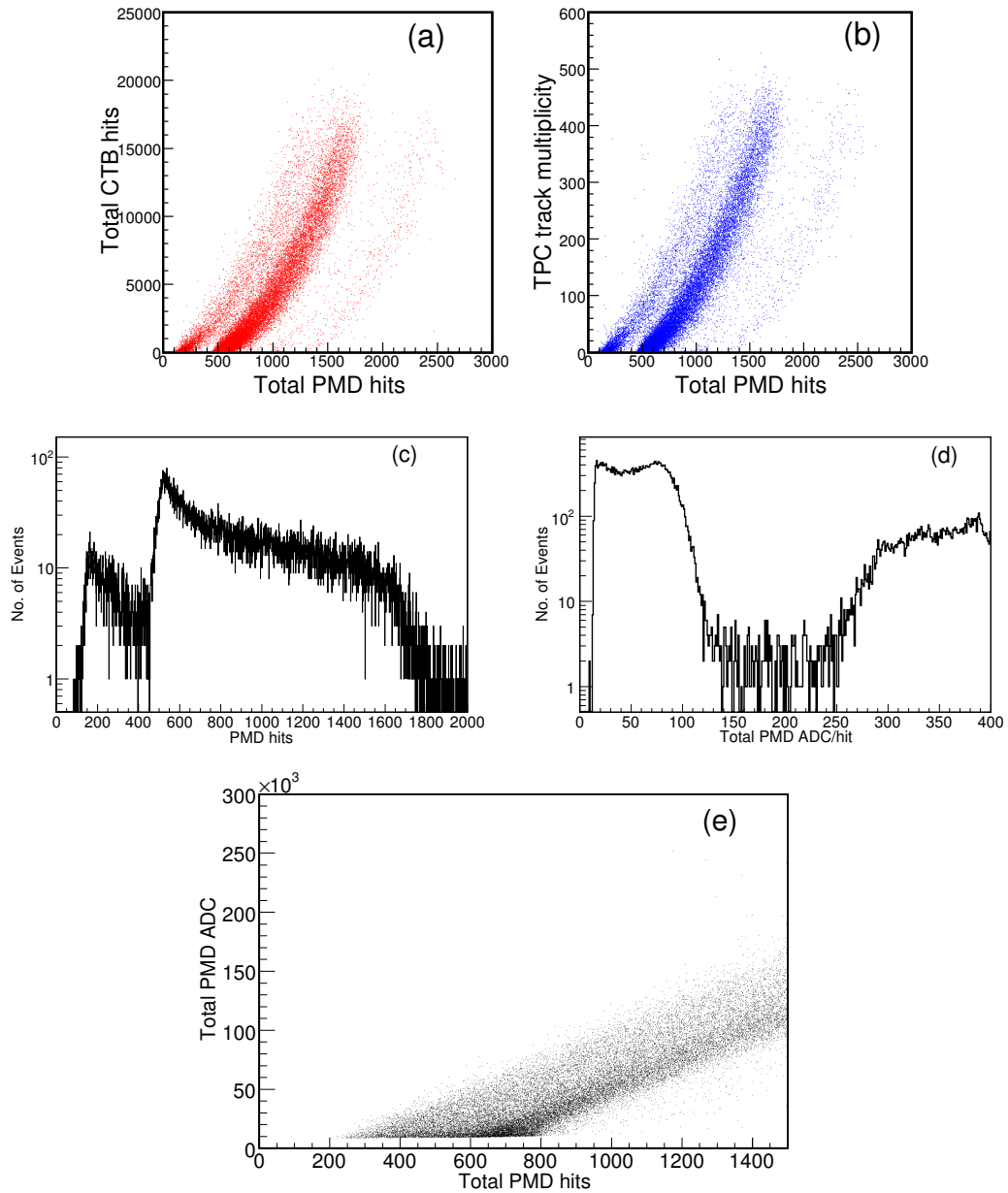


Figure 3.10: Global features of data before cleanup: (a) Correlation between CTB hits and PMD hits, (b) Correlation between TPC track multiplicity and PMD hits, (c) PMD hits distribution for a minimum bias trigger condition, (d) Total ADC per hit in PMD, and (e) Correlation between total ADC and total PMD hits.

The above problems with the data also led to odd shaped distribution for various global features. Fig 3.10 shows correlation between the hits on PMD with the (a) TPC track multiplicity and (b) CTB hits, (c) Minimum bias distribution of hits on PMD, (d) total ADC per hit on PMD and (e) correlation between total hits on PMD and total ADC in an event, for a large number of events before cleanup of data.

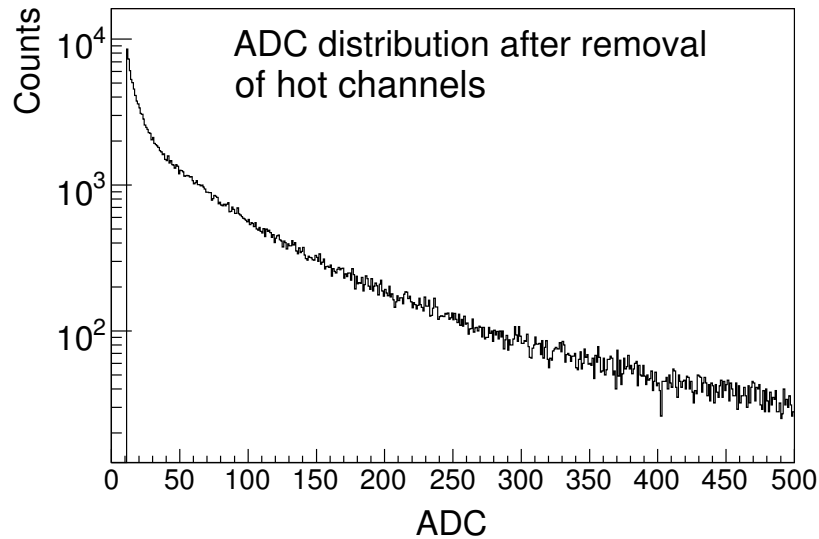


Figure 3.11: Typical cell ADC distribution for a group of 1728 cells in a chain after removal of hot channels and channel zero effect.

These distributions further emphasized the need of the data cleanup. The procedure to do cleanup is described below :

- (i) To remove the zeroth channel : We decided not to analyze the data for zeroth channel in every chain and make its ADC content zero. The resultant cell ADC distribution is shown in Fig. 3.11
- (ii) To remove the hot channels : For this we observed the two important features of such channels. (a) They fire abnormally large number of times in comparison to other channels in a chain for similar multiplicity and (b) they usually have low ADC values. As a first step, we find the frequency of channel hit for each chain for a large number of events for similar multiplicity. In the second

step, we obtain the distribution of number of times each channel is fired in a chain. The mean and RMS of these distributions are recorded for all chains. We assign a channel to be bad if it lies beyond 5 times the RMS from the mean of the distribution. To have a final check that we have removed these channels, we allow the channels for each chain to pass through such filtering process again with a cut off set to 6 times RMS of the distribution. The resultant cell ADC distribution of the good channels is shown in Fig. 3.11.

- (iii) To remove events having the PMD data acquisition problems (PMD busy) : For this we carefully studied the chain multiplicity vs. event number for each chain for the full data set analyzed. The events with PMD busy problem, which is reflected as an abrupt jump in chain multiplicity, were removed from the analysis. This led to almost 30-40% rejection of the the total event sample collected for Au+Au collisions at 62.4 GeV.
- (iv) To remove noise that is random low ADC hits : For this we put a cell level ADC threshold of greater than 10 ADC in the analysis.

After following the above procedures we obtained the cleaned data for PMD. The global features after clean up of PMD data can be seen in the Fig. 3.12.

3.3 Cell-to-Cell Gain Calibration

Before analyzing the data for getting any physics observables, it is essential to understand the response of each cell of the detector. This study is necessary for the following reasons :

- (a) Response of each cell reflects the gain of a cell.
- (b) It is important that this response should be stable and does not vary much.
- (c) Test beam results [3] indicate that charged hadrons mostly hit a single cell. For photons, the number of cells hit are usually larger with higher energy deposition compared to charged hadrons. The energy deposited by a charged hadron in an “isolated cell” of the detector can then be used to discriminate photons from hadrons.

A hexagonal cell is defined as isolated when it has a non zero ADC and its six neighbors have zero ADC. This is schematically shown in Fig. 3.13. The shaded

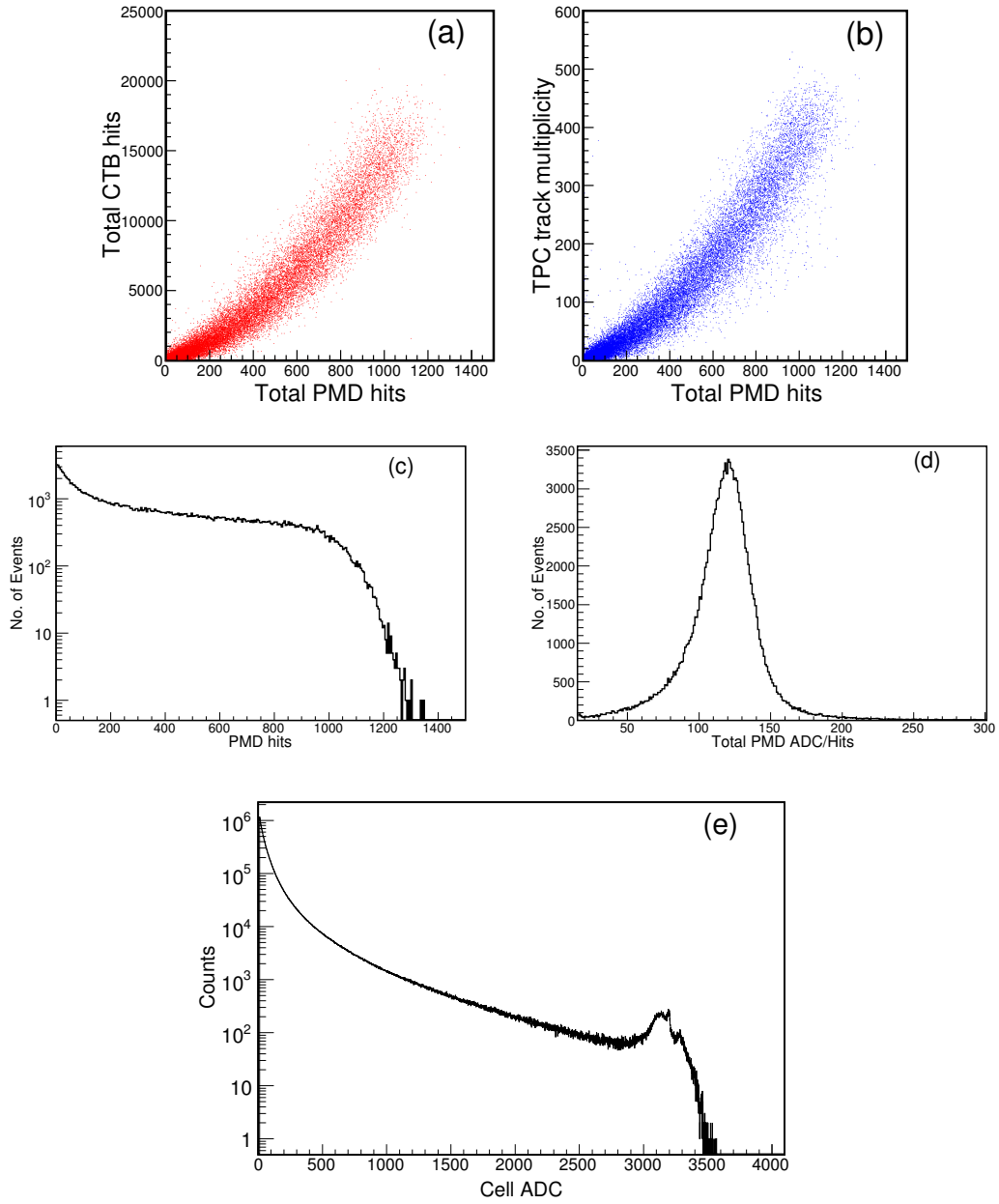


Figure 3.12: Global features of data after cleanup: (a) Correlation between CTB hits and PMD hits, (b) Correlation between TPC track multiplicity and PMD hits, (c) PMD hits distribution for a minimum bias trigger condition, (d) Total ADC per hits distribution, and (e) Cleaned cell ADC spectra.

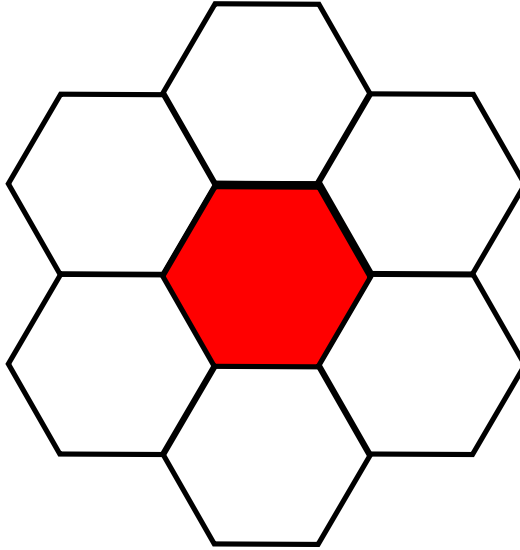


Figure 3.13: Schematic diagram of an isolated cell in PMD. A cell is said to be isolated (shaded) if it has a non zero ADC content and its six neighboring cells (non shaded) have zero ADC content.

cell represents the isolated cell. To obtain the response of each cell in the PMD, we study the isolated cell ADC spectra. From the test beam data we know that charged hadron hits are confined mostly to a single cell. The pulse height spectra obtained from the hit cell should follow a Landau distribution. The typical energy deposited for a minimum ionizing charged particle [8] (MIP) in a thin detector follows a Landau distribution [9]. In simulation we use all the cut off on E_{dep} (in keV) in terms of energy deposited by MIPs (E_{dep}^{MIP}) in the PMD. Fig. 3.14 (top) shows the isolated cell ADC distribution obtained from 62.4 GeV Au+Au data set with detector operating at -1400V for a gas mixture of Ar+CO₂ in the proportion 70:30. The pulse height spectrum is observed to follow Landau distribution. Also shown in Fig. 3.14 (bottom) is the typical isolated cell energy deposition obtained from the simulation studies. The simulation is performed by passing HIJING events through the full STAR detector simulation program. The isolated cell spectra were obtained in the same procedure in simulation as described above for data. We find that the most probable value (MPV) from isolated cell ADC spectra for the data lies around 36 ADC and the truncated mean ($20 \times \text{MPV}$) is around 90 ADC. In simulation the MPV and mean for the isolated cell energy deposited spectra is 1.1 keV and 2.5 keV respectively. From this we can conclude that the energy deposition of 1.1 keV corresponds to 36 ADC units. This sets our keV-ADC calibration for

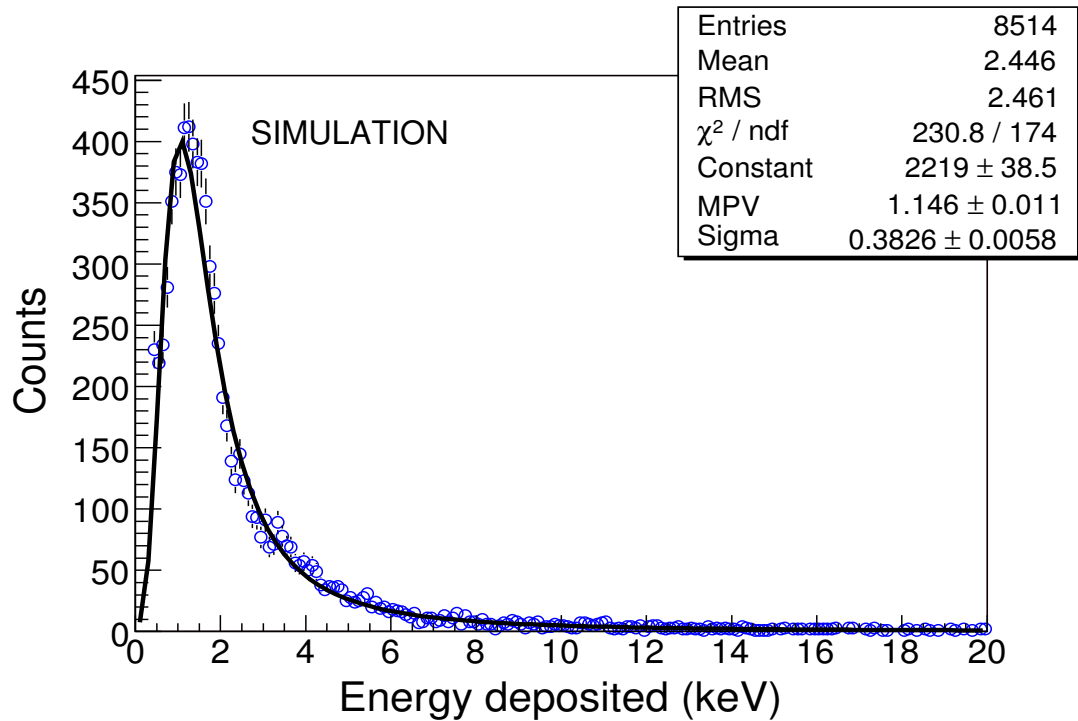
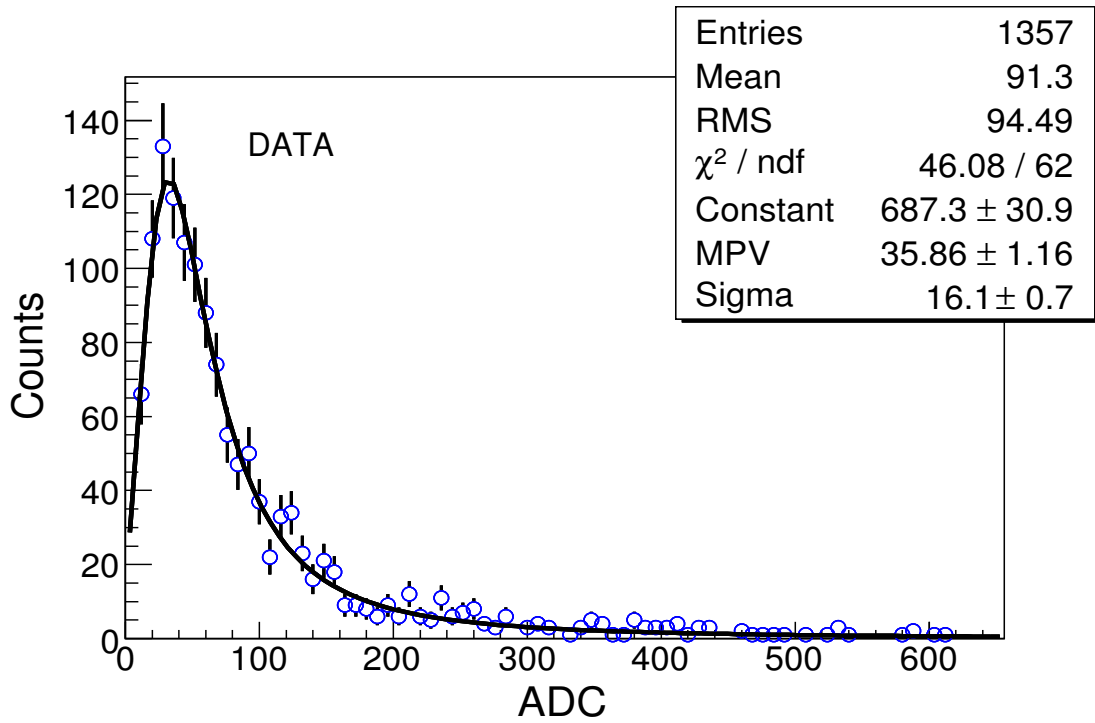


Figure 3.14: Top : Typical isolated cell ADC spectra, along with fit to a Landau distribution. Bottom : Typical isolated cell energy deposition spectra from simulated events, along with fit to a Landau distribution.

the rest of the study assuming linear behaviour over the full dynamic range.

To check the effect of particle density on the isolated cell finding procedure, we looked at the simulated isolated cell energy deposition spectra for different SMs which span different η space and hence experiences different particle density. The summary in terms of the MPV and mean values of these spectra is given in the Table. 3.2. We do not observe any significant variation in the values for different SMs.

Table 3.2: MPV and Mean for isolated cell E_{dep} distribution of cells in various SMs of PMD from simulation.

Super Module Number	MPV (keV)	Mean (keV)
13	1.091 ± 0.006	2.40 ± 0.37
14	1.093 ± 0.005	2.42 ± 0.35
15	1.096 ± 0.005	2.45 ± 0.36
16	1.098 ± 0.003	2.50 ± 0.34
17	1.098 ± 0.005	2.50 ± 0.36
18	1.093 ± 0.004	2.37 ± 0.36
19	1.090 ± 0.010	2.57 ± 0.35
20	1.097 ± 0.005	2.37 ± 0.35
21	1.092 ± 0.006	2.37 ± 0.36
22	1.092 ± 0.003	2.39 ± 0.34
23	1.102 ± 0.005	2.40 ± 0.36
24	1.100 ± 0.008	2.40 ± 0.35

It was observed that for some of the cells the peak of the distribution is not developed properly in real data. This resulted in isolated cell ADC spectra for many cases not having a well defined peak as expected from the Landau distribution. One such typical example is shown in Fig. 3.15. Such cells are believed to have low gain which has resulted in underdeveloped distribution. We have simulated the low gain effect and studied the variation in the mean and the MPV values of the isolated cell ADC spectra. From the data we selected a value of mean and MPV where the isolated cell ADC spectra were well defined. We then varied the mean and MPV values within the errors to simulated such low gain isolated cell ADC spectra. Then in the next step we apply the ADC cutoff ranging between 7 ADC and 30 ADC units to all the cells. This cutoff was applied in such a way that each entry in the isolated cell ADC spectra is shifted by the cutoff value, so that

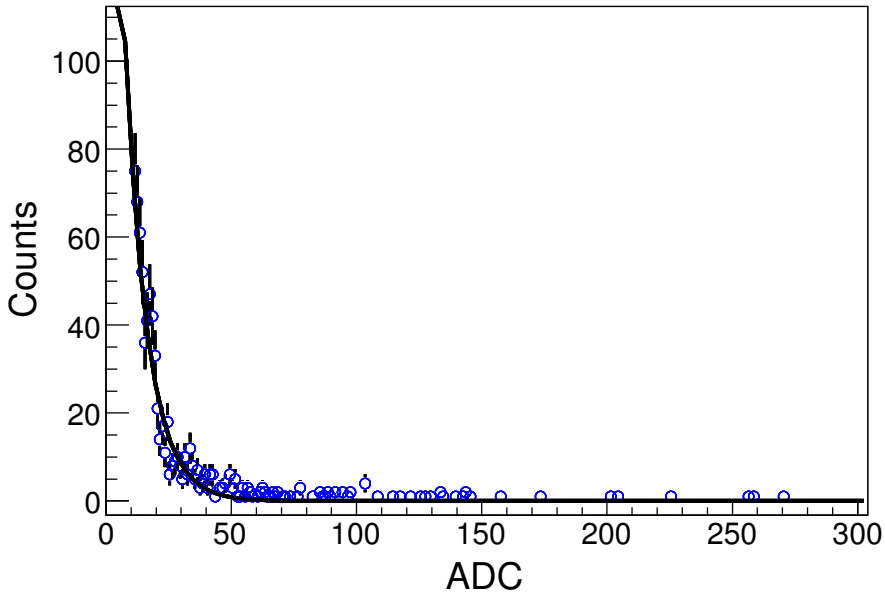


Figure 3.15: Typical isolated cell ADC spectra for a cell with low gain in data.

we can mimic the underdeveloped distributions as found in real data. We then tried to fit these distributions with Landau function and extract the mean and MPV values to see the variation in these quantities with respect to ADC cutoff values. Fig. 3.16 (a) and (b) shows the variation of mean and MPV values as a function of ADC cutoff for a sample of 100 simulated isolated cell ADC spectra respectively. Also shown is the effect of the cutoff applied to the 20% of cells out of the simulated isolated cell ADC spectra for calculation of mean and MPV values. The typical ADC cutoff used in data is ~ 7 ADC units. This study shows that the mean and MPV values are still good enough to be correlated even if we do not record good Landau distributions in some cells which are having relatively lower gains than other cells. Hence the peak of the distribution in data cannot be used for checking the uniformity of the gain for all cells in PMD or for finding out the cell-to-cell gain normalization factor. We further observe, for those cells which have well defined peak, the peak ADC (MPV) and mean ADC (MEAN) are linearly proportional. This is shown in Fig. 3.16 (c). So we have decided to use the mean ADC of the isolated cell ADC distribution for calibration and studying the uniformity of response of the cells in the detector. From Fig. 3.16(c) it is evident that the gain varies by a factor 3 over the entire detector in real data. To study the cell-to-cell response in more detail, we looked into the variation of mean of isolated cell ADC spectra in each SM of PMD. The variation of the mean for

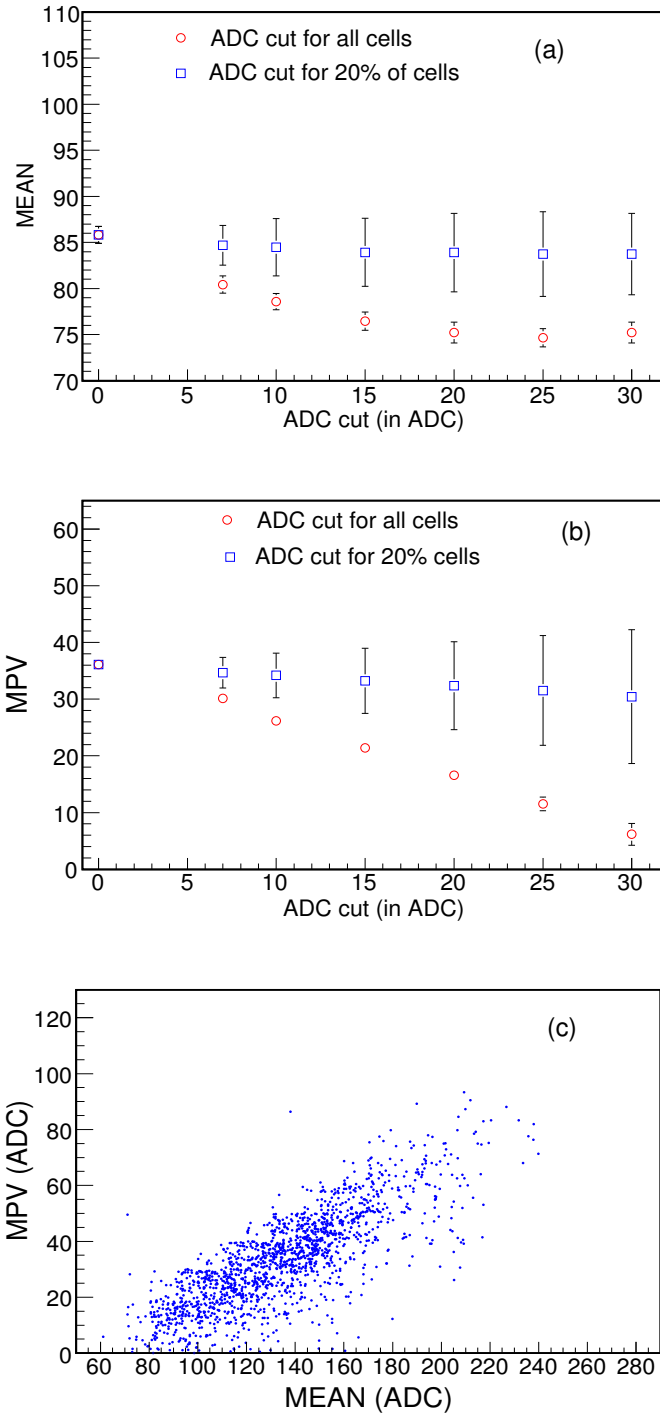


Figure 3.16: (a) Variation of the mean value obtained from the isolated cell ADC spectra as a function of ADC cutoff values. (b) Variation of most probable value (MPV) of the isolated cell ADC spectra as a function of ADC cutoff values. (c) Variation of most probable value and the mean of the isolated cell ADC spectra from real data. The correlation is linear.

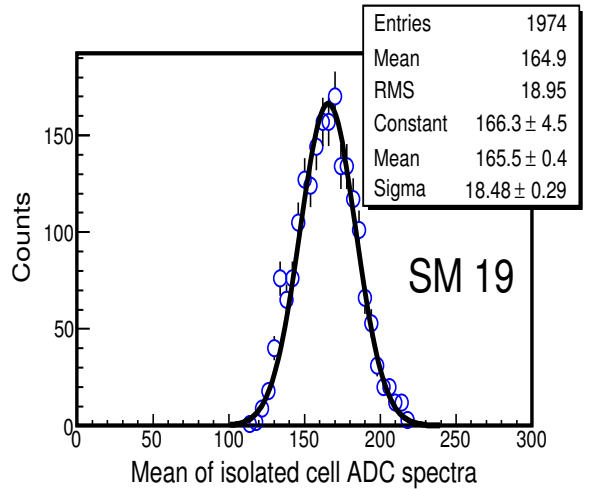
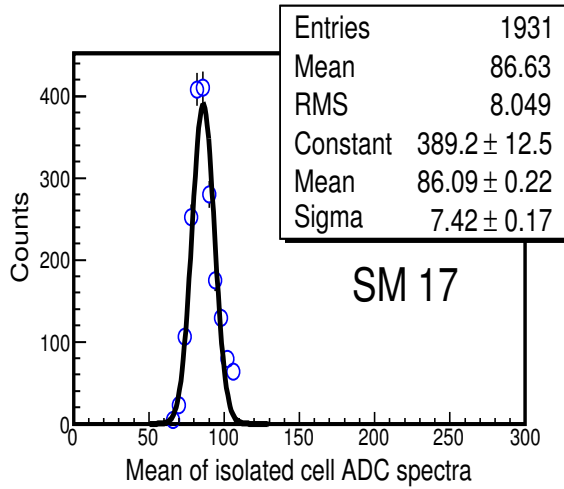
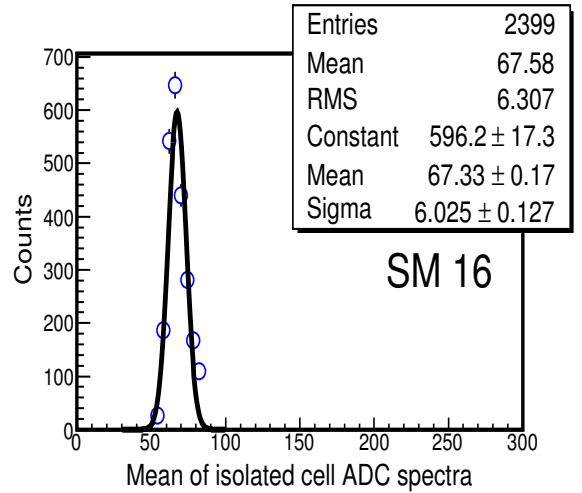
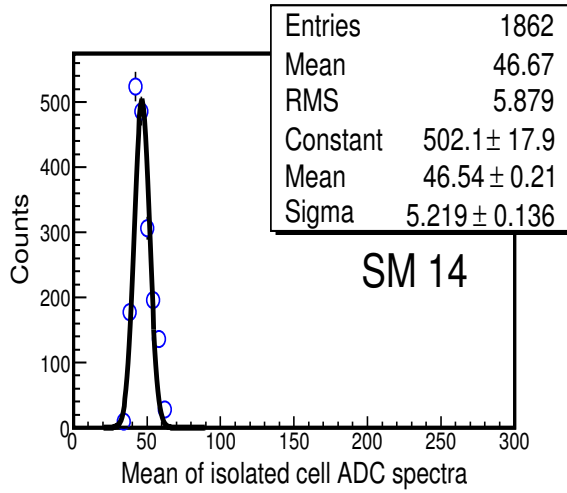


Figure 3.17: Variation of mean of isolated cell ADC spectra for various SMs of PMD.

few SMs are shown in the Fig. 3.17. From the figure we observe that the gain or response of the cells within a SM varies within $\sim 15\%$. However the mean of the response varies by a factor 3 over all the SMs as also observed in Fig. 3.17. It may be mentioned that each SM is a separate gas tight and high voltage entity. The

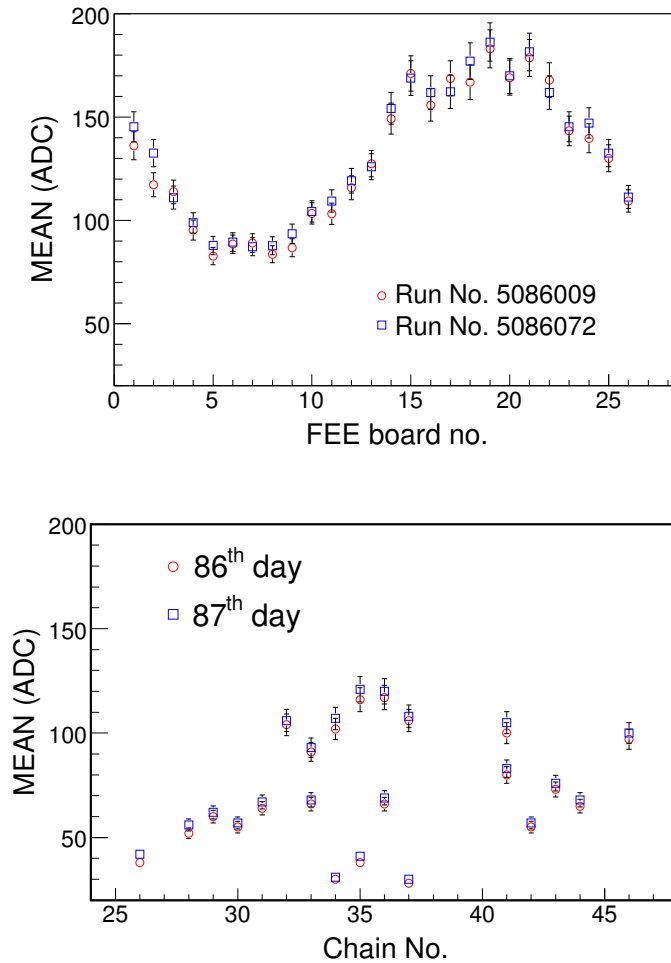


Figure 3.18: Run-to-Run and Day-to-Day variation of mean of mean isolated cell ADC spectra for different SMs in PMD.

reconstruction of PMD data is carried out SM-wise. So it is important to have uniformity of response over a SM, before reconstruction is carried out. For this purpose calibration is done SM-wise. Fig. 3.18 shows the response of cells in terms of the mean of mean cell ADC for all isolated cell in a SM during different times

Table 3.3: Global mean of the isolated cell ADC distribution of cells for working SMs of PMD.

Super Module Number	Mean in ADC units
14	46
15	87
16	67
17	86
18	40
19	165
21	102
22	79
23	98

of data taking in a day (i.e. for different RUNs in a day) as well as variation of the gains in different days (i.e. on different days).

We observe the Run-to-Run and Day-to-Day variation of gain for a particular SM is not observed. Hence a uniform calibration scheme can be used for the full dataset of Au+Au collisions at $\sqrt{s_{NN}} = 62.4$ GeV. The above study has showed the necessity of cell-to-cell gain calibration for PMD before further analysis of the data. The calibration was carried out separately for different SMs. For calibration, mean of all isolated cell ADC (global mean) distribution for each cell is obtained for a SM. Then the ratio of these global mean to the mean of each isolated cell ADC distribution for each cell in that SM, called the calibration factor, is obtained. The distribution of cellwise normalization value or the calibration factor for few SMs are shown in Fig. 3.19.

Each cell belonging to a particular SM, for all events, is then calibrated by the corresponding SM calibration factor to have a uniform response. The global means were later on used as a discrimination threshold, these values are given in table 3.3.

After calibration, the typical cell ADC and PMD hit distribution are shown in Fig. 3.20.

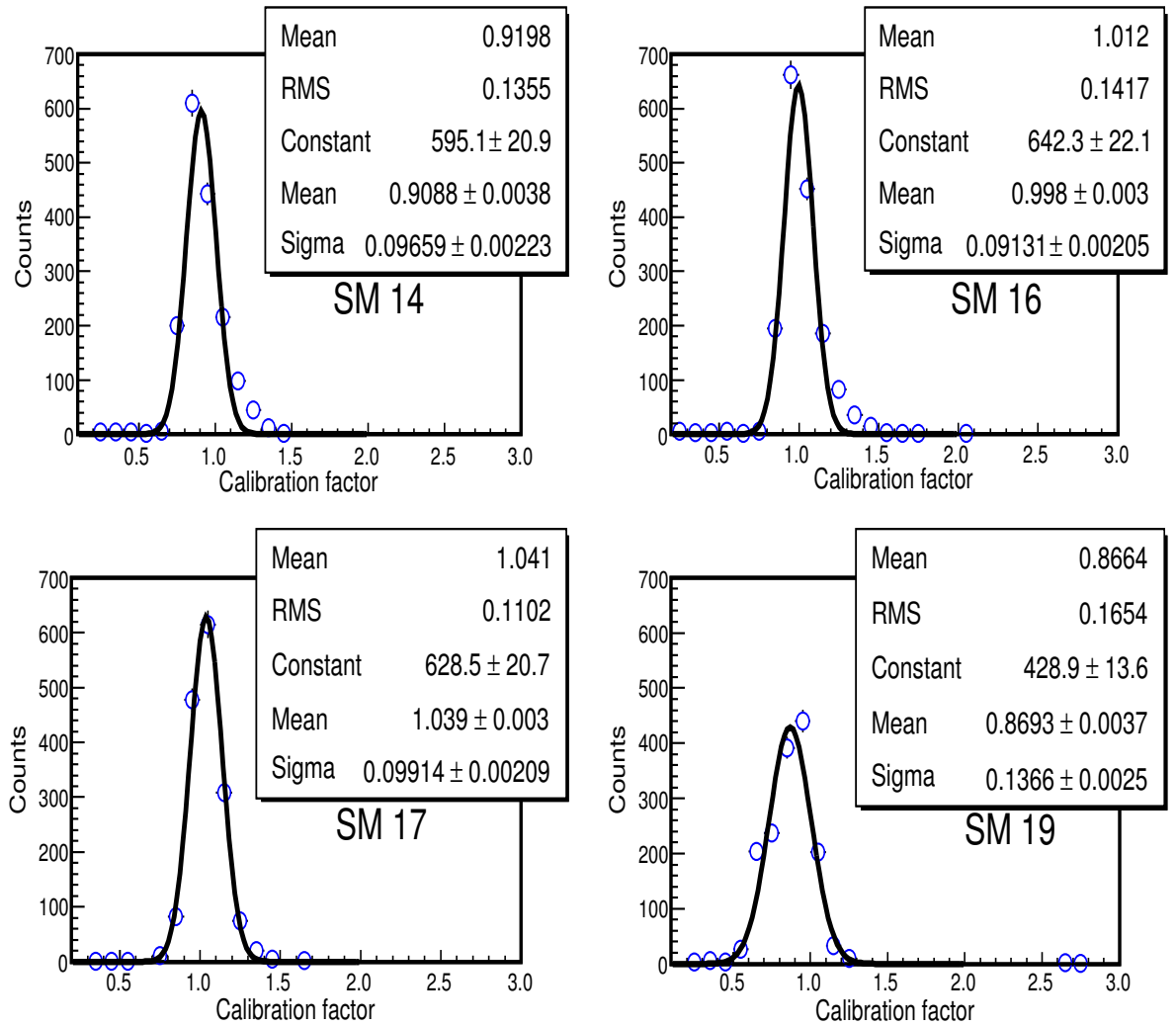


Figure 3.19: Gain calibration factor for few SMs of PMD.

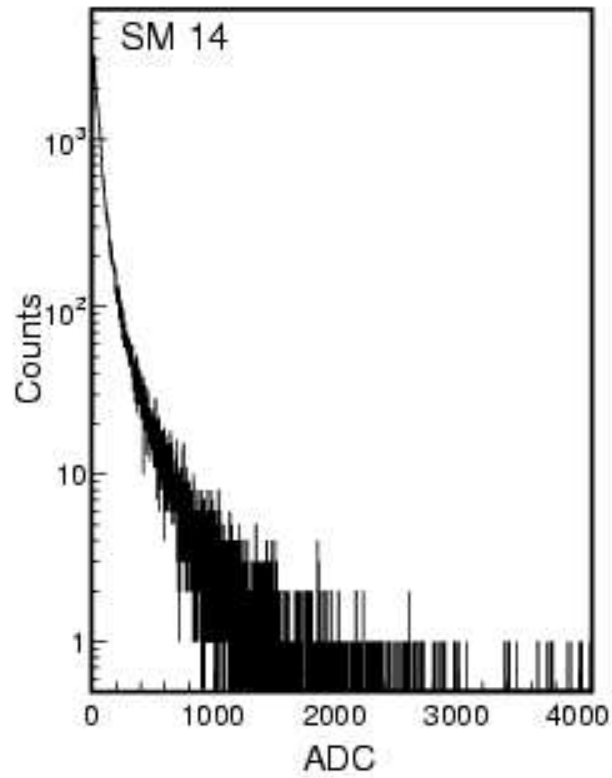
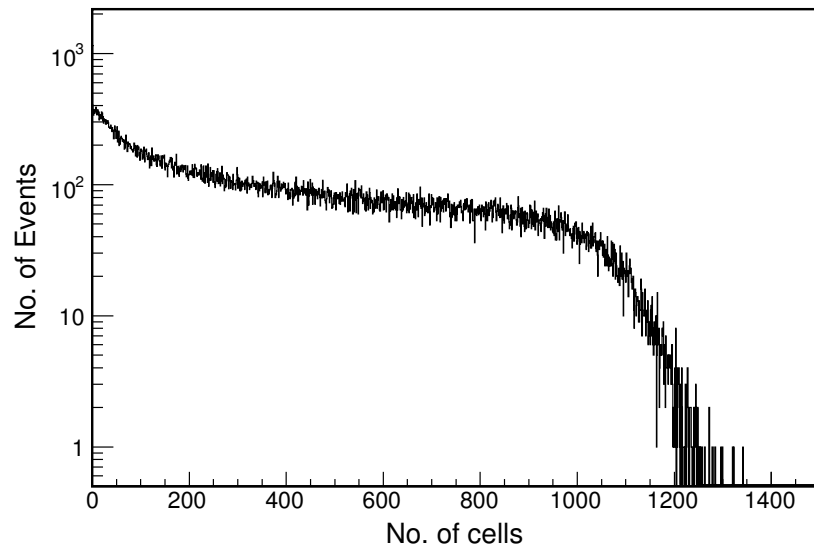


Figure 3.20: Typical PMD hits distribution and cell ADC distribution after cell-to-cell gain calibration for minimum bias trigger.

3.4 Occupancy

The occupancy for the STAR PMD is defined as the ratio of total number of cells hit to the total number of cells. The occupancy is reflective of the granularity of the detector and for a fixed granularity the particle density falling on the detector. The detector configuration is designed to keep the occupancy to a lower level, so that efficiency of particle identification and counting is good. Fig. 3.21 shows the

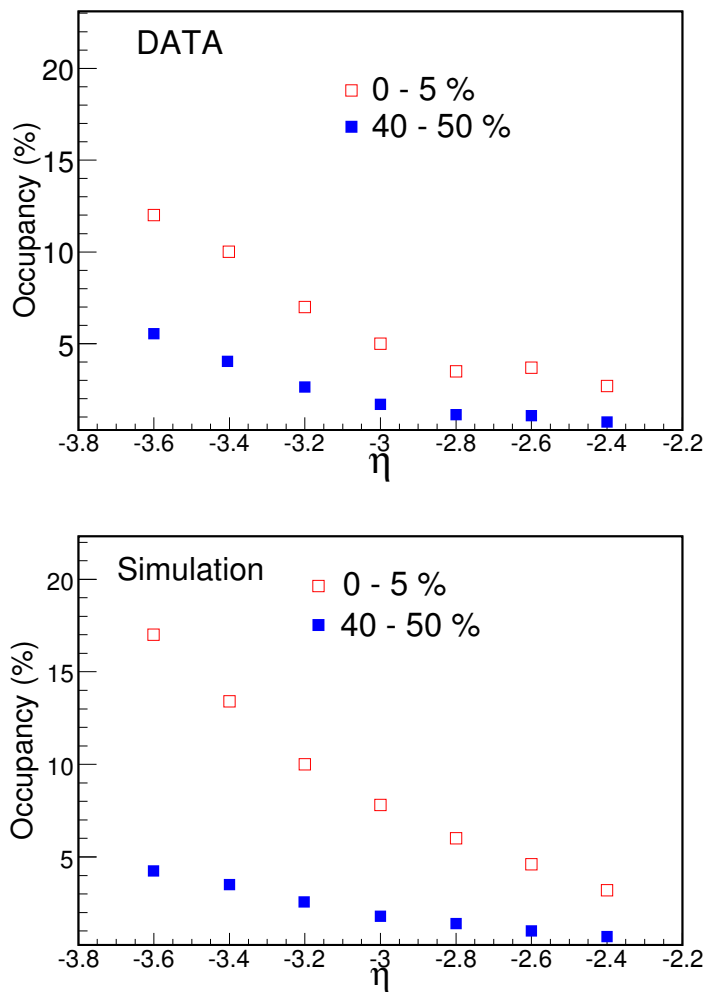


Figure 3.21: Occupancy of STAR PMD as a function of η from real data (top) and from simulation (bottom) for 0–5% central and 40–50% peripheral Au+Au collisions at $\sqrt{s_{NN}} = 62.4\text{GeV}$.

occupancy of STAR PMD as a function of η from real data (top) and simulated data (bottom) in Au+Au collisions at $\sqrt{s_{NN}} = 62.4$ GeV respectively. The 0-5% centrality corresponds to low impact parameter collisions or central collisions and the 40-50% centrality corresponds to higher impact parameter collisions or peripheral collisions. As the particle density is higher for central collisions the occupancy is higher compared to peripheral collisions. The increase in occupancy as we go from -2.4 to -3.6 in η , reflects the increase in particle multiplicity per unit area. It means the ratio of the number of particles falling on the detector to the number of cells in the $\eta \sim -3.6$ region is higher compared to corresponding number at $\eta \sim -2.4$. The occupancy in peripheral collisions is comparable between data and simulations, while for central collisions the results from simulations are slightly lower. Such similarity in the numbers also tells us that the backgrounds estimates for the multiplicity studies may be of similar in data and simulations. The maximum occupancy in data is less than 15%.

3.5 Clustering

A photon passing through the lead converter in front of the preshower plane gives electromagnetic showers. The electrons and positrons coming out of the shower then hit a group of cells on the preshower plane. So it is necessary to adopt a algorithm for clustering of these group of cells associated with the incident photon to obtain the photon clusters in an event [5]. This is schematically shown in the Fig. 3.22. Each cluster is then characterized by its total ADC (or E_{dep}) and (η, ϕ) position of its center.

3.5.1 Algorithm

The basic algorithm for clustering of hits on PMD is schematically shown in the form of a flow diagram in Fig. 3.22. In this subsection we briefly discuss each of the steps.

The clustering is done SM-wise. The first step in the analysis is to collect all the cells which have nonzero ADC (or energy deposition (E_{dep})) and are contiguous to each other in a group which we call a supercluster. Thus the superclusters are separated by cells having zero ADC (E_{dep}), or part of their boundary coincides with the SM boundary. Superclusters are made beginning from the cell with largest ADC (E_{dep}) and forming a cluster with contiguous nonzero ADC (E_{dep})

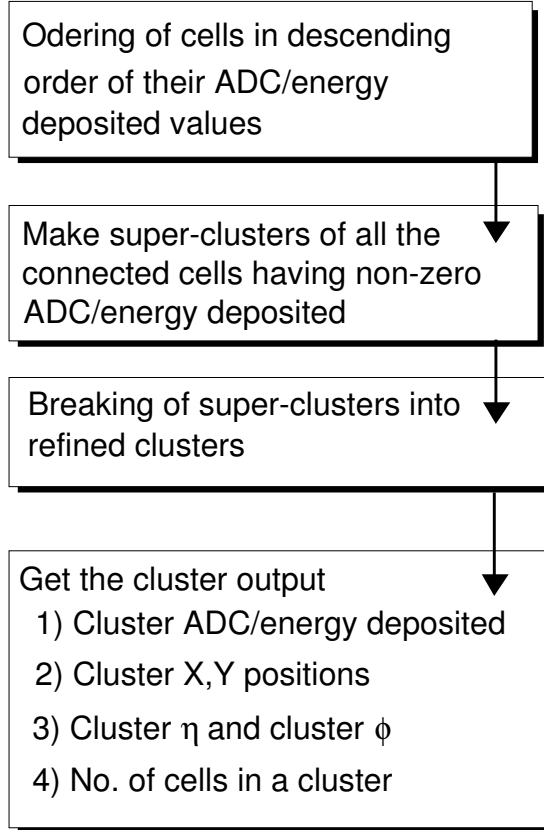


Figure 3.22: Schematic flow diagram of clustering algorithm used to obtain the photon clusters from hits on PMD.

cells. For making the subsequent superclusters we search for the next largest ADC (E_{dep}) cell (other than those cells which have already been used) and follow the same procedure of collecting contagious nonzero ADC (E_{dep}) cells. This process is repeated till all the nonzero ADC (E_{dep}) cells in a SM are exhausted.

If the number of cells having nonzero ADC (E_{dep}) is not very large, each supercluster would consist of few cells. In that case, these superclusters themselves can be identified with the particles (photons or charged particles) falling on the detector. The superclusters constructed having large number of cells may have arisen due to overlap of electromagnetic showers of different particles as a result of large particle density. In such a case, there is a need of breaking the superclusters further. For this the following scheme is devised :

- (a) When the supercluster consists of one cell, its coordinates are taken to be the center of the cell. Its strength is just the ADC (E_{dep}) of the cell. The number of cells (N_{cell}) of the cluster is 1 and the cluster width is taken to be zero.
- (b) For a supercluster having two cells, the cluster center is the center of gravity of the two cells. That is, if the positions of the two cells are $[(x_1, y_1)]$ and $[(x_2, y_2)]$ and their ADC (E_{dep}) values are $[z_1]$ and $[z_2]$ respectively, the cluster centers $[(x_c, y_c)]$ is given by $[x_c = \frac{z_1 x_1 + z_2 x_2}{z_1 + z_2}]$ and $[y_c = \frac{z_1 y_1 + z_2 y_2}{z_1 + z_2}]$. The cluster strength is $[z_1 + z_2]$. Number of cells is 2, the width along the line joining the two cells is $[\frac{z_1 z_2}{(z_1 + z_2)^2}]$ and the width perpendicular to the line joining the two cells is zero.
- (c) If the supercluster has more than two cells then it is broken into a number of clusters. For breaking up the supercluster we assume that the supercluster consists of overlapping clusters. The maxima in ADC (E_{dep}) are identified with the centers of the clusters. The proposed center should be at least one cell unit away from previously determined cluster centers. That is, neighboring cells cannot be cluster centers. It is also assumed that if the distance between the proposed center and the previously accepted center is between 1 and 2 cell units, the strength of the (new) cell should be larger than 25% of the previously accepted center cell. This is to ensure that fluctuations do not give rise to clusters. The number (25%) is ad hoc and needs to be fine tuned depending on the particle density. Note that this distance condition implies the two cells are next nearest neighbors. If the distance between the proposed center and the previously accepted center is 2 cell units (next-to-next nearest neighbor), the cell strength should be larger than 10% of the strength of the previously accepted cell. If the distance is larger than 2 cell units, it is accepted as new cell center.

It must be mentioned that the procedure outlined above is an ad hoc one and needs to be fine tuned keeping the results from test beam studies in mind and the particle density in actual experiment. For the particle density associated with the data set of Au+Au collisions at $\sqrt{s_{NN}} = 62.4$ GeV which forms the major part of this thesis, we have carried out a optimization study using simulated data and demonstrate that the algorithm up to supercluster formation is sufficient for obtaining the photon counting and determination of photon spatial positions. In

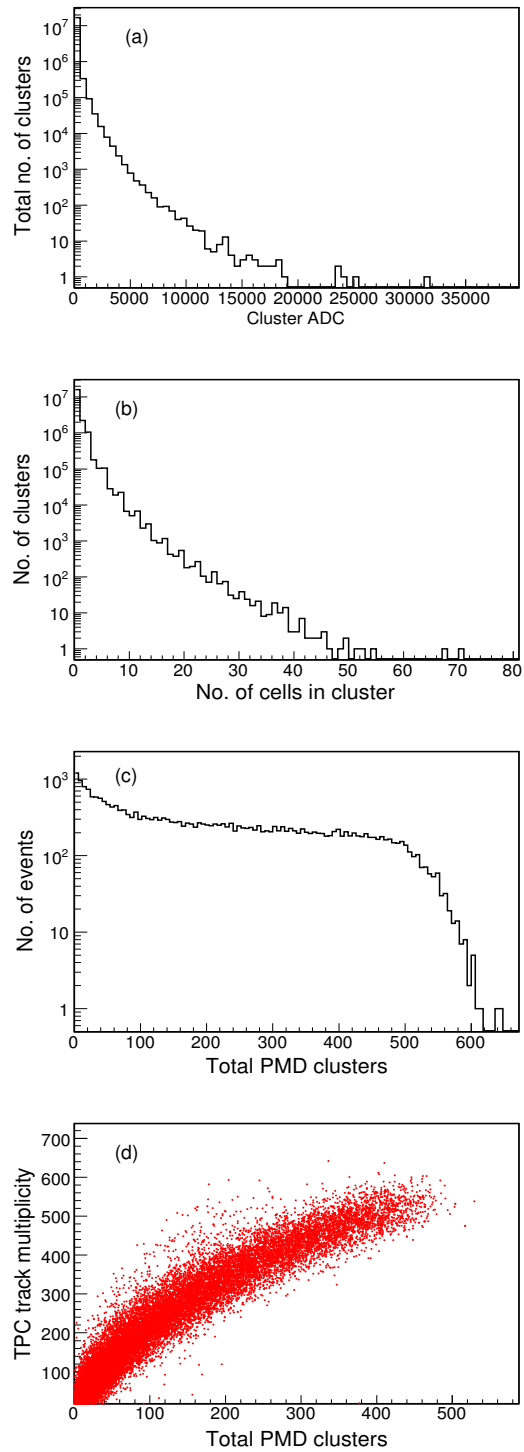


Figure 3.23: (a) Cluster ADC distribution, (b) number of cells in a cluster, (c) total number of clusters on PMD event-by-event and (d) correlation between total clusters on PMD and TPC track multiplicity from experimental data at $\sqrt{s_{NN}} = 62.4$ GeV.

addition, we discuss some of the important features which are necessary for understanding the photon counting and cluster properties of various particles. Fig. 3.23 show typical features of the clusters on PMD, like (a) cluster ADC distribution, (b) number of cells in a cluster, (c) total number of clusters on PMD event-by-event and (d) correlation between total clusters on PMD and TPC track multiplicity from data.

The physics performance of the preshower PMD is characterized by two quantities :

- (i) photon counting efficiency (ϵ_γ) and
- (ii) purity (f_p) of the detected photon sample.

These are defined by the following relations [10]: These two quantities are closely related with the clustering algorithms used.

$$\epsilon_\gamma = N_{\text{cls}}^{\gamma,\text{th}}/N_{\text{inc}}^\gamma , \quad (3.1)$$

$$f_p = N_{\text{cls}}^{\gamma,\text{th}}/N_{\gamma\text{-like}} . \quad (3.2)$$

where N_{inc}^γ is the number of incident photons from the event generator (in our case HIJING), $N_{\text{cls}}^{\gamma,\text{th}}$ is the number of photon clusters above the photon hadron discrimination threshold (discussed in detail in section 3.35) and $N_{\gamma\text{-like}}$ is the total number of clusters above the hadron rejection threshold. $(1-f_p)$ is the fractional contamination in the $N_{\gamma\text{-like}}$ sample. These two quantities will be discussed in more detail later this chapter.

3.5.2 Photon conversion efficiency

PMD has a 3 radiation length (X_0) of material (Lead + steel) in front of the preshower plane. Photon being a electromagnetic particle is converted into electromagnetic shower (electron and positron), and these being charged get detected in the preshower plane of the PMD. Low energy photons may get absorbed in the converter and hence will not be detected in the preshower plane of the PMD.

Photon conversion efficiency is defined as the ratio of number of photons incident on the converter material ($3X_0$ of lead+steel in our case) to the number of photons which give signal in the preshower plane of the PMD above the noise threshold ($\sim 0.2 \times E_{\text{dep}}^{\text{MIP}}$ in simulation). The conversion efficiency (shown in

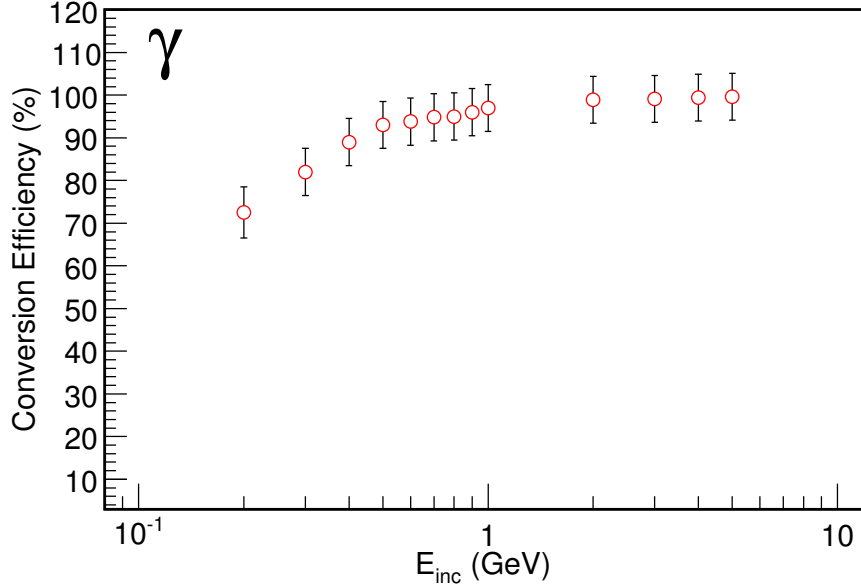


Figure 3.24: Typical conversion efficiency for photons as a function of incident energy in simulation.

Fig. 3.24) is calculated by using single incident photons of various energies in simulation. This (conversion efficiency) puts an upper limit on photon counting efficiency (ϵ_γ), discussed in detail later in this chapter. This implies that, we can not have the photon counting efficiency above the photon conversion efficiency. Fig. 3.24 shows the conversion efficiency for photons as a function of energy of incident photon. One sees that above an incident energy of 1 GeV the photon conversion efficiency is about 90% or higher.

In an event, photons are produced in all energy ranges following a distribution in p_T (discussed in Chapter 2). So it is important to know what is the average photon conversion efficiency in an event and how it varies with collision centralities. Fig. 3.25 (a) shows the photon conversion efficiency which is around 77% in Au+Au collisions at $\sqrt{s_{NN}} = 62.4$ GeV. This is the upper limit for the photon counting efficiency at this energy. Fig. 3.25 (b) show the number of incident photons and the detected photons (photons giving a signal in any of the cells on the preshower plane of the PMD) is linear. Fig. 3.25 (c) shows the dependence of photon conversion efficiency (is flat) on impact parameter of the collisions in Au+Au collisions at $\sqrt{s_{NN}} = 62.4$ GeV.

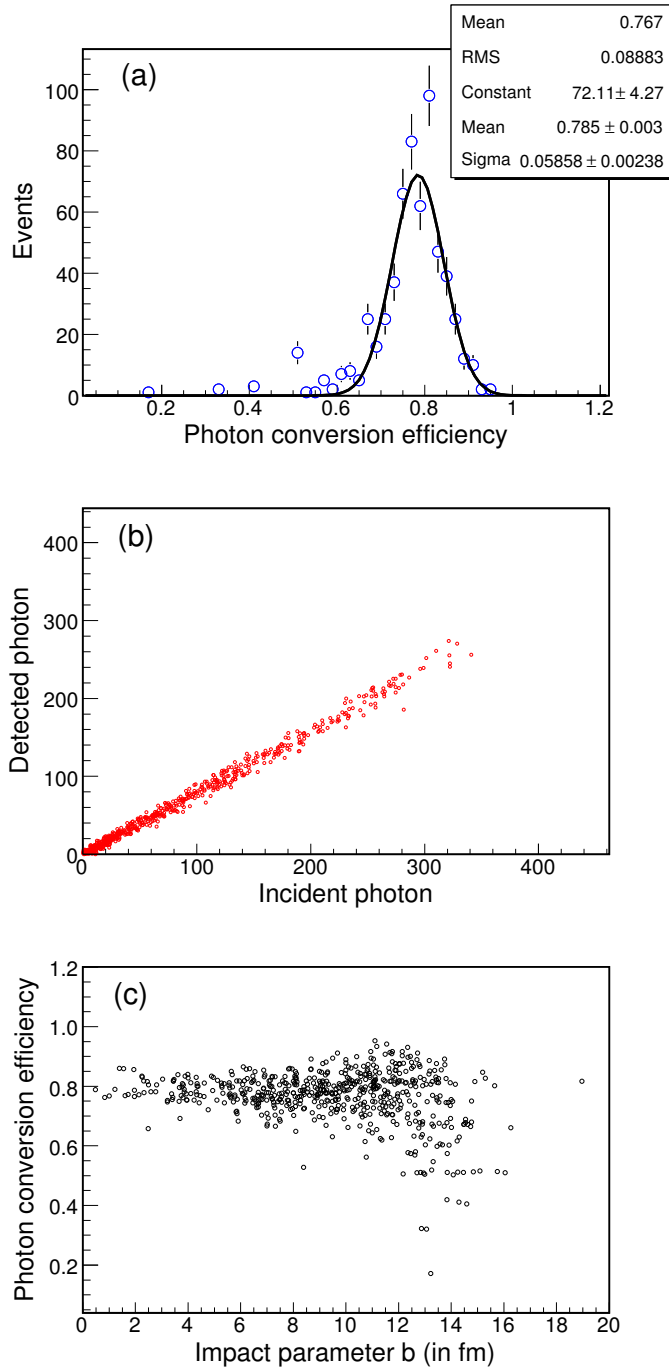


Figure 3.25: (a) The photon conversion efficiency for a large number of events in Au+Au collisions at $\sqrt{s_{NN}} = 62.4$ GeV. (b) Correlation between number of incident photons on PMD and number of detected photons on PMD, where a photon is considered to be detected if it gives signal in any of the cells on the preshower plane of the PMD. (c) Variation of average photon conversion efficiency over a set of events as a function of impact parameter.

3.5.3 Clustering efficiency

The photon after getting converted into electromagnetic shower particles, hits a group of cells of our detector in preshower plane. We then use a clustering algorithm (described in section 3.3) to detect these clusters and associate them with photons. Clustering efficiency is defined as the ratio of number of photon clusters (associated with converted photon tracks) obtained through the clustering algorithm in the detector to the number of photons (tracks) that has converted and given a signal on the preshower plane of the PMD. Fig. 3.26 (top) shows the

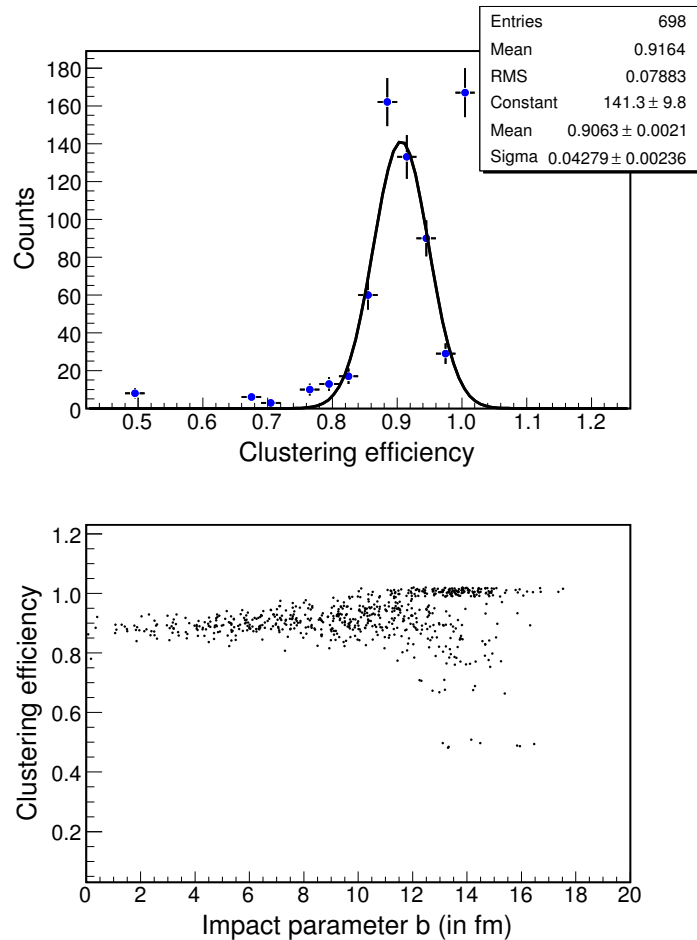


Figure 3.26: Top : The photon clustering efficiency for a large number of events. Bottom : Variation of photon clustering efficiency as a function of impact parameter of the collision for large number of events.

clustering efficiency for large number of events. The clustering efficiency as a function of centrality of collision and its event-by-event variation is shown in Fig. 3.26 (bottom). We find the clustering efficiency is $\sim 91\%$ and it does not have much a dependence on centrality for Au+Au collisions at $\sqrt{s_{\text{NN}}} = 62.4$ GeV. So the upper limit on photon counting efficiency we can have is 0.77 (photon conversion efficiency) $\times 0.91$ (clustering efficiency) = 0.70 (70%) for Au+Au collisions at $\sqrt{s_{\text{NN}}} = 62.4$ GeV.

3.5.4 Track, clusters and optimization of clustering algorithm

In order to estimate the photon counting efficiency and the background in the detected photon sample, it is essential to associate a incident track to a cluster. The background to the detected photon sample is not only from the hadron tracks but also from photon tracks (which should ideally give one cluster on the detector) that gives more than one cluster on the preshower plane of the PMD. These extra clusters are called as split clusters. These may arise due to the following reasons :

- (a) upstream materials in front of PMD,
- (b) limitations of the clustering algorithm and
- (c) the process of shower formation of photons may lead to large angle emission of particles, thus giving rise to two good clusters.

They have serious consequences as far as photon counting efficiency is concerned. The photon counting efficiency may go beyond 100% if split clusters are not properly accounted. The above quantities for the PMD are estimated from simulation studies, by passing HIJING generated events through the GEANT with implementation of all the STAR detectors during that period of data taking. The first step toward determining the above quantities is to associate every incident track to detected clusters on PMD. The quantities above mentioned can be optimized by applying cuts on:

- (i) Number of cells in a cluster (N_{cell}) and,
- (ii) Energy deposited by a particle in a cluster (E_{dep}).

The following algorithm is used :

- (a) Single track hit case:
 - (i) If a cluster is formed by an incident photon track, then it is assigned an identification number ($\text{Id} = 1$).
 - (ii) If a cluster is formed by an incident hadron track, then it is assigned an $\text{Id} = 8$.
- (b) Multiple track hit case:

In a photon cluster, there may be more than one incident photon tracks.

 - (i) If the cluster has a photon track which does not have a split cluster (track multiplicity = 1), we assign that cluster an $\text{Id} = 1$, irrespective of whether the cluster has any other photon track in it or not.
 - (ii) For clusters which does not correspond to a track with track multiplicity = 1, we assign the track which has deposited the largest energy to that cluster. So one cluster is associated with only one incident photon track.
- (c) For photon clusters which have associated photon tracks which belong to more than one cluster, we do the following :
 - (i) If the E_{dep} of the clusters $> 2 \times E_{dep}^{MIP}$, then the cluster with smaller number of cells is a split cluster and a cluster $\text{Id} = 2$ is assigned.
 - (ii) If the E_{dep} of any one of the clusters or both clusters is $< 2 \times E_{dep}^{MIP}$, then the cluster with smaller E_{dep} is identified as a split cluster and a cluster $\text{Id} = 2$ is assigned. For both the above cases, the other cluster has $\text{Id} = 1$. The clusters with $\text{Id} = 2$ are considered as backgrounds in the analysis.

Fig. 3.27 (top) shows the number of cells distribution for cluster finally assigned an $\text{Id} = 1$ and their corresponding split cluster number of cells. The number of cells in a split cluster never exceed the number of cells in the parent cluster (indicated by the line) for cases where cluster E_{dep} of both are greater than $2 \times E_{dep}^{MIP}$. Fig. 3.27 (bottom) shows the cluster E_{dep} and the E_{dep} of the corresponding split clusters. The split cluster E_{dep} is mostly lower than the cluster E_{dep} of the parent cluster. The split clusters can be reduced by applying suitable cuts on the number of cells (N_{cell}) in a cluster and the cluster E_{dep} . The effect of the cuts can be seen in Fig. 3.28.

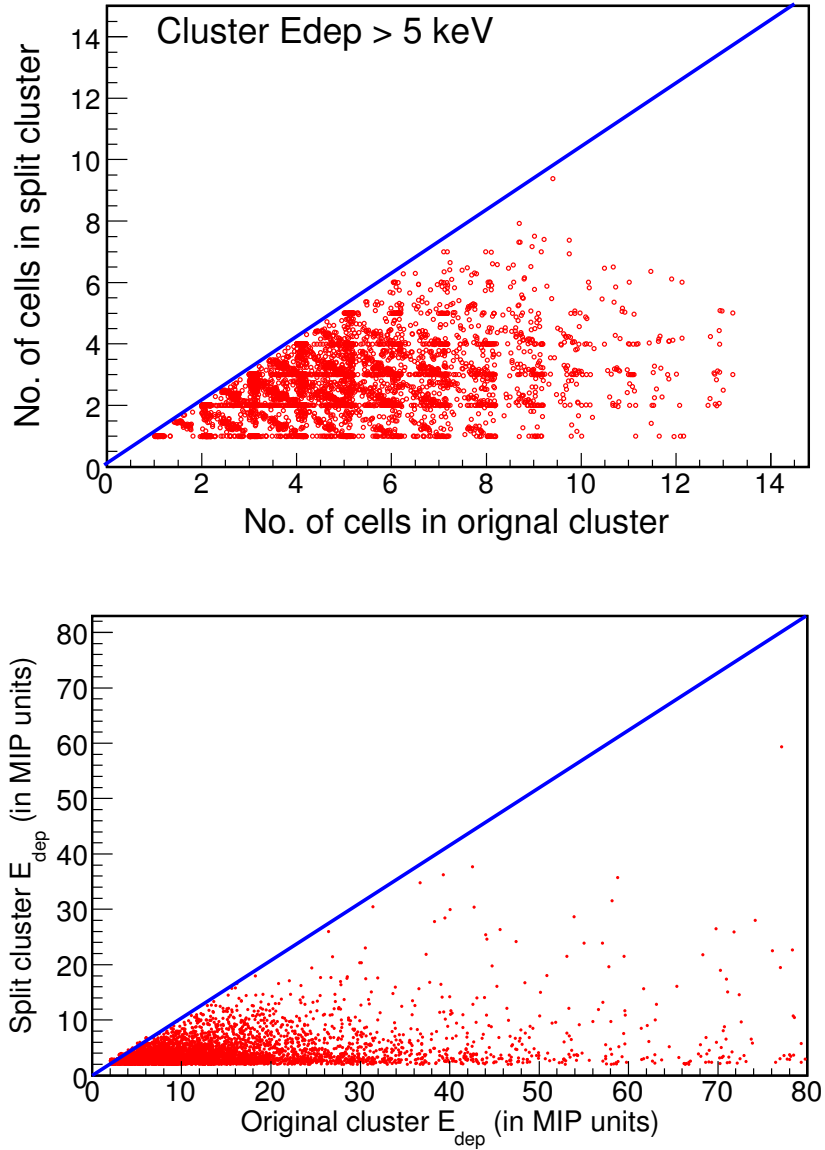


Figure 3.27: Top : The number of cells in a cluster vs. the number of cells in the corresponding split clusters for cluster $E_{dep} > 2 \times E_{dep}^{MIP}$. Bottom: Cluster E_{dep} vs. E_{dep} of the corresponding split clusters.

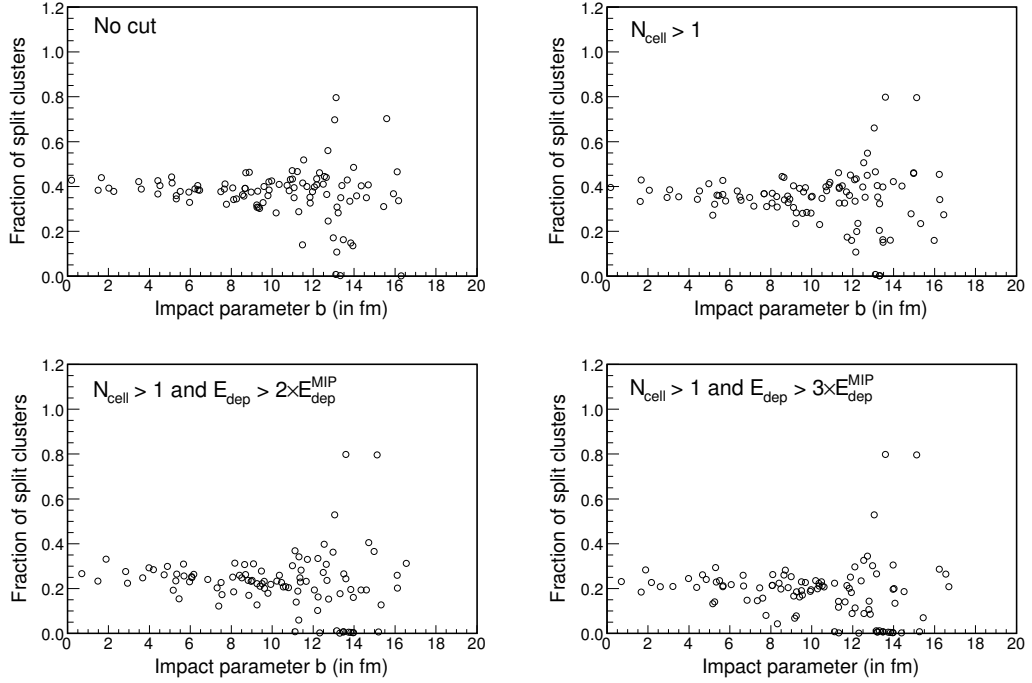


Figure 3.28: The variation of fraction of split clusters with impact parameter of the collision for no cuts applied on the cluster properties and for various cuts on N_{cell} and cluster E_{dep} .

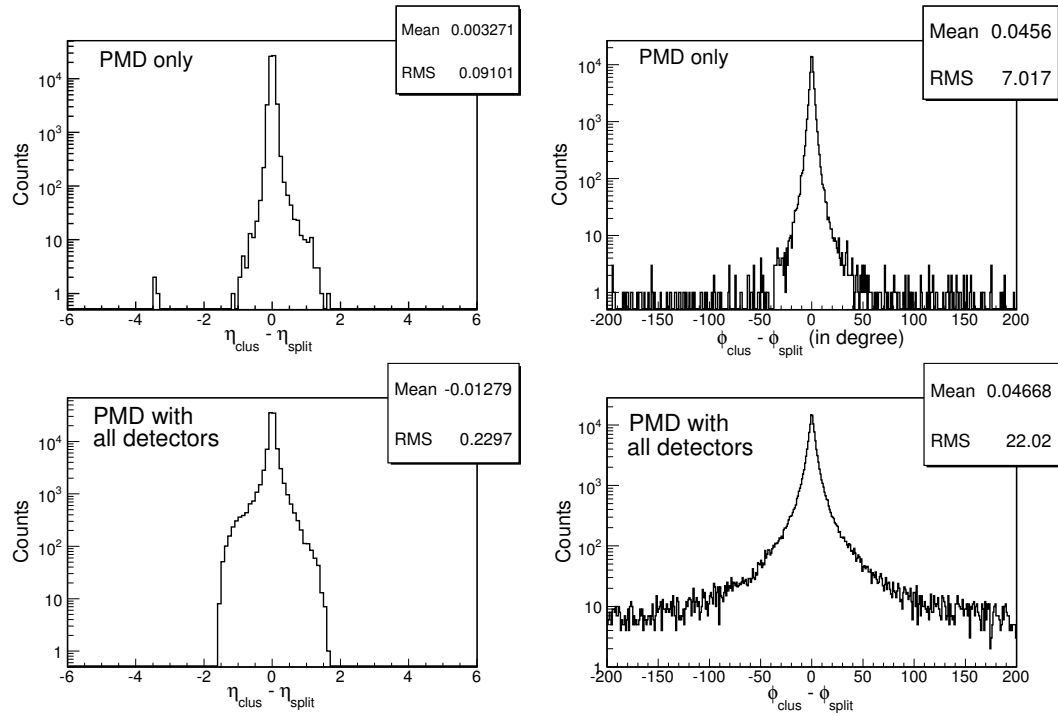


Figure 3.29: The difference in the cluster (η, ϕ) and its split cluster (η, ϕ) positions for PMD only and for PMD with all detectors case.

With cut on cluster E_{dep} the fraction of split clusters reduces. The separation of the split clusters from their parent clusters can be seen in Fig. 3.29 in terms of their separation in η and ϕ . The RMS of the distributions for PMD only case (i.e PMD is the only detector present in GEANT simulation) and for the case with all detectors differ by a factor of 2.5 and 3 in η and ϕ respectively. The presence of substantial amount of split clusters together with a pretty narrow distribution in cluster and its split cluster positions led us to a more detailed study and optimization of the clustering algorithm. Before attempting to make an optimization study, we tried

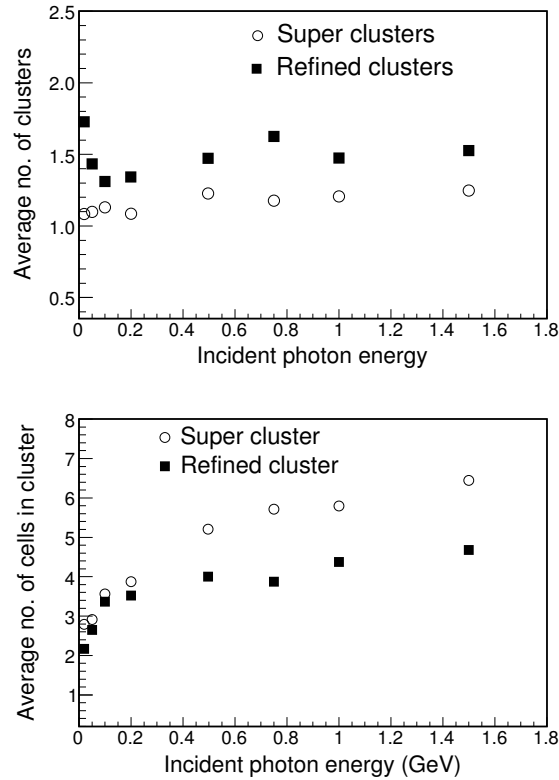


Figure 3.30: Top : Average number of super clusters and refined clusters for single photon track at different incident photon energy in simulation. Bottom : Average number of cells in super clusters and refined clusters for single photon track at different incident photon energy in simulation.

to understand the clustering algorithm in simulation where a single photon track is made to fall on the PMD. Fig. 3.30 (top) shows the average number of super clusters and refined clusters for single incident photon track on the PMD as a function of

incident photon track energy in simulation. We have also studied the average number of cells in a super and refined clusters for a single photon track of a given energy incident on PMD as shown in Fig. 3.30 (bottom). While we expect that the average number of super clusters to be around 1, it is observed to be 20% higher. The refined clustering algorithm has further broken up the super clusters with average number of clusters for a single incident photon track to 1.5. The average number of cells in a super cluster increases with increase in energy of the incident photon track on the expected lines. But the decrease in average number of cells in corresponding refined clusters is indicative of cluster splitting. Fig. 3.31 shows

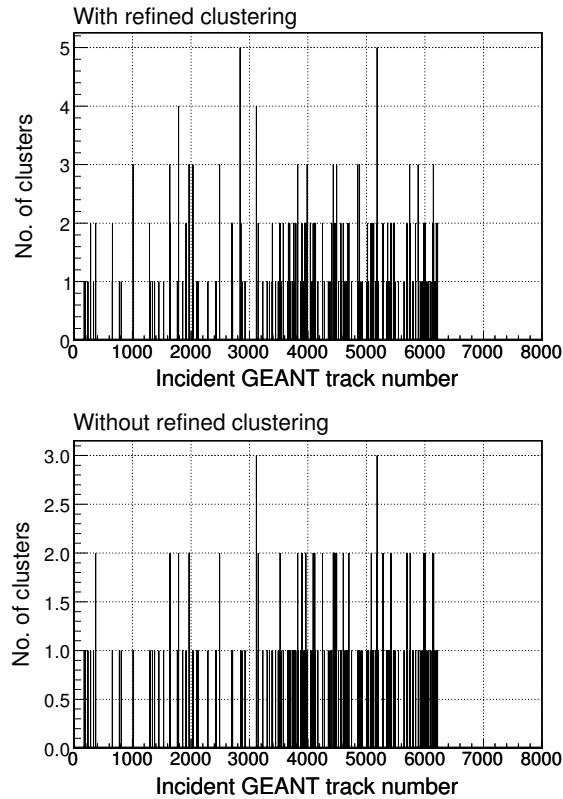


Figure 3.31: Top : Number of clusters formed for each incident photon with refined clustering algorithm. Bottom : Number of clusters formed for each incident photon without refined clustering algorithm.

the number of photon clusters a incident photon track forms on the preshower plane with (top) and without (bottom) the refined clustering algorithm. It clearly indicated that it is better to discard the refined clustering part of the algorithm

for the particle densities which are observed in Au+Au collisions at center of mass energy of 62.4 GeV. This aspect is further emphasized in the Fig. 3.32 where we plot the number of refined clusters as a function of number of cells in a super cluster (top) and the number of cells in a refined cluster vs. the number of cells in a super cluster (bottom). From the figures it is clear, that a super cluster having 3 cells is further broken into 2 refined clusters of 1 and 2 cells respectively. This

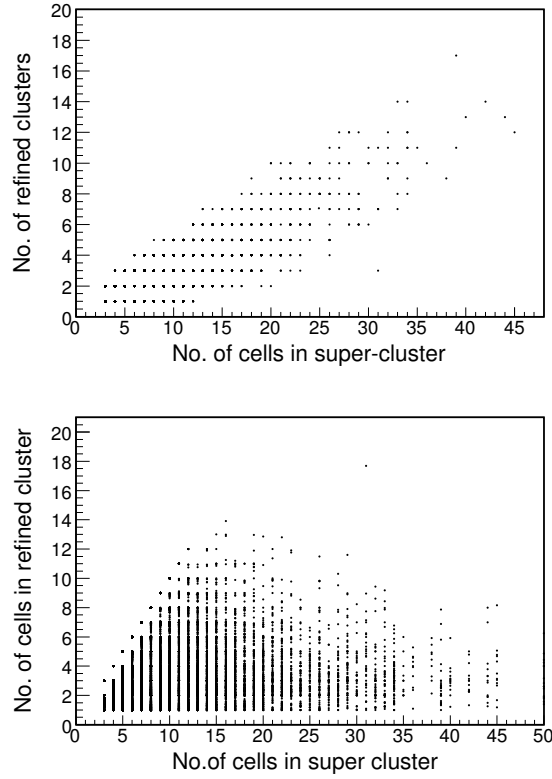


Figure 3.32: Top : Number of refined clusters as a function of number of cells in the corresponding super cluster. Bottom : Number of cells in refined cluster as a function of number of cells in the corresponding super clusters.

shows that for the data set of Au+Au collisions at $\sqrt{s_{NN}} = 62.4$ GeV it is sufficient to restrict ourselves up to the super cluster stage in the clustering algorithm.

Based on the above observations, we conclude that the parameters used in the refined clustering must be tuned properly for Au+Au dataset at $\sqrt{s_{NN}} = 62.4$ GeV to reduce the large number of split clusters. Hence we should optimize the parameters of the refined clustering by carrying out simulations studies for PMD

only case. One of the parameters of the refined clustering that can be tuned is the E_{dep} of the local maxima and its E_{dep} profile as a function of distance from the peak cell (cell having the largest E_{dep} among all the cells of the cluster). The default values of fractional E_{dep} are 0.30, 0.15, 0.05.

These values mean :

If the E_{dep} in the first ring of neighbors of the peak cell is less than 30% of its E_{dep} , then those cells belong to the cluster and the rest will form the part of another cluster. If the next ring of cells have E_{dep} less than 15% of peak cell E_{dep} , then they belong to the cluster and for the third ring the % value is 5. We tried to

Table 3.4: Tuning of local maxima parameters of spuer clusters.

Condition	Split clusters (%)
Default (0.3,0.15,0.05)	14.5
0.4,0.2,0.1	12.9
0.5,0.25,0.12	12.2
0.65,0.25,0.12	11.9
0.85,0.25,0.12	11.7

optimize these values by looking at the % split clusters. The results are shown in Table 3.4. We found that the results are fairly independent of the E_{dep} parameters used to find the local maxima of clusters.

The other way of tuning the clustering algorithm for the 62.4 GeV data set through simulations was to put a cut off on the E_{dep} value of the cell which is to be chosen as the peak or local maximum of a cluster. The idea is to have a clear choice of local maximum in the super cluster. This cut off can be $0.5 \times E_{dep}^{MIP}$, $1 \times E_{dep}^{MIP}$ or $2 \times E_{dep}^{MIP}$. The results of this study are shown in the following Table 3.5.

Table 3.5: Tuning of local maxima parameters of clusters by putting a cut off on E_{dep} of the cell in a super cluster.

Condition for peak of local maxima	Split clusters (%)
No cut	14.5
$E_{dep} > 0.5 \times E_{dep}^{MIP}$	13.4
$E_{dep} > 1.0 \times E_{dep}^{MIP}$	10.3
$E_{dep} > 2.0 \times E_{dep}^{MIP}$	7.9

This shows that by adopting the second procedure we can in fact reduce the split

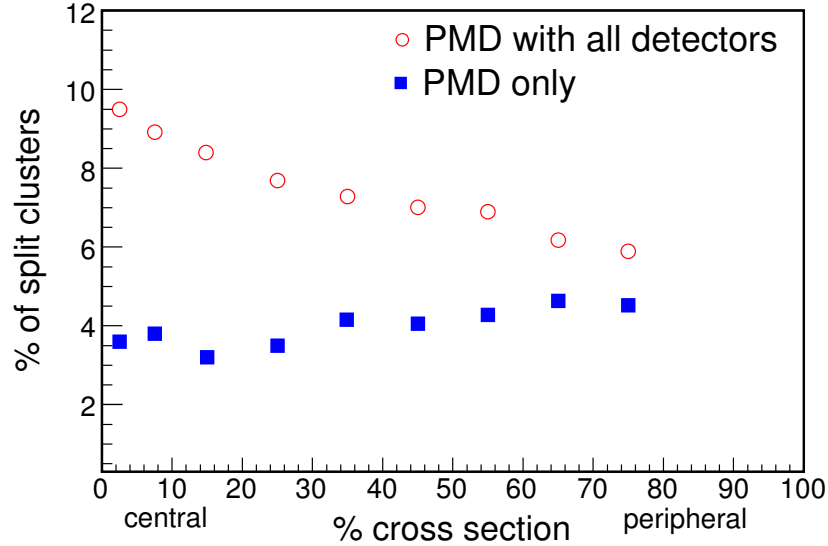


Figure 3.33: Variation of the % of split clusters with collision centrality for PMD only and PMD with all detectors in STAR. Both numbers obtained for the cutoff on cluster $E_{dep} > 3 \times E_{dep}^{MIP}$ and $N_{cell} > 1$.

clusters, but there is a higher chance of removing photon clusters of lower momentum. We also observed from the simulation studies for PMD only case, the % of super clusters with $N_{cell} < 10$ is $\sim 96\%$ and those with $N_{cell} < 7$ (slightly more than 6 neighboring cells of the local maxima) $\sim 90\%$. Based on the above study we decide to use the clustering without refined clustering algorithm for the Au+Au data set at $\sqrt{s_{NN}} = 62.4$ GeV.

With the clustering algorithm fixed, we have the final split cluster percentage for PMD only and PMD with all detectors for a cutoff on the cluster properties, i.e.

- (a) number of cells in a cluster, $N_{cell} > 1$ and
- (b) cluster $E_{dep} > 3 \times E_{dep}^{MIP}$.

Fig. 3.33 shows the variation of the % of split cluster with collision centrality for PMD only and PMD with all detectors in STAR. The fraction of photon split clusters is defined as the ratio of total number of photon split cluster in the event to the total number of photon clusters. We find the percentage of split clusters varies from 9.5% to about 6% for PMD with all detectors and it is $< 5\%$ for PMD only case. Ideally the cluster should have the same η and ϕ or x and y position as

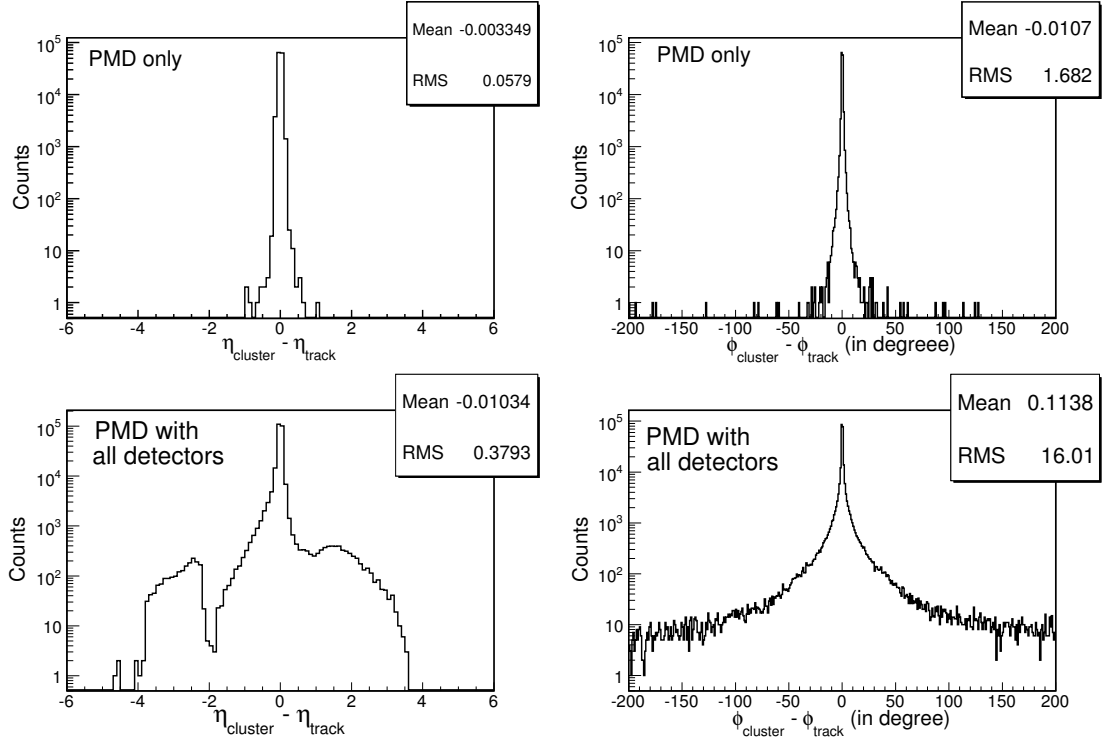


Figure 3.34: The difference in the cluster (η, ϕ) and its incident track (η, ϕ) positions for PMD only and for PMD with all detectors case for photons.

its incident track. If we take the difference between incident track η and its cluster η or incident track ϕ and its cluster ϕ , it should be zero. This may not happen due to the following reasons :

- (i) Upstream materials in front of PMD and
- (ii) Limitations of the clustering algorithm.
- (iii) Shower centroid shift due to transmission through the convertor.

Since one of the main observables in PMD is the spatial distribution of photons, it is crucial to see if we have most of photon clusters at the same position as its track. For knowing the best possible results expected from PMD, we compare the results from simulation for PMD only case with those from all detectors case. The comparison will reflect the effect of material in front of PMD. Due to the material effect, the cluster position (η, ϕ) on PMD from the incident photon track position (η, ϕ) will be different.

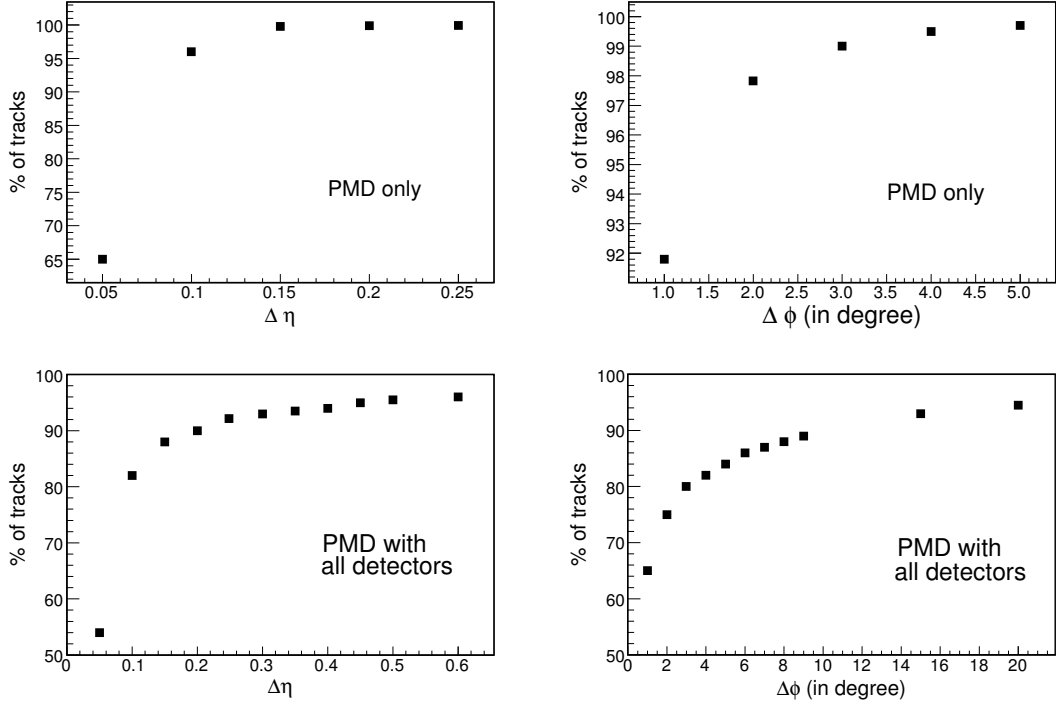


Figure 3.35: Total number of clusters (%) lying within certain $\Delta\eta$ and $\Delta\phi$ from its incident track for PMD only case and for PMD with all detectors case.

Fig. 3.34 shows the difference between incident track η and corresponding cluster η as well as incident track ϕ and corresponding cluster ϕ . The results are shown for PMD only and PMD with all detectors. The deviation of the clusters from the incident track position is very less for the PMD only case in comparison with PMD with all detector case. A high value of difference between cluster η and incident track η suggests that it is due to upstream material in front of PMD. More important is the sign of the difference. The negative sign means that η_{track} is high, which in turn means that these tracks are coming from close to the beam pipe. Since the difference is as high as 4, it is most likely due to scattering of the incident tracks from beam pipe and falling on the PMD.

In Fig. 3.35 we show the % of tracks within certain $\Delta\eta$ and $\Delta\phi$. We find that $\sim 97\%$ of the clusters have their positions within $\Delta\eta < 0.1$ for PMD only case and $\Delta\eta < 0.2$ of their incident tracks for PMD with all detectors. In the azimuthal angle, $\sim 90\%$ of the clusters have their position within $\Delta\phi < 1^\circ$ for PMD only case and about $\Delta\phi < 8^\circ$ of their incident tracks for PMD with all detectors. For a combined condition on both $\Delta\eta$ and $\Delta\phi$ we have the following % of incident

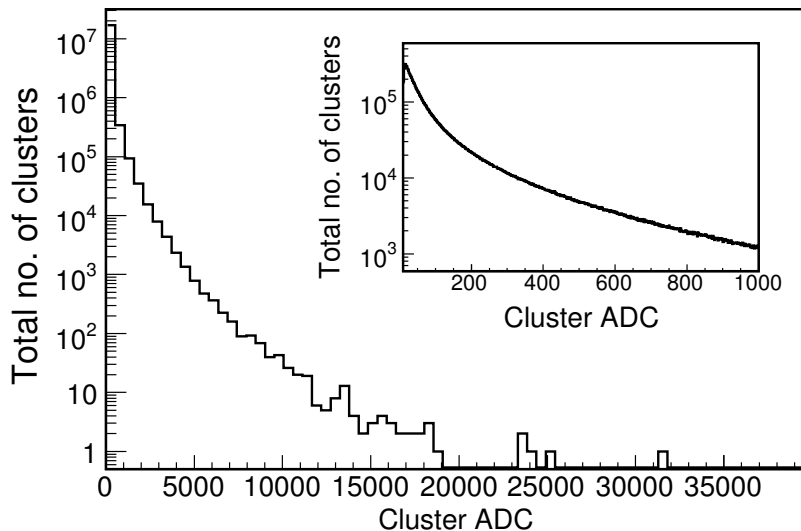


Figure 3.36: Cluster ADC distribution over large number of events. Inset shows the same cluster ADC distribution upto 1000 ADC units.

tracks for the PMD with all detectors case. For $\Delta \eta < 0.1$ and $\Delta \phi < 2^\circ$, we have 71% of the clusters, for $\Delta \eta < 0.2$ and $\Delta \phi < 4^\circ$, we have 81% of the clusters and for $\Delta \eta < 0.3$ and $\Delta \phi < 6^\circ$ we have 85% of the clusters recovered on preshower plane.

Before we discuss the photon hadron discrimination and study the properties of charged hadron and photon clusters in detail, in Fig. 3.36, we show the typical cluster ADC distribution over a large number of events.

3.5.5 Discrimination of photons and charged hadrons

Ideally one can make the following comparative statements for clusters due to photon track and clusters due to charged hadron track.

- (a) Photon cluster will deposit more energy in the sensitive medium of the detector as compared to the cluster formed due to charged hadron.
- (b) Photon cluster will have more number of cells hit in the preshower plane due to the electromagnetic shower of e^+, e^- coming from photon conversion in the $3X_0$ of lead converter. The charge hadrons, which essentially hit single cell, will form cluster with single isolated cell in the preshower plane.

These features can be used to discriminate a photon cluster from a charged hadron cluster. One expects a hadron to be a MIP and deposit some minimum energy (~ 2.5 keV from simulation studies) and give signal in only one cell in both pre-shower and veto plane, as seen in test beam studies [3]. But the following points need to be considered, which may lead to contrary results.

- (a) A low energy photon may have most of its shower particles (e^+, e^-) get absorbed in the $3X_0$ converter material. This may lead to less number of cells hit in preshower plane and hence depleting a photon cluster with less number of cells as well as less energy deposition in the preshower plane.
- (b) A charged particle may interact with the converter material (for $3X_0$ the interaction probability is about 10%). It may give signal in larger number of cells in preshower plane and can form a cluster with $N_{cell} > 1$, and hence deposit more energy ($> E_{dep}^{MIP}$).
- (c) The clustering algorithm in its attempt to separate overlapping clusters (expected in high particle density at forward rapidity in nucleus-nucleus collisions) may split a photon cluster into many small clusters. This results in the formation of clusters having smaller energy deposition and less number of cells.

We now study some of the properties of photon and charged hadron clusters for Au+Au collisions at center of mass energy of 62.4 GeV using simulations. Fig. 3.37 (top) shows the fraction of photon clusters on PMD having $N_{cell} = 1$. We observe 26% of photon clusters have $N_{cell} = 1$. So if we select clusters with $N_{cell} > 1$ to discriminate photons from charged hadrons, we loose 26% of the converted photons in the preshower plane. On the other hand we observe (Fig. 3.37 (bottom)) that 29% of the clusters due to charged hadrons interaction with $3X_0$ converter material gives a cluster which has $N_{cell} > 1$. If we put only $N_{cell} > 1$ condition, 29% of total charged hadrons giving clusters will contribute to impurity of detected photon sample. A further increase in N_{cell} cut improves the purity of photon sample but will lead to decrease in photon counting efficiency. These can be seen from Fig. 3.38. So it is important to consider the E_{dep} cutoff also on the detected clusters to extract photon clusters with reasonable efficiency and purity. For the next set of studies we concentrate on clusters with $N_{cell} > 1$. Fig. 3.39 shows the cluster E_{dep} distribution for photons (upper two pannels) and charged hadrons (lower two pannels) in MIP units for various $N_{cell} > 1$ conditions from simulation. From the

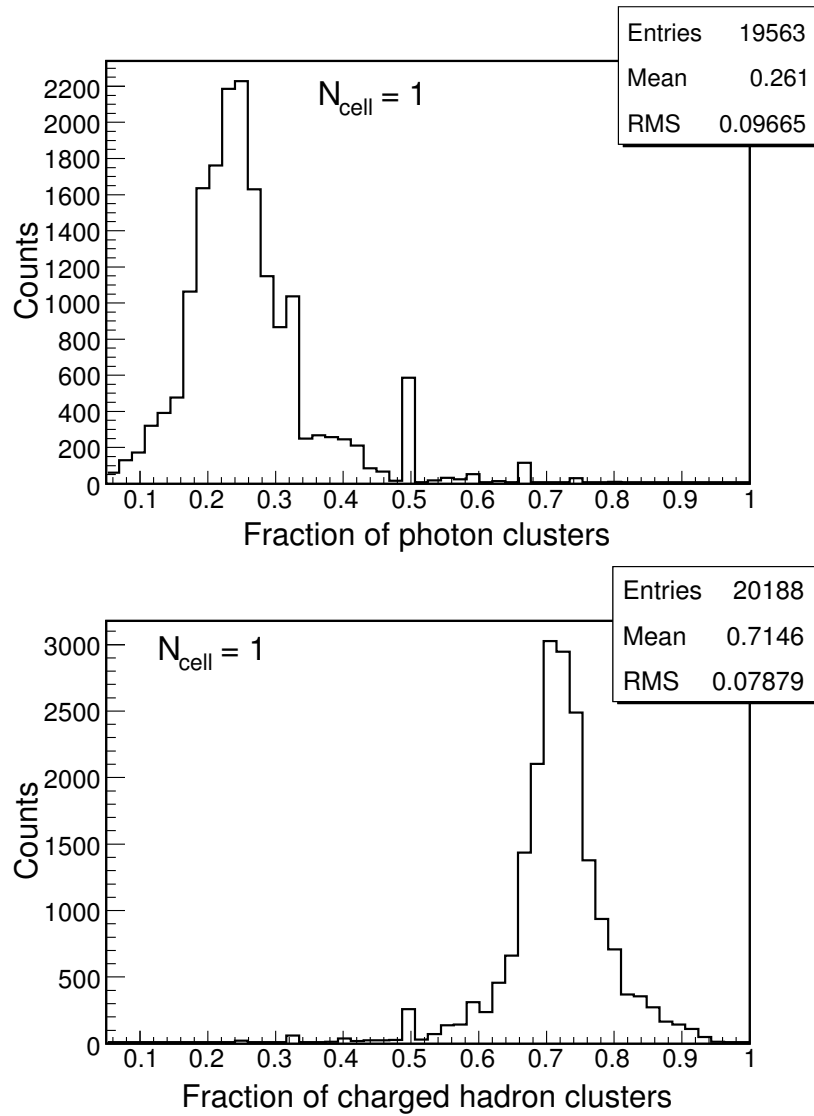


Figure 3.37: Fraction of photon (top) and charged hadron clusters (bottom) having $N_{cell} = 1$ from simulations.

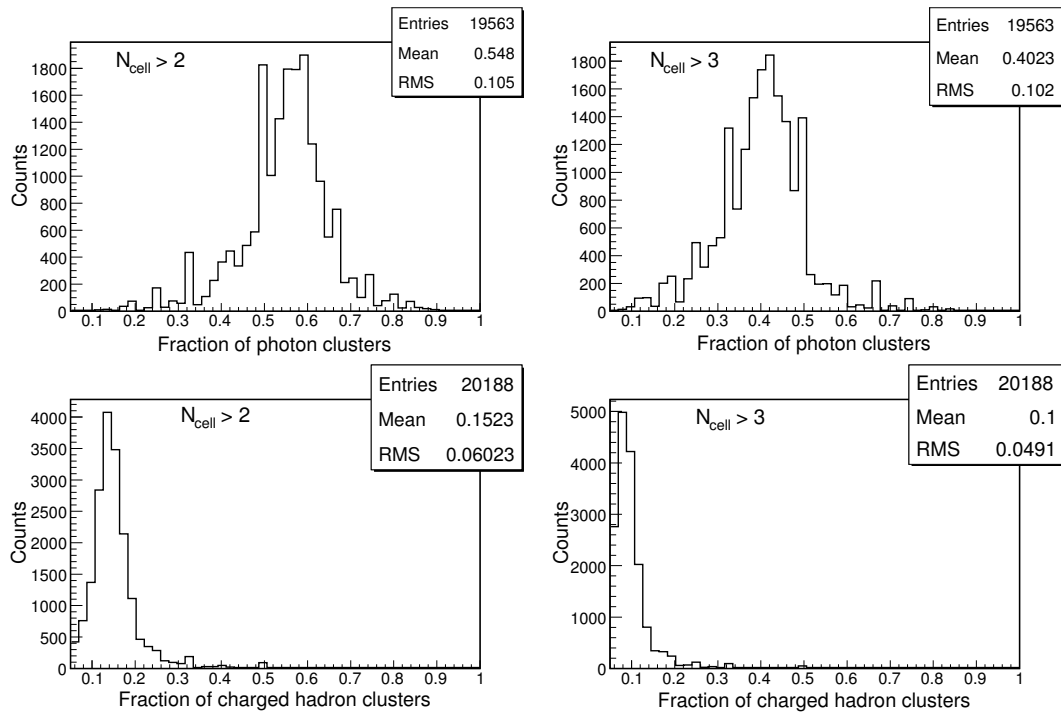


Figure 3.38: Fraction of photon (upper two panels) and charged hadron clusters (lower two panels) having $N_{cell} > 2$ and 3 from simulations.

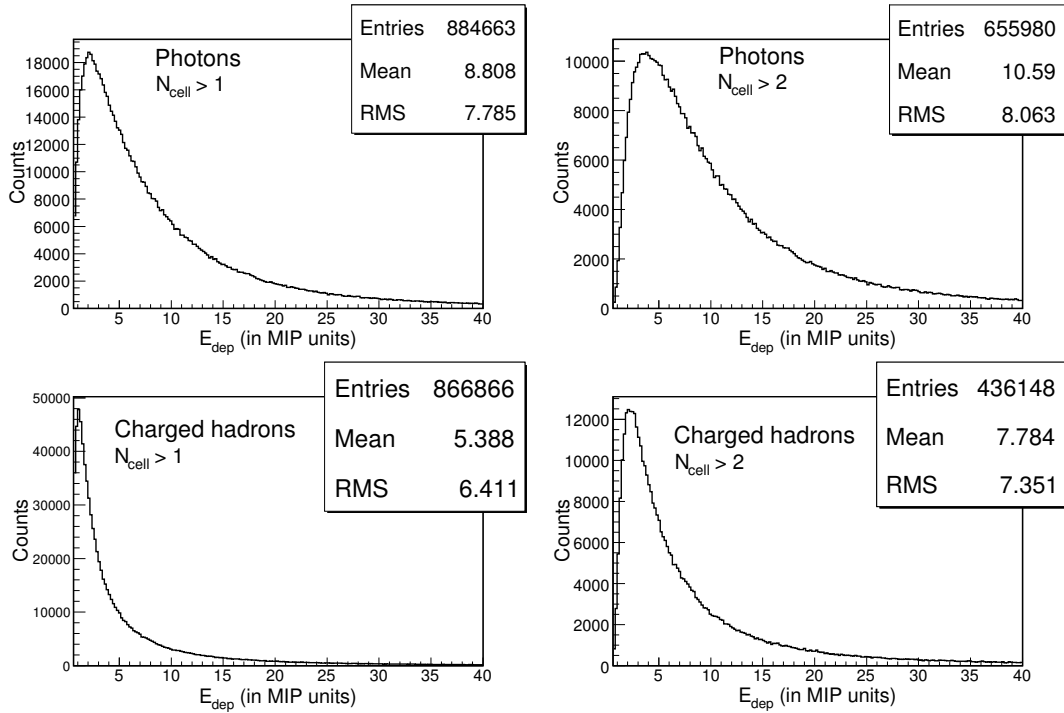


Figure 3.39: Cluster E_{dep} distribution for photons (upper two panels) and charged hadrons (lower two panels) in MIP units for various $N_{cell} > 1$ conditions from simulations.

figure it is clear that for a cluster E_{dep} cutoff around 2-3 times the E_{dep}^{MIP} for $N_{cell} > 1$ should be sufficient to select a substantial number of photon clusters and reject a large number of charged hadron clusters.

3.6 Photon counting efficiency and purity of photon sample

Our study of the photon conversion efficiency shows that low transverse momentum incident photons are mostly absorbed in the $3X_0$ converter material. So it is better to remove the low transverse momentum photons from the efficiency calculations. This can be optimized by selecting proper E_{dep} and N_{cell} cuts, as PMD does not have p_T information of the detected clusters. The photon counting efficiency and

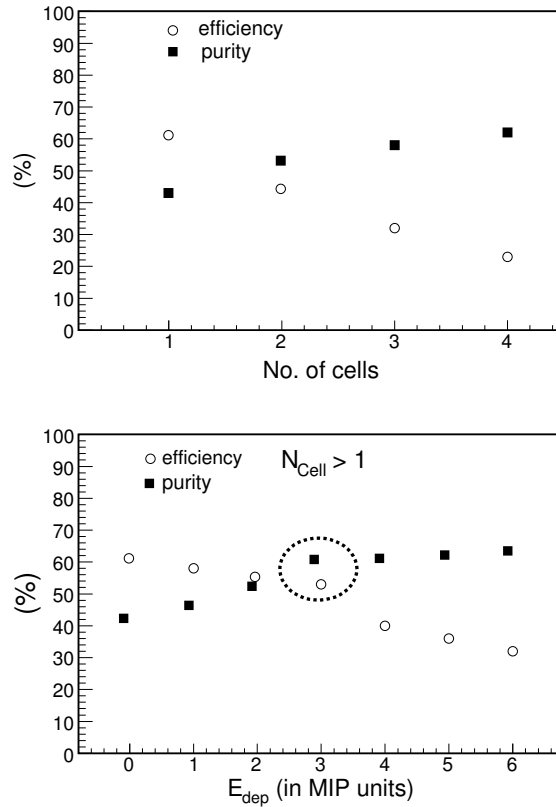


Figure 3.40: Photon counting efficiency (ϵ_γ) and purity of photon sample (f_p) for various E_{dep} and N_{cell} cuts on the detected clusters from simulations.

purity of the photon sample will be now redefined as: Photon counting efficiency (ϵ_γ) is ratio of the number of photons detected above certain threshold (energy deposited and/or number of cells) and above certain p_T cutoff to the number of photons incident from the vertex in the PMD coverage above the same p_T cutoff. Purity of photon sample (f_p) is ratio of the number of photons detected above certain threshold (energy deposited and/or number of cells) and above certain p_T cutoff to the number of clusters detected in the detector above the same p_T cutoff.

The studies on the optimization of the cuts on E_{dep} , N_{cell} and p_T is given in Fig. 3.40 and Tables 3.6, 3.7. The total number of photons incident on PMD with $p_T < 20$ MeV/ c is $\sim 7\%$ and for $p_T < 50$ MeV/ c is $\sim 22\%$. Table 3.8 shows the % of photons detected below $p_T < 20$ MeV/ c and 50 MeV/ c for various conditions.

Table 3.6: Photon counting efficiency (ϵ_γ) and purity of photon sample (f_p) calculated without p_T cutoff and with $p_T > 20$ MeV/ c on incident photons for PMD only case. The results are shown for various cutoffs on selection of photon clusters.

Condition	ϵ_γ (%) $p_T > 0$ MeV/ c	f_p (%) $p_T > 0$ MeV/ c	ϵ_γ (%) $p_T > 20$ MeV/ c	f_p (%) $p_T > 20$ MeV/ c
No condition	79.2	37.3	81.5	36.4
$N_{cell} > 1$	59.8	71.4	62.5	70.5
$E_{dep} > 1E_{dep}^{MIP}$	72.1	62.0	75.0	61.1
$E_{dep} > 2E_{dep}^{MIP}$	61.3	73.7	64.1	73.0
$E_{dep} > 2E_{dep}^{MIP}$ & $N_{cell} > 1$	59.0	73.0	61.5	72.5
$E_{dep} > 3E_{dep}^{MIP}$ & $N_{cell} > 1$	54.0	77.2	56.6	76.6

A p_T threshold of 20 MeV/ c is given for the subsequent calculations ϵ_γ and f_p . The incident photon p_T acceptance for PMD is $p_T > 20$ MeV/ c from simulation. From Fig. 3.40 we observe the optimized cutoff on E_{dep} and N_{cell} are $E_{dep} > 3 \times E_{dep}^{MIP}$ and $N_{cell} > 1$.

Table 3.7: Photon counting efficiency (ϵ_γ) and purity of photon sample (f_p) calculated with $p_T > 30 \text{ MeV}/c$ and with $p_T > 50 \text{ MeV}/c$ on incident photons for PMD only case. The results are shown for various cutoff on selection of photon clusters.

Condition	ϵ_γ (%) $p_T > 30 \text{ MeV}/c$	f_p (%) $p_T > 30 \text{ MeV}/c$	ϵ_γ (%) $p_T > 50 \text{ MeV}/c$	f_p (%) $p_T > 50 \text{ MeV}/c$
No cut	82.6	35.0	83.6	31.5
$N_{cell} > 1$	64.3	68.7	66.6	63.3
$E_{dep} > 1E_{dep}^{MIP}$	76.8	59.2	79.0	54.1
$E_{dep} > 2E_{dep}^{MIP}$	68.5	71.7	70.0	67.0
$E_{dep} > 2E_{dep}^{MIP}$ & $N_{cell} > 1$	63.4	71.1	66.0	65.7
$E_{dep} > 3E_{dep}^{MIP}$ & $N_{cell} > 1$	59.0	75.4	62.1	70.6

Table 3.8: The fraction of photons among those with $p_T < 20 \text{ MeV}/c$ and $p_T < 50 \text{ MeV}/c$ which give a signal on the preshower plane of PMD after passing through the $3X_0$ converter material. The results are shown for various cutoff on selection of photon clusters.

Condition	N_γ^{det} (%) $p_T < 20 \text{ MeV}/c$	N_γ^{det} (%) $p_T < 50 \text{ MeV}/c$
No condition	2.4	15.1
$N_{cell} > 1$	1.2	10.8
$E_{dep} > 1E_{dep}^{MIP}$	1.5	12.1
$E_{dep} > 2E_{dep}^{MIP}$	0.9	8.3
$E_{dep} > 2E_{dep}^{MIP}$ & $N_{cell} > 1$	1.1	10.2
$E_{dep} > 3E_{dep}^{MIP}$ & $N_{cell} > 1$	0.7	7.2

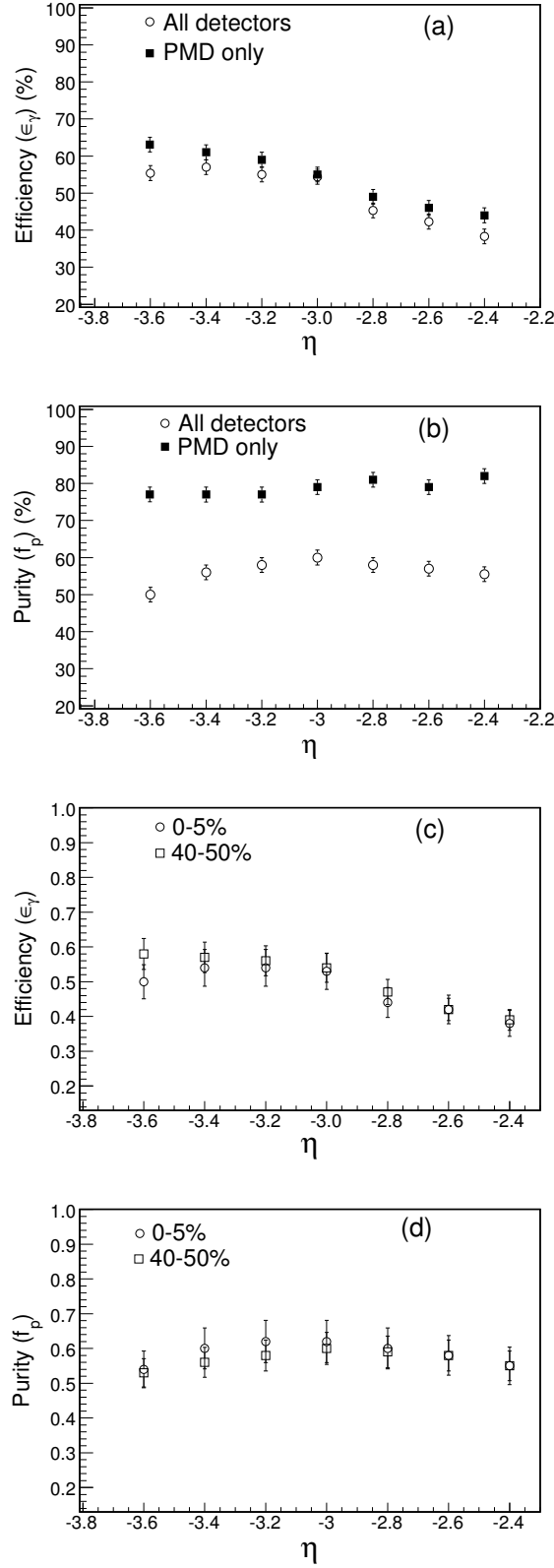


Figure 3.41: (a) ϵ_γ and (b) f_p as a function of η from simulations with PMD only and PMD with all detectors, (c) ϵ_γ and (d) f_p a function of η for 0–5% and 40–50% centrality. All the results are for cut of $E_{dep} > 3 \times E_{dep}^{MIP}$ and $N_{cell} > 1$ on the detected clusters from simulations.

The η dependence of (a) ϵ_γ and (b) f_p for the optimized cutoff for PMD only and PMD with all detector is shown in Fig. 3.41. Also shown in Fig. 3.41 is the centrality dependence of (c) ϵ_γ and (d) f_p with optimized cutoff for PMD with all detectors.

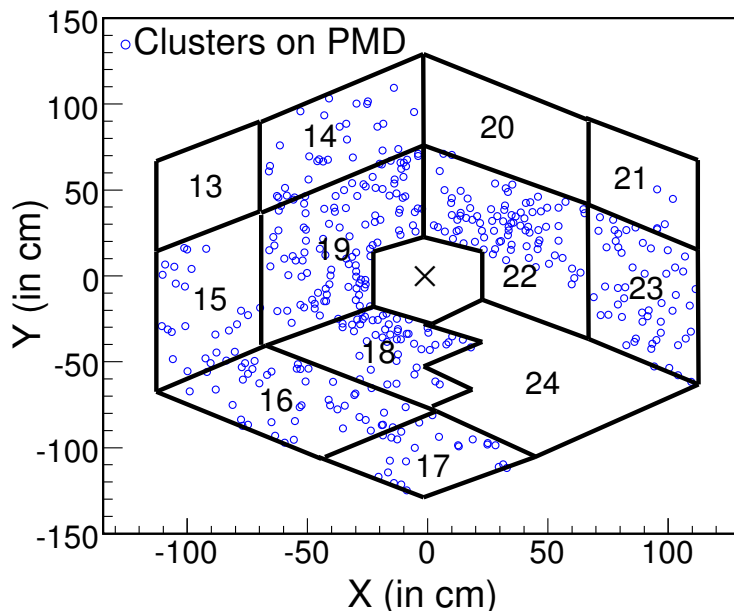


Figure 3.42: Cluster X and Y positions for the optimized cutoff of $E_{dep} > 3 \times E_{dep}^{MIP}$ and $N_{cell} > 1$ on the detected clusters from PMD data in Au+Au collisions at center of mass energy of 62.4 GeV

The cluster x and y positions for the optimized cutoff of $E_{dep} > 3 \times E_{dep}^{MIP}$ and $N_{cell} > 1$ on the detected clusters from PMD data in Au+Au collisions at $\sqrt{s_{NN}} = 62.4$ GeV is shown in Fig. 3.42.

3.7 Consistency checks

The photon pseudorapidity density distribution that we get from the data, has to be multiplied by the acceptance factor and the ratio of purity to efficiency to get the corrected photon pseudorapidity distribution. To have a consistency check on these factors we did the following:

3.7.1 Consistency check using simulated data

In simulation

- (a) We obtain the photon pseudorapidity distribution from HIJING within PMD coverage for two centrality class - 0–5% and 40–50%.
- (b) Obtain the photon-like pseudorapidity distribution within PMD coverage from HIJING events after passing them through GEANT simulation having all the STAR detectors. Then correct the photon-like pseudorapidity distributions with the acceptance, purity and efficiency factors obtained for corresponding centrality classes.

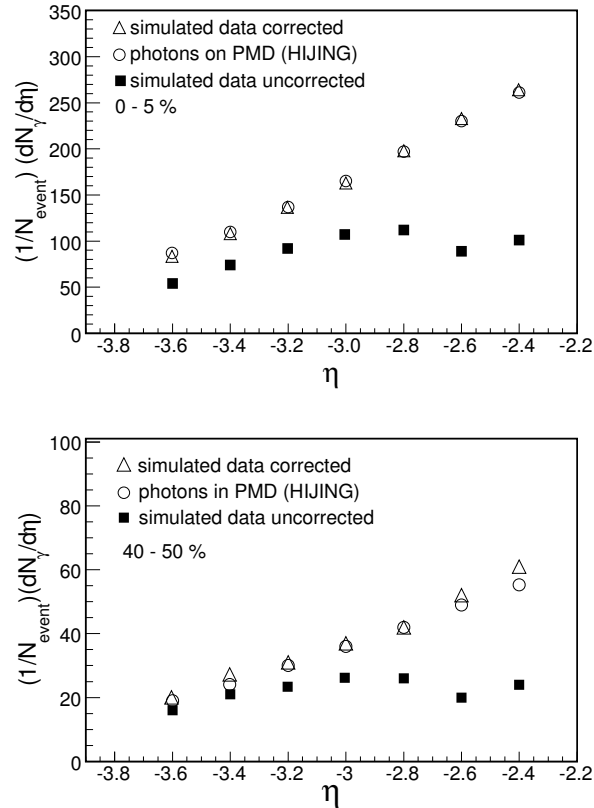


Figure 3.43: Photon-like and photon pseudorapidity distribution from simulated data for 0–5% (top) and 40–50% centrality from Au+Au collisions at $\sqrt{s_{NN}} = 62.4$ GeV. The photon pseudorapidity distributions are obtained from photon-like distributions after correction of acceptance, efficiency and purity.

The results from (a) and (b) should match. The results for different centrality class is demonstrated in Fig. 3.43.

3.7.2 Consistency check using real data

From the data of Au+Au collisions at $\sqrt{s_{NN}} = 62.4$ GeV

- (c) We obtain the photon-like pseudorapidity distribution for two centrality class - 0–5% and 40–50% with cluster cutoff of $E_{dep} > 3 \times E_{dep}^{MIP}$ and $N_{cell} > 1$. Then correct it for corresponding efficiency, purity and acceptance factors to get photon pseudorapidity distribution.
- (d) Obtain the photon-like pseudorapidity distribution for the above two centrality classes from Au+Au collision data with cluster cutoff of $E_{dep} > 2 \times E_{dep}^{MIP}$ and $N_{cell} > 1$. Correct it for corresponding efficiency, purity and acceptance factors to get photon pseudorapidity distribution.

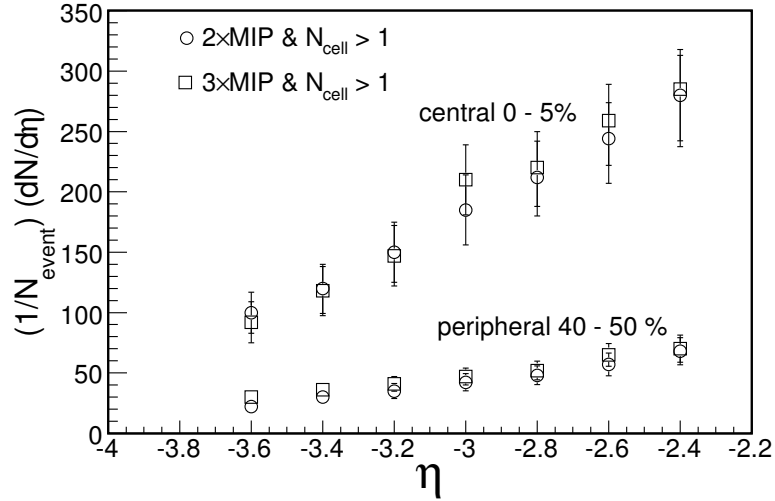


Figure 3.44: Photon pseudorapidity distribution for 0–5% (top) and 40–50% (bottom) from Au+Au collisions at $\sqrt{s_{NN}} = 62.4$ GeV. The distributions are obtained for two sets of cluster cutoff of ($E_{dep} > 3 \times E_{dep}^{MIP}$ and $N_{cell} > 1$) and ($E_{dep} > 2 \times E_{dep}^{MIP}$ and $N_{cell} > 1$).

The results from (c) and (d) should match. The results for different centrality class are demonstrated in Fig. 3.44.

3.7.3 Consistency check for the cell-to-cell gain variation

It may be mentioned that although the results agree for the choice of two different sets of cluster cutoffs, we have chosen the cut $E_{dep} > 3 \times E_{dep}^{MIP}$ and $N_{cell} > 1$ for the physics analysis keeping in mind high purity of photon sample with reasonable photon counting efficiency.

- (e) Obtain the photon pseudorapidity distribution from Au+Au collision data for all cells after following the full procedure of photon reconstruction as described in this chapter.
- (f) Obtain the photon pseudorapidity distribution for those cells which have similar gains (the cell-to-cell gain variation is limited to $\pm 0.5\sigma$), then follow the full procedure of photon reconstruction.

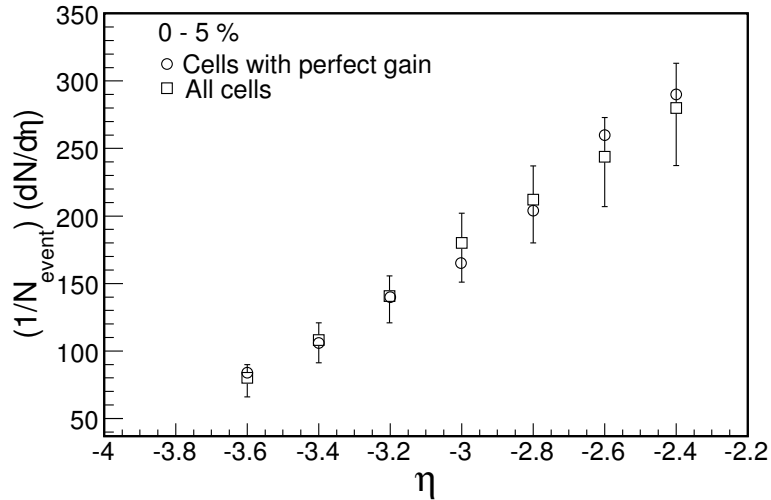


Figure 3.45: Photon pseudorapidity distribution from 0–5% central Au+Au collisions at $\sqrt{s_{NN}} = 62.4$ GeV for all working cells in PMD and those having a narrow cell-to-cell gain variation ($\pm 0.5\sigma$).

The results from (e) and (f) should match and thereby confirm the proper gain calibration of cells of PMD and the large variation of cell-to-cell gain is properly treated in the analysis. The results for central collisions are shown in Fig. 3.45. The above consistency checks show that the correction factors for acceptance, efficiency and purity are good.

Bibliography

- [1] X-N. Wang and M. Gyulassy, Phys. Rev. D **44**, (1991) 3501.
- [2] V. Fine and P. Nevski, in *Proceedings of CHEP-2000*, Padova, Italy.
- [3] M. M. Aggarwal *et al.*, Nucl. Instr. Meth. A **499**, (2003) 751; M. M. Aggarwal *et al.*, Nucl. Instr. Meth. A **488**, (2002) 131.
- [4] F. S. Bieser *et al.*, Nucl. Instrum. Meth. A **499**, (2003) 766.
- [5] S. C. Phatak, Clustering Algorithm for PMD,
<http://www.iopb.res.in/~phatak/cluster/>.
- [6] K. H. Ackermann *et al.*, Nucl. Instr. Meth. A **499**, (2003) 624.
- [7] STAR Collaboration, J. Adams *et al.*, nucl-ex/0311017.
- [8] Particle Data Group, C. Caso *et al.*, Eur. J. Phys. C **3**, (1998) 1.
- [9] L. Landau, J. Phys. (USSR) **8**, (1944) 201. W. R. Leo, Techniques for Nuclear and Particle Physics Experiments, Narosa Publishing house
- [10] STAR Collaboration, J. Adams *et al.*, Phys. Rev. Lett. **95**, (2005) 062301.
- [11] K. H. Ackermann *et al.*, Nucl. Instr. Meth. A **499**, (2003) 713.

Chapter 4

CHARGED PARTICLE RECONSTRUCTION

The need for reconstruction is already discussed while dealing with photon reconstruction. Here we discuss how we reconstruct the charged particles in FTPCs.

4.1 Reconstruction and simulation of the experimental data

The first step in the reconstruction of charged particle tracks is to calculate the track points (cluster finding) from the charge distribution measured by the readout electronics. In the second step (track finding), these track points are grouped to tracks. Using the magnetic field map, upto 10 position measurements (pad rows in FTPC) per track are then used to get the momentum. The flowchart of the reconstruction chain for FTPC data and simulation is given in Fig. 4.1. In the subsections we will discuss in detail all the steps followed in doing the track reconstruction. The reconstruction of the track points is done by the FTPC cluster finding program [1]. It is optimized to deal with high track densities while minimizing the use of the computing time. The program reads in the electronic signal data from the data acquisition system, looks for areas of nonzero charge(cluster), deconvolutes clusters and fits the point coordinates. The transformation from the pad position and the drift time into Cartesian coordinates includes the correction of the distortions introduced by the magnetic field.

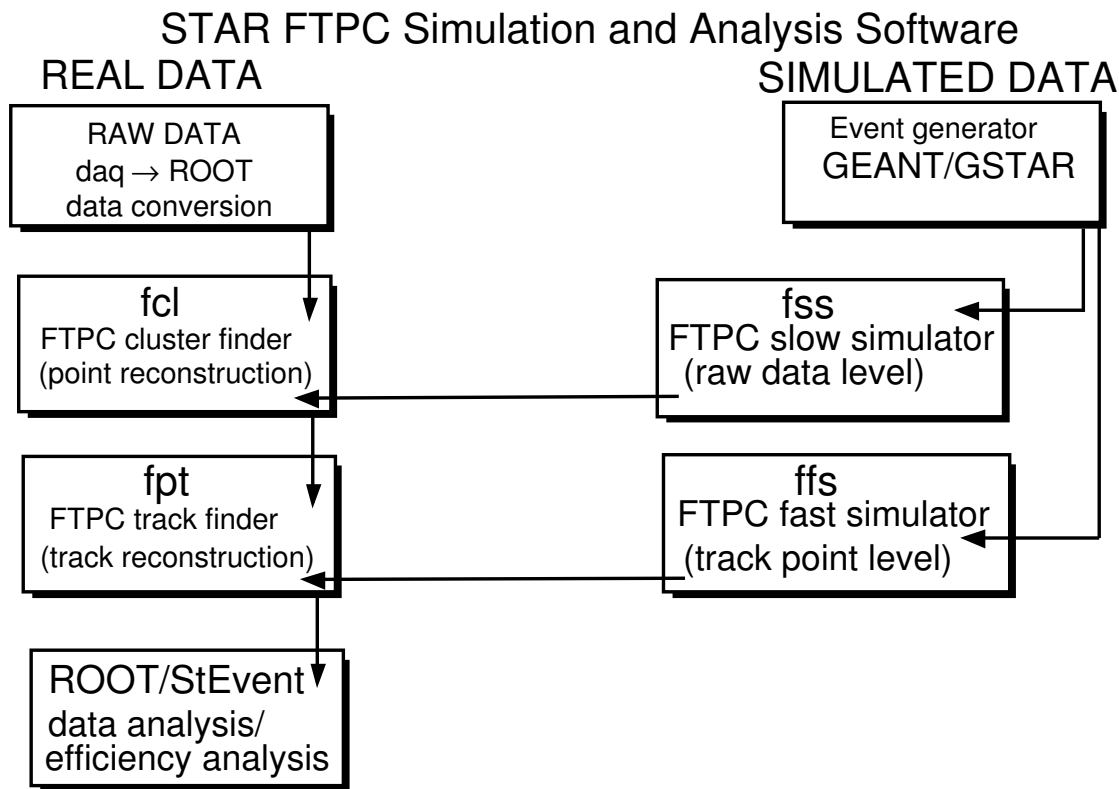


Figure 4.1: Overview of the STAR FTPC simulation and data reconstruction analysis chain.

4.1.1 Reconstruction of track points (Cluster finding)

For one trigger taken in both the FTPCs, the charge deposited on each of the 19200 pads is sampled 256 times over a period of 51.2 microseconds [2], generating a total of almost five million digitized amplitude value to be stored. It was found that the charge distribution in one padrow of the FTPC in a central collision, after diffusion and smearing in the gas amplification, fills only about 3% of the sensitive volume in the outer parts and upto 30% in the inner parts of the chamber. Only values exceeding a certain threshold in more than one consecutive time samples are stored. The optimization of this threshold is done keeping in mind that this value

is well above the average level of electronic noise, but for good position resolution, the threshold value should be low enough to allow a signal on at least three adjacent pads for every track over every padrow. The typical charge distribution from data in FTPC west (left) and east (right) are shown in Fig. 4.2.

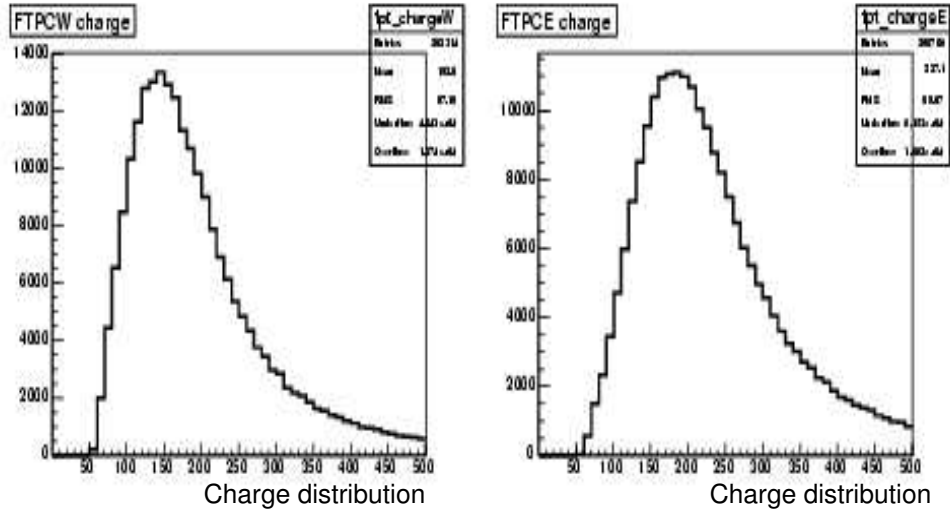


Figure 4.2: The typical charge distribution from data in FTPC east and west.

Each track crossing a padrow creates a signal in consecutive time samples on several adjacent pads. In pad-time plane, corresponding to a cut perpendicular to the beam line, these signals form a coherent area of charge, called a cluster. A cluster can include charge from more than one track if their signals overlap, which is common in the region of high track densities at low radii in the FTPC. The first step in the point reconstruction is to identify these clusters of charge in the raw data distribution. As the cluster finder iterates over all the pads in one sector, only the sequences on the current pad and on the last pad are kept in the memory and checked for adjacent sequences. Adjacent sequences are sorted as a cluster under construction (CUC) in a special memory block reserved for quick access. If the sequence on the last pad already belongs to a CUC, the sequence on the current pad is added, otherwise a new CUC is created. Each CUC that has not had any additions on the current pad or includes the last pad in the sector is considered a finished cluster and is passed on to the fit routine.

4.1.2 Cluster deconvolution and fitting of track points

Ideally, each track should produce one cluster in each padrow it crosses. In case of high track densities, a cluster can contain charge deposited by more than one track (merged clusters). The aim of the cluster finding algorithm is to identify these merged clusters and to reconstruct the single track points contributing to these clusters [3].

The identification of the merged cluster can be done in two ways:

- (i) Using information from partially constructed tracks, or
- (ii) By studying the charge distribution within the clusters.

The STAR FTPC uses the following cluster finder approach: Clusters are only treated as merged if their charge distribution has more than one local maximum. In this case, the single maxima is used as the starting point for deconvolution of the single charge distribution cluster. If a cluster has only one maximum, it is processed to one track point. The charge in the cluster is summed up, and the centroid and width of the charge distribution are calculated,. This is done independently in padrow (i.e. x and y position) and time direction (z coordinate) by either calculating the weighted mean and the mean squared deviation of the charge distribution or by assuming a Gaussian profile and fitting it to the maximum and its two neighboring values. If a cluster has more than one local maximum, then each maxima is deconvoluted into single track point. The STAR FTPC cluster finder uses a method, taking the non-iterative local Gaussian fits only as a first guess and then iteratively subtracting the influence of one track point on the other before recalculating the fits.

4.1.3 Calibration of electronics

The readout electronics records a charge amplitude, sampled for a series of time-bins. The time is defined by a common clock for all channels. So a constant additive calibration term for each channel is needed for the timing, to compensate for potentially different signal run times in the connections to the single channels. The amplitude calibration can in principle be done at any step in the raw data chain without losing precision. The only limitation is that the time offsets cannot be applied to the raw data before processing because the shifts introduced by the calibration are smaller than one time-bin. The STAR FTPC cluster finder incorporates both the calibrations in the cluster fitting process [4]. All charge values

are calibrated during the peak search process and the time values are calibrated at the moment when they are used in the position fit. After this calibration of time and amplitude values the corrections for distortion due to magnetic field and the transformation of pad/time to Cartesian coordinates is done. Due to the non linearity in the drift velocity because of radial electric field, the drift is also influenced by the magnetic field, which is almost perpendicular to the electric field lines, which are also not constant over the volume of the chamber. Neither of these effects are small enough to be treated as correction and hence coordinate transformation cannot be separated from distortion corrections. The cluster finder uses the drift parameter map which is obtained from MAGBOLTZ [5] and pressure measurements from the FTPC gas monitoring systems to convert the drift time information to a point radius and angular displacement during the electron drift for each padrow.

4.1.4 Gain Tables

The relative gains of different channels in the FTPCs are measured and recorded in the gain tables. The gain tables are prepared by the following procedure described below:

- (a) To prepare gain tables, first step is to analyze the pulsar runs. In these runs, the Frish grid of the detector is pulsed with a rectangular signal pulse. The rising edge of the signal induces charge in the readout pads. The response of the electronics is recorded.
- (b) By comparing the pulse height of the induced pulse in one channel with the mean of all the channels, the relative gain is determined.

The dead channels do not respond to the input signal, so they can also be identified by this pulsar run. Typically, the pulse induced by the pulsar is a short duration, high amplitude pulse corresponding to several minimum ionizing particles. It was observed that often the noise introduced by a faulty chip is not visible in these pulsar runs. To identify channels that have a high noise, which should be excluded in the data analysis, real data is used. By summing up the entries over all time bins for each channel and obtaining the average over large number of events, the noisy channels show up via significantly higher counts. This method is especially reliable in low multiplicity events. The threshold for noisy channels changes from run to run, since the average count rate depends on the

beam parameters, so it has to be adjusted for each run that is used to create the gain table. Channels above the threshold are deactivated in the gain table, and thus will be ignored while reconstructing the data.

4.2 Track reconstruction and particle momenta

The second step in the analysis of FTPC data is the reconstruction of particle tracks and their momenta. The reconstruction of the tracks (tracking) is defined as only to identify the points belonging to one track and to group them together in a data structure. The reconstruction of momenta (fitting) then uses the positions of these points and the magnetic field to determine the momentum a particle must have had to pass these points. The typical XY display of the first hit on track in FTPC east and west are shown in Fig. 4.3 (a) and (b) respectively. The void regions implies dead regions, sector boundaries and noisy channels (for which gain is set to zero). Also shown in the Fig. 4.3 (c) and (d) are the typical track lengths in FTPCs as a function of η .

To understand the track qualities and other performance parameters of FTPC, it is essential to carry out simulations and use techniques like embedding. These are discussed in the next sections.

4.3 Procedure to obtain performance parameters of FTPC

For understanding and estimating various correction factors such as track reconstruction efficiency, momentum resolution, contamination due to upstream material, error in charge determination, it is important to study the detector response in detail. One way to do this is to study the detector response using HIJING [6] generated events passed through STAR GEANT package [7] which has all the detectors geometries and material incorporated in it. The limitations of using the above mentioned technique are its inability to replicate the actual conditions during the time of experiment such as the electronics readout responses, applied high voltage conditions, background due to upstream material, temperature fluctuations in the active gas medium. To overcome this issue STAR experiment uses a technique to study the detector response which is termed as embedding. In this process the particles are generated using simulation and are embedded in the real event which

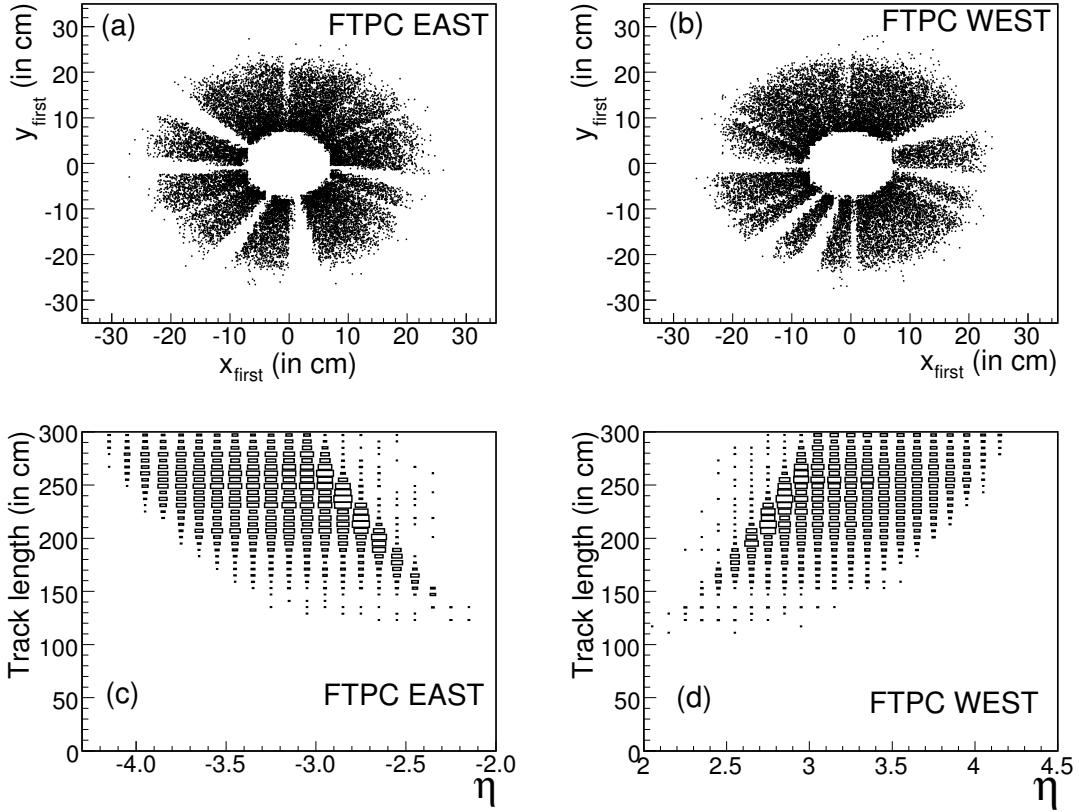


Figure 4.3: (a) X-Y display of the first hit on track in FTPC east, (b) X-Y display of the first hit on track in FTPC west, (c) track length in FTPC east as a function of η , (d) track length in FTPC west as a function of η .

helps in preserving real experimental conditions. The loss of electronics is expected to have significant impact on the detector performance, so it is mandatory to include this information in the embedding simulation. Thus simulations also use the same gain tables that are used for reconstruction of the real data. The gain table contains the information of the relative gain of each channel, and allows to deactivate dead and noisy channels in the analysis. Depending on the nature of the effects under investigation, different particles and event types are embedded. For 62.4 GeV Au+Au collision data, for calculating the efficiency and momentum resolution we have used charged pions tracks (as pions form the bulk of the produced charged particles) for embedding. These Monte-Carlo charged pion tracks are embedded in the minimum bias events. To study the influences from beam background and contaminations, HIJING events are embedded into zero bias data. This zero bias data is taken with the random trigger while beams are stored in

RHIC and produce collisions in the interaction region. Thus there is no correlation between the trigger time and the time an interaction took place. Zero bias events are a good presentation of background not originating from the triggered events.

4.3.1 The embedding procedure

The production of embedding files is carried out at the PDSF computing facility in Oakland, California. Here we have described the basic steps involved in the embedding process, highlighting the FTPC specific tasks [8]. Fig. 4.4 presents the flow chart for the simulation, including pure simulation and embedding procedure, pictorially. Before going to describe the embedding procedure, let us discuss about

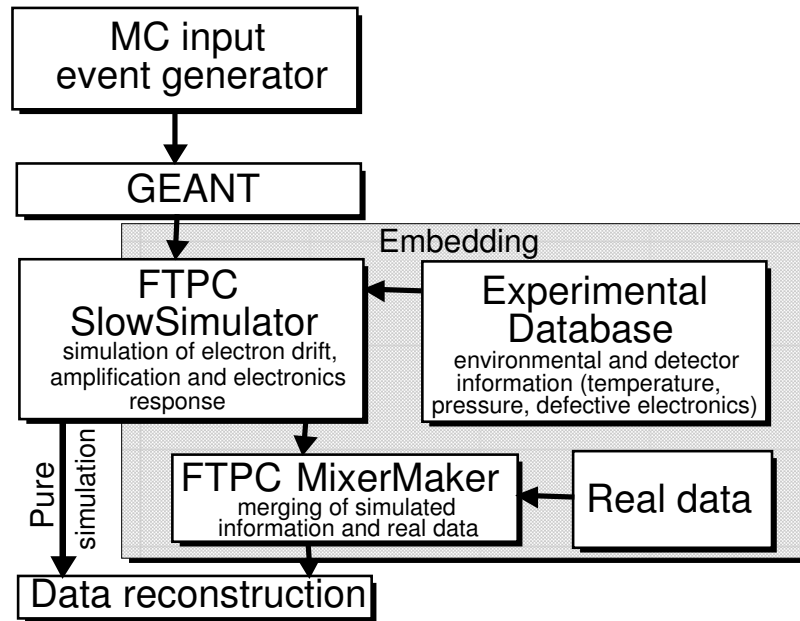


Figure 4.4: Flow chart of the FTPC simulation chain. For embedding simulations, the environmental parameters and possible defective electronics channels in the detector have to be taken into account.

the pure simulations (GEANT) and their usage. Pure simulations are the simulated data where there is no merging of the simulated information with the real data. They were used to study the detector performance in its design phase, and are still used to study physics performance with the simulated events created by event generators such as HIJING.

The first step in the embedding process is to acquire the full reconstructed data which will be used as one of the inputs for embedding. The other thing is to obtain all the necessary parameters for creating the Monte-Carlo particles which will be embedded into the real event. It is very important to know the position of the event vertex and event multiplicity before one tries to embed the Monte-Carlo particles in real events. In second step, the reconstructed primary vertex from the real event is used for simulating the Monte-Carlo particles which will be embedded. One of the important feature is to preserve the real event characteristics (such as particle multiplicity, vertex information) while embedding the simulated particles. Keeping this in mind, only 5% of the total tracks in a real event is chosen as the fraction of simulated tracks which will be embedded in that real event. The Monte-Carlo simulated particles which were used for embedding were chosen to be in the p_T range from 0.0 to 2.0 GeV/ c .

In the case of zero bias events usually no primary vertex exists. The complete HIJING events are embedded in these zero bias events. The event vertex is assigned by the HIJING event vertex. The embedded simulated particle multiplicity is given by the event generator (in our case HIJING). The simulated particles are then passed through GEANT detector simulation package to obtain the charge deposited in the detector.

To produce the embedded data output, the real event and the simulated particles, which have the information of the charge deposited in the detector given by GEANT, have to be handled simultaneously. This ensures that the data base information for the detector such as correct gain table, the gas temperates, gas pressure for the real event are available for the simulation. Next step in the process is to merge the simulated charge with the real data information for each pad, time-bin by time-bin. After merging, the zero suppression parameters used in the readout boards are applied. As a final step, the zero suppressed merged data is passed through standard reconstruction chain. Here, the primary vertex is fixed to the position obtained in the previous reconstruction pass to avoid possible shifts in vertex position due to the added simulated particles. In addition to the reconstructed information, data from the Monte-Carlo input is also written out which allows the matching of the simulated and reconstructed embedded particles.

4.3.2 Checks with the embedded data

To ensure that the embedding of the simulated tracks in the real event has been done properly, it is necessary to study the spatial resolution of the incident Monte-Carlo track after the full reconstruction. In Fig. 4.5 (a) and (b) show the difference in the radial (r) and azimuthal (ϕ) of the reconstructed embedded track and the incident Monte-Carlo track. This study was done using primary tracks only. The resolution is obtained by the RMS of the distributions. The spatial resolution in r is ~ 0.0027 cm and that in ϕ is ~ 0.00068 radians. Fig. 4.5 (c) and (d) show the difference in the x and y positions of the reconstructed and the incident Monte-Carlo hit.

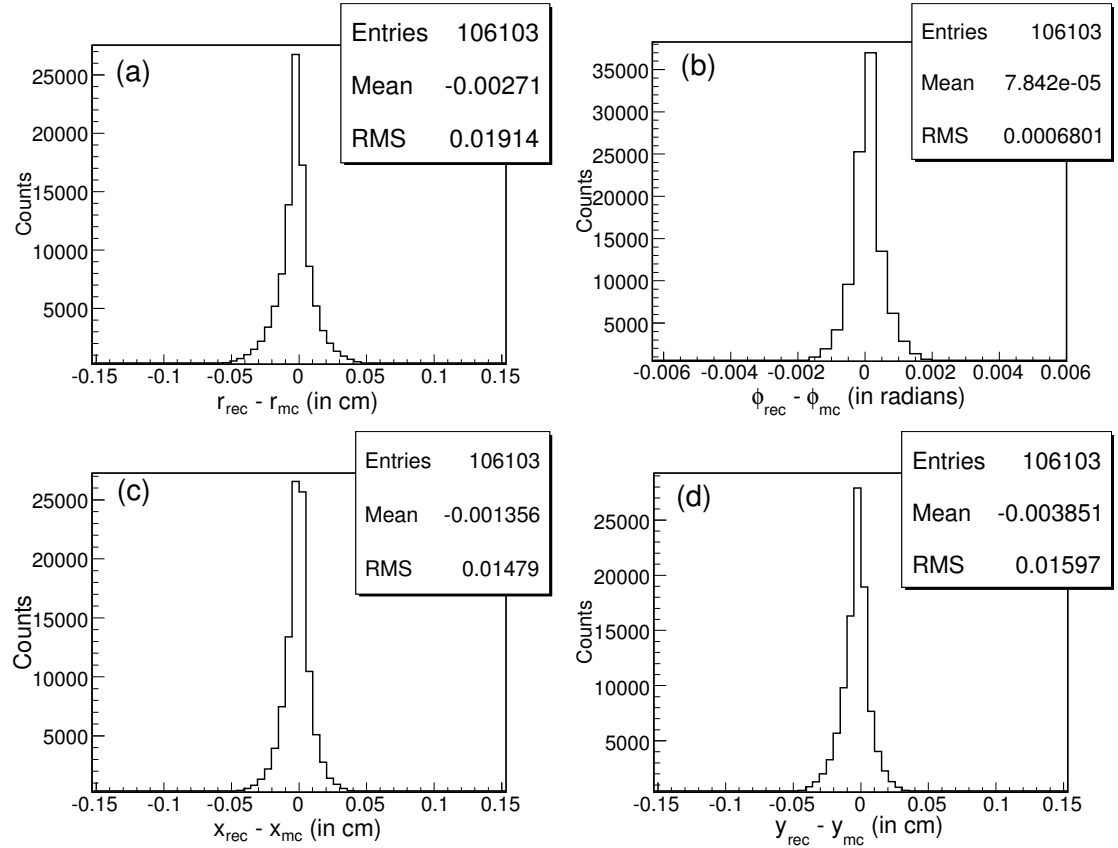


Figure 4.5: (a) and (b) Spatial resolution of the reconstructed and the incident Monte-Carlo track in r and ϕ . (c) and (d) spatial resolution of the reconstructed and the incident Monte-Carlo hit in x and y .

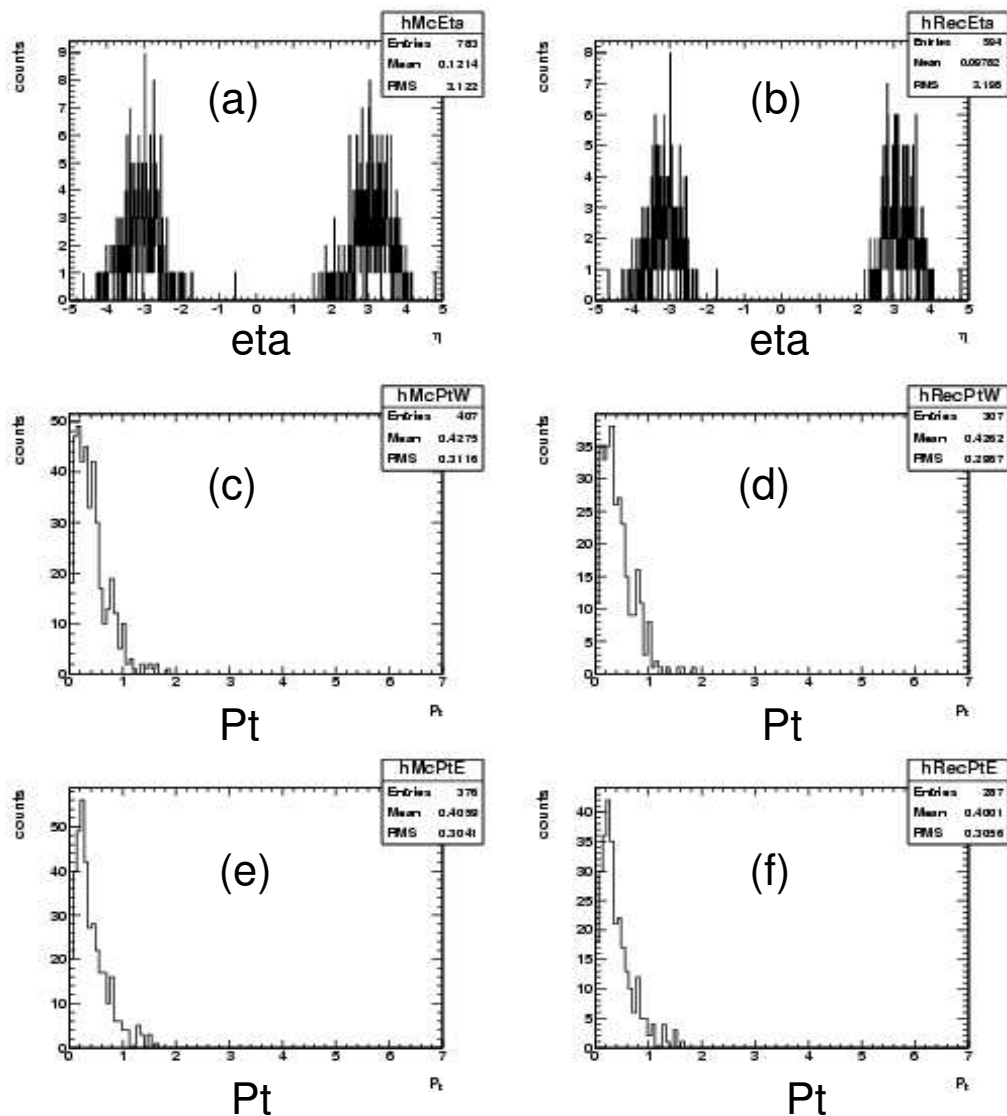


Figure 4.6: (a) η distribution of the Monte-Carlo tracks for FTPC west and east, (b) η distribution of the reconstructed tracks for FTPC west and east, (c) and (d) p_T distribution of the Monte-Carlo and reconstructed tracks for FTPC west, (e) and (f) p_T distribution of the Monte-Carlo and reconstructed tracks for FTPC east.

Another important point is to check the η and p_T distribution of the Monte-Carlo incident particles and the reconstructed tracks after embedding. In Fig. 4.6, (a) and (b) show the distributions of particles in η for both the Monte-Carlo and the reconstructed tracks in FTPCs. Fig. 4.6 (c)-(f) show the p_T distribution of the Monte-Carlo and the reconstructed tracks in FTPCs.

4.4 Tracking efficiency and momentum resolution

4.4.1 Matching of reconstruction and simulation

To study the efficiency and the momentum resolution of the detectors using simulations, a matching of the simulated and the reconstructed tracks is necessary. This association between simulated and the reconstructed tracks is done in the following steps:

- (i) For each reconstructed hit, all the Monte-Carlo hits within the detector acceptance are associated with that hit.
- (ii) For all hits on the reconstructed track, the simulated hits associated to its parent track are analyzed.
- (iii) If a Monte-Carlo simulated track has more than one detector specific number of hits in common with the reconstructed track, then it is assigned as an associated track of that simulated track.

One more important point to note is that a reconstructed track can have more than one associated simulated track. Likewise, one simulated track can be associated to more than one reconstructed track. Such additional tracks are called as split tracks [9]. The condition of having at least 5 hits for each track in the FTPC ensures a small contribution of split tracks. The split tracks contribution and background contamination are primarily from γ conversion electrons and positrons. These are also significantly reduced when we include those tracks which have transverse momentum in the range $0.1 < p_T < 3 \text{ GeV}/c$ in the analysis. The maximum fraction of split tracks was estimated from simulations to be ~ 0.015 (1.5%). The relative amount of split tracks decreases as we go from central to peripheral collisions. The fraction of split tracks increases to ~ 0.09 (9%) if lower p_T cut of $0.1 \text{ GeV}/c$ is not applied. Fig. 4.7 shows the fraction of split tracks

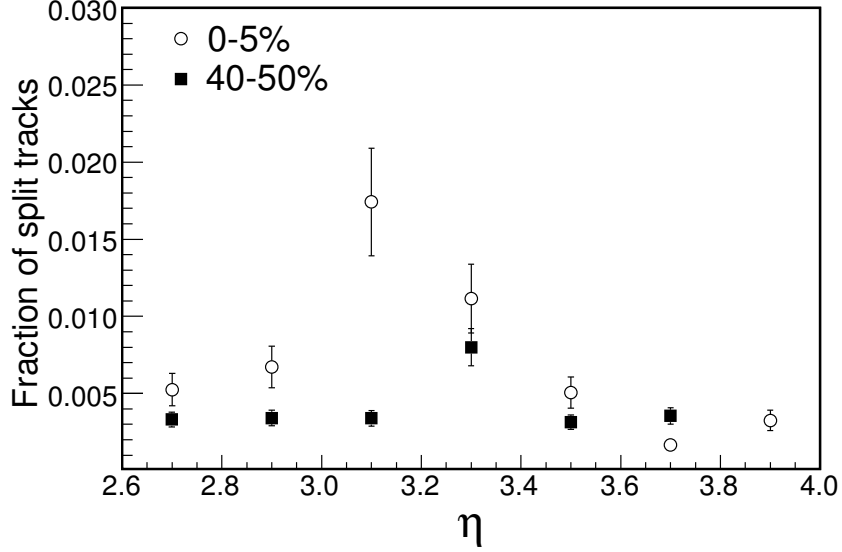


Figure 4.7: Fraction of split tracks as a function of η for FTTPC west for 0–5% and 40–50% collision centrality in Au+Au collisions at $\sqrt{s_{NN}} = 62.4$ GeV.

for 0–5% and 40–50% collision centrality classes for above conditions. The conditions applied are, number of FTTPC hits on track > 5 and track $p_T > 100$ MeV/ c .

Fig. 4.8 shows the fraction of e^+ and e^- contamination due to the photon conversion from the upstream material as a function of η . On an average this fraction is ~ 0.05 (5%) for both 0–5% and 40–50% collision centrality classes. Table 4.1 summarizes the parameters used for the association of FTTPC Monte-Carlo hit(track) with the reconstructed hit(track) [8].

Table 4.1: Association parameters for simulated FTTPC information.

Radial distance (mc hit - reconstructed hit)	≤ 3 mm
Azimuthal (ϕ) distance (mc hit - reconstructed hit)	$\leq 2^\circ$
Number of common hits of (mc and reconstructed track)	≥ 3

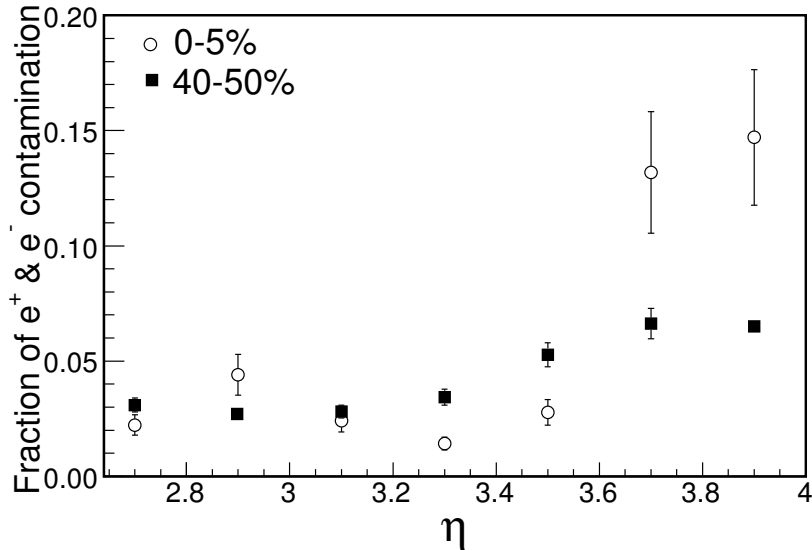


Figure 4.8: Fraction of e^+ and e^- contamination from photon conversion from the upstream material in FTPC west coverage as a function of η for 0–5% and 40–50% collision centrality in Au+Au collisions at $\sqrt{s_{NN}} = 62.4$ GeV.

The cuts mentioned above resolve most of the ambiguities due to the multiple associations of the simulated tracks. For the study of hits, only the best association, defined as the closest Monte-Carlo hit, is used. Likewise, for the tracks the association with the highest number of common hits is chosen. It has been taken into account while associating the Monte-Carlo tracks with the reconstructed tracks to avoid the selection of the same track more than once.

4.4.2 Tracking efficiency and purity

The tracking efficiency of the detectors is determined by the ratio of the number of the reconstructed tracks within a certain kinematic (η, ϕ) range to the total number of Monte-Carlo tracks which were simulated in the same kinematic range. Fig 4.9 shows the efficiency for the FTPC west obtained from embedding of the positively charged pions with a flat p_T spectrum ($0 < p_T < 2.0$ GeV/ c) into the Au+Au collisions at 62.4 GeV [9]. Only those events which satisfied the vertex cut of ± 30 cm from the nominal interaction points were used to ensure a reasonable

uniformity of the detector response.

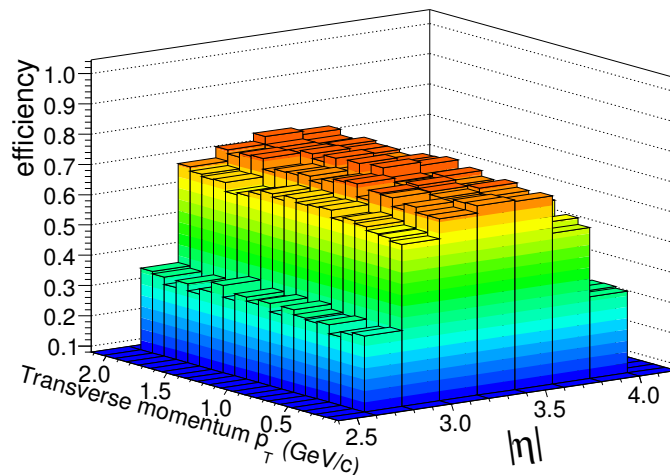


Figure 4.9: Efficiency obtained from the embedding of π^+ into Au+Au minimum bias events at $\sqrt{s_{NN}} = 62.4$ GeV in west FTPC as a function of η and p_T .

In the region $2.8 < \eta < 3.8$ the detectors reach a efficiency more than 60% for Au+Au minimum bias events at $\sqrt{s_{NN}} = 62.4$ GeV. This includes the contribution from the dead areas at the sector boundaries. Above $p_T > 0.2$ GeV/c the efficiency is constant as a function of transverse momentum. In general, the detector efficiency depends on the particle multiplicity in an event. In higher multiplicity environments, the hit and track reconstruction becomes increasingly difficult, leading to a decrease in the tracking efficiency. Fig 4.10 shows the efficiency of the FTPC west as a function of η for 0–5% and 40–50% collision centrality classes.

There may be contribution to the detected charged tracks from charged particles from photon-conversions (discussed above) in the material in front of FTPC or from split tracks (also discussed above). These contributions are drastically reduced by choosing proper cuts on number of FTPC hits on track and on the primary p_T of the tracks. The purity of the charged particle sample is estimated to be above 90% for a low p_T cut of > 100 MeV/c and requiring minimum number of FTPC hits on track to be > 4 . The purity of the charged hadron sample (f_{ch}) in the FTPC for central and peripheral collisions is shown in Fig. 4.11.

The systematic errors on the charged particle multiplicity (N_{ch} discussed in chapter 5) are due to uncertainties in estimates of ϵ_{ch} and f_{ch} . The uncertainty in

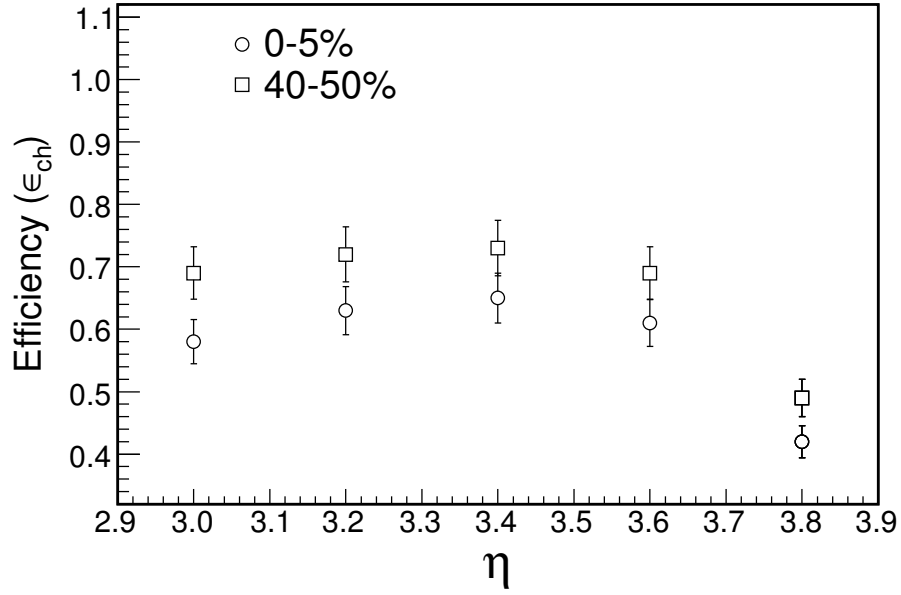


Figure 4.10: Charged particle reconstruction efficiency (ϵ_{ch}) in the FTPC as a function of pseudorapidity (η) for charged tracks with $0.1 \text{ GeV}/c < p_{\text{T}} < 3 \text{ GeV}/c$, for two different centralities.

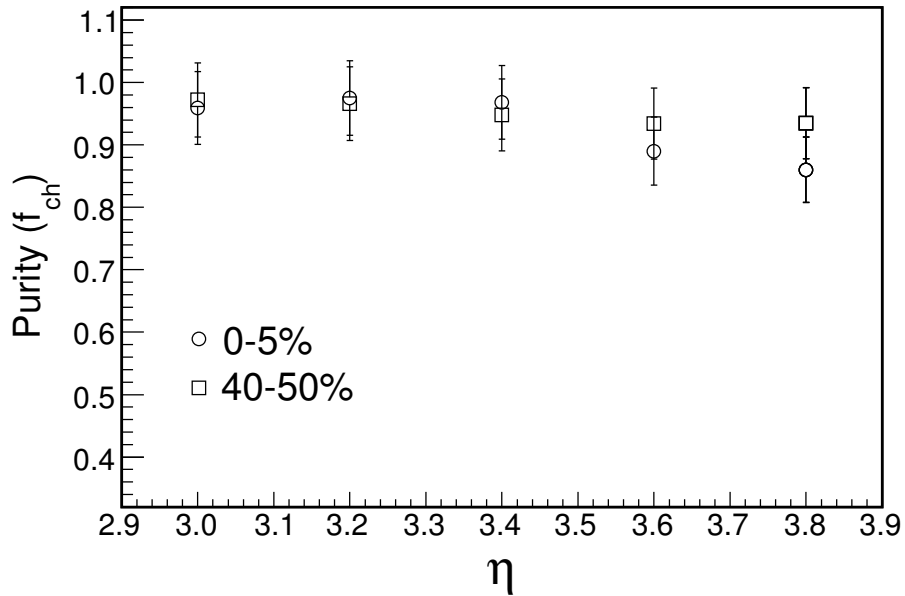


Figure 4.11: Purity of charged hadron sample (f_{ch}) in the FTPC as a function of pseudorapidity (η) for charged tracks with $0.1 \text{ GeV}/c < p_{\text{T}} < 3 \text{ GeV}/c$, for two different centralities.

the estimates are obtained through simulations by varying the track quality cuts. The value of the maximal distance of closest approach of a track to the primary vertex is varied by 0.5 *cm* leading to a maximum error on N_{ch} of $\sim 6\%$. The minimum number of hits required to form a track was varied from 5 to 4. This led to an error on N_{ch} of $\sim 1\%$. The uncertainty in the correction factor to obtain the N_{ch} yield for $p_{\text{T}} < 0.1 \text{ GeV}/c$ is $\sim 8\%$. This also contributes to the total systematic errors. The total systematic error in N_{ch} is $\sim 10\%$ for all the centrality classes studied. The systematic error for the region $\eta > 3.6$ is estimated to be about 15%, due to larger uncertainty in the reconstruction efficiency. This arises primarily due to uncertainty in realistic reproduction of electronic loss, at the extreme ends of the detector acceptance. This is estimated by studying the azimuthal dependence of charged particle density in a given η window.

4.4.3 Momentum resolution and charge determination error

The momentum resolution (Δp_{T}) is defined as the difference between the reconstructed track transverse momentum ($p_{\text{T,rec}}$) and the simulation track transverse momentum ($p_{\text{T,mc}}$) divided by the simulated track transverse momentum. This distribution as a function of p_{T} and η , is fit to a Gaussian function and the width (σ) from the fit is taken as the momentum resolution factor.

$$\Delta p_{\text{T}} = \sigma \left(\frac{p_{\text{T,rec}} - p_{\text{T,mc}}}{p_{\text{T,mc}}} \right). \quad (4.1)$$

Fig. 4.12 shows the momentum resolution obtained from the embedding of π^+ as a function of (a) pseudorapidity and (b) transverse momentum of the primary tracks, where the event vertex is included in the fit. Tracks from FTPC west within $2.8 < \eta < 3.9$ and $p_{\text{T}} < 2 \text{ GeV}/c$ are used. The resolution deteriorates with increasing η and p_{T} . Since these one dimensional plots are the average over the other coordinate (either p_{T} or η), they show mean resolution. At low η and low p_{T} values the momentum resolution $\sim 14\%$ is achieved. At high transverse momentum and high pseudorapidity where the poor determination of charge sign of the particle, starts to contribute in momentum resolution.

For doing studies separately for positive and negative charged particles it is essential to know the accuracy in charge determination of the tracks [9]. The charge determination error is defined as the ratio of the total number of embedded charged tracks whose charge has been reconstructed incorrectly, to the total

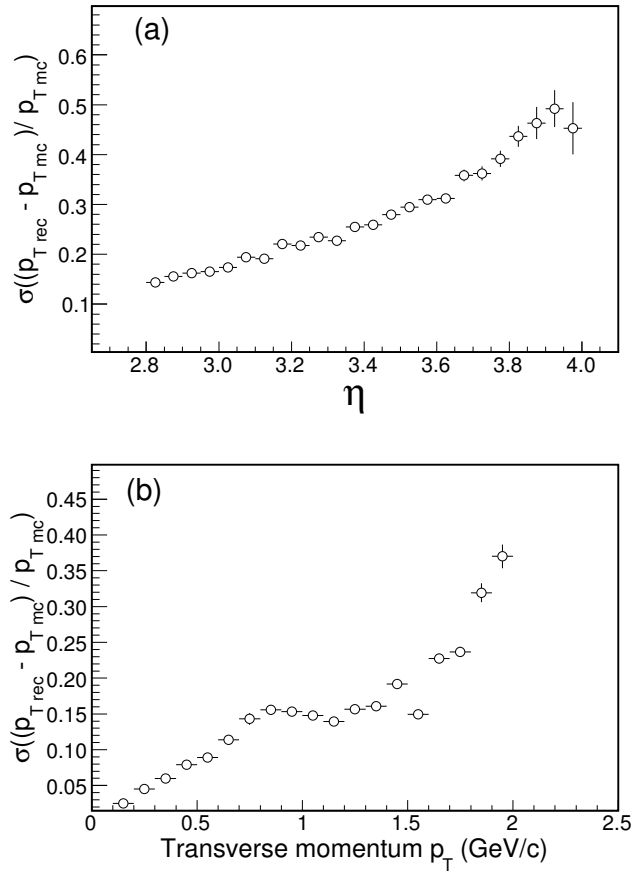


Figure 4.12: Resolution of transverse momentum as a function of (a) η and (b) p_T from embedding of π^+ with a flat p_T spectrum into Au+Au minimum bias collisions at 62.4 GeV in FTPC west.

number of charged tracks embedded. The error in charge determination was found to increase from 2% at $\eta = 2.9$ to 15% at $\eta = 3.9$. We have studied its η , p_T and collision centrality dependence. The error in determination of charge strongly depends on all the above three quantities. At a given η and magnetic field, the higher the momentum, less are the bending of the tracks, this leads to poor charge determination of the particle. As we go higher in η , for the same p_T of the track, the momentum of the tracks increases due to $\sin\theta$ factor, hence the charge determination of the particle is poor. Fig. 4.13 (a) shows the fraction of charge determination error as a function of number of participating nucleons, which is essentially measure of collision centrality. The charge determination error (in %) as a function of η and p_T are shown separately in Fig. 4.13(b) and Fig. 4.13(c)

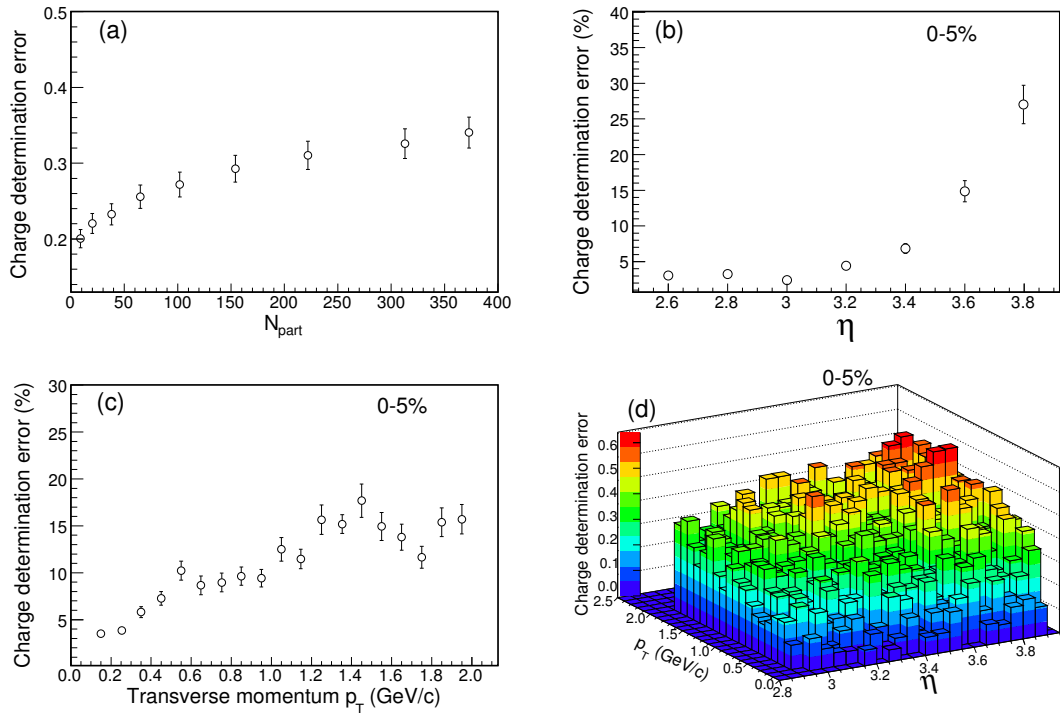


Figure 4.13: (a) Fraction of charge determination error as a function of number of participating nucleons (N_{part}) in the collision, (b) Charge determination error (%) as a function of η for 0–5% central collisions, (c) Charge determination error (%) as a function of p_T for 0–5% central collisions, (d) η and p_T dependence of charge determination error for 0–5% central Au+Au collisions at $\sqrt{s_{NN}} = 62.4$ GeV.

respectively for 0–5% central Au+Au collisions at $\sqrt{s_{NN}} = 62.4$ GeV. Fig. 4.13 (d) shows both the η and p_T dependence of charge determination error for 0–5% central Au+Au collisions at $\sqrt{s_{NN}} = 62.4$ GeV. Fig. 4.14 shows the p_T spectra of inclusive charged hadrons from FTPC for various collision centralities. The distributions are fit to power law function of the form $\sim A/(1 + p_T/p_0)^n$, where A , p_0 and n are the fit parameters. To get the yield for the low p_T region, the fit in the range $0.1 \text{ GeV}/c < p_T < 1 \text{ GeV}/c$ is extrapolated to $p_T = 0 \text{ GeV}/c$. In another procedure we calculate the yield of charged particles for $p_T < 0.1 \text{ GeV}/c$ by using the ratio of the yield in this p_T range to total yields from HIJING simulations. Both these procedures resulted in similar correction factors of the order of 15% in the region $2.9 \leq \eta \leq 3.9$ [9].

4.4.4 Limitations

Although simulations with full implementation of the faulty electronics channels reproduces reasonably good tracking efficiency, still there are some limitations in the accuracy that affects the analysis. Geometric imperfections in the detector

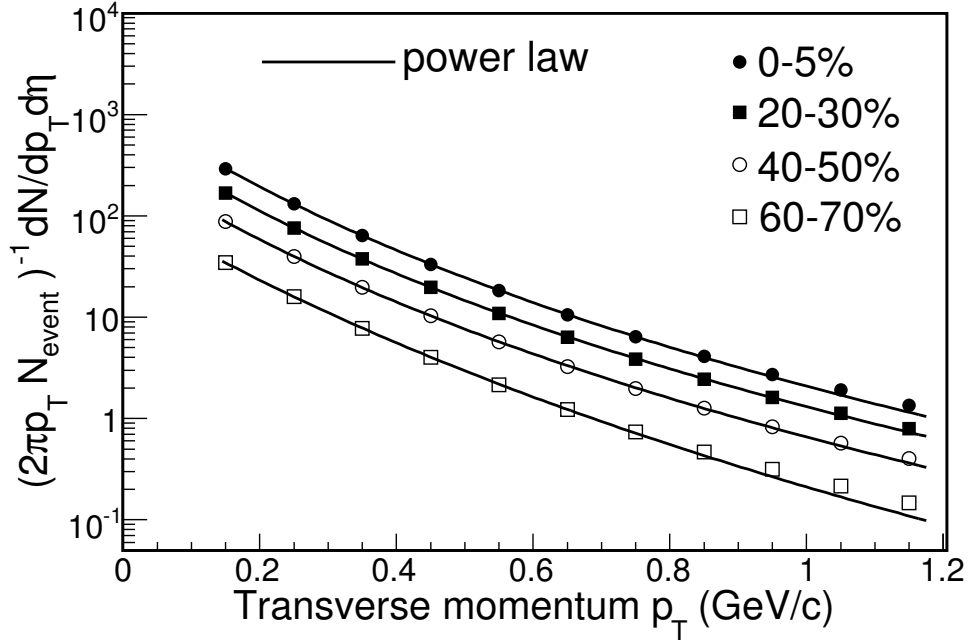


Figure 4.14: Corrected p_T spectra of inclusive charged hadrons from FTPC for various collision centralities. Solid lines are fit to power law function.

such as a shift of the inner cathode are observed and corrected for the first order in the reconstruction. In the simulation, these distortions are not present. However, distortions will lead to less precision in the track reconstruction, and thus to a broadening of the distribution of the distance of the closest approach (dca) to the primary vertex.

The average number of hits on a track is also overestimated in the simulations. Fig. 4.15 shows the variation of the efficiency by varying the selection of FTPC hits on the track. This is shown for 0–5% and 40–50% collision centrality. This overestimation of the track precision influences the dca to the primary vertex.

Fig. 4.16 shows the comparison of the dca to the primary vertex in the FTPC west for positive pions from embedding, HIJING and charged hadrons from real data. It is apparent that the dca distribution for data is considerably wider. However, it has to be taken into account that in embedding simulations, all the particles originate from the primary vertex, while the data also contains secondary particles that naturally have a larger dca . Fig. 4.17 shows the variation in the efficiency (ϵ_{ch}) with the variation in the dca cut in cm with fixed number of FTPC hits on track.

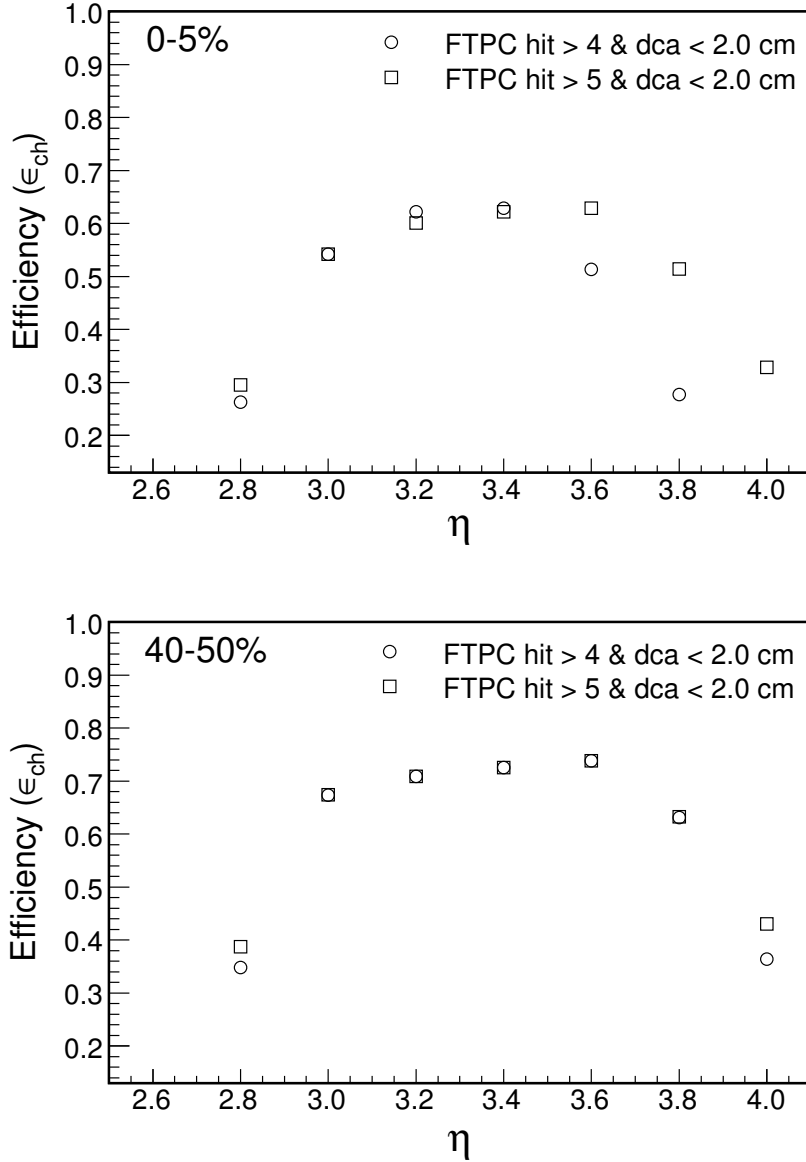


Figure 4.15: Variation of the efficiency (ϵ_{ch}) with varying the selection of FTPC hits on track by 1 for $dca < 2.0$ cm for 0–5% (top) and 40–50% (bottom) collision centrality for Au+Au collisions at 62.4 GeV.

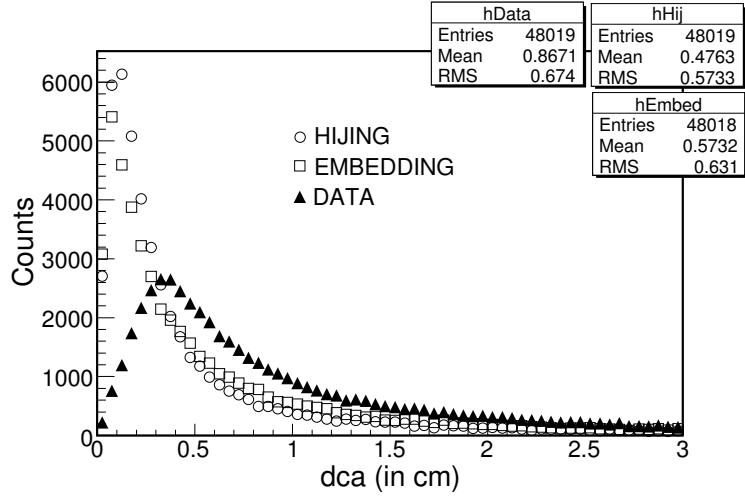


Figure 4.16: Comparison of the dca to primary vertex for embedding, HIJING and real data for FTPC west in Au+Au collisions at 62.4 GeV.

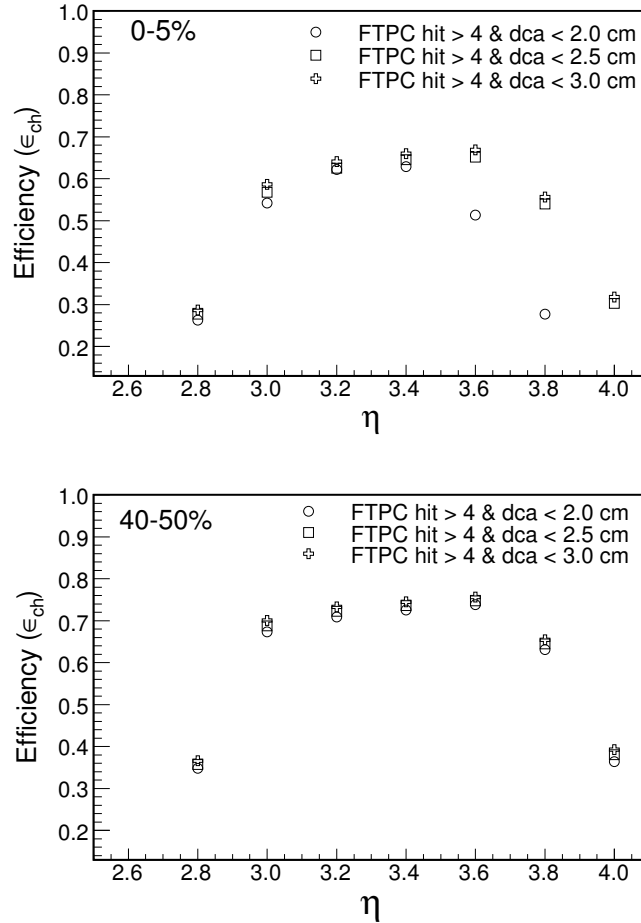


Figure 4.17: Variation of the efficiency (ϵ_{ch}) with varying the dca cut by 0.5 and 1.0 cm for fixed number of FTPC hits on track cut (> 4) for 0–5% (top) and 40–50% (bottom) collision centrality for Au+Au collisions at 62.4 GeV.

As a consequence of these effects, when dca and number of FTTPC hits on track cuts are applied in the analysis, the effects of these cuts on the simulation and on data have to be compared. These differences due to underestimation of the dca in simulations and embedding results contribute to $\sim 6\%$ of systematic error in the tracking efficiency and momentum resolution determination.

Bibliography

- [1] H. Huemmler, Ph.D. Thesis, Max-Planck-Institut für Physik, Munich (2000).
- [2] K. H. Ackermann *et al.*, Nucl. Instr. Meth. A **499**, (2003) 713.
- [3] M. Oldenburg, Ph.D. Thesis, Max-Planck-Institut für Physik, Munich (2002).
- [4] J. Putschke, Ph.D. Thesis, Max-Planck-Institut für Physik, Munich (2004).
- [5] S. Biagi, Nucl. Instr. Meth. A **283**, (1989) 716. Nucl. Instr. Meth. A **421**, (1999) 234-240;
- [6] X-N. Wang and M. Gyulassy, Phys. Rev. D **44**, (1991) 3501.
- [7] V. Fine and P. Nevski, in *Proceedings of CHEP-2000*, Padova, Italy.
- [8] F. Simon, Ph.D. Thesis, Max-Planck-Institut für Physik, Munich (2004).
- [9] STAR Collaboration, J. Adams *et al.*, Phys. Rev. C **73**, (2006) 034906.

Chapter 5

PHOTON AND CHARGED PARTICLE PRODUCTION

The conventional way of describing particle production in heavy ion collisions is by measuring the particle density in pseudorapidity (η). Within the framework of certain model assumptions, it provides information on energy density, initial temperature and velocity of sound in the medium formed in the collisions [1]. The widths of the pseudorapidity distributions are sensitive to longitudinal flow and re-scattering effects [2, 3]. The variation of particle density in η with collision centrality, expressed in terms of the number of participating nucleons (N_{part}) and/or the number of binary collisions (N_{coll}), can shed light on the relative importance of soft versus hard processes in particle production. The particle density in pseudorapidity also provides a testing ground for various particle production models, such as those based on ideas of parton saturation [4] and semi-classical QCD, also known as the color glass condensate (CGC) [5].

At RHIC, the particle production mechanism could be different in different regions of pseudorapidity. At mid-rapidity a significant increase in charged particle production normalized to the number of participating nucleons has been observed from peripheral to central Au + Au collisions [6]. This has been attributed to the onset of hard scattering processes, which scale with the number of binary collisions. However, the total charged particle multiplicity per participant pair, integrated over the whole pseudorapidity range, is independent of centrality in Au + Au collisions [7]. In the framework of the color glass condensate picture of particle production [5], the centrality dependence of particle production at mid-rapidity reflects the increase of gluon density due to the decrease in the effective

strong coupling constant. It will be interesting to see how the photon and charged particle production scales with the number of participating nucleons and with the number of binary collisions in a common η coverage at forward rapidity.

The dependence of particle production at mid-rapidity with increasing center-of-mass energy has been studied in detail at RHIC [7]. It is also of interest to see how particle production varies with center-of-mass energy at forward rapidity. The experimental data on hadron multiplicity and its energy, centrality and rapidity dependence so far have been consistent with the approach based on ideas of parton saturation. Recently it has been argued that this onset of saturation occurs somewhere in the center-of-mass energy ($\sqrt{s_{NN}}$) range of 17 GeV to 130 GeV [8]. This is one of the reasons cited for having different mechanisms of particle production at RHIC and SPS. The present experimental data at $\sqrt{s_{NN}} = 62.4$ GeV, analysis of which forms the major part of this thesis, may help to understand the transition energy for the onset of saturation effects in particle production if combined with data from other energies.

It has been observed that the inclusive charged particles at 19.6 GeV and 200 GeV follow an energy independent limiting fragmentation but centrality dependent longitudinal scaling [7]. It has been speculated that the charged baryons, an important constituent of inclusive charged particles, are responsible for the observed difference between photons and charged particles [7, 9]. The baryons coming from nuclear remnants and baryon transport, both of which change with centrality, may be the source of the centrality dependent limiting fragmentation for inclusive charged particles. The role of a new mechanism of baryon production as discussed in Refs. [10, 11] also needs to be understood. A comparative study of longitudinal scaling of positively and negatively charged particles and photons at the same collision energy and pseudorapidity interval as provided by the data presented in this thesis will help to understand the sources responsible for the observed features. On the theoretical side, reproducing the energy, centrality, and species dependence of limiting fragmentation observed in the experimental data can be a good test for various particle production models. One such attempt to explain the energy dependence of limiting fragmentation phenomena within the framework of CGC has been carried out in Ref. [12]. The importance of the limiting fragmentation curve on energy dependence of particle production has been demonstrated in Ref. [13].

Event-by-event measurements of photon and charged particle multiplicities can be used to study multiplicity fluctuations [14]. Fluctuations in physical observables

in heavy ion collisions may provide important information regarding the formation of a Quark-Gluon Plasma and help to address the question of thermalization [15]. The study of event-by-event fluctuations in the ratio of photon to charged particle multiplicities has also been proposed as a tool to search for production of Disoriented Chiral Condensates (DCCs) [16].

In this chapter of the thesis we address some of the above physics issues through the first simultaneous measurement of the charged particle and photon multiplicities for Au + Au collisions at $\sqrt{s_{\text{NN}}} = 62.4$ GeV in the forward rapidity. The charged particles are detected using the Forward Time Projection Chamber (FTPC) and the photons are detected using the Photon Multiplicity Detector (PMD) in the STAR experiment [17, 18, 19].

The chapter is organized as follows: In section 5.1 we present the results in terms of multiplicity and pseudorapidity distributions of photons and charged particles. In section 5.2 we discuss the importance of measuring the width of pseudorapidity distributions. In section 5.3 we study the scaling of particle production with number of participating nucleons, number of binary collisions and the number of constituent quark participants [20]. Finally we discuss the longitudinal scaling of particle production at RHIC in section 5.4.

5.1 Photon and charged particle pseudorapidity and multiplicity distributions

5.1.1 Multiplicity distributions for photons and charged particles

The charged particle multiplicity (N_{ch}) and photon multiplicity (N_{γ}) are obtained event-by-event in the FTPC and the PMD following the analysis procedure described in previous chapter. Fig. 5.1 shows the minimum bias distributions of N_{ch} and N_{γ} for Au + Au collisions at $\sqrt{s_{\text{NN}}} = 62.4$ GeV. The distributions have a characteristic shape with a steep rise that corresponds to the most peripheral events. The plateaus in the photon and charged particle multiplicity distributions correspond to mid-central events and the fall-off to the most central collision events. The shape of the curves in the fall-off region reflects the intrinsic fluctuations of the measured quantities and the limited acceptance of the detectors. The event-by-event charged particle and photon multiplicity distributions for 0–5% central collisions are also shown. Gaussian fits to these distributions have been made. The

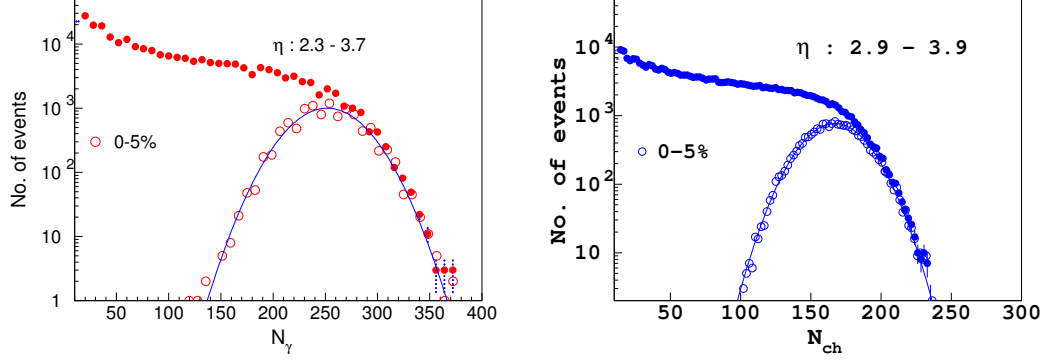


Figure 5.1: Minimum bias N_γ ($2.3 \leq \eta \leq 3.7$) and N_{ch} ($2.9 \leq \eta \leq 3.9$) and distributions for Au + Au collisions at $\sqrt{s_{\text{NN}}} = 62.4$ GeV. The charged particle and photon multiplicity distribution for top 5% central events are shown in open circles. The solid curve is the Gaussian fit to the data points.

values of the fit parameters for charged particles measured in $2.9 \leq \eta \leq 3.9$ are: mean = 167 and $\sigma = 20$; $\chi^2/\text{ndf} = 70.67/69$. The values of the fit parameters for photons measured in $2.3 \leq \eta \leq 3.7$ are: mean = 252 and $\sigma = 30$; $\chi^2/\text{ndf} = 37.3/34$.

The correlation between the average number of charged particles and average number of photons within the pseudorapidity coverage of the FTPC and PMD ($2.9 \leq |\eta| \leq 3.7$) for different collision centrality classes in Au + Au collisions at $\sqrt{s_{\text{NN}}} = 62.4$ GeV are shown in Fig. 5.2. The correlation between N_{ch} and N_γ can be expressed as $N_\gamma = (0.74 \pm 0.01)N_{\text{ch}} - (3.57 \pm 0.83)$. This is shown as a straight line in the figure and hold good for value of $N_{\text{ch}} > 25$. The correlation reflects the variation of N_γ and N_{ch} with collision centrality. The correlation coefficient is calculated to be 1.01 ± 0.01 .

5.1.2 Fluctuation of N_γ and N_{ch}

The near perfect Gaussian distributions of event-by-event N_{ch} and N_γ for central collisions (0-5%) motivates us to study the relative fluctuation in these quantities [14]. The relative fluctuation (ω_X) in an observable X can be expressed as $\omega_X = \frac{\sigma_X^2}{\langle X \rangle}$, where σ_X^2 is the variance of the distribution and $\langle X \rangle$ denotes the mean

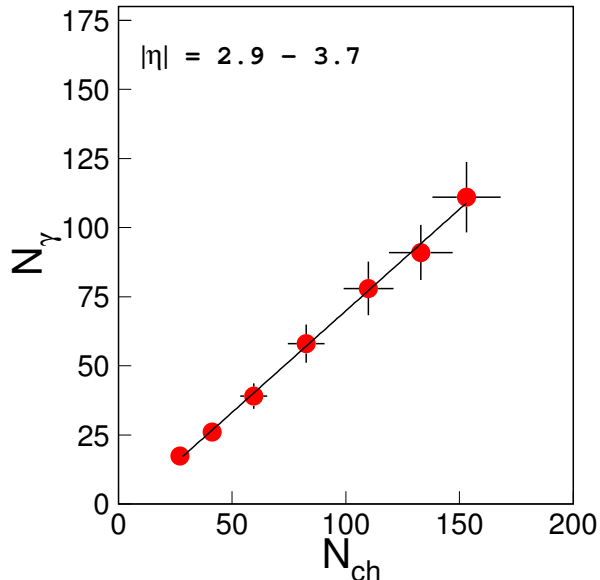


Figure 5.2: Correlation between average number of charged particles (N_{ch}) and average number of photons (N_γ) within the common η range of FTPC and PMD $2.9 \leq \eta \leq 3.7$ for different collision centrality classes in Au + Au collisions at $\sqrt{s_{NN}} = 62.4$ GeV. The solid line is a straight line fit to the data points (see text for details).

value. This leads to $\omega_{ch} = 2.4 \pm 0.34$ and $\omega_\gamma = 3.6 \pm 0.9$ for central collisions in the pseudorapidity region $2.9 \leq \eta \leq 3.9$ and $2.3 \leq \eta \leq 3.7$ respectively. It may be mentioned that the value of $\omega_X = 1$ would mean absence of any dynamical fluctuations in the observed quantity. A value of $\omega_X > 1$ can be attributed to dynamical sources, provided the effects such as finite particle multiplicity, limited acceptance of the detectors, detector effects, impact parameter fluctuations, fluctuations in the number of primary collisions, re-scattering of secondaries, resonance decays, and Bose-Einstein correlations are understood.

5.1.3 Pseudorapidity distributions for photons and charged particles

So far we have discussed the multiplicities of photons and charged particles over the full coverage of the detectors. In this subsection we study the variation in particle density with η . The results can then be directly compared to different models in order to understand the mechanism of particle production in heavy ion

collisions at forward rapidity.

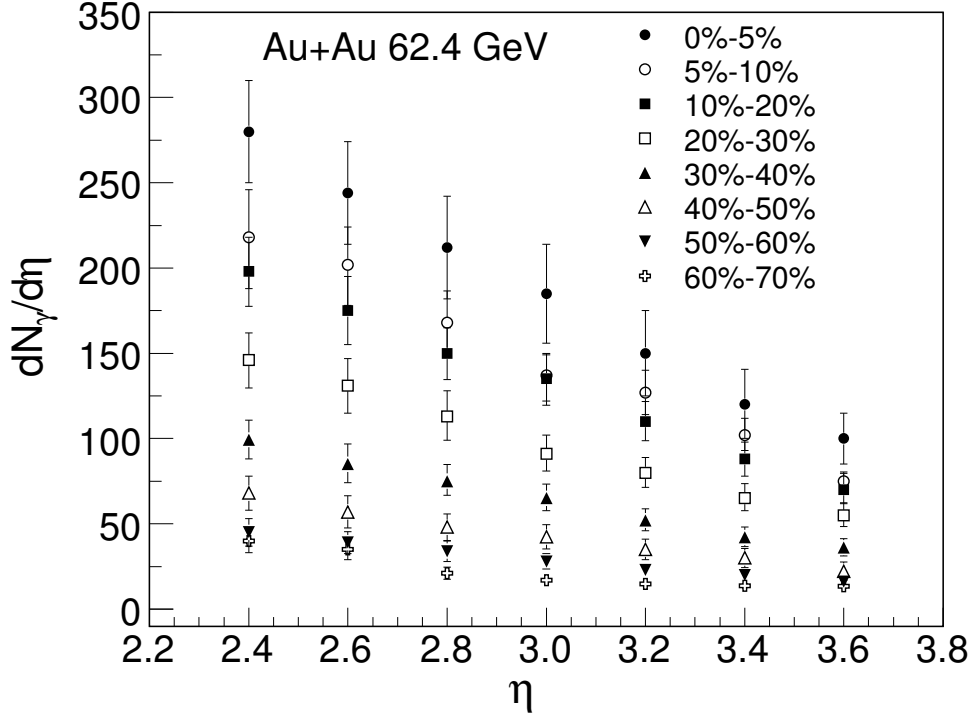


Figure 5.3: $dN/d\eta$ for photons for Au + Au collisions at $\sqrt{s_{\text{NN}}} = 62.4$ GeV for various event centrality classes.

Fig. 5.3 shows the pseudorapidity distributions of photons within $2.3 \leq \eta \leq 3.7$ and Fig. 5.4 shows the pseudorapidity distributions for charged particles within $2.9 \leq \eta \leq 3.9$ for various event centrality classes. As expected the particle density increases with decrease in η for both photons and charged particles.

5.1.4 Model comparison of pseudorapidity distributions for photons and charged particles

Fig. 5.5 shows the comparison of pseudorapidity distributions for charged particles (top) and photons (bottom) for 0–5% and 40–50% central Au + Au collisions at $\sqrt{s_{\text{NN}}} = 62.4$ GeV with the corresponding results from various theoretical models. The HIJING model [21] is based on perturbative QCD processes which lead to

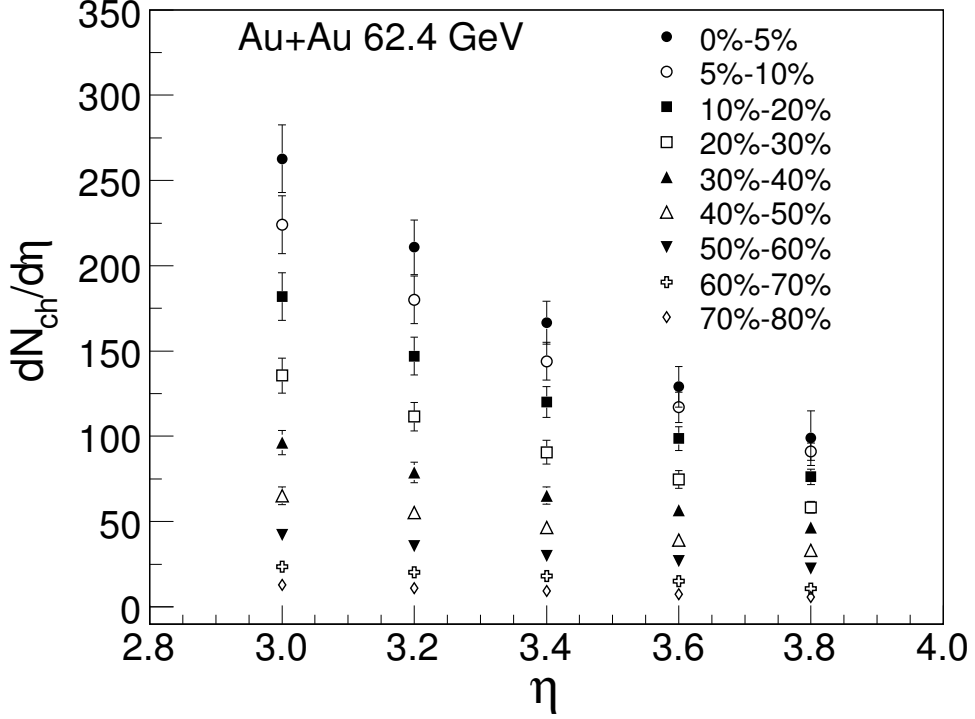


Figure 5.4: $dN/d\eta$ for charged particles for Au + Au collisions at $\sqrt{s_{NN}} = 62.4$ GeV for various event centrality classes.

multiple jet production and jet interactions in matter. In this pQCD inspired model, multiple minijet production is combined together with Lund-type model for soft interactions. Within this model, triggering on large p_T jet production automatically biases toward enhanced minijet production. Binary approximation and Glauber geometry for multiple interaction are to be used to simulate pA and AA collisions. A parametrized parton distribution function inside a nucleus is used to take into account parton shadowing. A simple color configuration is assumed for the multiple jet system and Lund jet fragmentation model is used for hadronization. HIJING seems to under-predict the measured photon multiplicity. However within the systematic errors it is difficult to make definitive conclusions. For charged particles, HIJING fails to explain the η distributions for central and peripheral collisions.

We have also compared our photon and charged particle data with a multi-phase transport model [22] (AMPT). The AMPT model includes both initial partonic and

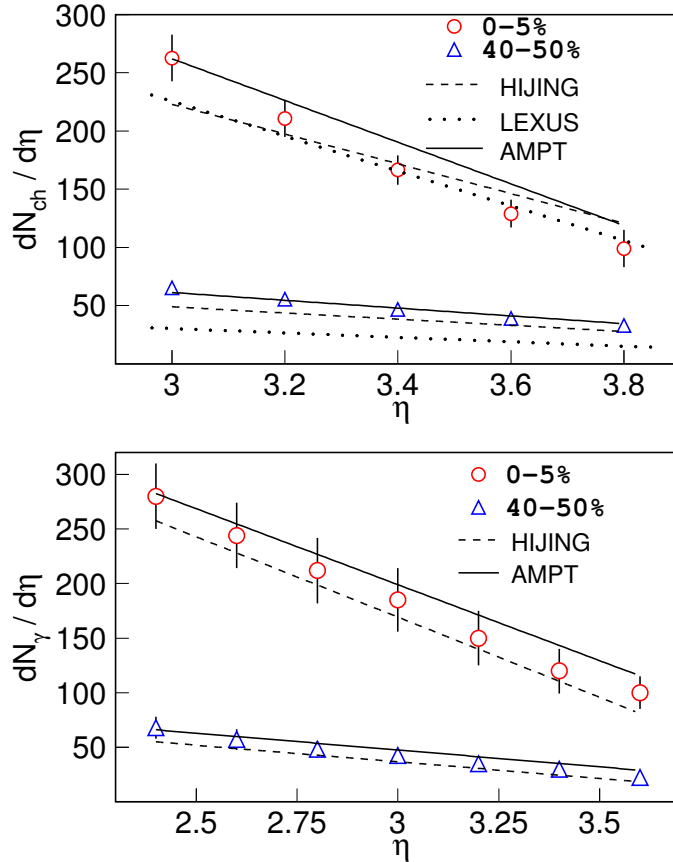


Figure 5.5: $dN/d\eta$ for charged particles (top) and photons (bottom) for central and peripheral Au + Au collisions at $\sqrt{s_{NN}} = 62.4$ GeV compared to corresponding results from theoretical models.

final hadronic interactions. It uses the parton distribution from HIJING model. For photons, the results from the AMPT model are in reasonable agreement with the data for central and peripheral events within the systematic errors. For charged particles in central collisions, the results from AMPT explain the data at lower η [23] and over-predict the charged particle yields at higher η . The LEXUS [24] model is based on linear extrapolation of nucleon-nucleon collisions to high-energy nucleus-nucleus collisions. For charged particles, the LEXUS model under-predicts the multiplicity at lower η and agrees with experimental data at higher η for central collisions [23]. It also under-predicts the charged particle yields for peripheral

collisions. In summary, we observe that the photon multiplicity within the systematic errors is reasonably well explained by HIJING and AMPT models. The detailed pseudorapidity dependence of the charged particle multiplicity is not reproduced by the above models.

5.1.5 Energy dependence of pseudorapidity distributions for photons and charged particles

We have so far studied the pseudorapidity distribution of particles at forward rapidity at $\sqrt{s_{NN}} = 62.4$ GeV. Now we will investigate the energy dependence of the shape of the η distribution of charged particles available at various energies of Au + Au collisions in RHIC.

The energy dependence of charged particle yields at mid-rapidity has been studied at RHIC [7]. Here we present the results on the energy dependence of particle yields at forward rapidity and compare them with yields at mid-rapidity.

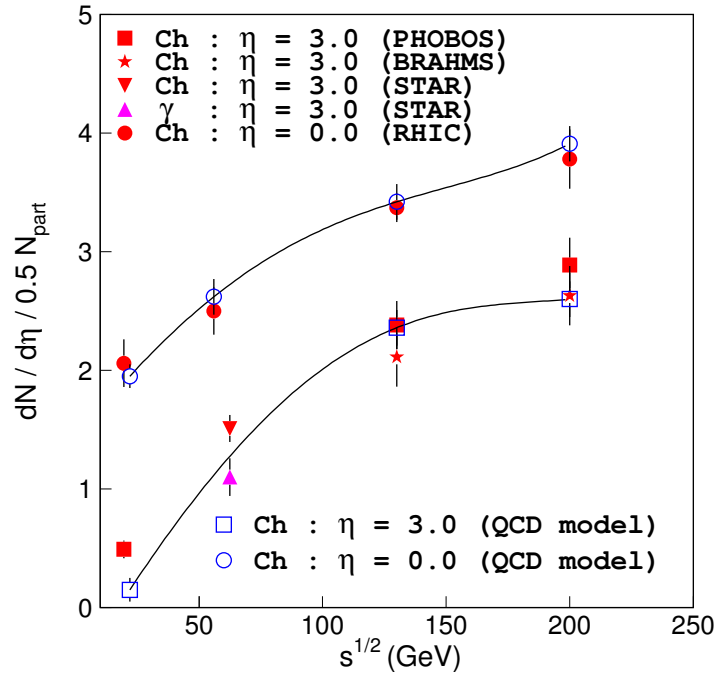


Figure 5.6: $dN/d\eta$ per participating nucleon pair at mid-rapidity ($\eta = 0$) and forward rapidity ($\eta = 3.0$) for various center-of-mass energies for central collisions.

Fig. 5.6 shows the charged particle pseudorapidity distribution scaled by the number of participating nucleon pairs at mid-rapidity ($\eta = 0$) and forward rapidity ($\eta = 3.0$) as a function of $\sqrt{s_{\text{NN}}}$ for central collisions at RHIC. The data for charged particles at $\sqrt{s_{\text{NN}}} = 19.6$ GeV, 56 GeV, 130 GeV and 200 GeV at $\eta = 3.0$ are from the PHOBOS [7] and BRAHMS [23] experiments. The photon yield at $\sqrt{s_{\text{NN}}} = 62.4$ GeV is also plotted. For comparison the results from a model based on parton saturation expected at high-density QCD [25] are also shown. The solid lines are polynomial fits to the values from the QCD model. There is no prediction for $\sqrt{s_{\text{NN}}} = 62.4$ GeV available from this model.

The data for charged particles at mid-rapidity are the averages of the values from the 4 RHIC experiments. The charged particle production at $\eta = 0$, can be expressed as

$$\frac{dN/d\eta}{0.5N_{\text{part}}} = 1.75(\pm 0.25) + 0.017(\pm 0.005) \ln[\sqrt{s_{\text{NN}}}] - 0.00003(\pm 0.00002)(\ln[\sqrt{s_{\text{NN}}}]^2).$$

The charged particle production at $\eta = 3.0$, can be expressed as

$$\frac{dN/d\eta}{0.5N_{\text{part}}} = -0.03(\pm 0.13) + 0.028(\pm 0.004) \ln[\sqrt{s_{\text{NN}}}] - 0.00007(\pm 0.00002)(\ln[\sqrt{s_{\text{NN}}}]^2).$$

The ratio of charged particle production at $\eta = 0$ to that at $\eta = 3.0$ decreases from a factor 4 to 1.3 as $\sqrt{s_{\text{NN}}}$ increases from 19.6 GeV to 200 GeV. The photon result at $\sqrt{s_{\text{NN}}} = 62.4$ GeV for $\eta = 3.0$ is also shown. The photon yields at other $\sqrt{s_{\text{NN}}}$ values at forward rapidity and mid-rapidity are not yet available at RHIC. The photon production at $\sqrt{s_{\text{NN}}} = 62.4$ GeV is about 35% lower than the charged particle production for the same energy at $\eta = 3.0$. The charged particle yield at $\eta = 3.0$ for $\sqrt{s_{\text{NN}}} = 62.4$ GeV is a factor 1.6 and 1.9 lower compared to the corresponding yields at 130 GeV and 200 GeV and a factor 3.0 higher than the charged particle yields at 19.6 GeV. For comparison, also shown in Fig. 5.6 are the results from a model based on parton saturation, which is expected in high-density QCD [25]. The results from the model agree with the measured charged particle yields at mid-rapidity for all energies at RHIC. However, the model's prediction for forward rapidity at the lowest energy (22 GeV) is lower compared to data (19.6 GeV). There is no prediction for $\sqrt{s_{\text{NN}}} = 62.4$ GeV available from this model. It would be interesting to have the predictions to understand the transition energy for the onset of saturation effects at RHIC.

5.1.6 Parametrization of pseudorapidity distribution for charged particles at RHIC

In this subsection we will estimate the full η distribution for charged particles for $\sqrt{s_{\text{NN}}} = 62.4$ GeV from the available higher and lower energy charged particle measurements at RHIC and try to extract the full charged particle pseudorapidity distribution at $\sqrt{s_{\text{NN}}} = 62.4$ GeV. Then we compare this extracted distribution to the present measurements.

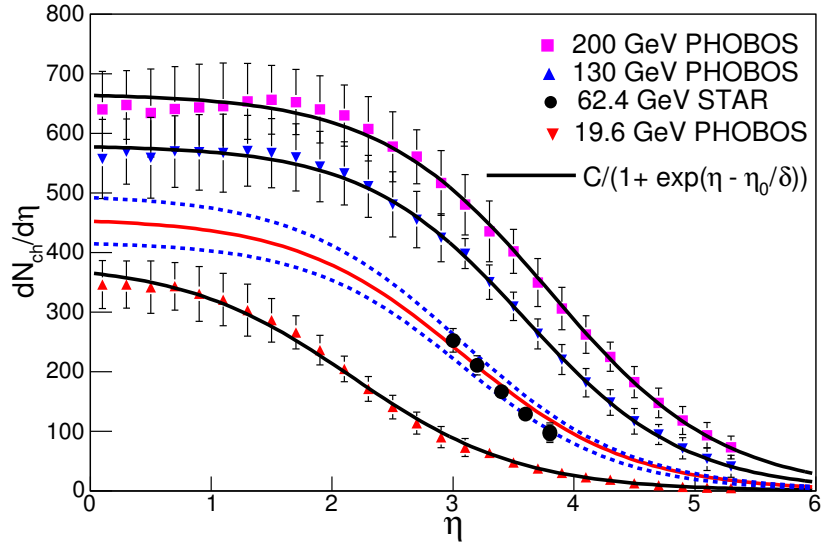


Figure 5.7: Pseudorapidity distributions of charged particles for various center-of-mass energies in Au + Au central collisions. The pseudorapidity distributions for $\sqrt{s_{\text{NN}}} = 200$ GeV, 130 GeV and 19.6 GeV are from the PHOBOS experiment. The solid lines are the results of the fits described in the text.

The full pseudorapidity distribution of charged particles at RHIC for central collisions can be parametrized by the following 3-parameter formula:

$$\frac{dN}{d\eta} = \frac{C}{1 + \exp\frac{\eta - \eta_0}{\delta}} \quad (5.1)$$

This formula is chosen to describe the central plateau and the fall off in the fragmentation region of the distribution by means of the parameters η_0 and δ respectively. Using this formula we can describe the 200 GeV, 130 GeV and 19.6

Table 5.1: Parameters C , η_0 and δ for different $\sqrt{s_{\text{NN}}}$.

$\sqrt{s_{\text{NN}}}$ (GeV)	C	η_0	δ
19.6	382 ± 33	2.16 ± 0.17	0.7 ± 0.06
62.4 (interpolated)	458 ± 40	3.08 ± 0.35	0.69 ± 0.06
130	580 ± 21	3.59 ± 0.076	0.66 ± 0.05
200	667 ± 22	3.80 ± 0.082	0.71 ± 0.06

GeV pseudorapidity distributions of charged particles from the PHOBOS experiment [7]. The values of the parameters C , η_0 and δ are given in Table 5.1 and the fits to data are shown in Fig. 5.7.

The value of η_0 is found to increase with increasing $\sqrt{s_{\text{NN}}}$. The value of the parameter δ is found to be independent of energy within errors. This feature is another way of testing the concept of limiting fragmentation, which will be discussed later. Using the average value of δ and interpolating the value of η_0 to 62.4 GeV we are able to predict the full pseudorapidity distribution for charged particles at 62.4 GeV. This is shown as solid curve in Fig. 5.7, together with our measured charged particle data for 62.4 GeV at forward rapidity. The dashed curves represent the error in obtaining the full pseudorapidity distribution for charged particles using the interpolation method described.

5.1.7 Comparison of N_{ch} and N_γ

The STAR experiment at RHIC has the unique capability to study the yields of charged particle and photons at forward rapidity. Fig. 5.8 shows the ratio of N_{ch} to N_γ for 0–5% and 40–50% central Au + Au collisions at $\sqrt{s_{\text{NN}}} = 62.4$ GeV as a function of η in the common η coverage of the FTPC and the PMD. The ratio is around 1.4 for central collisions and 1.6 for peripheral collisions within $3.0 < \eta < 3.6$. The results from HIJING indicate similar values. The correlated systematic errors, mainly arising due to uncertainties in the Monte Carlo determination of reconstruction efficiencies and normalization errors, are not plotted on the data points and are shown as a shaded band. The photon production is dominated by photons from the decay of π^0 s [9]. The charged particle yields have a substantial contribution from baryons at forward rapidity [26]. Apart from the kinematics, this may be the reason for higher charged particle yields compared to photons. In

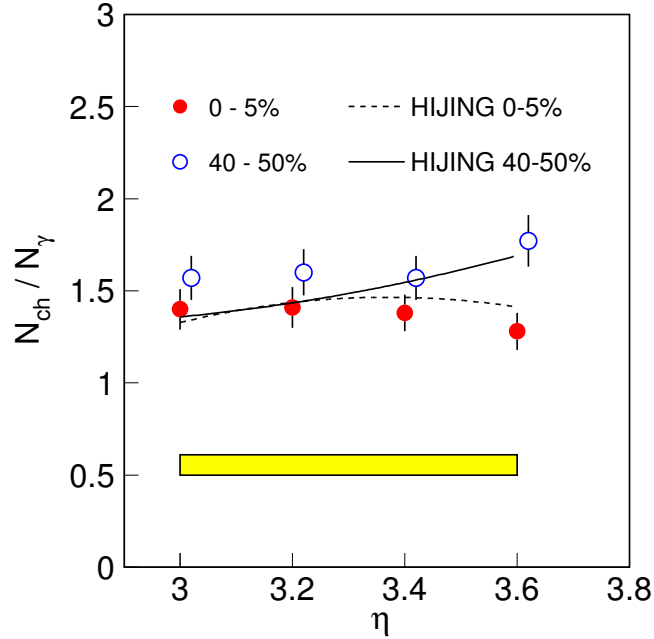


Figure 5.8: Ratio of N_{ch} to N_{γ} for 0–5% and 40–50% central Au + Au collisions at $\sqrt{s_{\text{NN}}} = 62.4$ GeV as a function of η . Results from HIJING are also shown for comparison. The lower band reflects the common errors in ratio for the two centrality classes.

the future, event-by-event study of N_{ch} and N_{γ} correlations in common η and ϕ coverage of the FTPC and the PMD can be used to look for possible formation of disoriented chiral condensates [16].

5.2 Width of rapidity and pseudorapidity distributions

The evolution of the pseudorapidity density at mid-rapidity with beam energy and centrality has been one of the main interests of study in heavy ion collisions [6, 27]. Its scaling with the number of participating nucleons and/or with the number of collisions is believed to provide information on the dynamics of the particle production [6, 25, 27, 28]. The pseudorapidity density at mid-rapidity is also related to the entropy density [29]. However similar importance has not been given to the width of the rapidity distributions of the particles (σ_Y). With the advent of large acceptance detectors such as in RHIC experiments [30] and the

energy scan being high on the agenda of the RHIC program, one can study the evolution of the width of the rapidity distribution as a function of beam energy and centrality. The width of the rapidity distribution is believed to be sensitive to the following physics effects:

- (a) Final state re-scattering [31], hence a p_T dependence study of the width may help in estimating the value of p_T that separates the initial hard scattering regime from the later stage in heavy ion collisions which is dominated by re-scattering.
- (b) The width of the rapidity distribution contains the information of longitudinal flow [2].
- (c) For a given freeze-out temperature, the width of the rapidity distribution in the Landau hydrodynamical model is found to be sensitive to the velocity of sound in the medium [32].

In this section we will show how longitudinal flow, velocity of sound and re-scattering affect the width of rapidity distribution. Qualitatively the variation in width of the rapidity distribution with center-of-mass energy and centrality can be understood on the basis of above mentioned processes. We also study the scaling of width of pseudorapidity distribution with ratio of total multiplicity of produced particles to the center-of-mass energy in $p+p$ at ISR and Au+Au collisions at RHIC.

5.2.1 \sqrt{s} and centrality dependence of width of rapidity and pseudorapidity distributions

In Fig. 5.9 we have plotted the width of the rapidity distribution, σ_Y , for π^- and K^\pm as a function of $\sqrt{s_{NN}}$ [2, 33, 34]. The solid curve corresponds to the theoretical prediction from Ref. [35] based on the Landau model, developed for studying the rapidity distribution for pions in $p+p$ collisions [24]. In this model the width of the rapidity distribution is given as $\sqrt{\ln(\sqrt{s_{NN}}/2m_p)}$. The dashed curve corresponds to the experimentally determined width of the rapidity distribution for pions produced in $p+p$ collisions. Where not provided in the references directly, the widths were obtained by fitting Gaussian distributions with center at $Y = 0$ to the rapidity distributions. The following observations can be made from the figure:

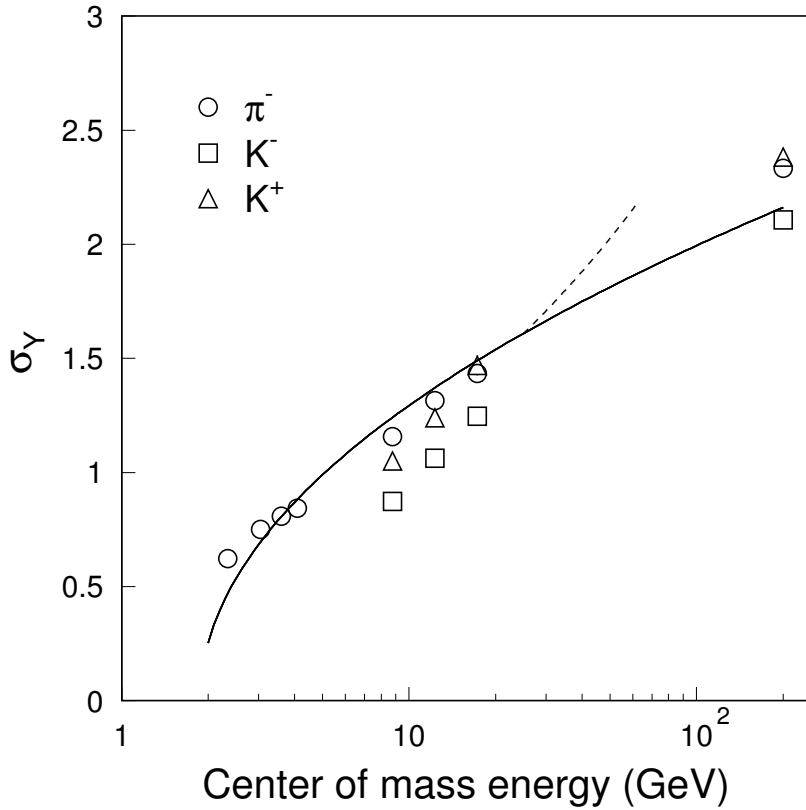


Figure 5.9: Variation of the width of the rapidity distribution for π^- , K^+ , and K^- with center-of-mass energy. The symbols are for nucleus-nucleus collisions and the dashed curve for pions in nucleon-nucleon collisions. The solid curve, prediction based on Landau model, corresponds to $\sqrt{\ln(\sqrt{s_{NN}}/2m_p)}$. The dashed curve follows the solid curve up to $\sqrt{s_{NN}} = 25$ GeV. The errors on the data point are small and are within the symbol size.

- The width of the rapidity distribution increases with increase in $\sqrt{s_{NN}}$ for both nucleon-nucleon and nucleus-nucleus collisions.
- The width of the rapidity distribution for $p+p$ collisions deviates from the predictions based on the Landau model for $\sqrt{s_{NN}} > 25$ GeV.
- $\sigma_{K^+} > \sigma_{K^-}$ in nucleus-nucleus collisions. This reflects their different interaction cross sections with other particles in the medium.
- The nucleus-nucleus data for pions shows a similar trend as the curve corresponding to $\sqrt{\ln(\sqrt{s_{NN}}/2m_p)}$. σ_π values are comparable to σ_{K^+} and they are higher than σ_{K^-} values for SPS and RHIC energies.

In Fig. 5.10 we have plotted the widths of the pseudorapidity distributions of the charged particles (σ_{ch}) as a function of % cross section for $\sqrt{s_{NN}} = 8.76$ and

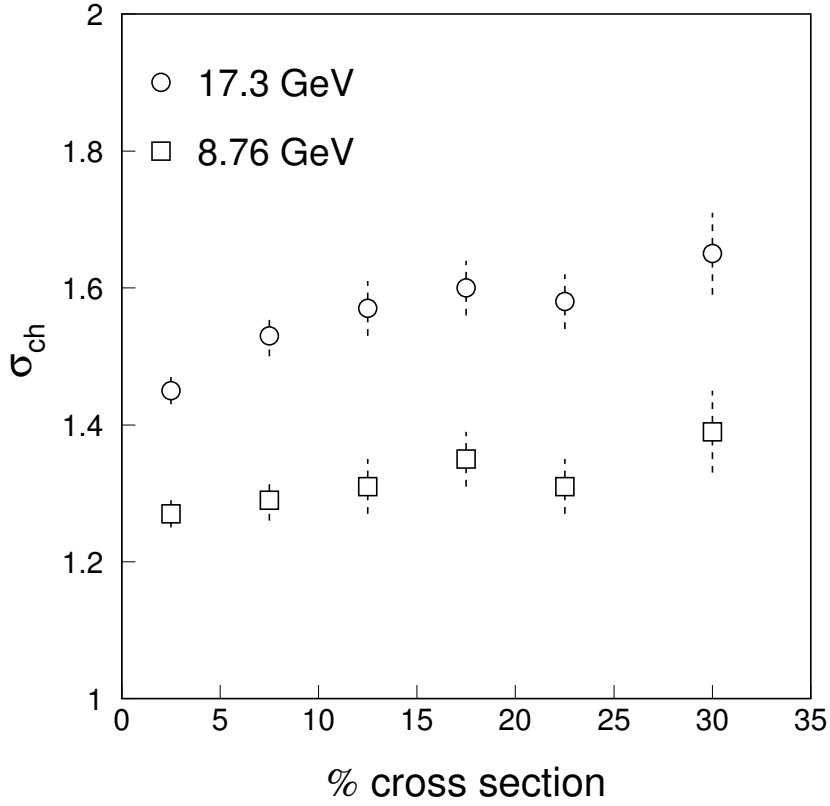


Figure 5.10: Variation of the width of the pseudorapidity distribution of charged particles as a function of percentage of cross section for two center-of-mass energies $\sqrt{s_{NN}} = 17.3$ GeV and 8.76 GeV.

17.3 GeV [36]. We observe that σ_{ch} increases as we go from central to peripheral collisions.

5.2.2 Effect of longitudinal flow on width of rapidity and pseudorapidity distributions

The rapidity distribution can be used to study the longitudinal flow [2]. In Fig. 5.11 we have plotted the rapidity distribution of π^- for $\sqrt{s_{NN}} = 8.76$ GeV [33]. Our calculations from a static isotropic thermal emission model where the rapidity density is given as

$$\frac{dN_{th}}{dY} = AT^3 \left[\frac{m^2}{T^2} + \frac{m}{T} \frac{2}{\cosh Y} + \frac{2}{\cosh^2 Y} \right] \times e^{[-(\frac{m}{T}) \cosh Y]} \quad (5.2)$$

is shown by the dashed curve. The temperature T is taken as 120 MeV [37], m is mass of the pion and A is the normalization constant. The temperature is fixed from the study of the transverse momentum spectra for the produced particles. This temperature is found to around 100 - 120 MeV. The longitudinal

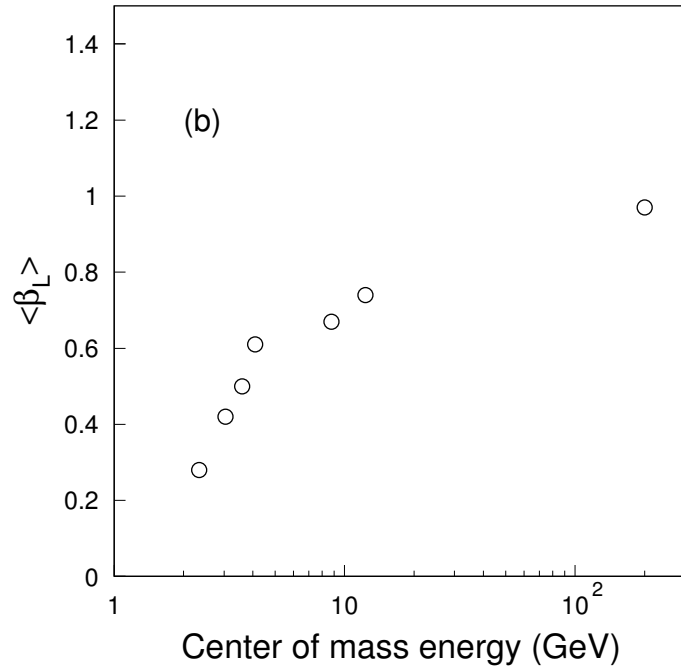
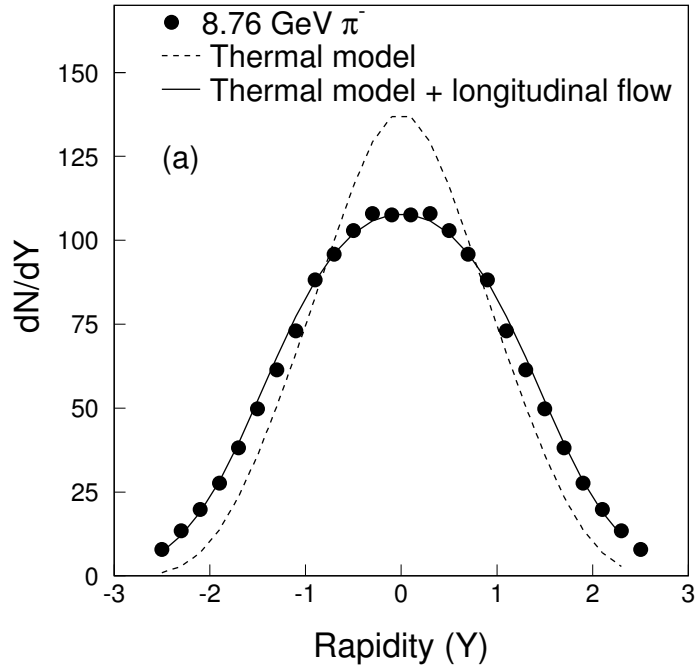


Figure 5.11: (a) Rapidity distribution for π^- at $\sqrt{s_{\text{NN}}} = 8.76$ GeV from SPS. Comparison to a thermal model calculation and a thermal model with longitudinal flow ($\langle\beta_L\rangle = 0.6$). (b) Variation of average longitudinal flow velocity, $\langle\beta_L\rangle$, with center-of-mass energy.

flow is then reflected by the β_L values extracted from the study of the rapidity distributions. We observe that the thermal model fails to explain the width of the rapidity distribution. After including the longitudinal flow within the ambit of Bjorken hydrodynamics as discussed in Ref. [2, 32], in the above thermal model, the rapidity distribution of pions is found to be well explained (solid curve). The rapidity distribution is now given as

$$\frac{dN}{dY} = \int_{-\eta_{max}}^{\eta_{max}} \frac{dN_{th}}{dY}(Y - \eta) d\eta \quad (5.3)$$

and the average longitudinal velocity is defined as $\langle\beta_L\rangle = \tanh(\eta_{max}/2)$. $\langle\beta_L\rangle = 0.6$ is found to explain the pion data at $\sqrt{s_{NN}} = 8.76$ GeV as shown by the solid curve in Fig. 5.11(a).

We fit the rapidity distributions for pions from $\sqrt{s_{NN}} = 2$ to 200 GeV to results from the thermal model with longitudinal flow to obtain the $\langle\beta_L\rangle$. Variation of $\langle\beta_L\rangle$ with $\sqrt{s_{NN}}$ is shown in Fig. 5.11(b). We find the average longitudinal velocity for pions approach a value of 1 at RHIC from a value of 0.3 at AGS energies. This is indicative of the higher degree of nuclear transparency attained at RHIC compared to SPS or AGS. It is observed that the results in Fig. 5.11(b) show qualitatively a similar trend with $\sqrt{s_{NN}}$ as seen for the σ_Y for pions in Fig. 5.9. This indicates that the collective behavior and the final state interactions of the produced particles in nucleus-nucleus collisions play an important role in determining the width of the rapidity distribution.

5.2.3 Effect of velocity of sound on width of rapidity and pseudorapidity distributions

The width of the rapidity distribution is sensitive to the velocity of sound in the medium formed at freeze-out [32]. Fig. 5.12 shows the rapidity distribution of pions at $\sqrt{s_{NN}} = 8.76$ GeV compared to rapidity distribution obtained for various values of velocity of sound using Landau hydrodynamics. Within the ambit of Landau hydrodynamics one can show, with certain assumptions [32], that the rapidity distribution has the form

$$\frac{dN}{dY} \sim Const. \frac{\exp(-\frac{Y^2}{2\sigma^2})}{\sqrt{2\pi\sigma^2}} \quad (5.4)$$

where $\sigma = 2\omega_f/(1 - c_s^2)$, $\omega_f = \ln(T_f/T_0)$, T_f is the freeze-out temperature, T_0 is the initial temperature, c_s is the velocity of sound in the medium. We observe that for a

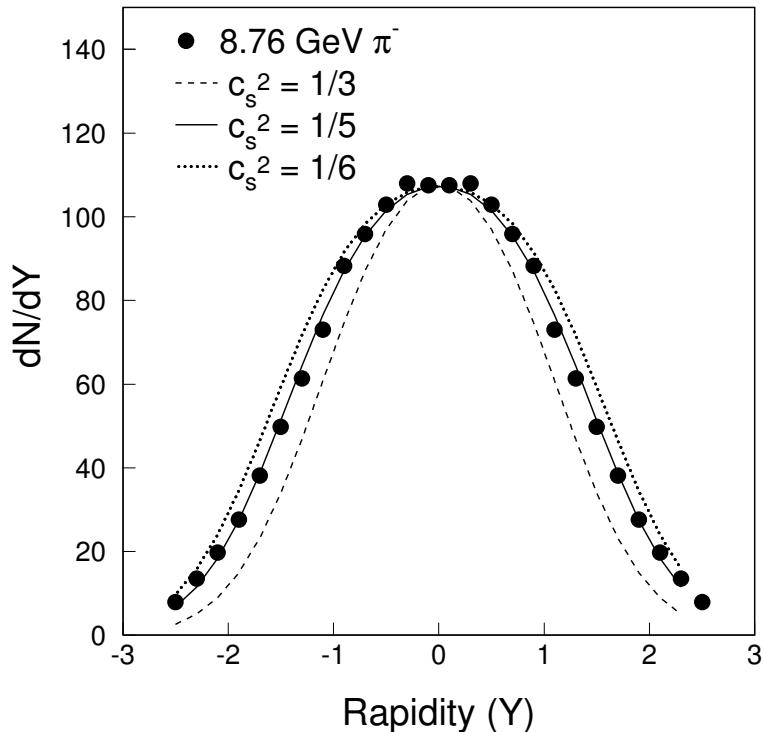


Figure 5.12: Rapidity distribution of π^- at center-of-mass energy 8.76 GeV compared to the rapidity spectra obtained from the Landau hydrodynamical model for $c_s^2 = 0.166, 0.2$ and 0.33 .

$T_f = 120$ MeV [37] and $T_0 = 230$ MeV (obtained from the total multiplicity [29]), $c_s^2 = 1/5$ explains the data very well. A c_s^2 value of $1/6$ over-predicts the data and a c_s^2 value of $1/3$ (ideal gas) under-predicts the data. The χ^2 values for the distributions with $c_s^2 = 1/3, 1/5$ and $1/6$ are 51, 1, 7 respectively. This shows that the width of the rapidity distribution of data is sensitive to the parameter c_s^2 representing the velocity of sound in the medium in the above model. It may be mentioned that the results are sensitive to the choice of initial and freeze-out temperatures also [32].

It has been shown in the Ref. [32] that the rapidity distributions of pions, kaons and protons at AGS and SPS energies all reveal the same value of $c_s^2 \sim 1/5$ which explains the data. This may indicate some kind of universality of the matter formed at the freeze-out stage. It may be mentioned that the value of $c_s^2 \sim 1/5$ has been found to be a characteristic value of the speed of sound for a gas of hadrons [38]. $c_s^2 \sim 1/5$ indicates that the expansion of the system is slower than that in an ideal gas scenario ($c_s^2 = 1/3$). Thus the system formed in heavy ion

collisions gets more time to interact and to reach thermal equilibrium.

5.2.4 Effect of initial and final state re-scattering on width of rapidity and pseudorapidity distributions

Sensitivity of the width of the rapidity distribution to re-scattering effects is studied here by using AMPT model. We found that σ_{ch} obtained from the AMPT model

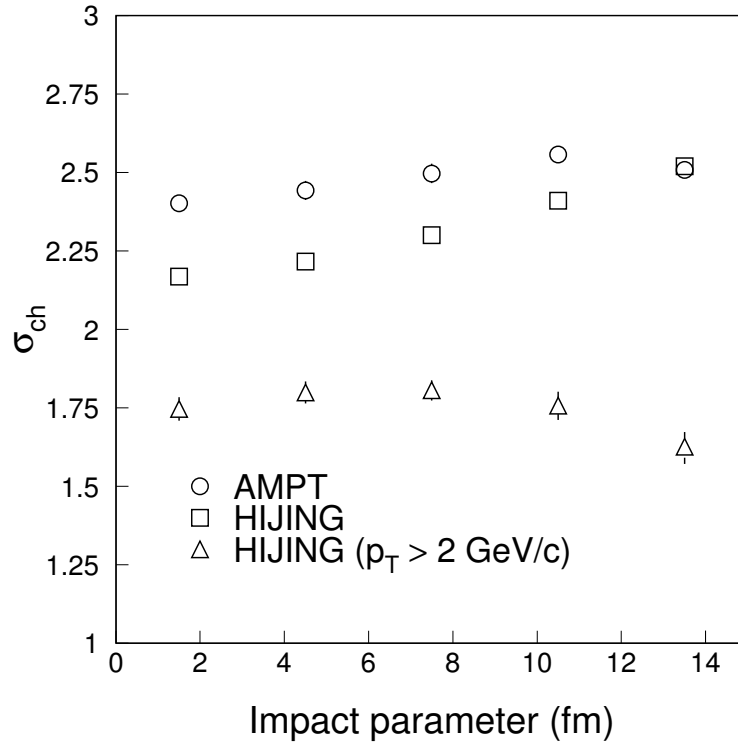


Figure 5.13: Variation in the width of the rapidity distribution as a function of impact parameter for $\sqrt{s_{NN}} = 62.4$ GeV for Au on Au collisions from AMPT and HIJING models. Also shown width of rapidity distribution from HIJING for particles having $p_T > 2$ GeV/c.

increases with $\sqrt{s_{NN}}$. The values at $\sqrt{s_{NN}} = 17.3, 62.4, 130$ and 200 GeV are 1.57, 2.4, 2.6 and 2.8 respectively for the impact parameter range from 0 to 3 fm in Au+Au collisions. In Fig. 5.13 the widths of the rapidity distributions for charged particles is plotted as a function of impact parameter for $\sqrt{s_{NN}} = 62.4$ GeV for Au

on Au collisions using AMPT and HIJING models. We observe that σ_{ch} increases as we go towards higher values of impact parameter for both AMPT and HIJING models. We also observe such a trend at lower and higher center-of-mass energies. This trend is qualitatively similar to that observed in the data shown in Fig. 5.10. The variation in the width is smaller for AMPT than for HIJING. This indicates that final state re-scattering has an effect on the width of the rapidity distribution.

Also shown in Fig. 5.13 is the variation of the σ_{ch} from HIJING for the particles with $p_T > 2$ GeV/c as a function of impact parameter. We observe that for particles having $p_T > 2$ GeV/c, σ_{ch} decreases as we go higher in collision impact parameter. Qualitatively one can think of the following picture, re-scattering leads to more isotropic momentum distributions (for example radial flow in a hydrodynamical picture) and hence will lead to narrower rapidity distributions. Particles with very high transverse momentum which are basically coming from the initial state will not exhibit such isotropy in the momentum distribution. The width of their rapidity distribution is expected to show a different variation with centrality. $p_T > 2$ GeV/c was chosen for this study as RHIC results on elliptic flow show that hydrodynamical calculations agree with the data for $p_T < 2$ GeV/c [39]. Thus studying σ_{ch} as a function of centrality for various p_T ranges may indicate the possibility of finding a value of transverse momentum at which the initial hard scattering stage can be distinguished from the later final state re-scattering.

5.2.5 Scaling of the width of pseudorapidity distributions at ISR and RHIC

We have also studied the widths of the pseudorapidity distributions of charged particles at RHIC and compared them to those from $p + p$ collisions at ISR [40]. In Fig. 5.14 we show the variation of the half width at half maximum (η_h) of the charged particle pseudorapidity distributions as a function of total charged particle multiplicity normalized to the center-of-mass energy ($N_T/\sqrt{s_{NN}}$) for $p + p$ and Au + Au collisions. The data shown is for various centrality classes in Au + Au collisions [7] and for various intervals of observed total multiplicity in $p + p$ collisions. We observe that the half width at half-maximum obeys an interesting scaling law in $p + p$ collisions and is found to depend on a single variable ($N_T/\sqrt{s_{NN}}$). In Au + Au collisions this scaling seems to be valid for 200 GeV and 130 GeV. Although the width decreases with $N_T/\sqrt{s_{NN}}$ for 19.6 GeV, the data lies below the higher energy data unlike the energy independent behavior

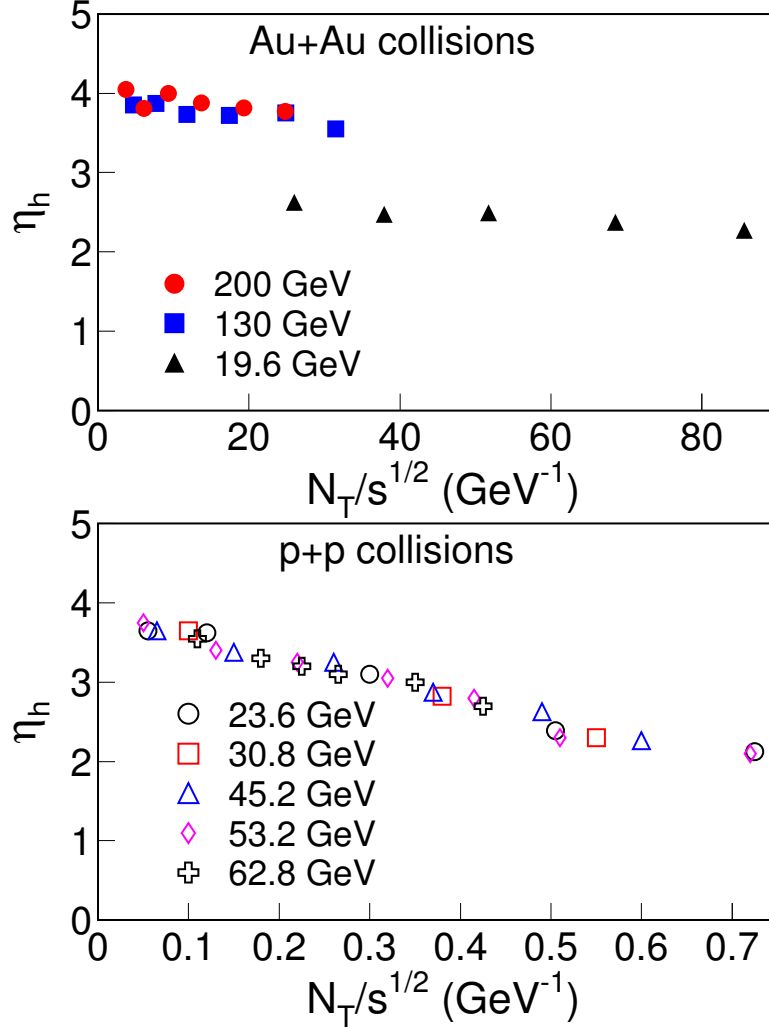


Figure 5.14: Half width at half maximum of the pseudorapidity distributions (η_h) of charged particles as a function of total charged particle multiplicity (N_T) normalized to the center-of-mass energy. The Au + Au collision data are from the PHOBOS experiment and $p + p$ collision data are from the ISR experiments.

observed in $p + p$ collisions. This may reflect the change in the mechanism of particle production over the full pseudorapidity range as we increase the $\sqrt{s_{NN}}$ from 19.6 GeV to $\sqrt{s_{NN}} > 130$ GeV in Au + Au collisions at RHIC.

5.3 Scaling of particle production

After having discussed the event-by-event measurement of photon and charged particle multiplicities in the previous section, we now discuss the variation of average (averaged over number of events) photon and charged particle multiplicities within

the full coverage of the PMD and FTTPC, respectively, with centrality. Collision centrality is expressed in terms of either number of participating nucleons or number of binary collisions. This will provide information on the contribution of hard (pQCD jets) and soft processes to particle production at forward rapidity. The scaling of particle production with the number of participating nucleons indicates the dominance of soft processes while scaling with the number of binary collisions indicates the onset of hard processes.

The pseudorapidity density ($dN/d\eta$) and transverse energy pseudorapidity density ($dE_T/d\eta$) at mid-rapidity is found to increase with increase in centrality of the reaction at SPS [41, 42] and RHIC energies [7, 43, 44]. This has been claimed to be understood using a simple geometrical picture of collision. At SPS energies, it was found that the particle production scales with the number of participating nucleons (N_{part}).

$$\frac{dN}{d\eta} \propto N_{\text{part}}^\alpha \quad (5.5)$$

The value of α for photons and charged particles at SPS energies were found to be 1.12 ± 0.03 and 1.07 ± 0.05 respectively [41, 42]. While that for E_T is 1.08 ± 0.06 . Within the quoted systematic errors the value of α is similar for both photons, charged particles and transverse energy. The value of α indicates a deviation from the picture of a naive wounded nucleus model ($\alpha = 1$).

At RHIC energies, it was found that the contribution from hard processes had a major role in understanding particle production [25]. The centrality dependence of charged particle pseudorapidity density ($dN_{\text{ch}}/d\eta$) was explained using the following relation,

$$\frac{dN_{\text{ch}}}{d\eta} \propto \beta N_{\text{part}} + (1 - \beta) N_{\text{coll}} \quad (5.6)$$

where N_{coll} is the number of binary collisions, the parameter β is the relative fraction of particles produced in soft collisions, and $(1 - \beta)$ is the relative fraction produced in hard collisions. It was observed that the fraction of the hadron multiplicity originating from hard processes at center-of-mass energy $\sqrt{s_{\text{NN}}} = 56$ GeV was 22% and that at 130 GeV was 37%. However this fraction does not increase much for 200 GeV, thereby bringing in some inconsistency with such an approach. This is because one expects the relative contribution from hard process to increase with increase in collision energy.

Another approach is to consider that the nucleus-nucleus collision is a superposition of constituent quarks collisions. Such a model has been used to show that the centrality dependence of charged particle pseudorapidity density at mid-rapidity

for RHIC energies is proportional to the number of participating constituent quarks (N_{qpart}) [45].

In this thesis we would like to examine the possibility of scaling of $dN_{\text{ch}}/d\eta$ and $dN_{\gamma}/d\eta$ from STAR experiment at forward rapidity for $\sqrt{s_{\text{NN}}} = 62.4$ GeV with N_{part} , N_{coll} and N_{qpart} . We will also briefly review the mid-rapidity results at SPS [41, 42] and RHIC energies [7, 43, 44].

5.3.1 Scaling of particle production with N_{part}

In Fig. 5.15 the upper panel of the plot shows the variation of total number of charged particles normalized to number of participating nucleon pair in the pseudorapidity coverage of ($2.9 \leq \eta \leq 3.9$) from FTPC as a function of centrality of the collision. The lower panel of the plot shows the variation of total number of photons normalized to the number of participating nucleon pair in the pseudorapidity coverage of ($2.3 \leq \eta \leq 3.7$) from the PMD as a function of collision centrality. The centrality of the collision system in heavy ion collision is defined with the help of number of participating nucleons during the collision. Higher N_{part} values correspond to more central collisions, or collisions with smaller impact parameter. The charged particle yield per participating nucleon pair at forward rapidity decreases from peripheral to central collisions. The photon production per participant pair is found to be approximately constant with centrality in the forward η range studied.

5.3.2 Scaling of particle production with N_{coll}

Figure 5.16 shows the variation of the total number of charged particles normalized to the number of collisions in the FTPC coverage ($2.9 \leq \eta \leq 3.9$) and the total number of photons normalized to the number of collisions in the PMD coverage ($2.3 \leq \eta \leq 3.7$) as a function of the number of binary collisions. Higher N_{coll} values correspond to more central collisions, or collisions with smaller impact parameter. Both the charged particle yield and photon yield normalized to the number of binary collisions do not scale with the number of binary collisions at forward rapidity. The data value decreases from peripheral to central collisions. This indicates that the contribution of hard processes to particle production at forward rapidity is small.

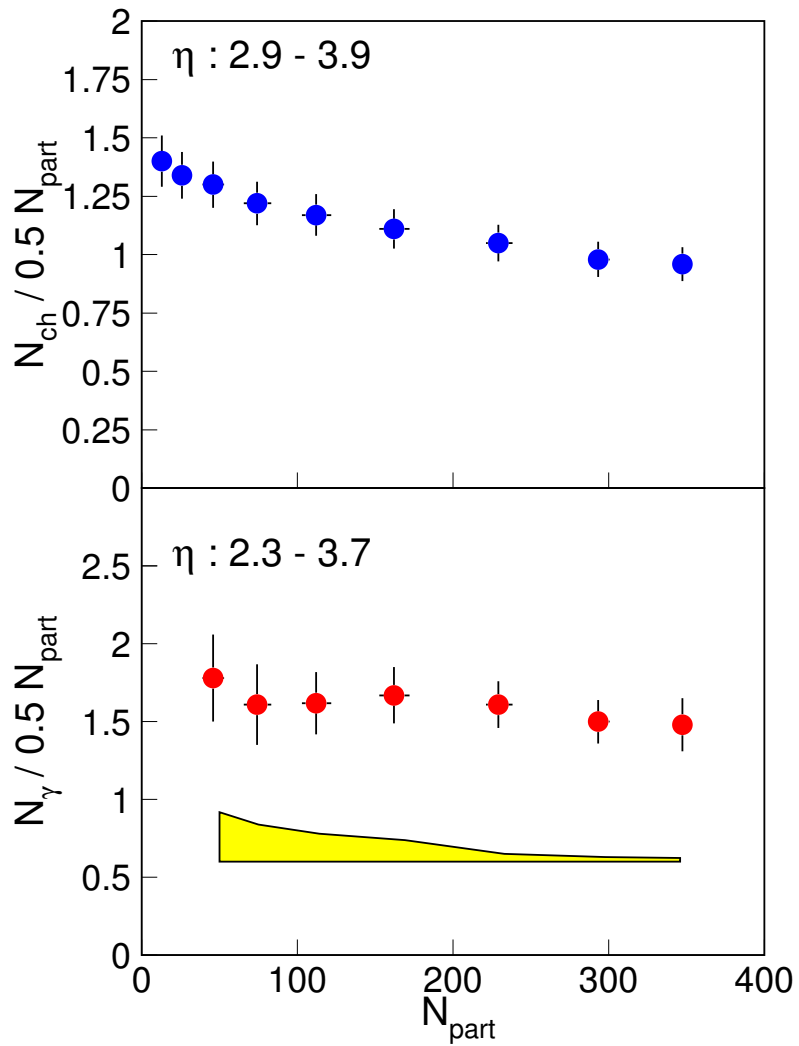


Figure 5.15: Variation of N_{ch} normalized to the number of participating nucleon pair in the FTPC coverage ($2.9 \leq \eta \leq 3.9$) and N_{γ} normalized to the number of participating nucleon pair in the PMD acceptance ($2.3 \leq \eta \leq 3.7$) as a function of N_{part} . The lower band shows the uncertainty in the ratio due to uncertainties in N_{part} calculations.

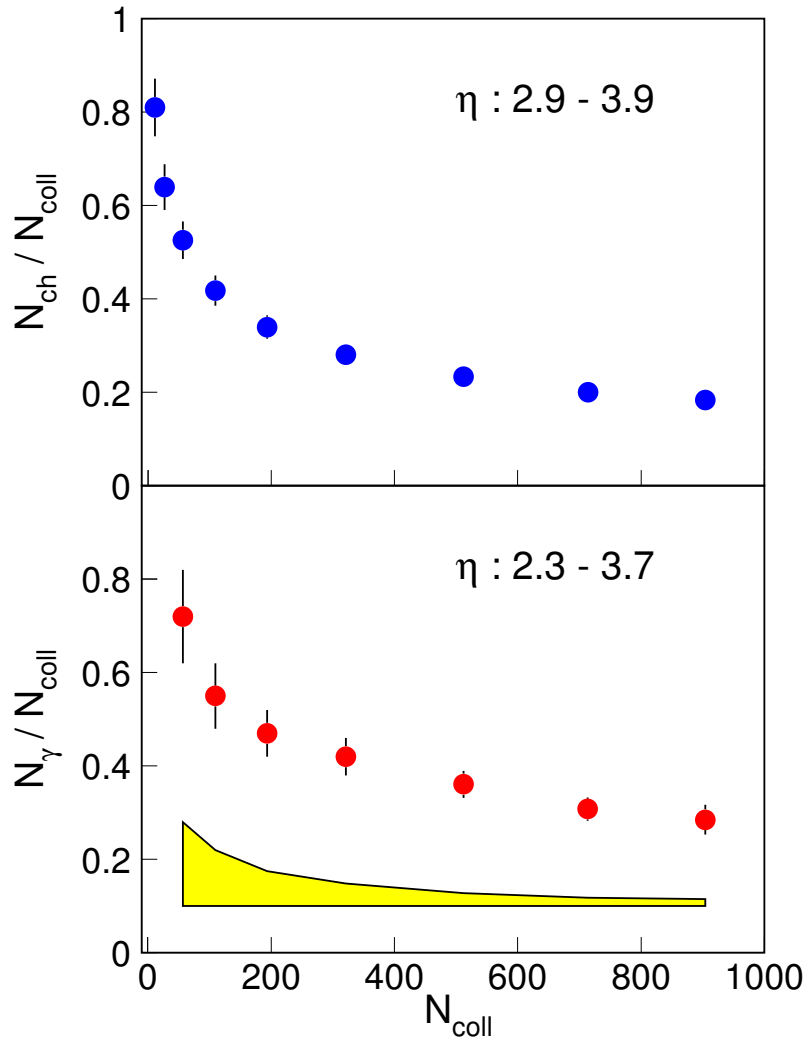


Figure 5.16: Variation of N_{ch} normalized to the number of collisions in the FTPC coverage ($2.9 \leq \eta \leq 3.9$) and N_{γ} normalized to number of collisions, in the PMD coverage ($2.3 \leq \eta \leq 3.7$) as a function of N_{coll} . The lower band shows the uncertainty in the ratio due to uncertainties in N_{coll} calculations.

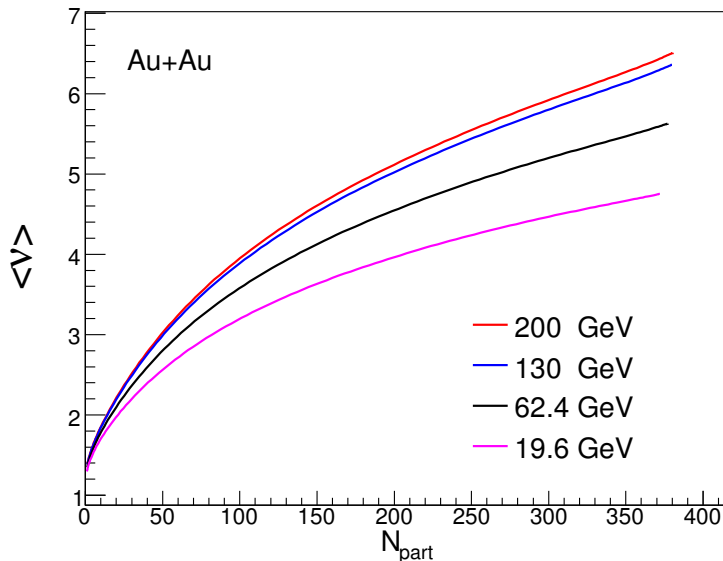


Figure 5.17: Variation of average number of binary collisions ($\langle \nu \rangle$) suffered by single nucleon in Au+Au collisions at various $\sqrt{s_{\text{NN}}}$ at RHIC as a function of N_{part} .

5.3.3 Scaling of particle production with N_{qpart}

Before going to discuss the results of the scaling of the $dN_{\text{ch}}/d\eta$ and $dE_T/d\eta$ with N_{qpart} let us briefly discuss the process of obtaining the N_{qpart} and N_{part} in heavy ion collisions. The mean number of nucleon and quark participants is calculated in a similar manner as in Ref. [45]. A Wood - Saxon nuclear density profile as given below, is used for our calculations.

$$n_A(r) = \frac{n_0}{1 + \exp[(r - R)/d]} \quad (5.7)$$

with parameters $n_0 = 0.17 \text{ fm}^{-3}$, $R = (1.12A^{1/3} - 0.86A^{-1/3}) \text{ fm}$, $d = 0.54 \text{ fm}$. The N_{part} for nucleus-nucleus (AB) collisions is calculated using the relation,

$$N_{\text{part,AB}} = \int d^2s T_A(\vec{s}) \{1 - [1 - \sigma_{\text{NN}} T_B(\vec{s} - \vec{b})/B]^B\} + \int d^2s T_B(\vec{s}) \{1 - [1 - \sigma_{\text{NN}} T_A(\vec{s} - \vec{b})/A]^A\} \quad (5.8)$$

where $T(b) = \int_{-\infty}^{+\infty} dz n_A(\sqrt{b^2 + z^2})$, is the thickness function which is defined as the probability for having a nucleon - nucleon (NN) collision within the transverse area element db when one nucleon is situated at an impact parameter b relative to another nucleon. We use the inelastic NN cross section $\sigma_{\text{NN}} = 30 \text{ mb}$, 41 mb , 42 mb at $\sqrt{s_{\text{NN}}} = 17.3 \text{ GeV}$, 130 GeV , 200 GeV respectively. The average number of binary collisions ($\langle \nu \rangle$) suffered by a nucleon in the collision of Au nuclei for various $\sqrt{s_{\text{NN}}}$ as calculated in this model is shown in Fig. 5.17. The $\langle \nu \rangle$ increases with increase in $\sqrt{s_{\text{NN}}}$ and with N_{part} for a given $\sqrt{s_{\text{NN}}}$ at RHIC energies. In a similar manner the N_{qpart} is also calculated keeping in mind, the density was changed

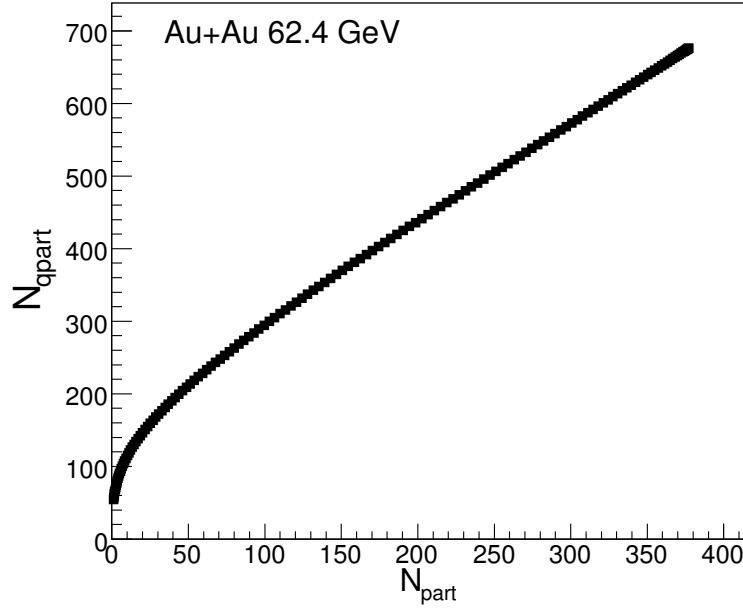


Figure 5.18: Variation of N_{qpart} with N_{part} for Au+Au collisions at $\sqrt{s_{\text{NN}}} = 62.4$ GeV.

to three times that of the nucleon density ($n_0^q = 3n_0 = 0.51 \text{ fm}^{-3}$). The cross sections are also changed in accordance with $\sigma_{qq} = \sigma_{NN}/9 = 3.33 \text{ mb}$, 4.55 mb , 4.66 mb for $\sqrt{s_{\text{NN}}} = 17.3 \text{ GeV}$, 130 GeV , 200 GeV respectively [45]. The variation of N_{qpart} with N_{part} for Au+Au collisions at $\sqrt{s_{\text{NN}}} = 62.4 \text{ GeV}$ is shown in Fig. 5.18.

Fig. 5.19 shows the $(dN_{\text{ch}}/d\eta)/N_{\text{part}}$, $(dN_{\gamma}/d\eta)/N_{\text{part}}$ and $(dE_{\text{T}}/d\eta)/N_{\text{part}}$ as a function of centrality at SPS energy. The lower panel shows the values for per quark participant. The error bars shown are the systematic errors. The data values are for the WA98 experiment [41, 42]. It is observed that the values of the observables per nucleon participant increases as one goes from peripheral collisions to central collisions. Whereas it remains fairly constant for the case of quark participants. It may also be noted that the values for charged particles and photons are of similar order. Fig. 5.20 shows the $(dN_{\text{ch}}/d\eta)/N_{\text{part}}$, and $(dE_{\text{T}}/d\eta)/N_{\text{part}}$ as a function of centrality for $\sqrt{s_{\text{NN}}} = 130 \text{ GeV}$ and $(dN_{\text{ch}}/d\eta)/N_{\text{part}}$ for $\sqrt{s_{\text{NN}}} = 200 \text{ GeV}$ at RHIC. The lower panel shows the values for per quark participant. The error bars shown are the systematic errors. The data taken are from the PHENIX [43] and PHOBOS experiments [7, 44]. Similar to the case of SPS energy, here also the values of the observables per nucleon participant increases as one goes from peripheral collisions to central collisions. While it remains fairly constant for the case of quark participants. The differences between $(dN_{\text{ch}}/d\eta)/N_{\text{part}}$ or $(dN_{\text{ch}}/d\eta)/N_{\text{part}}$ at $\sqrt{s_{\text{NN}}} = 130 \text{ GeV}$ and 200 GeV is not much. However there is a general trend of increase in value of $(dN_{\text{ch}}/d\eta)/N_{\text{qpart}}$ and $(dE_{\text{T}}/d\eta)/N_{\text{qpart}}$ with increase in $\sqrt{s_{\text{NN}}}$.

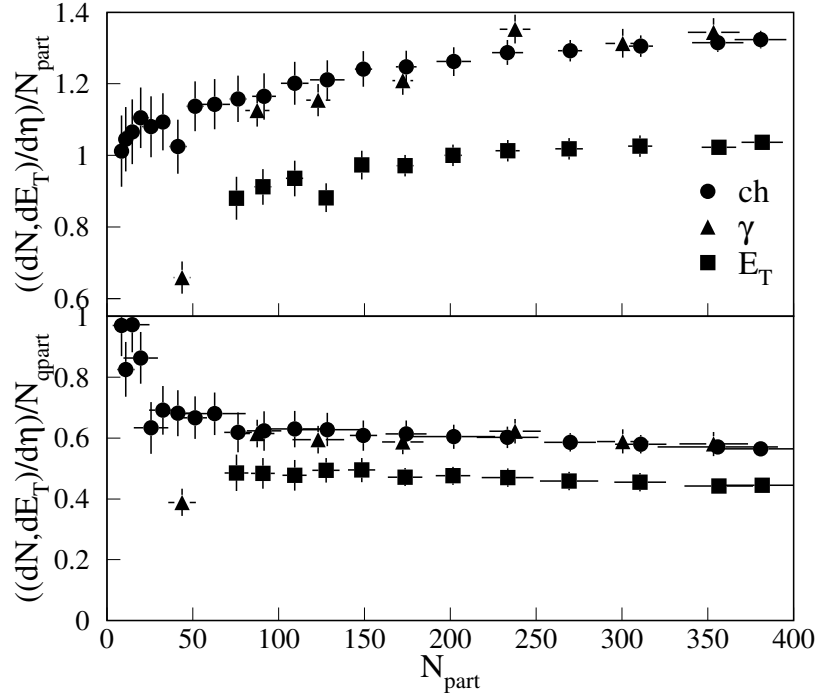


Figure 5.19: $N_{\text{ch}}, N_{\gamma}$ and E_T per nucleon (N_{part}) and per constituent quark participant (N_{qpart}) as a function of number of participating nucleons for SPS energy.

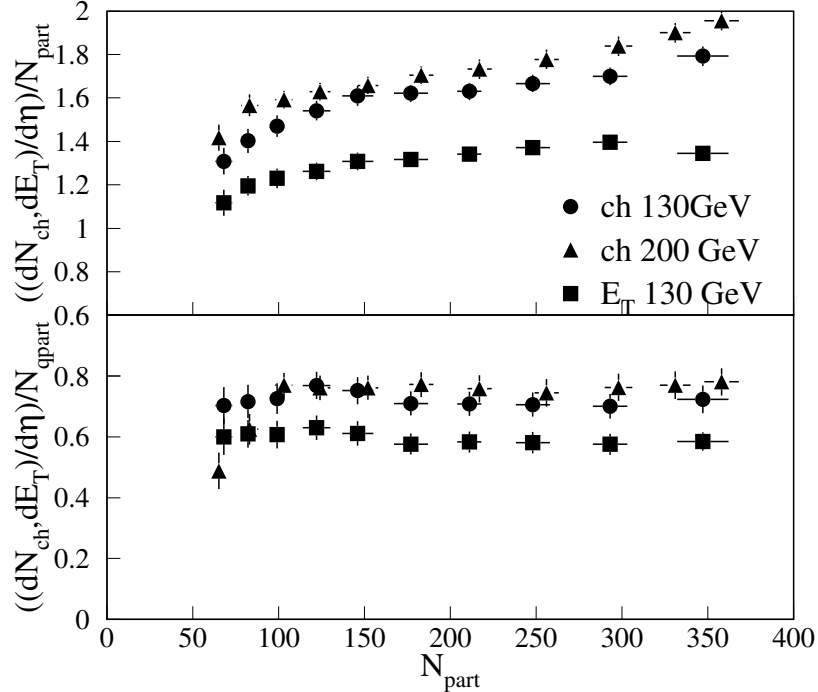


Figure 5.20: N_{ch} and E_T per nucleon (N_{part}) and per constituent quark participant (N_{qpart}) as a function of number of participating nucleons for RHIC energies.

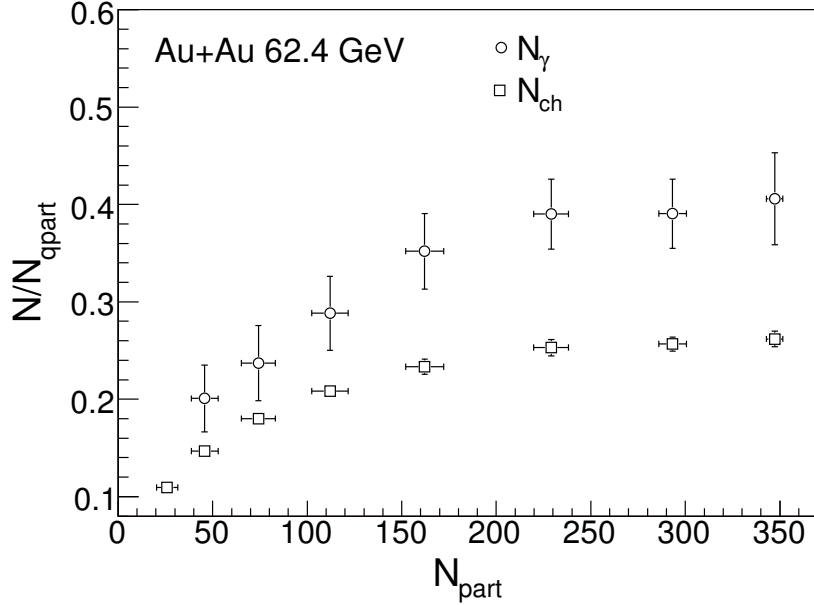


Figure 5.21: N_{γ} and N_{ch} per quark participant as a function of number of participating nucleons at forward rapidity for Au+Au collisions at 62.4 GeV.

However at forward rapidities, the particle production does not scale with N_{qpart} . This is shown in Fig. 5.21 for the photons and charged particles for Au+Au collisions at $\sqrt{s_{\text{NN}}} = 62.4$ GeV.

5.4 Longitudinal Scaling

The particle production in high energy collisions, is observed to be associated with smaller transverse momenta of the produced particles compared to the beam momentum. The incoming projectile and target have large longitudinal momenta. These breaks apart in the collision process, producing particles, some of which carry a large longitudinal momentum. These outgoing particles would prefer to travel in the beam momentum direction. The produced particle distribution when plotted as a function of $y - y_{\text{beam}}$, where y_{beam} is the beam rapidity, for various center-of-mass energies approaches limiting distributions. This intuitive picture of a high-energy collision process as two extended objects going through each other, breaking into fragments in the process, is described within the framework of a

hypothesis of Limiting Fragmentation as discussed in the reference [46, 47]. The variable rapidity is chosen as it is related to the longitudinal momentum p_L through the relation,

$$y = \frac{1}{2} \ln \frac{E + p_L}{E - p_L} \quad (5.9)$$

where, E is the energy of the particle. The beam rapidity of the projectile or target is defined as

$$\frac{\sqrt{s_{NN}}}{2m_n} = \cosh(y_{beam}) \quad (5.10)$$

where, $m_n =$ mass of nucleon.

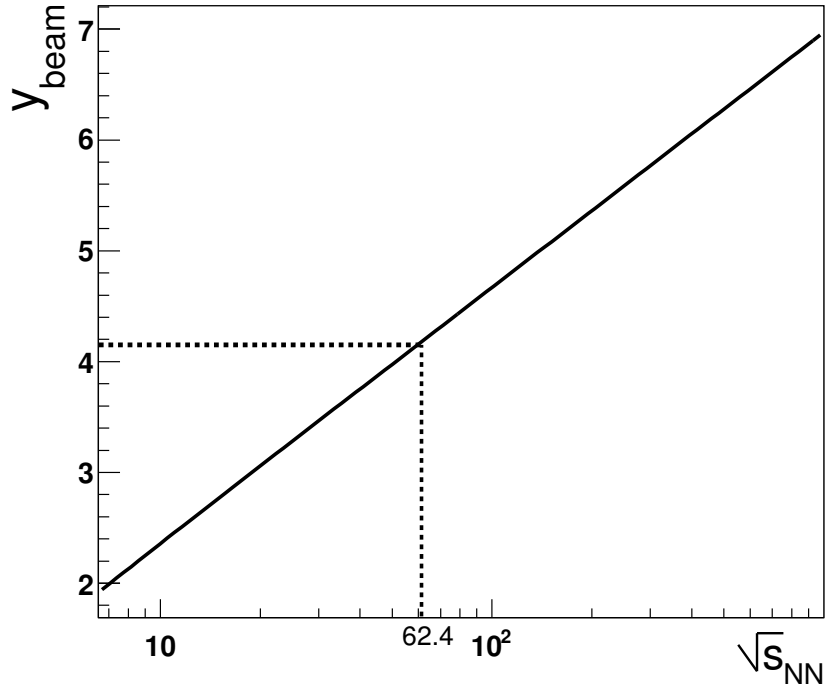


Figure 5.22: The figure shows the relation between the center-of-mass energy ($\sqrt{s_{NN}}$) and the beam rapidity(y_{beam}).

The Fig. 5.22 shows the relation between the center-of-mass energy and the beam rapidity. For e.g. $\sqrt{s_{NN}} = 62.4$ GeV center-of-mass energy the beam rapidity (y_{beam}) is 4.19.

5.4.1 Longitudinal scaling for $e^+ + e^-$, $p+p(\bar{p})$ and $p(d)+\text{Au}$ collision

In this sub-section we discuss the longitudinal scaling from $e^+ + e^-$, $p+p$ and $d+\text{Au}$ collisions. In Fig. 5.23 (top) the dN_{ch}/dy_T as a function of $y_T - y_{\text{jet}}$ is plotted for various center-of-mass energies from the $e^+ + e^-$ collision. y_T is defined as rapidity value corresponding to the thrust axis of a jet and $y_{\text{jet}} \equiv \ln(\sqrt{s}/M_j)$, where M_j is the mass of the jet ~ 1 GeV.

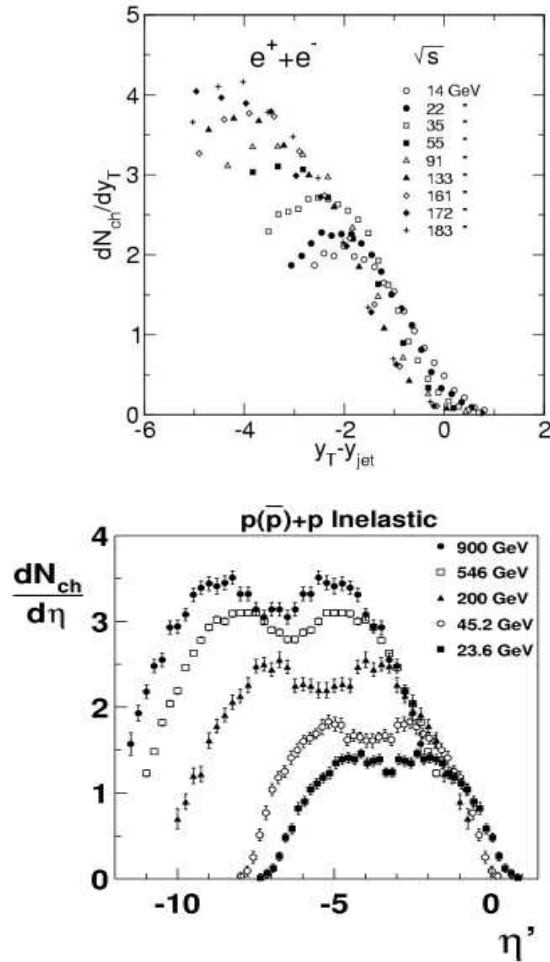


Figure 5.23: Top : Longitudinal scaling in $e^+ + e^-$ collisions. dN_{ch}/dy_T is plotted as a function of $y_T - y_{\text{jet}}$. Bottom : Longitudinal scaling in $p(\bar{p})+p$ inelastic collisions. $dN_{\text{ch}}/d\eta$ is plotted as a function of $y - y_{\text{beam}}$.

The longitudinal scaling is observed in the elementary particle ($e^+ + e^-$) collisions over a factor of 10 variation in \sqrt{s} . In Fig. 5.23 (bottom) the $dN_{\text{ch}}/d\eta$ is plotted as a function of $y - y_{\text{beam}}$ for $p(\bar{p})+p$ inelastic collisions for various center-of-mass energies ranging from 23.6 GeV to 900 GeV. The longitudinal scaling for charged particles is observed in the $p(\bar{p})+p$ collisions for various center-of-mass energies [40, 48, 49].

In d+Au collisions at RHIC the longitudinal scaling is studied by the PHOBOS experiment. The Fig. 5.24 shows the $dN_{\text{ch}}/d\eta$ in the effective rest frame of both projectile beam (a) and target (b). The results from d+Au have been compared with

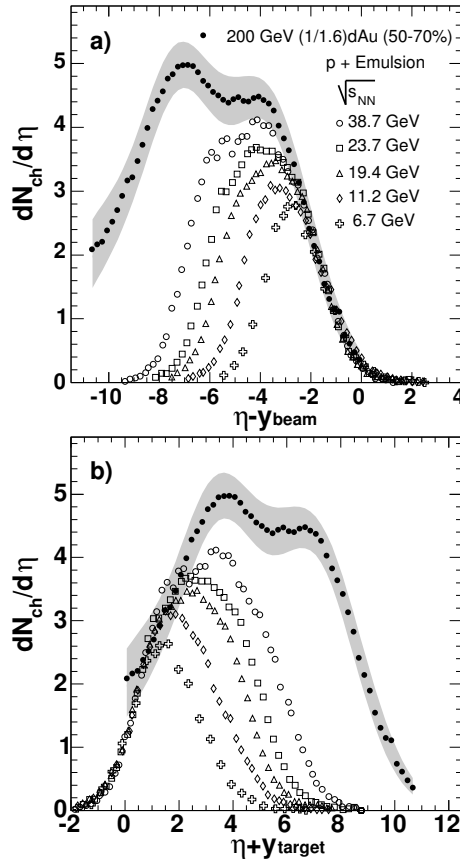


Figure 5.24: (a): The comparison of $dN_{\text{ch}}/d\eta$ distributions for d+Au collisions at $\sqrt{s_{\text{NN}}} = 200$ GeV to p+Em collisions at five energies. the η measured in the center-of-mass system has been shifted to $\eta - y_{\text{beam}}$ in order to study the fragmentation regions in deuteron/proton rest frame. (b): similar to (a) but shifted to $\eta + y_{\text{beam}}$ in order to study the fragmentation regions in gold/Emulsion rest frame.

the p+Emulsion(EM) collisions at five energies [50]. A good agreement(limiting fragmentation) is observed in the fragmentation regions of deuteron(gold) between d+Au and p+Em collisions at different energies. Furthermore, the overlap between the fragmentation regions of deuteron(gold) and proton(Em) extends to lower $|\eta|$ with increasing collision energy.

5.4.2 Energy dependence of longitudinal scaling in nucleus-nucleus collisions

In this section we study the longitudinal scaling of photons and charge particles in the forward pseudorapidity region to test the limiting fragmentation hypothesis in heavy ion collisions. In Fig. 5.25 we present the energy dependence of limit-

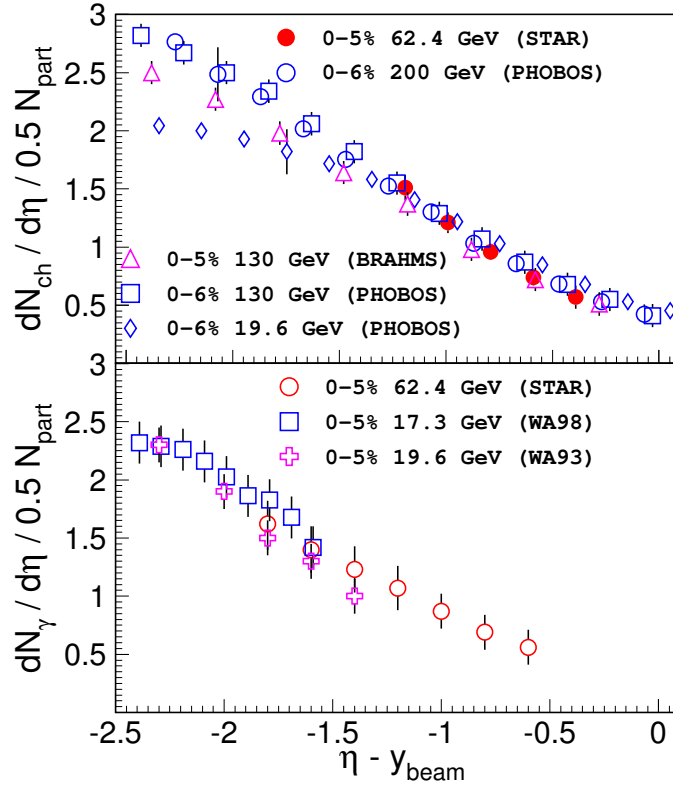


Figure 5.25: Top : Variation of $dN_{\text{ch}}/d\eta$ normalized to N_{part} with $\eta - y_{\text{beam}}$ for different collision energies for central collisions. Bottom : Variation of $dN_{\gamma}/d\eta$ normalized to N_{part} with $\eta - y_{\text{beam}}$ for different collision energies for central collisions.

ing fragmentation for inclusive charged particles and photons. The pseudorapidity distributions normalized to the number of participating nucleons are plotted as a function of $\eta - y_{\text{beam}}$. The charged particle pseudorapidity distribution for central (0–5%) Au + Au collisions at $\sqrt{s_{\text{NN}}} = 62.4$ GeV is compared to the charged particle pseudorapidity distributions from PHOBOS for central (0–6%) collisions at 19.6 GeV, 130 GeV and 200 GeV [7] and charged particle pseudorapidity distribution from BRAHMS for central (0–5%) collisions at 130 GeV [23]. The photon pseudorapidity distributions for central (0–5%) Au + Au collisions at $\sqrt{s_{\text{NN}}} = 62.4$ GeV is compared with central (0–5%) photon data for Pb + Pb collisions at 17.3 GeV from the WA98 experiment [41] and 19.6 GeV central (0–5%) S + Au collision data from the WA93 experiment [51]. We observe in Fig. 5.25 that the SPS and RHIC (62.4 GeV) photon results are consistent with each other, suggesting that photon production follows an energy independent limiting fragmentation behavior. The charged particles at 62.4 GeV also show an energy independent limiting fragmentation behavior.

5.4.3 Centrality dependence of longitudinal scaling in nucleus-nucleus collisions

In Fig. 5.26 we show the centrality dependence of limiting fragmentation for charged particles and photons. The charged particle and photon pseudorapidity distributions normalized to number of participating nucleon pair as a function of $\eta - y_{\text{beam}}$ are plotted. The charged particle and photon pseudorapidity distributions for 0–5% is compared to 40–50% central Au + Au collisions at $\sqrt{s_{\text{NN}}} = 62.4$ GeV. We observe, at forward rapidity, the charged particle yield normalized to the number of participating nucleons as a function of $\eta - y_{\text{beam}}$ is higher for peripheral collisions compared to central collisions, whereas within the measured η range of 2.3 to 3.7, the photon yield normalized to the number of participating nucleons as a function of $\eta - y_{\text{beam}}$ is found to be independent of centrality. The dependence of longitudinal scaling on the collision system is most clearly seen in the comparison between results from heavy ion collisions with those from $p + p$ and $p + \bar{p}$ collisions [52]. We observe in Fig. 5.26 that the photon results in the forward rapidity region from $p + \bar{p}$ collisions at $\sqrt{s} = 540$ GeV are in close agreement with the measured photon yield in Au + Au collisions at $\sqrt{s_{\text{NN}}} = 62.4$ GeV. However the $p + p$ and $p + \bar{p}$ inclusive charged particle results are very different from those for Au + Au collisions at $\sqrt{s_{\text{NN}}} = 62.4$ GeV. It may be mentioned that the photon

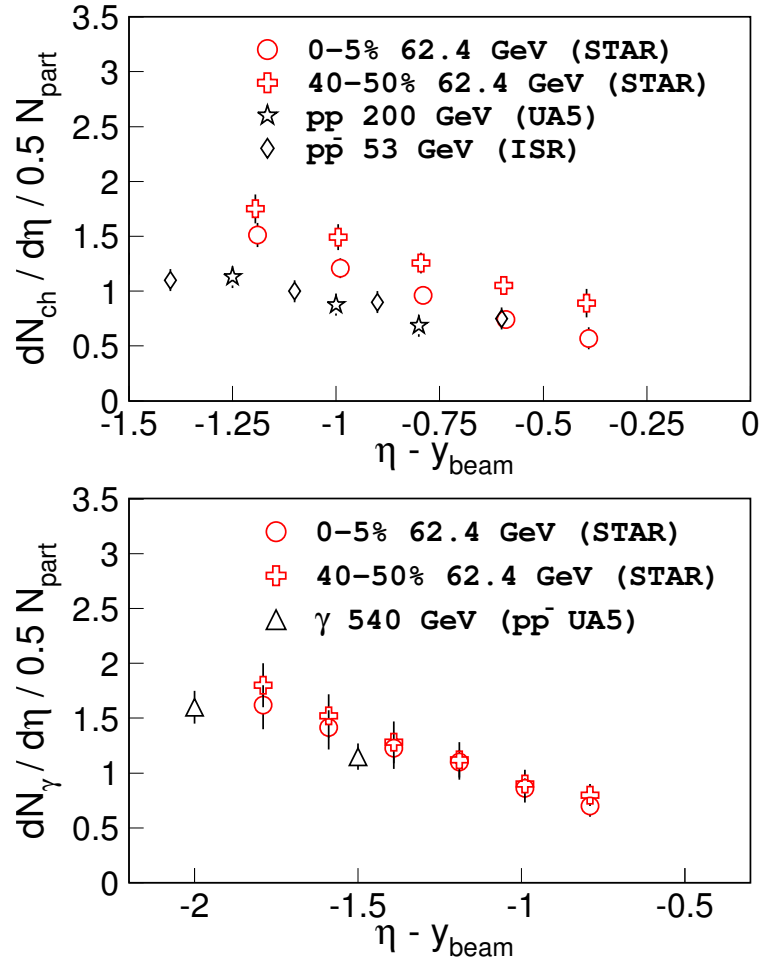


Figure 5.26: Top : Variation of $dN_{\text{ch}}/d\eta$ normalized to N_{part} with $\eta - y_{\text{beam}}$ for the central and peripheral collisions. Bottom : Variation of $dN_{\gamma}/d\eta$ normalized to N_{part} with $\eta - y_{\text{beam}}$ for the central and peripheral. Also shown are the charged particle and photon yields in $p + p$ at and $p + \bar{p}$ collisions.

yield is dominated by photons from decay of π^0 s [9]. The presented photon results and their comparison with nucleon-nucleon collisions indicate that in the η region studied, there is apparently a significant charged baryon contribution in nucleus-nucleus collisions. Similar centrality dependent behavior of longitudinal scaling for charged particles was also observed by PHOBOS [7]. The centrality dependence of longitudinal scaling in charged particles has been speculated to be due to nuclear remnants and baryon stopping [7, 10] both of which changes with centrality. The role of a new mechanism of baryon production as discussed in Refs. [10, 11] also needs to be understood. The centrality independent longitudinal scaling for

photons has been attributed to mesons being the dominant source of photon production [9]. HIJING [21] calculations indicate that about 93–96% of the photons are from π^0 decays.

It may be mentioned that, there have been contradictory results reported from inclusive charged particle measurements regarding the centrality dependence of the longitudinal scaling. Results from PHOBOS show a centrality dependence [7], while those from BRAHMS show a centrality independent behavior [23]. Next we will investigate the source of centrality dependence of longitudinal scaling for charged particles at $\sqrt{s_{\text{NN}}} = 62.4$ GeV in detail. In order to understand the role of nuclear remnants and baryon stopping in the observed centrality dependent behavior of longitudinal scaling of charged particles, we have studied the longitudinal scaling for positively and negatively charged hadrons separately. The contribution from protons coming from beam remnants can be understood by studying the longitudinal scaling of positively charged hadrons. In Fig. 5.27 we have plotted

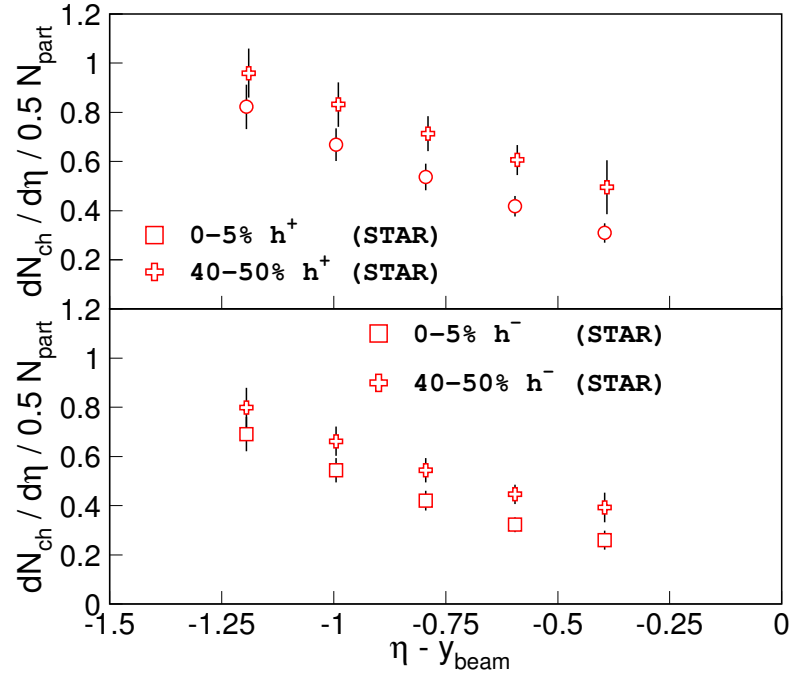


Figure 5.27: Top : Variation of $dN_{\text{ch}}/d\eta$ normalized to N_{part} with $\eta - y_{\text{beam}}$ for central and peripheral collisions for positively charged hadrons (h^+) (top) and negatively charged hadrons (h^-) (bottom) in Au+Au collisions at $\sqrt{s_{\text{NN}}} = 62.4$ GeV.

$\frac{dN_{ch}}{d\eta}$ normalized to the number of participating nucleons for 40–50% and for 0–5% central collisions for positively (h^+) and negatively charged (h^-) hadrons. In addition to the systematic errors discussed earlier, and shown in the Fig. 5.27, there is an error due to the uncertainty in the charge determination. The uncertainty has been studied by embedding charged Monte Carlo tracks into real data and then following the full reconstruction chain. This error was obtained as a function of η . It is defined as the ratio of the total number of embedded charged tracks whose charge has been reconstructed incorrectly, to the total number of charged tracks embedded. The error in charge determination was found to increase from 2% at $\eta = 2.9$ to 15% at $\eta = 3.9$. We find that both h^+ and h^- show a centrality dependent longitudinal scaling. When compared to the centrality independent longitudinal scaling for photons (Fig. 5.26) and to results from nucleon-nucleon collisions (Fig. 5.26), our measurements indicate that baryon transport at forward rapidity also plays an important role in the observed centrality dependent behavior of longitudinal scaling for charged particles. We find that the ratio for yields of h^+ from peripheral to central collisions increases from 1.17 ± 0.06 at $\eta = 3.0$ to 1.61 ± 0.07 at $\eta = 3.8$ (closer to beam rapidity). The values for h^- are 1.16 ± 0.06 at $\eta = 3.0$ and 1.51 ± 0.07 at $\eta = 3.8$. From these values we find that the increase in the ratio with η seems to be weaker for h^- compared to h^+ . However, within the systematic errors, it is difficult to conclude on the role of the beam remnants (beam protons in h^+) in the centrality dependent behavior of longitudinal scaling for charged particles at forward rapidity.

5.4.4 Species dependence of longitudinal scaling

The observation of centrality dependent and energy independent longitudinal scaling for inclusive charged particles, along with the centrality and energy independent longitudinal scaling for photons (presented in previous sections), motivates us to study the longitudinal scaling of identified particles. Fig. 5.28 shows the charged pion rapidity density in central Au + Au collisions at RHIC [53], Pb + Pb collisions at the SPS [54] and Au + Au collisions at AGS [2]. Also shown is the estimated π^0 rapidity density from the present measurement of the photon rapidity density at $\sqrt{s_{NN}} = 62.4$ GeV, all as a function of $y - y_{beam}$ [9]. We obtained the ratio of the photon to π^0 yields from HIJING. This ratio is used to estimate the π^0 yield from the measured photon yield. The results indicate that the pion production in heavy ion collisions in the fragmentation region agrees with the energy independent limiting fragmentation. Fig. 5.29 shows the net proton ($p - \bar{p}$) rapidity density in central

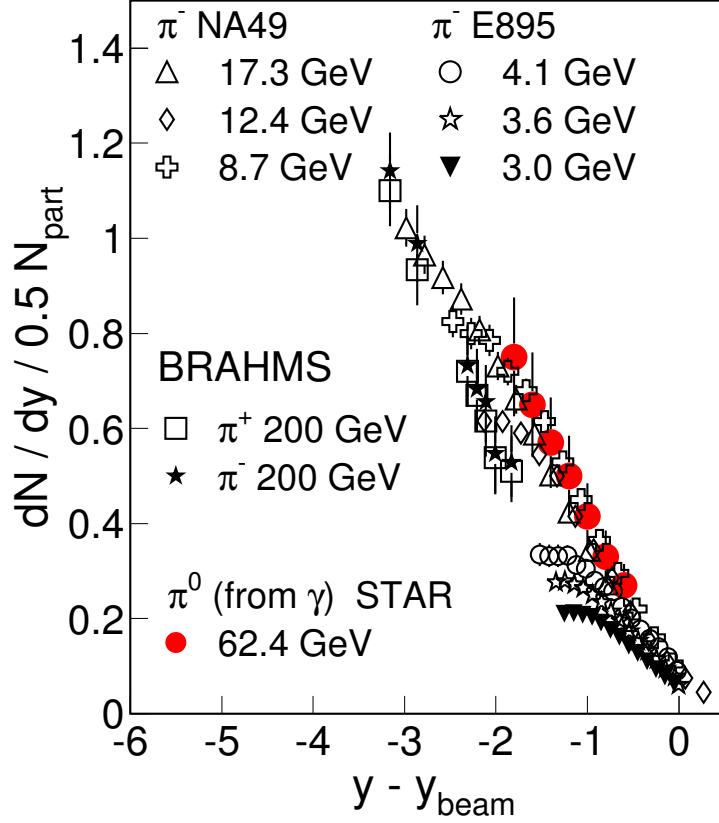


Figure 5.28: Variation of pion rapidity density normalized to N_{part} with $y - y_{\text{beam}}$ for central collisions at various collision energies. Also shown is the estimated dN_{π^0}/dy obtained from dN_{γ}/dy normalized to N_{part} .

Au + Au collisions at RHIC [26] energies and Pb + Pb collisions at SPS [55] energies. For AGS energies [2, 56] we plot only the proton rapidity density in Au + Au collisions. Since the anti-proton yields are very low ($\bar{p}/p \sim 2 \times 10^{-4}$ at top AGS energy), the proton rapidity density reflects the net proton rapidity distribution. The net protons violate the energy dependence of limiting fragmentation. These results show that baryons and mesons differ in the energy dependence of limiting fragmentation. The results for identified particles, along with the centrality dependence of longitudinal scaling for inclusive charged hadrons, and the centrality independence of longitudinal scaling for identified mesons, shows that the baryon transport in heavy ion collisions plays an important role in particle production at

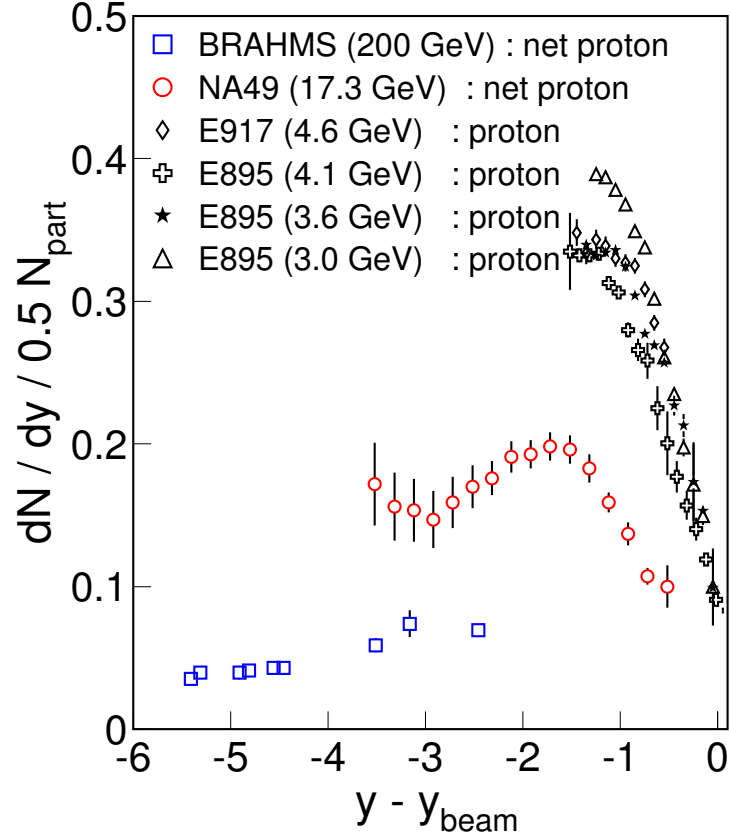


Figure 5.29: Variation of net proton rapidity density normalized to N_{part} with $y - y_{\text{beam}}$ for central collisions at various collision energies.

forward rapidity. The results also show that although baryon stopping is different in different collision systems, the pions produced at forward rapidity are not affected by baryon transport. The limiting fragmentation study for net protons may also indicate the validity of a baryon junction picture [10]. If the baryon numbers are carried by the valence quarks, then at forward rapidity the baryons should also follow an energy independent limiting fragmentation behavior, like pions (originating from valence quarks). This may indicate that the baryon number is not carried by the valence quark, which is suggested in the baryon junction picture, where the baryon number resides in a non-perturbative configuration of gluon fields, rather than in the valence quarks.

5.4.5 Longitudinal scaling in particle production models

Energy and centrality dependence longitudinal scaling for charged particles can be a test for particle production models. We have observed that particle production models such as HIJING and AMPT are not able to describe fully the η distribution of charged particles at forward rapidity. However, it is interesting to investigate whether they can qualitatively reproduce the longitudinal scaling features of experimental data. Our calculations show that in the HIJING and AMPT models the charged particles show energy independent longitudinal scaling. The centrality dependent behavior of longitudinal scaling for charged particles is more clearly observed in the AMPT model than in HIJING. In Fig. 5.30 and Fig. 5.31 we show the results from the AMPT model and HIJING respectively.

5.4.6 Longitudinal scaling in particle production models

In Fig. 5.30 results are for the $\sqrt{s_{\text{NN}}} = 19.6$ GeV, 62.4 GeV and 130 GeV Au + Au collisions for 0–3 fm (top) and 9–12 fm (bottom) impact parameter from AMPT model [22] calculations. For the centrality dependence we only show the results for $\sqrt{s_{\text{NN}}} = 19.6$ GeV (bottom), the energy at which the centrality dependent effect is most prominent in the data [7]. The AMPT model has qualitative longitudinal scaling features similar to those of experimental data (shown in Fig. 5.26). We find in the model that the central yields, when normalized to number of participating nucleons, are also lower than the corresponding peripheral yields at forward rapidity when η is shifted by the beam rapidity.

In Fig 5.31 we show the $dN_{\text{ch}}/d\eta$ normalized to N_{part} with $\eta - y_{\text{beam}}$ from HIJING model [21] for $\sqrt{s_{\text{NN}}} = 19.6$ GeV, 62.4 GeV, 130 GeV and 200 GeV for 0–3 fm (top) and 9–12 fm (middle) centrality classes. Also shown is the comparison of $dN_{\text{ch}}/d\eta$ normalized to number of participating nucleons as a function of $\eta - y_{\text{beam}}$ for 0–3 fm and 9–12 fm collision centrality classes for $\sqrt{s_{\text{NN}}} = 19.6$ GeV (bottom). The energy independent longitudinal scaling is observed in HIJING for the given center-of-mass energies, however a small centrality dependence is observed in the results from 19.6 GeV.

In Fig 5.32 we show the $dN_{\text{ch}}/d\eta$ normalized to N_{part} with $\eta - y_{\text{beam}}$ from HIJINGBB model [57] for $\sqrt{s_{\text{NN}}} = 19.6$ GeV, 62.4 GeV, 130 GeV and 200 GeV for 0–3 fm (top) and 9–12 fm (middle) centrality classes. Also shown is the comparison of $dN_{\text{ch}}/d\eta$ normalized to number of participating nucleons as a function of $\eta - y_{\text{beam}}$ for 0–3 fm and 9–12 fm collision centrality classes for $\sqrt{s_{\text{NN}}} = 19.6$ GeV

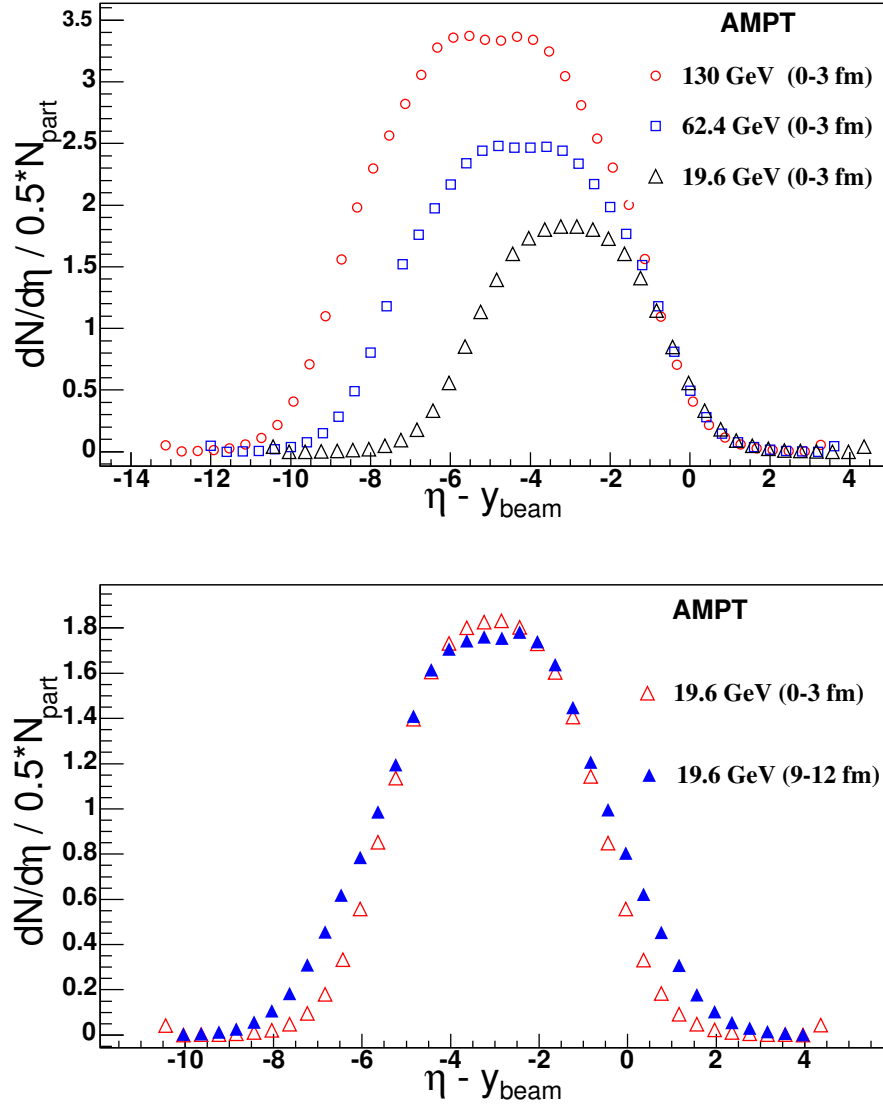


Figure 5.30: Top : Variation of $dN_{\text{ch}}/d\eta$ normalized to N_{part} with $\eta - y_{\text{beam}}$ from AMPT model calculations for various $\sqrt{s_{\text{NN}}}$ in 0-3 *fm* central collisions. Bottom : Variation of $dN_{\text{ch}}/d\eta$ normalized to N_{part} with $\eta - y_{\text{beam}}$ from AMPT model in 0-3 *fm* central and 9-12 *fm* peripheral collisions at $\sqrt{s_{\text{NN}}} = 19.6$ GeV.

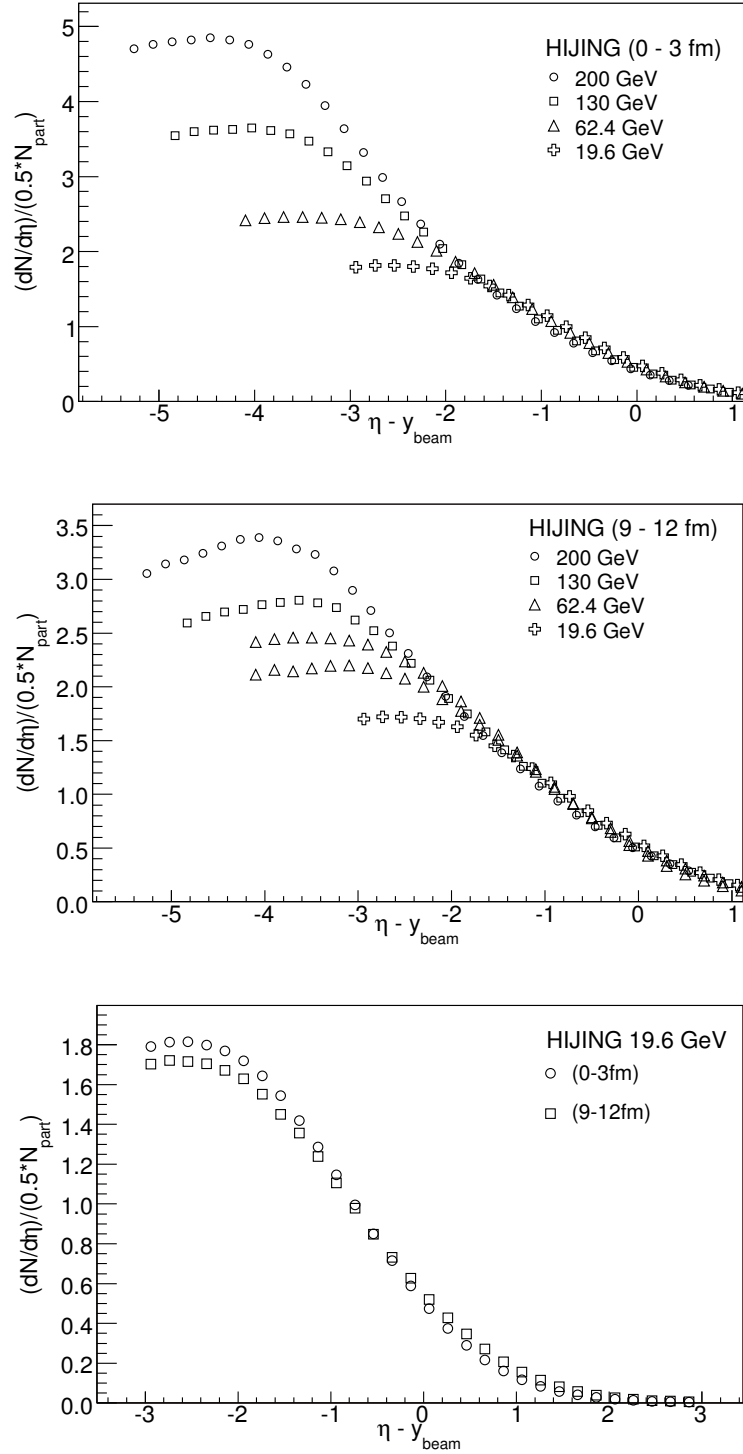


Figure 5.31: Variation of $dN_{ch}/d\eta$ normalized to N_{part} with $\eta - y_{beam}$ from HIJING model calculations for $\sqrt{s_{NN}} = 19.6$ GeV, 62.4 GeV, 130 GeV and 200 GeV in 0–3 *fm* central (top) and 9–12 *fm* peripheral (middle) collisions for energy independent longitudinal scaling. The comparison of central and peripheral collisions at $\sqrt{s_{NN}} = 19.6$ GeV for centrality dependent longitudinal scaling is shown in the bottom panel.

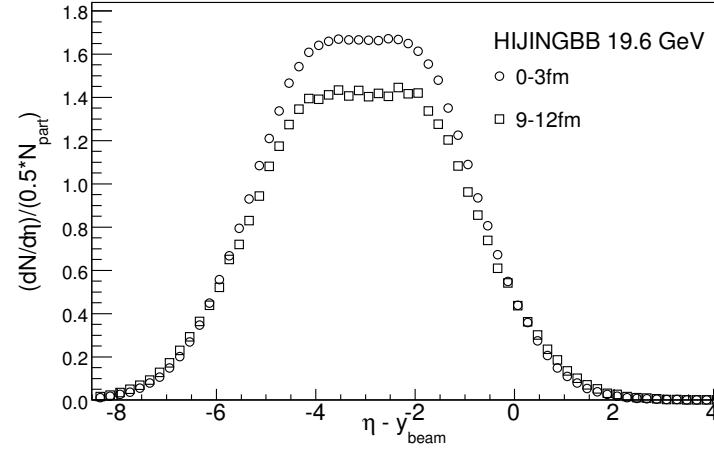
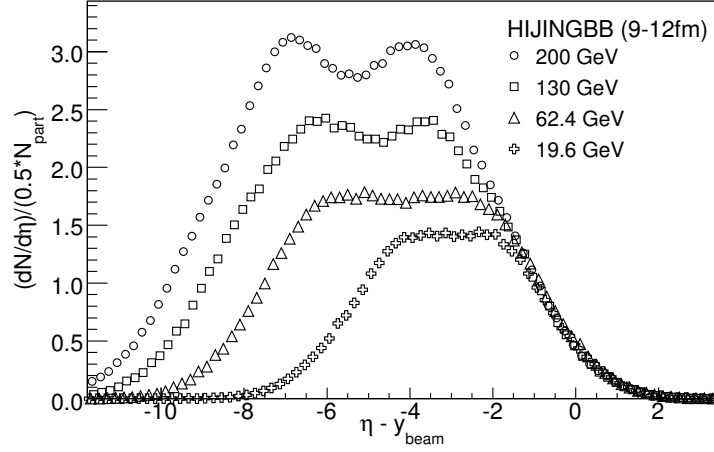
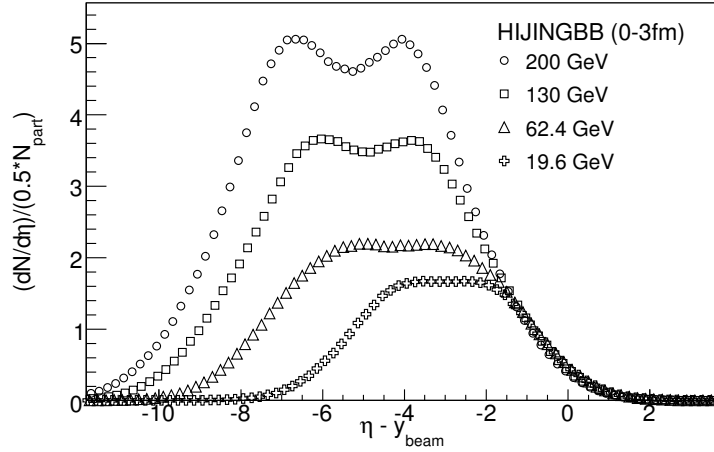


Figure 5.32: Variation of $dN_{\text{ch}}/d\eta$ normalized to N_{part} with $\eta - y_{\text{beam}}$ from the HIJINGBB model calculations for $\sqrt{s_{\text{NN}}} = 19.6$ GeV, 62.4 GeV, 130 GeV and 200 GeV in 0–3 fm central (top) and 9–12 fm peripheral (middle) collisions for energy independent longitudinal scaling. The comparison of central and peripheral collisions at $\sqrt{s_{\text{NN}}} = 19.6$ GeV for centrality dependent longitudinal scaling is shown in the bottom panel.

(bottom). The energy independent longitudinal scaling is observed in HIJINGBB (Fig. 5.32) for the given $\sqrt{s_{NN}}$, however a very weak centrality dependence is observed in the results from $\sqrt{s_{NN}} = 19.6$ GeV.

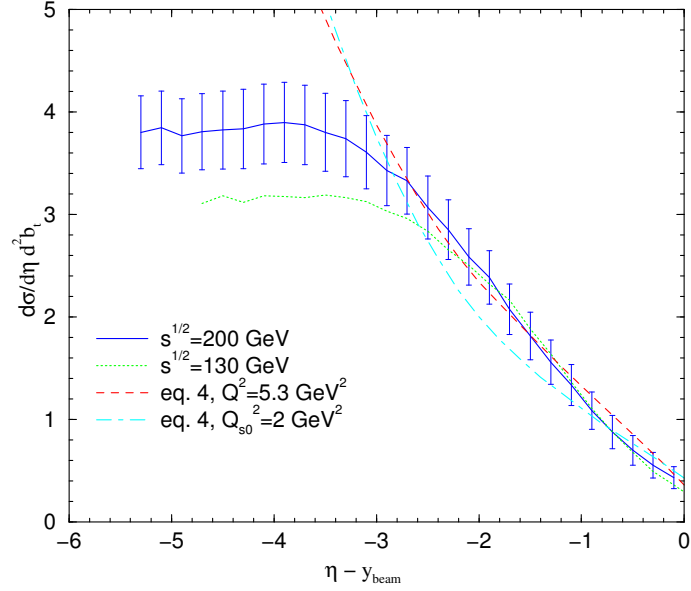


Figure 5.33: Limiting fragmentation from CGC model compared to 0-6% central data from PHOBOS at $\sqrt{s_{NN}} = 200$ GeV.

The color glass condensate picture of particle production has been found to be successful in explaining the pseudorapidity distributions of charged particle from PHOBOS experiment [7] at $\sqrt{s_{NN}} = 200$ GeV. Recently the energy dependence of limiting fragmentation phenomena has also been explained within the framework of CGC carried out in Ref. [12] as shown in Fig. 5.33.

Bibliography

- [1] J. D. Bjorken, Phys. Rev. D **27**, (1983) 140; L. D. Landau, Izv. Akad. Nauk Ser. Fiz. **17**, (1953) 51; S. Belenkij and L. D. Landau, Usp. Fiz. Nauk. **56**, (1955) 309; Nuovo Cim. Suppl. **3S10**, (1956) 15; R. C. Hwa and K. Kajantie, Phys. Rev. D **32**, (1985) 1190; J. Alam *et al.*, Annals of Phys. **286**, (2000) 159; B. Mohanty and J. Alam, Phys. Rev. C **68**, (2003) 064903.
- [2] E895 Collaboration, J. L. Klay *et al.*, Phys. Rev. Lett. **88**, (2002) 102301; E895 Collaboration, J. L. Klay *et al.*, Phys. Rev. C **68**, (2003) 054905.
- [3] P. K. Netrakanti and B. Mohanty, Phys. Rev. C **71**, (2005) 047901; J. Aichelin and K. Werner, Phys. Lett. B **300**, (1993) 158.
- [4] L. V. Gribov, E. M. Levin and M. G. Ryskin, Phys. Rep. **100**, (1983) 1; J. P. Blaizot and A. H. Mueller, Nucl. Phys. B **289**, (1987) 847.
- [5] L. McLerran and R. Venugopalan, Phys. Rev. D **49**, (1994) 2233; L. McLerran and R. Venugopalan, Phys. Rev. D **50**, (1994) 2225; Y. V. Kovchegov, Phys. Rev. D **54**, (1996) 5463; E. Iancu and L. McLerran, Phys. Lett. B **510**, (2001) 145; A. Krasnitz and R. Venugopalan, Phys. Rev. Lett. **84**, (2000) 4309.
- [6] PHENIX Collaboration, K. Adcox *et al.*, Phys. Rev. Lett. **86**, (2001) 3500.
- [7] PHOBOS Collaboration, B. B. Back *et al.*, Phys. Rev. Lett. **87**, (2001) 102303; PHOBOS Collaboration, B. B. Back *et al.*, Phys. Rev. Lett. **91**, (2003) 052303.
- [8] D. Kharzeev, E. Levin and M. Nardi, Phys. Rev. C **71**, (2005) 054903.
- [9] STAR Collaboration, J. Adams *et al.*, Phys. Rev. Lett. **95**, (2005) 062301.
- [10] D. Kharzeev, Phys. Lett. B **378**, (1996) 238; V. T. Pop *et al.*, Phys. Rev. C **70**, (2004) 064906.

- [11] K. Itakura, Y. V. Kovchegov, L. McLerran and D. Teaney, Nucl. Phys. A **730**, (2004) 160.
- [12] J. Jalilian-Marian, Phys. Rev. C **70**, (2004) 027902.
- [13] S. Jeon, V. T. Pop and M. Bleicher, Phys. Rev. C **69**, (2004) 044904.
- [14] WA98 Collaboration, M. M. Aggarwal *et al.*, Phys. Rev. C **65**, (2002) 054912.
- [15] H. Heiselberg, Phys. Rep. **351**, (2001) 161.
- [16] B. Mohanty and J. Serreau, Phys. Rep. **414**, (2005) 263; WA98 Collaboration, M. M. Aggarwal *et al.*, Phys. Rev. C **64**, (2001) 011901(R).
- [17] K. H. Ackermann *et al.*, Nucl. Instr. Meth. A **499**, (2003) 624.
- [18] K. H. Ackermann *et al.*, Nucl. Instr. Meth. A **499**, (2003) 713.
- [19] M. M. Aggarwal *et al.*, Nucl. Instr. Meth. A **499**, (2003) 751; M. M. Aggarwal *et al.*, Nucl. Instr. Meth. A **488**, (2002) 131.
- [20] P. K. Netrakanti and Bedangadas Mohanty, Phys. Rev. C **70**, (2004) 027901
- [21] X-N. Wang and M. Gyulassy, Phys. Rev. D **44**, (1991) 3501.
- [22] B. Zhang *et al.*, Phys. Rev. C **61**, (2000) 067901.
- [23] BRAHMS Collaboration, I. G. Bearden *et al.*, Phys. Lett. B **523**, (2001) 227; BRAHMS Collaboration, I. G. Bearden *et al.*, Phys. Rev. Lett. **88**, (2002) 202301.
- [24] S. Jeon and J. I. Kapusta, Phys. Rev. C **63**, (2001) 011901.
- [25] D. Kharzeev and M. Nardi, Phys. Lett. B **507** (2001) 121; D. Kharzeev and E. Levin, Phys. Lett. B **523** (2001) 79.
- [26] BRAHMS Collaboration, I. G. Bearden *et al.*, Phys. Rev. Lett. **93**, (2004) 102301.
- [27] PHOBOS Collaboration. B. B. Back *et al.*, Phys. Rev. Lett **85**, (2000) 3100; P.K. Netrakanti and B. Mohanty, Phys. Rev. C **70**, (2004) 027901.
- [28] X-N. Wang and M. Gyulassy, Phys. Rev. Lett **86**, (2001) 3496; A. Capella and D. Sousa, Phys. Lett. B **511** (2001) 185.

- [29] B. Mohanty, J. Alam and T. K. Nayak, Phys. Rev. C **67**, (2003) 024904.
- [30] Proceedings of Quark Matter 2004 [Jour. of Phys. G **30** (2004)].
- [31] J. Aichelin and K. Werner, Phys. Lett. B **300**, (1993) 158.
- [32] B. Mohanty and J. Alam, Phys. Rev. C **68**, (2003) 064903.
- [33] NA49 Collaboration, S. V. Afanasiev *et al.*, Phys. Rev. C **66**, 054902 (2002) 054902.
- [34] BRAHMS Collaboration, I. G. Bearden *et al.*, nucl-ex/0403050.
- [35] P. Carruthers and M. Duong-van, Phys. Lett. B **41**, (1972) 597; Phys. Rev. D **8**, (1973) 859.
- [36] NA50 Collaboration, M. C. Abreu *et al.*, Phys. Lett. B **530**, (2002) 43.
- [37] N. Xu and M. Kaneta, Nucl. Phys. A **698**, (2002) 306.
- [38] D. Teaney, J. Lauret and E. V. Shuryak, nucl-th/0110037.
- [39] STAR Collaboration, K. H. Ackermann *et al.*, Phys. Rev. Lett **86**, (2001) 402.
- [40] Aachen-CERN-Heidelberg-Munich Collaboration, W. Thorne *et al.*, Nucl.Phys. B **129** (1977) 365.
- [41] WA98 Collaboration, M. M. Aggarwal *et al.*, Phys. Lett. B **458**, (1999) 422.
- [42] WA98 Collaboration, M. M. Aggarwal *et al.*, Eur. Phys. J. C **18**, (2001) 651.
- [43] PHENIX Collaboration, K. Adcox *et al.*, Phys. Rev. Lett **87**, (2001) 052301.
- [44] PHOBOS Collaboration, B. B. Back *et al.*, Phys. Rev. C **65**, (2002) 061901.
- [45] S. Eremin and S. Voloshin, Phys. Rev. C **67**, (2003) 064905.
- [46] J. Benecke and T. T. Chou, C. N. Yang and E. Yen, Phys. Rev. **188** (1969) 2159
- [47] R. Beckmann, S. Raha, N. Stelte and R.M. Weiner, Phys. Lett. B **105**, (1981) 411.
- [48] CDF Collaboration, F. Abe *et al.*, Phys. Rev. D **41** (1990) 2330.

- [49] UA5 Collaboration, R. E. Ansorge *et al.*, Z.Phys. C **43** (1989) 1.
- [50] PHOBOS Collaboration, B. B. Back *et al.*, Phys.Rev. C **72** (2005) 031901.
- [51] WA93 Collaboration, M. M. Aggarwal *et al.*, Phys. Rev. C **58**, (1998) 1146;
WA93 Collaboration, M. M. Aggarwal *et al.*, Phys. Lett. B **403**, (1997) 390.
- [52] UA5 Collaboration, K. Alpgard *et al.*, Phys. Lett. B **115**, (1982) 71; G. J. Alner *et al.*, Z. Phys. C **33**, (1986) 1.
- [53] BRAHMS Collaboration, I. G. Bearden *et al.*, Phys. Rev. Lett. **94**, (2005) 162301.
- [54] NA49 Collaboration, S. V. Afanasiev *et al.*, Phys. Rev. C **66**, (2002) 054902.
- [55] NA49 Collaboration, H. Appelshäuser *et al.*, Phys. Rev. Lett. **82**, (1999) 2471.
- [56] E917 Collaboration, B. B. Back *et al.*, Phys. Rev. C **66**, (2002) 054901.
- [57] S. E. Vance, M. Gyulassy and X. -N .Wang, Phys. Lett. B **443**, (1998) 45;
S. E. Vance and M. Gyulassy, Phys. rev. Lett. **83** (1999) 1735.

Chapter 6

CONCLUSION

The STAR experiment at RHIC is primarily designed to study relativistic heavy ion collisions at center-of-mass energies ($\sqrt{s_{NN}}$) ranging from 20 GeV to 200 GeV. The present thesis deals with the first measurement of photon multiplicity in STAR experiment at RHIC. The photon multiplicity is measured using the PMD and is compared to charged particle multiplicity measured by FTPC in forward rapidity. The results discussed in this thesis are from Au+Au collisions at $\sqrt{s_{NN}} = 62.4$ GeV. The data are also compared to results from other experiments at higher and lower center-of-mass energies to draw physics conclusions on particle production mechanism at RHIC.

The inclusive photon multiplicity was measured over a wide range of pseudorapidity (η) from 2.3 to 3.7 units with a highly granular preshower detector, the PMD, which works on the principle of proportional counter. The PMD is made using an array of $\sim 82,000$ small hexagonal copper cells with a 8mm of gas depth. The sensitive medium used was a gas mixture of argon and carbon-di-oxide ($\text{Ar}+\text{CO}_2$) in 70:30 ratio by weight. It consists of two planes, one is preshower plane and other is veto plane, sandwiched is a 3 radiation length photon converter (lead) between these two planes. The charge particle multiplicity was measured by the FTPC which covers $2.6 < |\eta| < 4.2$ on both sides of the nominal collision point in the STAR experiment. It is cylindrical in shape, inside magnetic field and has 10 padrows in each side to measure the spatial position, charge sign and momentum of the charge particles. The sensitive medium used is a gas mixture of argon and carbon-di-oxide ($\text{Ar}+\text{CO}_2$) in 50:50 ratio. In this thesis we have briefly described the detector parameters of PMD and FTPC. This is followed by presentation of the procedures involved in the data cleanup, calibration and reconstruction for

both the detectors. The estimation of efficiency and purity of photon and charged particle multiplicity has been discussed in detail.

The data from PMD and FTPC have been used to study the pseudorapidity distributions of photons and charge particles respectively at forward rapidity. The pseudorapidity distributions are studied for various centrality classes. These distributions have been compared to various particle production models like HIJING, AMPT and LEXUS. We observe that AMPT model gives relatively better explanation of the data compared to other models at forward rapidity. The width of the pseudorapidity distribution has been shown to be sensitive to various physics effects, such as longitudinal flow, velocity of sound in the medium formed in heavy ion collisions and re-scatterings between the particles. Energy dependence of particle production is studied and compared to models based on parton saturation to see at what energies such a phenomena sets in. To understand the role of soft and hard (e.g jets) processes to particle production, the scaling of photon and charge particle multiplicity at forward rapidity with number of participating nucleons (N_{part}) and number of binary collisions (N_{coll}) has been studied. The photon multiplicity is found to scale with the number of participating nucleons while the charge particle multiplicity does not follow the participant scaling at the forward rapidity. Both photon and charge particle production do not scale with the number of binary collisions at forward rapidity. We have also observed an interesting scaling with number of quark participants in various global observables like $dN_{ch}/d\eta$, $dN_{\gamma}/d\eta$ and $dE_T/d\eta$ at mid-rapidity in heavy ion collisions.

The longitudinal scaling of particle production has been reported earlier in nucleon-nucleon, nucleon-nucleus and nucleus-nucleus collisions for charge particles. In such studies one looks at the pseudorapidity distributions of particles normalized to N_{part} at various center-of-mass energies as a function of rapidity shifted by beam rapidity ($\eta - y_{beam}$). This phenomenon is called limiting fragmentation. In this thesis we have investigated this phenomena by studying the pseudorapidity distributions for photons and charged particles in Au+Au collisions at $\sqrt{s_{NN}} = 62.4$ GeV. The longitudinal scaling of photon production in heavy ion collisions as a function of $\eta - y_{beam}$ has been presented for first time. It was found that the photon production normalized to N_{part} is energy as well as centrality independent when studied as a function of $\eta - y_{beam}$ at forward rapidity, whereas for charged particles it is found to be independent of energy only. To understand the breaking of such scaling as a function of collision centrality for charged particles we have

also presented the charge particle production normalized to N_{part} and differentiated in charge (for h^+ and h^-) as a function of $\eta - y_{beam}$ for central and peripheral collisions. Breaking of the scaling for positively charged particles will indicate the role of beam remnants and that for both positively and negatively charged particles will show the contribution from baryon transport mechanism. We found that the difference in positively charge particle production normalized to N_{part} as a function of $\eta - y_{beam}$, between central and peripheral collisions is more pronounced than that for negatively charge particles. This led us to the conclusion that beam remnants and baryon transport are both responsible for breakdown of longitudinal scaling in charge particle production at forward rapidity in Au+Au collisions. In this thesis we have also studied the identified particle longitudinal scaling in heavy ion collisions. We have presented the longitudinal scaling for pions and net protons for various center-of-mass energies. The scaling is observed for pions while it breaks down for net protons when particle production is studied as a function of $\eta - y_{beam}$.